

ATLAS OF STRUCTURAL GEOLOGY

SECOND EDITION



EDITED BY
SOUMYAJIT MUKHERJEE

Atlas of Structural Geology

Atlas of Structural Geology

Second edition

Edited by

Soumyajit Mukherjee

Associate Professor

Geodynamics Lab

Department of Earth Sciences

Indian Institute of Technology Bombay

Powai, Mumbai 400 076, Maharashtra, India



ELSEVIER

Elsevier
Radarweg 29, PO Box 211, 1000 AE Amsterdam, Netherlands
The Boulevard, Langford Lane, Kidlington, Oxford OX5 1GB, United Kingdom
50 Hampshire Street, 5th Floor, Cambridge, MA 02139, United States

Copyright © 2021 Elsevier Inc. All rights reserved.

No part of this publication may be reproduced or transmitted in any form or by any means, electronic or mechanical, including photocopying, recording, or any information storage and retrieval system, without permission in writing from the publisher. Details on how to seek permission, further information about the Publisher's permissions policies and our arrangements with organizations such as the Copyright Clearance Center and the Copyright Licensing Agency, can be found at our website: www.elsevier.com/permissions.

This book and the individual contributions contained in it are protected under copyright by the Publisher (other than as may be noted herein).

Notices

Knowledge and best practice in this field are constantly changing. As new research and experience broaden our understanding, changes in research methods, professional practices, or medical treatment may become necessary.

Practitioners and researchers must always rely on their own experience and knowledge in evaluating and using any information, methods, compounds, or experiments described herein. In using such information or methods they should be mindful of their own safety and the safety of others, including parties for whom they have a professional responsibility.

To the fullest extent of the law, neither the Publisher nor the authors, contributors, or editors, assume any liability for any injury and/or damage to persons or property as a matter of products liability, negligence or otherwise, or from any use or operation of any methods, products, instructions, or ideas contained in the material herein.

Library of Congress Cataloging-in-Publication Data

A catalog record for this book is available from the Library of Congress

British Library Cataloguing-in-Publication Data

A catalogue record for this book is available from the British Library

ISBN: 978-0-12-816802-8

For information on all Elsevier publications
visit our website at <https://www.elsevier.com/books-and-journals>

Cover photo courtesy: C. Frassi, Raffaele Gazzola, and Giovanni Musumeci. See Fig. 2.6
and its caption for detail.

Publisher: Candice Janco
Acquisitions Editor: Peter J. Llewellyn
Editorial Project Manager: Ruby Smith
Production Project Manager: Paul Prasad Chandramohan
Cover Designer: Matthew Limbert

Typeset by SPi Global, India



Contents

List of Contributors	vii		
Preface to the First Edition	xv		
Preface to the Second Edition	xvii		
Acknowledgements to the First Edition	xix		
Acknowledgements to the Second Edition	xxi		
1. Folds	1	4. Boudins and mullions	173
2. Ductile shear zones	67	5. Veins	191
3. Brittle faults	111	6. Various structures	199
		Author Index	251
		Subject Index	257

List of Contributors

Cantarero Abad, E-mail: i_cantarero@ub.edu

Peace Alexander, E-mail: peacea2@mcmaster.ca, School of Geography and Earth Sciences, Room 220, McMaster University, Hamilton, ON, Canada, L8S 4K1, + 1 905-525-9140 x 23152 + 39 0502215700

Marco Antonellini, E-mail: m.antonellini@unibo.it

Max Arndt, E-mail: max.arndt@emr.rwth-aachen.de Info: EMR - Energy & Mineral Resources Group, Geologie - Endogene Dynamik, RWTH Aachen University, Lochnerstrasse 4-20, D-52056 Aachen, Germany; Tel: +49-241-80-98438

Paola Ferreira Barbosa, E-mail: paolafeba@yahoo.com.br Info: Center of Microscopy, Universidade Federal de Minas Gerais, Avenida Perimetral Sul, 91-129 - Campus da UFMG, Belo Horizonte - MG, Brazil; CEP: 31255-040; Tel: (55 31) 3409-7575

G.C. Barik, E-mail: gagan.barik@gsi.gov.in

Ananya Basu, E-mail: an.basuju@gmail.com Info: Department of Geological Sciences, Jadavpur University, Kolkata, West Bengal, India; Pin-700 032; 0919007684783 (M)

Francisco Hilario R. Bezerra, E-mail: bezerrafh@geologia.ufrn.br

Anindya Bhattacharya, E-mail: anindya.bhattacharya@gsi.gov.in

Aparajita Bhattacharya, E-mail: aparajita.bhattacharya@gsi.gov.in

Andrea Billi, E-mail: andrea.billi@cnr.it Info: Consiglio Nazionale delle Ricerche, IGAG, c.o. Dipartimento Scienze della Terra, Sapienza Università di Roma, P.le A. Moro 5, 00185, Rome, Italy; 390649914955 (M)

Ankita Biswas, E-mail: ankita.iitr09@gmail.com, Geological Survey of India, +91 8885011773

Tuhin Biswas, E-mail: tbtuhin24@gmail.com Info: Department of Earth Sciences, Indian Institute of Technology Bombay, Powai, Mumbai, Maharashtra, India; Pin-400 076; 919167517063 (M)

Chloë Bonamici, E-mail: chloebee@lanl.gov Info: Los Alamos National Laboratory, Chemistry Division (C-NR), Los Alamos, NM 87545; +1 505 664 0115

Svetoslav Bontchev, E-mail: srbontchev@gmail.com Info: Graf Ignatiev St. 53 G 1142, Sofia, Bulgaria; 359-884 338 115

Narayan Bose, E-mail: narayan.bghs@gmail.com Info: Department of Earth Sciences, Indian Institute of Technology Bombay, Powai, Mumbai, Maharashtra, India; Pin-400 076; 919029787238 (M)

Luis A. Buatois, E-mail: luis.buatois@usask.ca Info: Department of Geological Sciences, University of Saskatchewan, 114 Science Place, Saskatoon, Saskatchewan, Canada, S7N5E2; Phone: 1-306-966-5730

Paul K. Byrne, E-mail: pbyrne@carnegiescience.edu Info: Lunar and Planetary Institute, Universities Space Research Association, 3600 Bay Area Blvd., Houston, TX 77058; Phone office: 281-486-2140

Jonathan Saul Caine, E-mail: jscaine@usgs.gov Info: U. S. Geological Survey, P. O. Box 25046, MS 964, Denver, CO 80225-0046; 303 236 1822

Fernando Calamita, E-mail: calamita@unich.it

Zoé Candaux, E-mail: Candaux@gmail.com

Eloi Carola, E-mail: eloi.carola@gmail.com, Departament de Geodinamica i Geofísica, Facultat de Ciències de la Terra, Universitat de Barcelona, Martí i Franqués s/n, 08028, Barcelona, Spain, Irene, +34 616616829

Rusudan Chagelishvili, E-mail: rchagelishvili@gmail.com

L.S. Chamyal, E-mail: lschamyal@gmail.com

Sadhana M. Chatterjee, E-mail: sadhanamahato@gmail.com Info: Department of Geological Sciences, Jadavpur University, Kolkata, West Bengal, India; Pin-700 032; 9434217749 (M)

Sreejita Chatterjee, E-mail: sreejitach@gmail.com Info: Department Earth Sciences, Indian Institute of Technology Bombay, Powai, Mumbai, Maharashtra, India; Pin-400 076; 8879048571 (M)

T.R.K. Chetty, E-mail: trkchetty@gmail.com Info: National Geophysical Research Institute, Hyderabad, Andhra Pradesh, India; Pin-500 007; 9885676086 (M)

- Mainak Choudhuri**, E-mail: mainak_ch@yahoo.co.in Info: Reliance Industries Limited, Petroleum Business (E & P), Mumbai, India; Pin-400 071; 919967535923 (M)
- D. Cirillo**, E-mail: d.cirillo@unich.it
- Félix Compaired**, E-mail: compaired@aragon.es, 9^oB, 50006, Zaragoza, Spain
- Raffaele Di Cuia**, E-mail: rdiucia@delteng.com, Via Ludovico Ariosto 58, 44121, Ferrara, Italy
- Muller Daniel**, E-mail: danielmuller33@yahoo.com, Leonardo da Vinci 7074, Apto 203, Las Condes, Santiago, Chile, 56934204284
- Rohini Das**, E-mail: romiyadas@gmail.com Info: Department of Earth Sciences, Indian Institute of Technology Roorkee, Roorkee, Uttarakhand, India; Pin-247 667; 8126694552 (M), 9831518422 (M)
- Sankha Das**, E-mail: sankhad56@gmail.com Info: Geological Survey of India, State Unit, Andhra Pradesh, Southern Region, Bandlaguda, Hyderabad, Andhra Pradesh; Pin-500068; 09642276706 (M), 09830154951 (M)
- Sudipta Dasgupta**, E-mail: sudipta.dasgupta@usask.ca Info: Department of Geological Sciences, University of Saskatchewan, 114 Science Place, Saskatoon, Saskatchewan, Canada S7N 5E2; 13069662457 (O)
- Swagato Dasgupta**, E-mail: swagato.dg@gmail.com Info: Reliance Industries Ltd., Exploration & Production, Navi Mumbai, Maharashtra, India; Pin-400 701; 919987538641 (M)
- Bhushan S. Deota**, E-mail: bdeota@rediffmail.com Info: Department of Geology, Faculty of Science, The Maharaja Sayajirao University of Baroda, Vadodara, Gujarat; 390002; 9898097211 (M)
- Tine Derez**, E-mail: Tine.Derez@ees.kuleuven.be Info: Department of Earth and Environmental Sciences, KU Leuven, Celestijnenlaan 200E box 2410, B-3001 Heverlee, Belgium; +32(0)496502579
- Natalie Deseta**, E-mail: suridae@gmail.com Info: School of Geosciences, University of the Witwatersrand, Private Bag 3, WITS 2050; 27796096295 (M)
- Marc Diraison**, E-mail: marc.diraison@espe.unistra.fr
- Arindam Dutta**, E-mail: arindam.dutta@gsi.gov.in, Geological Survey of India, Kolkata, India, +91 9724794399
- Dripta Dutta**, E-mail: dripta.dutta@gmail.com Info: Department of Earth Sciences, Indian Institute of Technology Bombay, Powai, Mumbai, Maharashtra, India; Pin-400 076; 919167521824 (M)
- Shukla Dutta**, E-mail: shukla.bhattacharya@gsi.gov.in
- Amy Ellis**, E-mail: amyellis@hotmail.co.uk Info: Ikon Science Ltd, Rivergreen Centre, Durham, DH1 5TS, UK; +44 (0) 191 383 7362 (M)
- Onise Enukidze**, E-mail: onise.enukidze@tsu.ge
- Balsamo Fabrizio**, E-mail: fabrizio.balsamo@unipr.it, Department of Chemistry, Life Sciences and Environmental Sustainability, University of Parma, Parco Area delle Scienze 157/A, Campus Universitario, I-43124 Parma, Italy, +39 3393916459
- Ake Fagereng**, E-mail: FagerengA@cardiff.ac.uk Info: School of Earth & Ocean Science, Cardiff University, Main Building, Park Place, Cardiff, CF10 3AT, UK; +44 (0)29 208 70760 (O)
- Sanchez Felipe**, E-mail: felipe.reinoso2018@gmail.com, Departamento de Geología, Universidad de Atacama, Copayapu 485, Copiapó, Chile, +56 9 86636340
- Carlos Fernández**, E-mail: fcarlos@uhu.es Info: Departamento Geodinámica y Paleontología, Facultad de Ciencias Experimentales, Universidad de Huelva, Campus El Carmen, Avenida 3 de Marzo, 21071 Huelva, Spain; Phone: +34 959219857
- F. Ferrarini**, E-mail: f.ferrarini@unich.it
- Luigi De Filippis**, E-mail: luigidefilippis1@gmail.com Info: Dipartimento di Scienze, Università Roma Tre, Largo S.L. Murialdo 1, I-00146 Roma; +39-3286138869
- László Fodor**, E-mail: asz.fodor@yahoo.com Info: Hungarian Academy of Sciences MTA-ELTE, Geological, Geophysical and Space Sciences, Research Group at Eötvös University, Pázmány P. sétány 1/C; Phone: 36-1-3722500/8714
- Brozzetti Francesco**, E-mail: f.brozzetti@dst.unich.it, CRUST-DiSPUTer, University "G. d'Annunzio" of Chieti-Pescara, Chieti, Italy, ++39 871 3556416
- Chiara Frassi**, E-mail: chiarafrassi@gmail.com, Dipartimento di Scienze della Terra, Università di Pisa, via S. Maria 53, 56126, Pisa, Italy, 050 2215781
- M.S. Gadhavi**, E-mail: mahendrasinh@gmail.com Info: Civil Engineering Department, L. D. College of Engineering, Ahmedabad, 380 015 Gujarat, India; +91-9426272328 (M)
- Raffaele Gazzola**, E-mail: raffaele.gazzola@gmail.com, Dipartimento di Scienze della Terra, Università di Pisa, via S. Maria 53, 56126, Pisa, Italy, +39 0502215700
- Yves Géraud**, E-mail: yves.geraud@univ-lorraine.fr
- Rajkumar Ghosh**, E-mail: rajkumargheol@gmail.com Info: Department of Earth Sciences, Indian Institute of Technology Bombay, Powai, Mumbai, Maharashtra, India; Pin-400 076; 9167520347 (M)

- Guido Gosso**, E-mail: Guido.Gosso@unimi.it Info: Department of Earth Sciences, Università degli Studi di Milano; Città Studi, Via Mangiagalli 34, 20133 Milano, Italy; 3902 5031 55 55
- Sukanta Goswami**, E-mail: sukantagoswami@iitb.ac.in Info: Atomic Minerals Directorate for Exploration and Research (AMD), Department of Atomic Energy (DAE), Southern Region, Nagarbhavi, Bangalore, India; Pin-560 072; 8088872383 (M)
- Tapos Kumar Goswami**, E-mail: taposgoswami@gmail.com Info: Department of Applied Geology, Dibrugarh University, Dibrugarh, Assam, India; Pin-786 004; 919435352889 (M)
- Jens Carsten Grimmer**, E-mail: jens.grimmer@kit.edu Info: Institute of Applied Geosciences, Adenauerring 20b, 76131 Karlsruhe, Germany; +49 721 608 41888
- Ranjan Gupta**, E-mail: gupta.ranjan256@gmail.com Info: Rampura Agucha Mine, Hindustan Zinc Limited, Rajasthan, India; 91-9799175999 (M)
- Saibal Gupta**, E-mail: saibl2008@gmail.com Info: Department of Geology and Geophysics, Indian Institute of Technology Kharagpur, Kharagpur, West Bengal, India; Pin: 721302; +91-3222-283370 (M)
- Mohamed Th.S. Heikal**, E-mail: mohamedheikal52@gmail.com, Geology Department, Faculty of Science, Tanta University, Egypt, + 2 01012392925
- Ghatak Hindol**, E-mail: hindol.ghatak@hdr.mq.edu.au, ARC Centre of Excellence for Core to Crust Fluid Systems (CCFS), Department of Earth and Planetary Sciences, Macquarie University, Sydney, Australia, +61 470659066
- Tomokazu Hokada**, E-mail: hokada@nipr.ac.jp Info: Geology Group, National Institute of Polar Research, 10-3 Midori-cho, Tachikawa, Tokyo 190-8518, Japan; Phone: +81-42-512-0714
- Guillermo Alvarado Induni**, E-mail: GAlvaradoI@ice.go.cr Info: Área de Amenazas y Auscultación Sismológica y Volcánica, C.S. Exploración Subterránea/NIC-Electricidad. Apdo 10032-1000; Landline: 00506 89383752
- Cantarero Irene**, E-mail: i_cantarero@ub.edu, Departament de Mineralogia, Petrologia i Geologia Aplicada, Facultat de Ciències de la Terra, Universitat de Barcelona, Martí i Franqués s/n, 08028, Barcelona, Spain, +34 934031165
- Esther Izquierdo-Llavall**, E-mail: estheriz@unizar.es Info: Departamento Ciencias de la Tierra, Universidad de Zaragoza, Pedro Cerbuna St., 12, 50.009 Zaragoza, Spain; Phone: +34-976-762127
- Hibbard James**, E-mail: jphibbar@ncsu.edu, MEAS, NCSU, Raleigh, NC 27695, 919-818-7498
- Greenberg Jeffrey**, E-mail: jeffrey.greenberg@wheaton.edu, Wheaton College, Wheaton, IL 60187, USA; Home address: 811 N. President St., Wheaton, IL, 60187, USA, 331-431-3003
- Magloughlin Jerry**, E-mail: Jerry.Magloughlin@colostate.edu, Department of Geosciences, Colorado State University, Fort Collins, CO, 80523, USA, 970-491-1812, 970-290-6630
- Place Joachim**, E-mail: joachim.geo@gmail.com, Sweco Civil AB, Gjörwellsgatan 22, Box 340 44, SE-100 26, Stockholm, Sweden, + 46 (0) 18 471 7161
- Scott Johnson**, E-mail: johnsons@maine.edu Info: School of Earth and Climate Sciences, 5790 Bryand Global Sciences, University of Maine, Orono, ME 04469-5790, USA; (207)581-2142
- Büchner Jörg**, E-mail: Joerg.Buechner@senckenberg.de, Senckenberg Museum für Naturkunde Görlitz
- Aditya Joshi**, E-mail: adityaujoshi@gmail.com Info: Department of Geology, Faculty of Science, The M.S. University of Baroda, Vadodara, Gujarat, India; Pin-390 002; 918000421451 (M)
- Eirin Kar**, E-mail: sakurakar5@gmail.com Info: Department of Earth Sciences, Indian Institute of Technology Roorkee, Roorkee, Uttarakhand, India; Pin-247 667; 8439731513 (M)
- Rahul Kar**, E-mail: rkar48@gmail.com Info: Department of Geology and Geophysics, Indian Institute of Technology Kharagpur, West Bengal, India; Pin-721 302; 919749469334 (M)
- R.V. Karanth**, E-mail: r_v_karanth@yahoo.co.in Info: 104-Aarth Apartments, 29 - Pratapgunj, Vadodara - 390 002, Gujarat, India; 919998485468 (M)
- Amar Karaoui**, E-mail: amar.karaoui@yahoo.com
- Brahim Karaoui**, E-mail: karaouibrahim@yahoo.fr, P.O. Box 11201 Zitoune Meknès, Morocco
- Miklós Kázmér**, E-mail: mkazmer@gmail.com Info: Department of Palaeontology, Eotvos University, Pazmany Peter setany 1/c; 36-20-494-5275
- Subodha Khanal**, E-mail: skhanal@crimson.ua.edu Info: Department of Geological Sciences, University of Alabama, Tuscaloosa, AL, 35487, USA; 1(347)400-3645
- Christian Klimczak**, E-mail: cklimczak@ciw.edu Info: Department of Geology, 210 Field Street, University of Georgia, Athens, GA 30602-2501; 706-542-2977
- Hemin Koyi**, E-mail: Hemin.Koyi@geo.uu.se
- Samanta Susanta Kumar**, E-mail: susanta_ju@hotmail.com, Department of Geological Sciences, Jadavpur University, Kolkata, - 700 032, West Bengal, India, 91 9433168050

Leonardo Evangelista Lagoeiro, E-mail: lagoeiro@icloud.com
Info: Microanalysis and Microscopy Laboratory – MICROLAB, Universidade Federal de Ouro Preto, Geology Department, Morro do Cruzeiro, s/n, Ouro Preto, MG, CEP: 354000-000, Minas Gerais MG, Brazil; Tel: (55 31) 3559-1859; (55 31) 9838-5328 (M)

Mariano A. Larrovere, E-mail: marianlarro@gmail.com
Info: Centro Regional de Investigaciones Científicas y Transferencia Tecnológica de La Rioja (CRILAR-CONICET). Entre Ríos y Mendoza s/n. Anillaco (5301), La Rioja, Argentina; INGeReN-CENIIT-UNLaR. Av. Gob. Vernet y Apóstol Felipe, La Rioja (5300), Argentina; 540387715440689 (M)

G. Lavecchia, E-mail: glavecchia@unich.it

Del Sole Leonardo, E-mail: leonardo.delsole@unibo.it, BiGeA - Department of Biological Geological and Environmental Sciences, University of Bologna, Via Zamboni 67, 40126, Bologna, BO, Italy, 0039-051-2094574

M.A. Limaye, E-mail: manoj_geol@rediffmail.com
Department of Geology, Faculty of Science, The M.S. University of Baroda, Vadodara, Gujarat, India; Phone: 91 9824071285 (M)

Aasif Mohmad Lone, E-mail: aasifml@iiserb.ac.in, Department of Earth and Environmental Sciences, Indian Institute of Science Education and Research (IISER), Bhopal 462066, Madhya Pradesh, India, + 91- 09003952077, + 91-9682129478

Paul Lubrano-Lavadera, E-mail: paul.lavadera@sweco.se

Shengli Ma, E-mail: masl@ies.ac.cn
Info: State Key Laboratory of Earthquake Dynamics, Institute of Geology, China Earthquake Administration, P. O. Box 9803, Beijing 100029, China; Tel: 86-13426054959

Kankajit Maji, E-mail: kankajit.maji0@gmail.com
Info: Department of Earth Sciences, Indian Institute of Technology Bombay, Powai, Mumbai, Maharashtra, India; Pin-400 076; +91-022-2576-7281

Neil Mancktelow, E-mail: neil.mancktelow@erdw.ethz.ch
Info: Geological Institute, ETH Zurich, CH-8092 Zurich, Switzerland; +41 44 632 3671

Subhadip Mandal, E-mail: smandal@crimson.ua.edu
Info: Department of Geological Sciences, University of Alabama, 201 7th Avenue, Room No. 2003, Bevil Building, Tuscaloosa, AL 35487, USA; +1 (205) 348-5095

Yousuf Maqbool, E-mail: makyousuf@hotmail.com, Department of Civil Engineering, National Institute of Technology, Srinagar, Jammu and Kashmir, Pin 190006, India, 91 968258131

Cacador Marco, E-mail: martinsmarco@gmail.com, Universidade Federal de Goiás - UFG, Faculdade de Ciências e Tecnologia, Goiânia, GO, Brazil, +55 61 998484208

Jean-Michel Marthelot, E-mail: marthelot@unistra.fr

George Mathew, E-mail: gmathew@iitb.ac.in
Info: Department of Earth Sciences, Indian Institute of Technology Bombay, Powai, Mumbai, Maharashtra, India; Pin-400 076; 919820287275 (M)

Deepak M. Maurya, E-mail: dmmaurya@yahoo.com

Francesco Mazzarini, E-mail: mazzarini@pi.ingv.it
Info: Istituto Nazionale di Geofisica e Vulcanologia, Sezione di Pisa, Via della Faggiola 32, 56126 Pisa, Italy; Tel: +39 050 8311956

Patrick Meere, E-mail: p.meere@ucc.ie
Info: School of Biological, Earth & Environmental Sciences, University College Cork, Cork, Ireland; T: +353-21-490-3000; F: +353 21 490 3000

Biswas Mery, E-mail: merybiswas@gmail.com, Department of Geography, Presidency University, 86, 1, College Street, Kolkata, West Bengal 700073, India, 9804394758

Fondriest Michele, E-mails: michelefondriest@yahoo.it, michele.fondriest@univ-grenoble-alpes.fr, Office: 339, ISTerre - Université Grenoble Alpes, 1381 rue de la piscine, 38400, Saint Martin d'Heres (France), +39 3338189547

Petroccia Alessandro Giovanni Michele, E-mail: alessandro.petroccia@edu.unito.it, Università degli Studi di Torino, Dipartimento di Scienze della Terra, Italy, Via Valperga Caluso, 35 -, 10125, Torino (IT), + 39 3475693375

Achyuta Ayan Misra, E-mail: achyutaayan@gmail.com
Info: Department of Earth Sciences, Indian Institute of Technology Bombay, Powai, Mumbai, Maharashtra, India; Pin-400 076; Reliance Industries Limited, Petroleum Business (E & P), Mumbai, India; Pin-400 071; 919967017133 (M)

Perrot Morgan, E-mail: perrot.morgann@gmail.com, Université du Québec à Montréal (UQAM), Département des sciences de la Terre et de l'atmosphère, 201 av. du Président Kennedy, Montréal, (Qc), H2X 3Y7, Canada, + 1 514 994 2135

Awais Muhammad, E-mail: awais.geo@uoswabi.edu.pk, Department of Geology, University of Swabi, Swabi, Khyber Pakhtunkhwa (KP), Pakistan, +923449025508, +923159902636

Atanu Mukherjee, E-mail: atanu.pathor@gmail.com
Info: Atomic Minerals Directorate for Exploration and Research, Department of Atomic Energy, Bangalore, India; Pin-500 016; 7483028746 (M)

- Soumyajit Mukherjee**, E-mail: soumyajitm@gmail.com Info: Department of Earth Sciences, Indian Institute of Technology Bombay, Powai, Mumbai, Maharashtra, India; Pin-400 076; 9167625339 (M)
- Kieran F. Mulchrone**, E-mail: k.mulchrone@ucc.ie Info: Department of Applied Mathematics, School of Mathematical Sciences, University College, Cork, Ireland; 353214205822 (O)
- Giovanni Musumeci**, E-mail: giovanni.musumeci@unipi.it, Dipartimento di Scienze della Terra, Università di Pisa, via S. Maria 53, 56126, Pisa, Italy, +39 0502215745
- Vanik Naimisha**, E-mail: naimishavanik28@gmail.com, Department of Geology, Faculty of Science, The M S University of Baroda, Vadodara, - 390002, Gujarat, India, 91-9824438424
- Soreng Namrata**, E-mail: namrata.soreng22.ns@gmail.com, Department of Earth Sciences, Indian Institute of Technology Bombay, Powai, Mumbai, 400 076, Maharashtra, India, 7977231974
- Shruthi Narayanan**, E-mail: 123060007@iitb.ac.in Info: Department of Earth Sciences, Indian Institute of Technology Bombay, Powai, Mumbai, Maharashtra, India; Pin-400 076; 91-9967042788 (M)
- Payman Navabpour**, E-mail: payman.navabpour@gmail.com Info: Friedrich Schiller Universität Jena, Institut für Geowissenschaften, Jena, Germany; 49-17672244672
- Lucie Novakova**, E-mail: lucie.novakova@irms.cas.cz Info: Department of Seismotectonics, Institute of Rock Structure and Mechanics, Academy of Sciences of the Czech Republic, V Holešovičkách 41, 182 09 Prague 8; Phone: +420605117392
- Belén Oliva-Urcia**, E-mail: boliva@unizar.es Info: Departamento de Ciencias de la Tierra, Universidad de Zaragoza, 50009 Zaragoza, Spain; +34 976 762 127 (M)
- Yasuhito Osanai**, E-mail: osanai@scs.kyushu-u.ac.jp Info: Division of Earth Sciences, Department of Environmental Changes, Faculty of Social and Cultural Studies, Kyushu University, 744 Motooka, Fukuoka, 819-0395 Japan; Phone: +81-92-802-5660
- Masaaki Owada**, E-mail: owada@sci.yamaguchi-u.ac.jp Info: Graduate school of Science and Technology, Division of Earth Sciences, Yamaguchi University, Yoshida 1677-1, Yamaguchi, 753-8512 Japan; Phone: +81-83-933-5751
- Paolo Pace**, E-mail: p.pace@unich.it Info: Dipartimento di Ingegneria e Geologia, Università degli Studi "G.d'Annunzio" di Chieti Pescara, Via dei Vestini, 31, 66013, Chieti Scalo (CH), Italy; 393490825427 (M)
- Dipak C. Pal**, E-mail: dipak.pal@gmail.com
- Jorge Manuel Vieira Pamplona**, E-mail: jopamp@dct.uminho.pt, ICT, Departamento de Ciências da Terra, Escola de, +351 253604300
- M.K. Panigrahi**, E-mail: mkp@gg.iitkgp.ernet.in Info: Department of Geology and Geophysics, Indian Institute of Technology Kharagpur, Kharagpur, West Bengal, India; Pin: 721302; +91-3222-283376 (O)
- Singh Paramjeet**, E-mail: psinghgeol@gmail.com, Wadia Institute of Himalayan Geology, 33, General Mahadev Singh Rd, Vijay Park, Dehradun, Uttarakhand 248001, India, Phone: (O) +91-135-2525130, Mobile: +91-9410763990
- Jyotirmoy Paul**, E-mail: djyo.geos01@gmail.com Info: Department of Geological Sciences, Jadavpur University, Kolkata, West Bengal, India; Pin-700 032; 0919051469485 (M)
- Victoria Pease**, E-mail: vicky.pease@geo.su.se Info: Department of Geological Sciences, PetroTectonics Facility, Stockholm University, SE-106 91 Stockholm, Sweden; 468674-7321
- Giorgio Pennacchioni**, E-mail: giorgio.pennacchioni@unipd.it Info: Dipartimento di Geoscienze, University of Padova, Via Gradenigo 6, Italy; +39 338 6718488 (M)
- Roberto Vizeu Lima Pinheiro**, E-mail: vizeu@ufpa.br Info: Universidade Federal do Para - Faculdade de Geologia -, Brazil; (0055 91) 32017393
- Suellen Olívia Cândida Pinto**, E-mail: suellen_olivia@yahoo.com.br Info: Federal University of Ouro Preto, Geology Engineering Department, Ouro Preto, Brazil
- Andrés Pocoví**, E-mail: apocovi@unizar.es Info: Geotransfer Res. Group, Department of Earth Sciences, Pedro Cerbuna 12, 50009 Zaragoza; +34 976 76 20 72
- Brian R. Pratt**, E-mail: brian.pratt@usask.ca Info: Department of Geological Sciences, University of Saskatchewan, 114 Science Place, Saskatoon, Saskatchewan, Canada, S7N5E2; Phone: 1-306-966-5725
- Emilio L. Pueyo**, E-mail: unaim@igme.es, Instituto Geológico y Minero de España, Unidad de Zaragoza, C/Francisco Lasala 44, +34 976 650412
- Debjani Raychaudhuri**, E-mail: debjani.raychaudhuri@gsi.gov.in
- Guido Sibaja Rodas**, E-mail: guisibro@gmail.com Info: San Isidro de Coronado. 50 m al este de la entrada al Restaurante Lone Star Grill, Condominio Quintana de los Reyes número 21. Vásquez de Coronado. San José, Costa Rica; (506) 2292-2296, (506) 8998-6018
- B.J.C. Rodrigues**, E-mail: bjcrodrigues@gmail.com, Ciências, Universidade do Minho, Campus de Gualtar, 4710-057, Braga, Portugal

- Federico Rossetti**, E-mail: federico.rossetti@uniroma3.it Info: Dipartimento di Scienze, Università degli Studi Roma Tre, L.go S.L. Murialdo, 1, 00146 Rome, Italy; +39 06 57338043 (M)
- Priyom Roy**, E-mail: roy.priyom@gmail.com, Hyderabad, India
- Rajib Sadhu**, E-mail: imrajib.geo@gmail.com Info: Office address: Premiere Miniere Du Katanga P.M.K. Sprl 4 Avenue Des Cypres N R C: 10316 ID. NAT:6-118-N60935L Lubumbashi R.D.Congo; 243-976325555
- Nino Sadradze**, E-mail: ninosadradze@gmail.com, M. Alexidze str.1, 0171, Tbilisi, Georgia
- Dilip Saha**, E-mail: sahad.geol@gmail.com Info: Geological Studies Unit, Indian Statistical Institute, 203 B T Road, Kolkata, India; Pin-700 108; 919433559563 (M)
- Hossain Sakawat**, E-mail: sakawat@juniv.edu, Department of Geological Sciences, Jahangirnagar University, Dhaka, -1342, Bangladesh
- Dnyanada Salvi**, E-mail: salvidnyanada@gmail.com Info: Department of Earth Sciences, Indian Institute of Technology Bombay Powai, Mumbai 400 076, Maharashtra, India; Phone: +91-022-2576-7251; 9869007336 (M)
- Anupam Samanta**, E-mail: anupam.jugeology@gmail.com Info: Department of Geological Sciences, Jadavpur University, Kolkata, West Bengal, India; Pin-700 032; 91-9046368545 (M)
- Elisa M. Sánchez**, E-mail: emsanchez@ubu.es Info: Paleomagnetic Laboratory, Physics Dept. Universidad de Burgos, Avda. de Cantabria, s/n, 09006 Burgos, Spain; +34 947 25 8978
- De Sanjukta**, E-mail: sanjuktade2401@gmail.com, Department of Geology & Geophysics, Indian Institute of Technology Kharagpur, Pin 721302, West Bengal, India, 91-918697161633
- Moloy Sarkar**, E-mail: moloy.sarkar1992@gmail.com Info: Department of Earth Sciences, Indian Institute of Technology Roorkee, Roorkee, Uttarakhand, India; Pin-247 667; 09038850981 (M), 08791258153 (M)
- Judith Sausse**, E-mail: judith.sausse@univ-lorraine.fr
- Petr Schnabl**, E-mail: schnabl@gli.cas.cz, The Czech Academy of Sciences, Institute of Geology, Rozvojová 269, 160 00, Prague, 6, Czech Republic, + 420 272 690 115
- Jennifer J. Scott**, E-mail: jjscott@ualberta.ca Info: Department of Geological Sciences, University of Saskatchewan, 114 Science Place, Saskatoon, SK, Canada S7N 5E2
- Souvik Sen**, E-mail: souvikseniitb@gmail.com Info: Department of Earth Sciences, Indian Institute of Technology Bombay, Powai, Mumbai, Maharashtra, India; Pin-400 076; 918348690112 (M)
- Sudipta Sengupta**, E-mail: sudiptasg@yahoo.com Info: Department of Geological Sciences, Jadavpur University, Kolkata, West Bengal, India; Pin-700 032; 0910332457 2712 (O)
- Mohammedharoon Shaikh**, E-mail: haroonshaikh00@gmail.com
- Hetu Sheth**, E-mail: hcsheth@iitb.ac.in Info: Department of Earth Sciences, Indian Institute of Technology Bombay, Powai, Mumbai, Maharashtra, India; Pin-400 076; 9102225767264 (O)
- Toshihiko Shimamoto**, E-mail: shima_kyoto@yahoo.co.jp Info: State Key Laboratory of Earthquake Dynamics, Institute of Geology, China Earthquake Administration, P. O. Box 9803, Beijing 100029, China; 18600262139 (M)
- Ichiko Shimizu**, E-mail: ichiko@eps.s.u-tokyo.ac.jp Info: Department of Earth and Planetary Science, University of Tokyo, 7-3-1 Hongo, Bunkyo-ku, Tokyo 113-0033, Japan; 81-3-5841-4513
- Kazuyuki Shiraishi**, E-mail: kshiraishi@nipr.ac.jp Info: Geology Group, National Institute of Polar Research, 10-3 Midori-cho, Tachikawa, Tokyo 190-8518, Japan; Phone: +81-42-512-0603
- Luiz Sérgio Amarante Simões**, E-mail: lsimoes@rc.unesp.br Info: Universidade Estadual Paulista Júlio de Mesquita Filho, Institute of Geosciences and Exact Sciences of Rio Claro, Department of Petrology and Metallogeny, Av. 24-A, n° 1515, Bela Vista, CEP: 13506-900, Rio Claro, SP – Brazil; Tel: (55 19) 3526-9257
- Masoch Simone**, E-mail: simone.masoch@phd.unipd.it, Dipartimento di Geoscienze, Università degli Studi di Padova, Via G. Gradenigo, 6, Padua, Italy, + 39 3473535642
- Aabha Singh**, E-mail: aabs_22@yahoo.co.in Info: Department of Geology, Fergusson College, F.C. Road, Shivaji Nagar, Pune, Maharashtra, India; Pin-411 004; 9920166093 (M)
- Bikramaditya Singh**, E-mail: rkaditya17@rediffmail.com Info: Wadia Institute of Himalayan Geology, GMS Road, Dehradun, Uttarakhand, India; Pin-248 001; 01352525103 (O)
- Shailendra Singh**, E-mail: singhgaur4@gmail.com Info: Geological Survey of India, GSITI, FTC Bhimtal, Northern Region, Lucknow, Uttarpradesh, India; 9450093216 (M)
- Manuel Sintubin**, E-mail: manuel.sintubin@ees.kuleuven.be Info: Geodynamics & Geofluids Research Group, Department of Earth & Environmental Sciences, KU Leuven, Celestijnenlaan 200E - box 2410, BE-3001 Leuven; Phone: +32 (0)16 32 64 47 - +32 (0)16 32 78 00
- Ruth Soto**, E-mail: r.soto@igme.es Info: Instituto Geológico y Minero de España (IGME), Unidad de Zaragoza. C/ Manuel Lasala, 44, 9B, 50006 Zaragoza, Spain; +34 976 555 153 (ext 26)

- Frank Strozyk**, E-mail: frank.strozyk@emr.rwth-aachen.de Info: EMR - Energy & Mineral Resources Group, Geological Institute, RWTH Aachen University, Wuellnerstr. 2, 52062 Aachen, Germany; Phone: +49-241-80-95718
- Yutaka Takahashi**, E-mail: takahashi-yutaka@aist.go.jp Info: Orogenic Process Research Group, Institute of Geology and Geoinformation, Geological Survey of Japan, AIST, 1-1-1 Higashi, Tsukuba, Ibaraki 305-8567, Japan; Phone: +81-29-861-3933
- Solanki Tarun**, E-mail: tarunsolanki86@yahoo.in, Institute of Seismological Research, Raisan, Gandhinagar, -382007, Gujarat, India, 91-9510336914
- Enrico Tavarnelli**, E-mail: tavarnelli@unisi.it
- Tetsuhiro Togo**, E-mail: duketogotetsu@gmail.com Info: Institute of Earthquake Volcano Geology, National Institute of Advanced Industrial Science and Technology (AIST), 1-1-1 Umezono, Tsukuba, Ibaraki 305-8568 Japan; Tel: 81-9099699526
- Balázs Törő**, E-mail: torobala@gmail.com Info: Department of Geological Sciences, University of Saskatchewan, Canada; +1 306 966 5737
- Giulio Di Toro**, E-mail: giulio.ditoro@unipd.it
- Tsuyoshi Toyoshima**, E-mail: ttoyo@geo.sc.niigata-u.ac.jp Info: Department of Geology, Faculty of Science, Niigata University, 8050 Ikarashi-2-nocho, Niigata 950-2181, Japan; +81-25-262-6199 (O)
- Toshiaki Tsunogae**, E-mail: tsunogae@geol.tsukuba.ac.jp Info: Graduate school of Life and Environmental Sciences (Earth Evolution Sciences), University of Tsukuba, Ibaraki, 305-8572, Japan; Phone: +81 29 853 5239
- Janos L. Urai**, E-mail: j.urai@ged.rwth-aachen.de Info: EMR - Energy & Mineral Resources Group, Geologie - Endogene Dynamik, RWTH Aachen University, Lochnerstrasse 4-20, D-52056 Aachen, Germany; Tel: +49-241-80-95723
- Alania Victor**, E-mail: victor.alania@tsu.ge, Institute of Geophysics, Tbilisi State University, +995 (32) 395476
- Gianluca Vignaroli**, E-mail: gianluca.vignaroli@uniroma3.it Info: Dipartimento di Scienze, Università degli Studi Roma Tre, L.go S.L. Murialdo, 1, 00146 Rome, Italy; +39 06 57338043 (M)
- Simon Virgo**, E-mail: s.virgo@ged.rwth-aachen.de Info: EMR - Energy & Mineral Resources Group, Geologie - Endogene Dynamik, RWTH Aachen University, Lochnerstrasse 4-20, D-52056 Aachen, Germany; Tel: +49-241-80-98438
- Marko Vrabec**, E-mail: marko.vrabec@geo.ntf.uni-lj.si Info: University of Ljubljana, Faculty of Natural Sciences and Technology, Department of Geology, Privoz 11, SI-1000 Ljubljana, Slovenia; 38612445412 (O)
- Xin Wang**, E-mail: wx@zju.edu.cn
- Zakarya Yajoui**, E-mail: yajoui91@gmail.com, Department of Geology, Faculty of sciences, Moulay Ismail University, + 212 680650827
- Lu Yao**, E-mail: yaolu_cug@163.com Info: State Key Laboratory of Earthquake Dynamics, Institute of Geology, China Earthquake Administration, P. O. Box 9803, Beijing 100029, China; Tel: 86-13426054959
- Eyal Yehuda**, E-mail: eyal@bgu.ac.il, Department of Geological and Environmental Sciences, Ben-Gurion University of the Negev, Beersheba, Israel, 972-8-6461332
- Hongwei Yin**, E-mail: hwyin@nju.edu.cn
- Ran Zhang**, E-mail: Ran.Zhang@bhpbilliton.com Info: BHP Billiton Petroleum, 1360 Post Oak Blvd., Ste. 150, Houston, TX 77056-3030 USA; +1 713 297 6568
- Wu Zhenyun**, E-mail: zhenyun_wu@ecut.edu.cn, School of Geosciences, East China University of Technology, Nanchang, 330013, Jiangxi, China, (+ 86) 15005183920

Preface to the First Edition

Documentation of structures in different scales is the first step in many structural geological studies. This edited atlas gives an overview of diverse structures. Due to lack of space or inappropriateness, sometimes interesting structural snaps cannot be published in journals. This book fills that gap.

Preface to the Second Edition

Despite structural geology getting superspecialized in several (interdisciplinary) branches, the identification of structures from the field and under optical microscopes remains one of the most fundamental exercises. The first edition of this book was highly appreciated worldwide and found great use among researchers, instructors, and students. The book received an honorable mention in the *Prose Award* 2018. Further, the book was referred to in the syllabus of Toronto University's structural geology course.

About 145 new figures and captions have been included in this edition. A few references have been updated. Like the previous edition, one can observe that the style and the amount of writing of the different captions are nonuniform. This is because many authors contributed and their style of writing are almost always kept intact. Second, the book does not give morphological detail of all the structures, but attempts to do so as much as possible.

How to use this book: Obviously, this book is not a “textbook” of structural geology. (1) Before visiting their structural geological fieldwork, students can have a look at the images to train their eyes. (2) While teaching standard textbooks in class, such as those by M.P. Billings or H. Fossen, instructors can display structural geological photographs from this book. In this way, this book can act as a good supplement. (3) Modelers can look for the diversity of morphologies of the same structures, and simulate them (e.g., [Gogoi et al., 2017, in press](#)).

Our lab has already produced several structural atlases ([Mukherjee 2013, 2014, 2015](#)), and hope to serve the common purpose. I look forward to receiving comments on the interpretation of the structures presented here.

Cite this book as:

Mukherjee S. 2020. Atlas of Structural Geology. Second Edition. Elsevier. ISBN: 978-0-12-816802-8.

Cite contribution as:

Bose N, Mukherjee S. 2020. Rectangular boudinaged quartz veins in calc-schist. In: Mukherjee, S. (Ed) Atlas of Structural Geology. Second Edition. Elsevier. ISBN: 978-0-12-816802-8.

Soumyajit Mukherjee
Editor

soumyajitm@gmail.com
smukherjee@iitb.ac.in

References

- Gogoi, M.P., Mukherjee, S., Goswami, T.K., 2017. Analyses of fold profiles by changing weight parameters of NURB Curves. *Journal of Earth System Science* 126, 98.
- Gogoi MP, Mukherjee S, Goswami TK (in press) Asymmetric fold profiles simulated by cubic Bezier curves. *International Journal of Earth Sciences*. <https://doi.org/10.1007/s00531-020-01945-2>.
- Mukherjee, S., 2013. Deformation Microstructures in Rocks. Springer Geochemistry/Mineralogy, Berlin, ISBN: 978-3-642-25608-0, pp. 1–111.
- Mukherjee, S., 2014. Atlas of Shear Zone Structures in Meso-scale. Springer Geology, Cham, pp. 1–124. ISBN: 978-3-319-0088-6.
- Mukherjee, S., 2015. Atlas of Structural Geology. Elsevier, Amsterdam, ISBN: 978-0-12-420152-1, pp. 1–165.

Acknowledgements to the First Edition

Thanks to Mohanapriyan Rajendran, Priya Srikumar, Marisa LaFleur, Amy Shapiro, Louisa Hutchins, and John Fedor (Elsevier) for editing, and to all the contributors and reviewers. Philippe Herve Leloup, Chris Talbot and an anonymous reviewer are thanked for reviewing the book proposal and for providing positive comments. Research students and teaching assistants helped and I thank them: Tuhin Biswas, Narayan Bose, Achyuta Ayan Misra, Aninda Ghosh, Rajkumar Ghosh, Dripta Dutta, Uddipan Das, and many others. Thanks to my wife Payel Mukherjee for her patience.

Acknowledgements to the Second Edition

Amy Shapiro (Elsevier) took the preliminary initiative to go for the second edition of *Atlas of Structural Geology*. **Peter Llewellyn** (Elsevier) joined in the late phase of this book project and he is thanked for his quick assistance. Positive critical reviews of the book proposal received from **Bruce Hobbs**, **Alejandro Ruiz Fuentes**, and **two anonymous reviewers** greatly helped to decide how to proceed. However, depending on the type of contribution (figures and captions) received, not all of their points could be fulfilled, and there remains a chance in the future for a third edition of this book. I would like to thank the entire Elsevier team, **Ruby Smith** (editorial project manager), **Paul Prasad Chandramohan** (project manager), and **Sathya Narayanan** (copyright coordinator) for all the assistance and efforts. **Dripta Dutta** (IIT Bombay) helped greatly in finalizing the second edition of this book. My wife **Payel Mukherjee** singlehandedly took care of our family during the 2020 coronavirus pandemic, and gave me free time to compile the second edition of this book. Discussions with my dissertation students **Nidhi Lohani** and **Aashu Pawar** (Panjab University); **Shriza Acharya**, **Nupur Pant**, and **Mohammad Walid** (IIT Bombay); and **Mayur Dhawale** (IISER Pune) have been fruitful in understanding structures better.

Chapter 1

Folds

Two of the most intensely studied aspects in structural geology are morphology and the genesis of folds (Ramsay, 1967; Hudleston and Lan, 1993; Ez, 2000; Harris et al., 2002; Harris, 2003; Alsop and Holdsworth, 2004; Carreras et al., 2005; Bell, 2010; Hudleston and Treagus, 2010; Godin et al., 2011; Harris et al., 2012a,b; Llorens et al., 2013; Mukherjee et al., 2015; Gogoi and Mukherjee, 2019). Of particular importance is whether folds found inside ductile shear zones are related to ductile shear (e.g., Carreras et al., 2005; Bell, 2010). This chapter presents folds of different geometries and generations, some related with ductile shear zones, from different scales (Figures 1.1–1.118). Figure 1.38 describes the compaction of mudstone. For general principles of compaction, consult the recent publications Mukherjee and Kumar (2018) and Dasgupta and Mukherjee (2020). Interestingly, hook-shaped folds typical of reverse shear kinematics are presented in Figure 1.57. A detailed review of reverse shear is available in Dutta and Mukherjee (2019); also see Dutta and Mukherjee (2020). See Mukherjee et al. (2020) for fold morphologies from other terrains. Folded surfaces, some of which taken from this chapter, have been used in fitting curves, for example, Gogoi et al. (2017, 2020). This shows a potential of use of snaps of structures with a similar purpose (e.g., Biswas and Mukherjee, 2020).

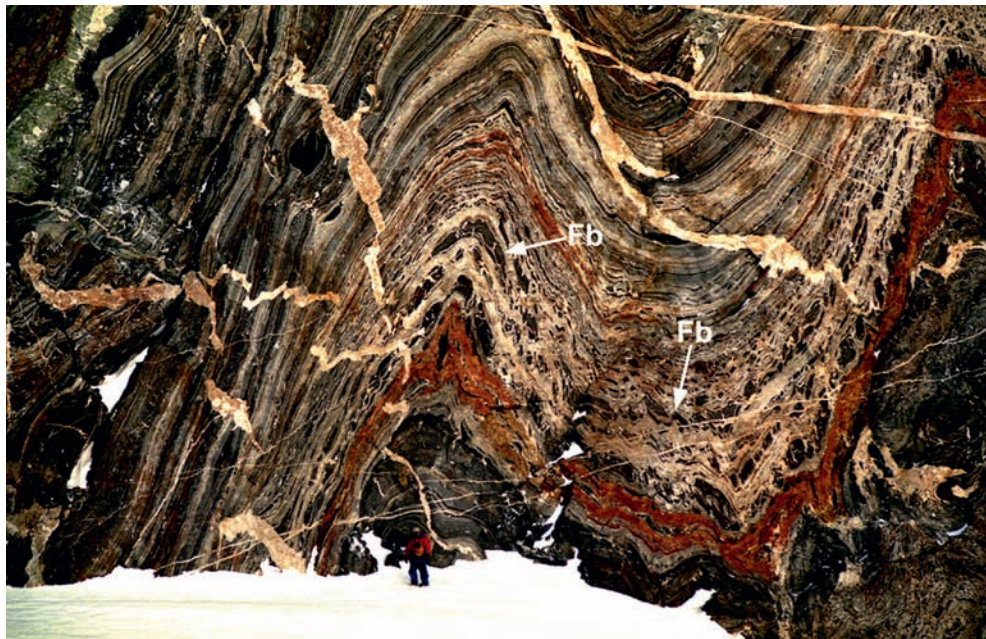


FIGURE 1.1 Upright folds and folded boudins resulting from the continental collision of East and West Gondwana. The boudins of dark-colored amphibolite (Fb) in light-colored biotite-hornblende gneiss originally had pancake shapes with a flattening parallel to the compositional layering of gneiss, and resulted from the layer-parallel extension and thinning of crustal rocks within 640–600 Ma (Toyoshima et al., 1995). The folds with wavelengths of 20–30 m are parasitic upright folds of a larger-scale upright fold related to 600–560 Ma sinistral transpression and crustal shortening during the collision (Toyoshima et al., 2013). The boudins (Fb) folded by the parasitic folds suggest that the tectonic regime changed from layer-normal to layer-parallel compression (Toyoshima et al., 2013). Osanai et al. (2013) presented SHRIMP U–PB ages for metamorphic rocks from the Sør Rondane Mountains, East Antarctica, and recognized periods of ultrahigh-temperature metamorphism (premain metamorphic stage) during 750–700 Ma and granulite-to amphibolite-facies metamorphism during 640–600 Ma. Location: 72°09′42″S, 25°31′50″E, the southern part of Salen in the Sør Rondane Mountains, East Antarctica. Tsuyoshi Toyoshima, Masaaki Owada, and Kazuyuki Shiraishi



FIGURE 1.2 Large-scale folds. Large-scale folds of Lower Cambrian shales and limestone in the Eastern side of the Bas Draa inlier, Western Anti-Atlas (Karaoui, 2014). Note that the decametric disharmonic folds are accompanied by minor folds. Folds axes are plunging toward the SW with a regional vergence to the SE. Photographed by Prof. Karaoui Brahim (Moulay Ismail University). **Zakarya Yajjoui**

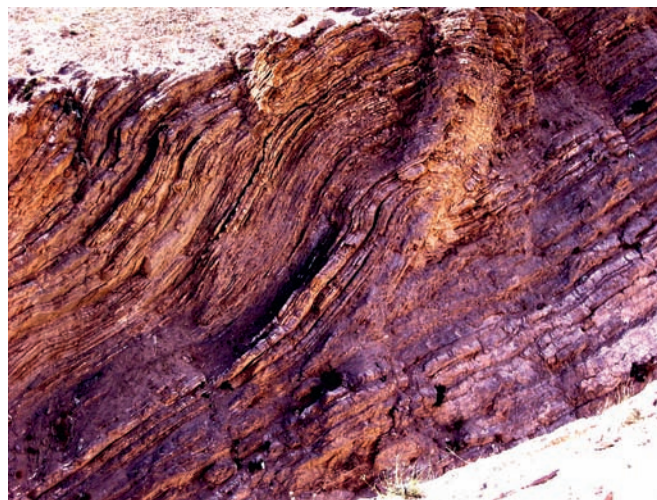


FIGURE 1.3 Fault-bend fold viewed along NNW-SSE section within Tethyan Himalayan succession. Compression in the Tethyan Himalaya indicated. Width of view: ~80 ft. The fold is developed within thinly bedded, presumably less viscous, argillaceous rocks of the Lower Cretaceous age. North vergent folding in the Tethyan Himalaya resulted from strong drag induced by channel flow extrusion of the Greater Himalaya at south, as Godin et al. (2011) proposed from Nepal Himalaya. Note opposite senses of normal drag (Grasemann et al., 2005; Mukherjee, 2007; Mukherjee and Koyi, 2009; Mukherjee, 2010, 2011a, 2014a,b) across the fault plane. Latitude 32°19'54"N, Longitude 78°0'29"E. Kibber village, Spiti, Himachal Pradesh, India. **Mainak Choudhuri**



FIGURE 1.4 Tri-shear fault-propagation folding, Greater Himalayan gneissic rocks. The fold axis trends N330 degrees. Location: 28°32′48.61″N; 94°13′47.24″E. Scale: Hammer (white circled). **George Mathew and Dnyanada Salvi**

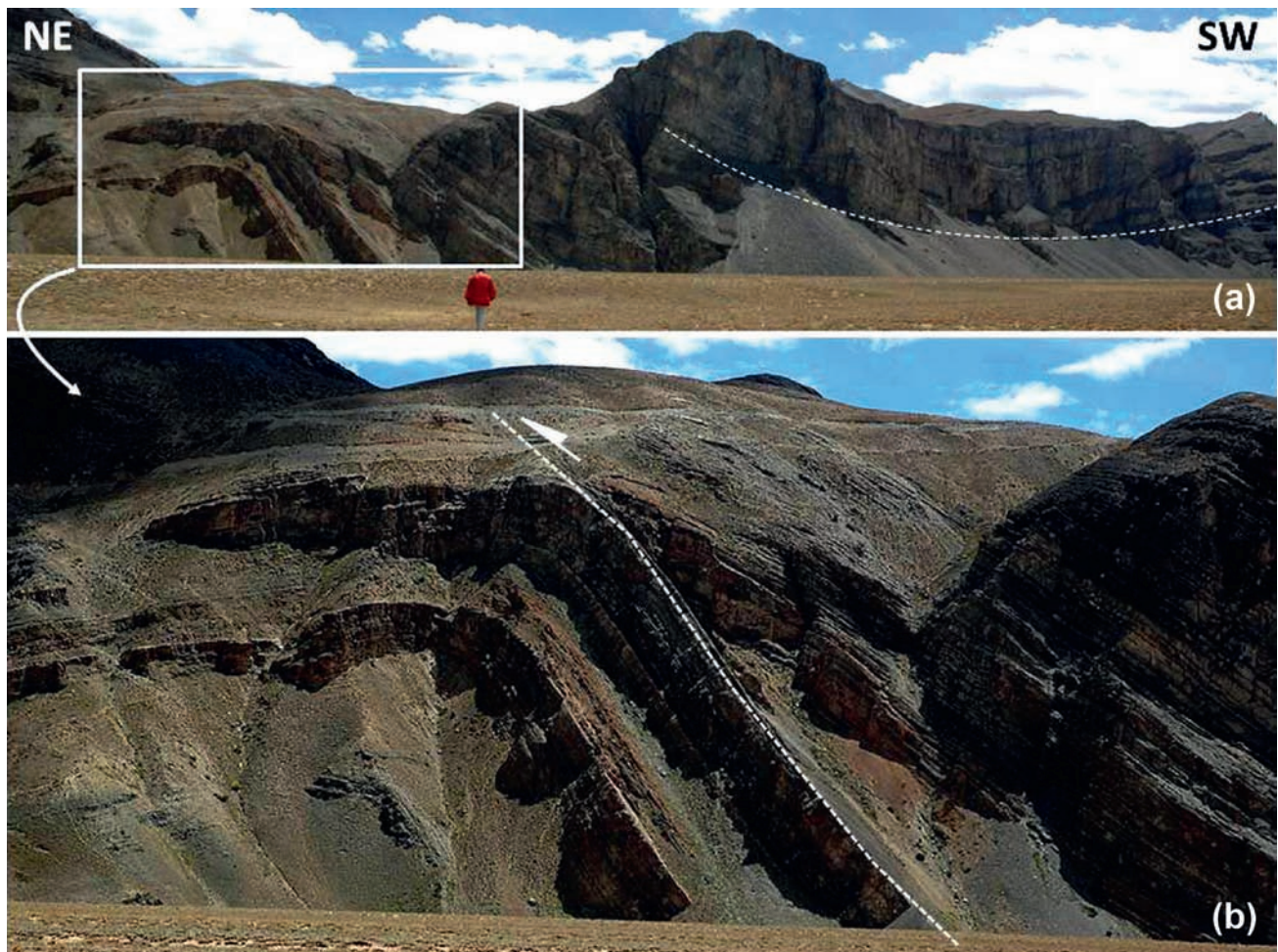


FIGURE 1.5 (a) Full section and (b) zoomed into an excellent outcrop-scale example of an “out-of-syncline” fold accommodation fault (Mitra, 2002; Deng et al., 2013), Triassic limestones, Spiti valley, near Losar village, Himachal Pradesh, India. Fold accommodation faults accommodate strain on the fold limbs. Here, the synform is present to the SW. Its NE limb accommodated strain. Location: 32°23′47.63″N, 77°57′2.09″E. **Achyuta Ayan Misra**



FIGURE 1.6 Fold-related deformed growth strata. Upper Miocene growth strata are developed within the back limb of the anticline. Deformed growth strata folds have scarps inclined toward the axis of the syncline. The unconformity in the growth folds is mainly caused by the fold kinematics—kink-band migration of the active synclinal axis (Hardy and Poblet, 1994). This resembles the model clearly observed on the seismic profiles in the Kura foreland fold-and-thrust belt (Alania et al., 2008, 2017). Location: Near Georgia-Azerbaijan border zone, Central Caucasus. **Rusudan Chagelishvili and Victor Alania**



FIGURE 1.7 Detachment folds. The developed folds are thinly bedded sandstones and shales of Middle Miocene age. Location: $41^{\circ}47'8.88''\text{N}$, $45^{\circ}9'36.87''\text{E}$. Near V. Ujarma, Kura foreland fold-and-thrust belt, Georgia. **Victor Alania, Rusudan Chagelishvili, and Onise Enukidze**



FIGURE 1.8 Chevron folds. Chevron folded Paleogene sandstones and shales. Location: Near v. Tianeti, South part of the Greater Caucasus, Georgia. Victor Alania and Onise Enukidze

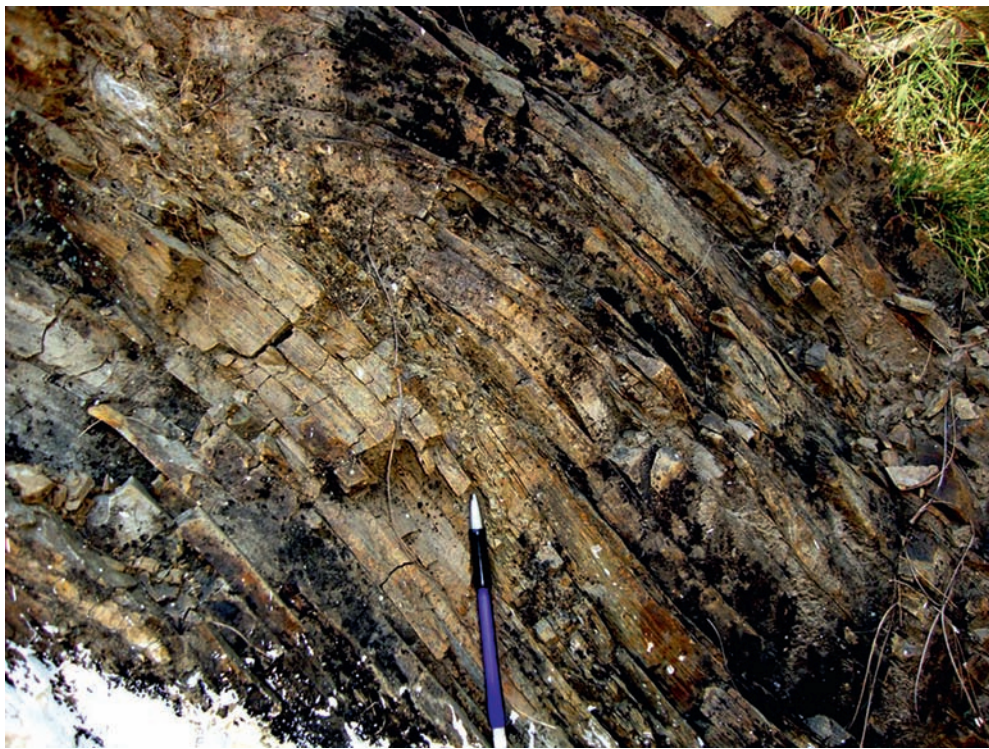


FIGURE 1.9 Fault-bend fold. The fault plane is not perfectly straight. Presuming a “normal drag,” reverse faulting deciphered. Thinly bedded meta-siltstone. 15 mm pencil for scale. Location: Chail Group, SE of Shimla, Himachal Pradesh, India. Subhadip Mandal



FIGURE 1.10 Recumbent fold. Recumbent fold within mylonitic quartzite. Jahazpur, Rajasthan, India. **Hindol Ghatak**



FIGURE 1.11 Minor folds. Symmetrical minor “M” folds in the hinge zone of a regional scale fold, at Jahazpur (Rajasthan), observing on plan. **Hindol Ghatak**

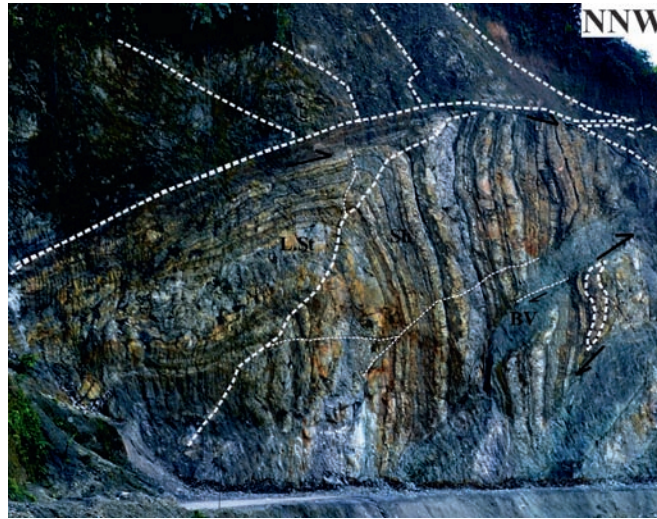


FIGURE 1.12 The Eocene limestone–shale sequences of the Siang fold-and-thrust belt, Arunachal Pradesh, India. The sequence is bounded by parallel and arcuate thrusts at N (Acharyya and Saha, 2008). The southward propagating Eocene sequence is thrust and folded. Here, the fold has its right limb steeper than the left one. The right limb rotated dextrally and is traversed by two basic dykes (BV). The left dyke is also slipped dextrally, the middle part was boudinaged, and the lower part dislocated, creating a subvertical fault. Because the two dykes follow surfaces of opposite movement, the sequence within the dykes becomes horses between the floor and the roof thrust (McClay and Insley, 1986) with top-to-right shear. The horses are sigmoidal. Thick white broken lines: axial trace of the fold and one sigmoid. L.St.: Limestone, Sh: shale, BV: Basic volcanics. Lower Siang district, Arunachal Pradesh, India. N28°10'8", E95°12'7". Several Neogene N-trending rifts present in the Eastern Himalaya (Yin, 2006). The geometry of the Siang fold thrust belt is not studied so far, considering the orientation and extension of the rifts in the E. Himalayan Syntaxis. **Tapos Kumar Goswami**



FIGURE 1.13 Spectacular exposure of a thrust fault and related footwall syncline at the summit of Mt Prena belonging to the E-W-trending Gran Sasso thrust system in the Central Apennines fold-and-thrust belt of Italy. The thrust emplaces the massive paleo-platform dolostones of the Upper Triassic Dolomia Principale Formation, in the hanging wall, onto the well-bedded slope-to-basin calcarenites and pelagic limestones of the Middle Jurassic–Lower Cretaceous Calcarei Bioclastici inferiori and Maiolica Formations, in the footwall, which are involved in a close overturned syncline. Further details about the structures of the Gran Sasso thrust system can be found in Calamita et al. (2004, 2009) and Satolli et al. (2005). Location: view of Mt. Prena from the W (42.449190° 13.651570°) ~6kmS to the Isola del Gran Sasso d'Italia village, province of Teramo (Italy). Mt. Prena (2561 m.a.s.l.) is one of the highest peaks among the summits in the Gran Sasso d'Italia, which is the highest mountain of the Apennines. Width of view ~2 km. **Paolo Pace**



FIGURE 1.14 Plunging folds. NW verging, steeply inclined, and gently to moderately plunging folds preserved in the Ayer's Cliff Formation in southern Québec. Reproduced from [Perrot et al. \(2020\)](#). Morgann Perrot



FIGURE 1.15 Folded strata in the Tibetan Himalaya. Rock consists of shale, metasandstone, and carbonates. Photo view toward NW. Location: Near Kagbeni, Tibetan Himalaya, Kali-Gandaki section, Central Nepal Himalaya. Subodha Khanal



FIGURE 1.16 A disharmonic fold. A disharmonic fold, ~10 m high. The lower part is rich in shales of the Gerofit Formation. The upper part of the section is not much disturbed, Nahal Eteq, Elat area, Israel. **Yehuda Eyal**



FIGURE 1.17 Recumbent fold in mesoscale. Photo at Ordesa and Monte Perdido National Park (Spanish Pyrenees) to the Northeast, in Llanos de Salarons. 30T 740329.94E 4,728,732.43N. Paleocene and Eocene limestones (Salarons and Gallinera Formations) in gray and overlying Eocene turbidites (Hecho Group) in brown (Séguret, 1972; Ternet et al., 2008). **Ruth Soto**



FIGURE 1.18 Recumbent chevron folds. Recumbent chevron fold, Marsa Alam area, Eastern Desert of Egypt. Mohamed Th.S.Heikal



FIGURE 1.19 Drag fold (reviewed in Mukherjee, 2014a,b) produced by faulting within Gulcheru Quartzite. Quartzite is of Paleoproterozoic age. SSW of Vempalli village, Andhra Pradesh, India. Atanu Mukherjee

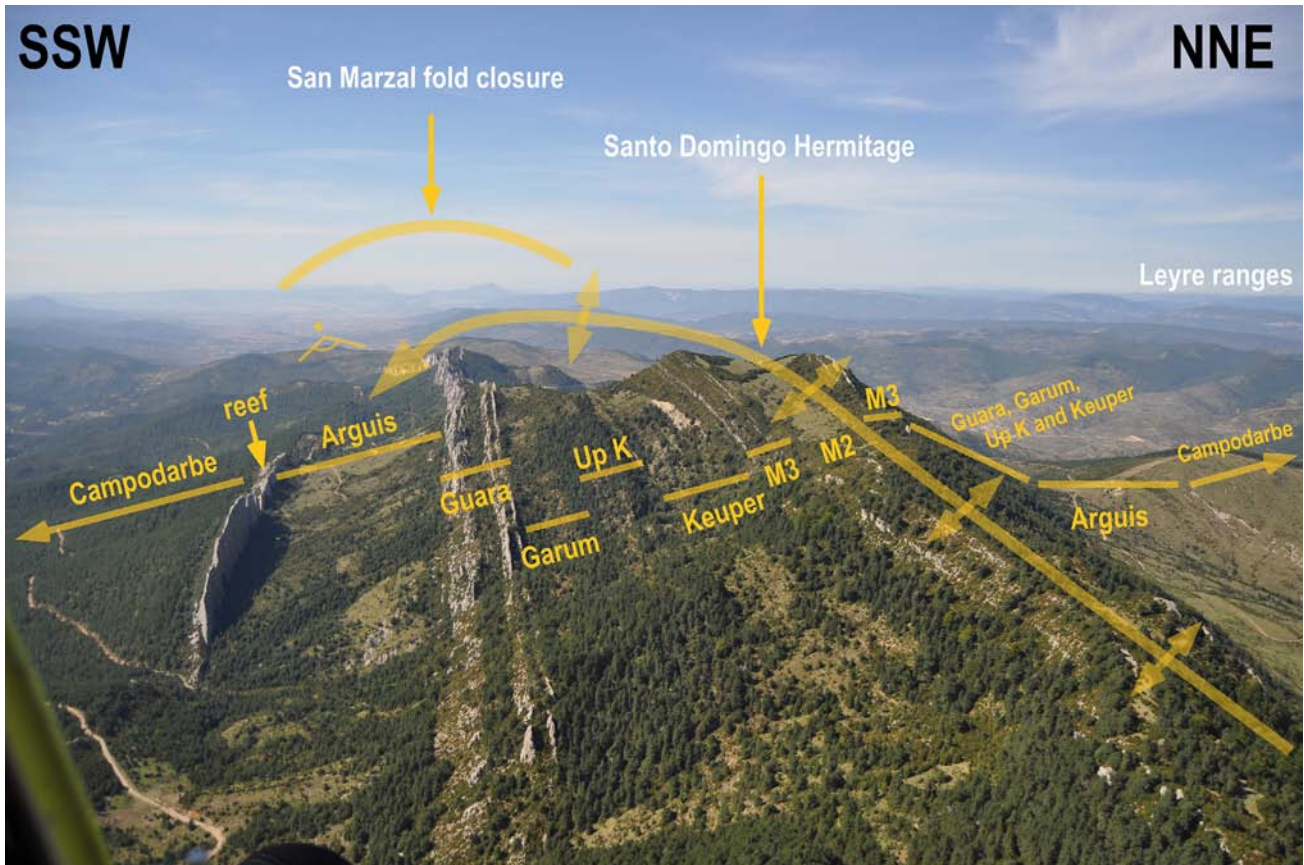


FIGURE 1.20 The Santo Domingo anticline. Aerial photograph of the Santo Domingo anticline (Southwestern Pyrenees) taken at 1675 m altitude in September 2014. The South Central Pyrenean basal thrust laterally passes to the west to a large-scale detachment fold that abruptly vanishes in the San Marzalpericline closure. The fold displays a southern vergence and steep to overturned flanks in the southern limb almost parallel to the northern limb (Nichols, 1987; Oliva-Urcia et al., 2012). Salt movements in the salty core of the anticline may produce overturned limbs in some positions of the northern flank. The gypsiferous Muschelkalk facies (M2) acts as the detachment level and crops out where the homonymous hermitage is placed near the range's summit (1520 m) at the foreground of the picture. Focusing on the southern limb, with complete stratigraphic sequences, we find the M3 dolostomes, the Keuper facies (stark in the hillside), a very thin Upper Cretaceous platform limestone (mostly hidden in the forest), the Maastrichtian-Paleocene redbeds (Garum facies), the Eocene platform (Guara limestones), and the talus rocks (Arguis marls). The Lutetian limestones help delineate the anticline geometry. The continental molassic sedimentation, after a remarkable reef only outcropping in the southern limb, began during the Priabonian (Campodarbe Fm.) and dominates the background of the picture due to its important thickness (4500 m in the area). The sudden fold closure is enhanced by the strong plunge of the fold (N305W, 70°) that has been linked to a conical geometry with an elliptical section (Millán Garrido et al., 1995; Pueyo et al., 2020). This remarkable feature is visible in the background in a topographic depression delineated by the lower levels of the Campodarbe Fm. See also additional panoramic views from the West and South published in the book Mukherjee (2015). Previous interpretations (Millán Garrido et al., 1995; Teixell and García-Sansegundo, 1995) on the subsurface geometry (detachment fold vs. ramp anticline) have been clarified by recent gravimetric studies (Calvín et al., 2018). The Santo Domingo anticline was active during the Late Oligocene–Early Miocene when the two main regional episodes of deformation (Gavarnie and Guarga) took place and almost overlapped in this sector of the External Sierras (Millán et al., 2000). The kinematics of this fold are fully recorded by outstanding syntectonic sedimentation both in the hanging wall (Hogan and Burbank, 1996) and in the footwall one (Oliva-Urcia et al., 2016, 2019; Anastasio et al., 2020). **Emilio Pueyo and Félix Compairé**



FIGURE 1.21 Plunging anticline. NE plunging Anticline in Triassic Limestone, Northwest Himalaya. Maqbool Yousuf

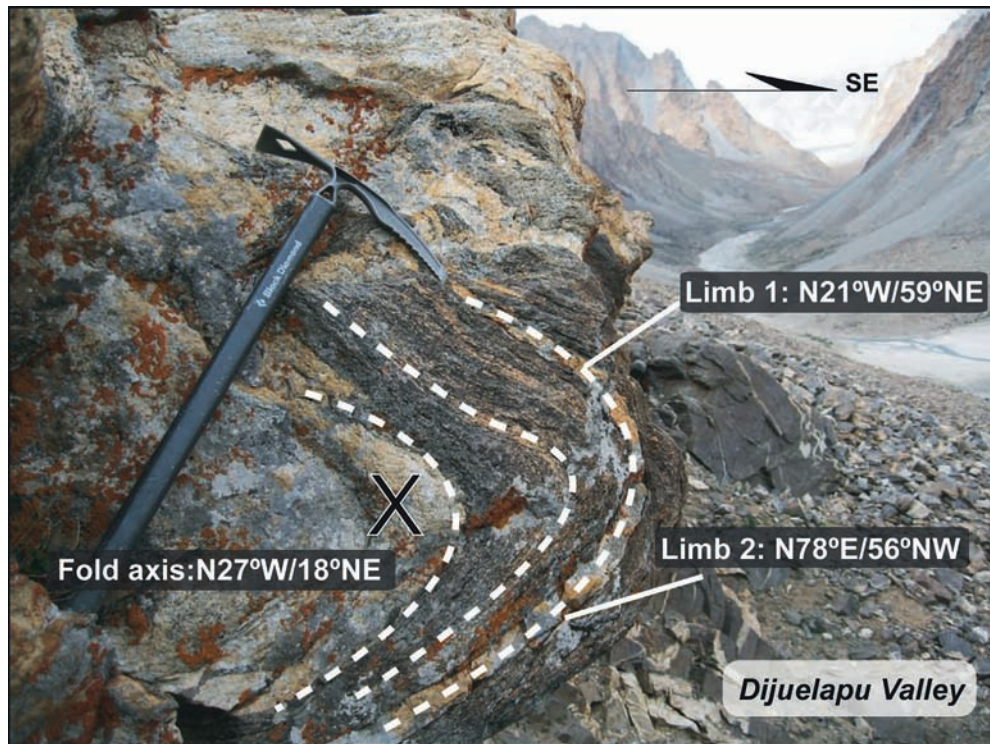


FIGURE 1.22 The Ayishan detachment lies between the Karakoram fault on its E and the Great Counter thrust on its W, in West Tibet. The detachment mantles two NW-SE elongated large doubly plunging gneiss domes. The detachment consists of low-angle top-to-SE extensional faults that overlie a thick top-to-SE shear zone, which juxtaposes Cretaceous–early Tertiary granitoids in its hanging wall against mylonitic rocks in its footwall. Both the faults and underlying shear zone are folded about an axis that parallels the strike of the range. See Wang et al. (2014) for details of tectonics. Ran Zhang



FIGURE 1.23 Kink folded intercalated layers of shales and limestones bound by an SE dipping detachment/décollement at the bottom. Note (1) different geometries of folds along the fold train, (2) folding varies in style from intrados up to the extrados, and (3) fracture along axial traces. Lesser Himalaya, N31°14.578', E76°58.96', Mangu village, district: Solan, Himachal Pradesh, India. See recent papers on the tectonics of the Lesser Himalaya from [Banerjee et al. \(2019\)](#) and [Bose and Mukherjee \(2019a,b\)](#). **Tuhin Biswas**



FIGURE 1.24 Folding in quartzite-mica schist rock. Folding noted in quartzite-mica schist rock in Ghatsila—Galudih stretch under Ghatsila anticline, Chaibasa Formation of the Singhbhum Group. Location: Near Kharsoti River, Tentuldanga, Ghatsila, India. **Mery Biswas**



FIGURE 1.25 Location: Near Kharsoti River, Tentuldanga, Ghatsila, India. Identify structures in this image. Ask students in the class to point out other structural features. Zooming in on different parts of the image on the computer screen will be very helpful. **Mery Biswas**



FIGURE 1.26 Folded “khaki” green shale at Jitpur (India), Talchir Formation. Initially folded layers later brittle deformed producing two joint sets at a high angle. Thus, needle-shaped shale is formed. **Ananya Basu**

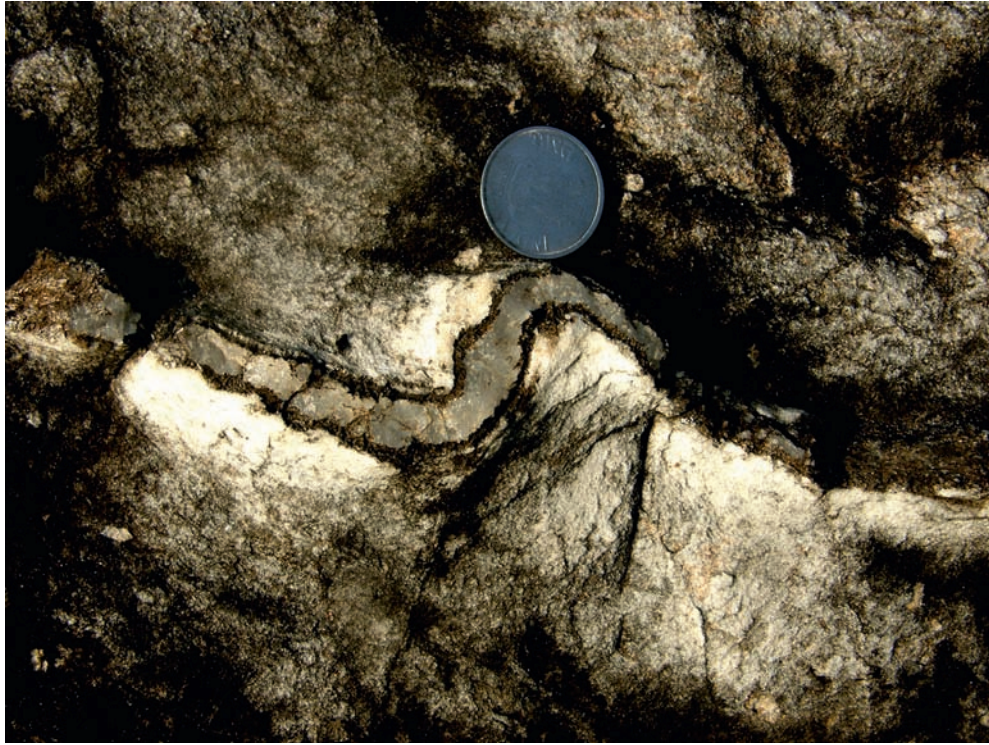


FIGURE 1.27 A folded quartz vein: tremolite grew along its boundary. Surrounding rock: dolomite. N23°07.742' E79°48.809' to N23°07.563' E79°48.665'. Bhedaghat, Jabalpur, Madhya Pradesh, India. Sreejita Chatterjee



FIGURE 1.28 Cusped folds of quartz vein within metagreywacke. Kumbhalgarh Formation, ~85 km NW of Udaipur, Rajasthan, India. Swagato Dasgupta



FIGURE 1.29 **Folded intrusions.** Horizontal outcrop of Archean quartzofeldspathic gneiss just east of Kenora, Ontario. Primary banding is intruded by anatectic melts during deformational stress, causing the folding of the intrusions into later gneiss bodies. Lens cap for scale. **Jeff Greenberg**



FIGURE 1.30 **Folded migmatitic rock.** Melanosome layer is overturned folded with arrowhead hinge. Competency contrast between the melanosome layer and the remaining portion of the rock probably is one of the key controlling parameters of such folding. Maithon, West Bengal, India. **Ananya Basu**



FIGURE 1.31 Intensely deformed lower limb of tight isoclinal folds in highly foliated garnetiferous gabbroic rocks. The lower limb shows a variety of folds and a series of small-scale brittle-ductile shear zones. All the folds show gentle to moderate plunge toward S/SE. The shear zones strike $\sim E-W$ and often associate with flanking structures of negative slip. Those are slipped sinistrally. The magnitude of the slip increases, forming an arcuate shear zone, and that finally coincides with the axial plane of the fold. On the right side of the photograph, notice the presence of folded quartzofeldspathic layers with sinistral displacement along the axial plane and the stretching of one of the limbs. The outcrop is located in the NW part of the E-W trending closed structural form of the Kanjamalai Hills (~ 5 km W of Salem). These structures form a part of the detachment zone, which is characterized by complex folding with predominant tight/isoclinal folds with variable trend, limb rotations, and hinge line variations often leading to lift-off like fold geometries and deformed sheath folds. See [Drury and Holt \(1980\)](#), [Gopalakrishnan \(1994\)](#), [Chetty \(1996\)](#), and [Santosh et al. \(2009\)](#) for regional geology and tectonics. **T.R.K. Chetty**



FIGURE 1.32 Asymmetric folds. Asymmetric folds of conglomerate layer within the Chaibasa Formation near the village Bundu, Jharkhand, India. Individual pebbles are folded with the quartzitic matrix. En-echelon extension fractures formed parallel to the axial plane of the fold later in progressive shearing. **Susanta Kumar Samanta and Dipak C. Pal**



FIGURE 1.33 A chevron fold with planar limbs and sharp/pointed hinge. Planar subvertical axial plane. From quartzite, Ajmer, Rajasthan, India. Moly Sarkar



FIGURE 1.34 Tight recumbent kink folds. Small-scale tight recumbent folds affecting bituminous dolostones (Dolomie Bituminose Formation—Upper Triassic; Adamoli et al., 1990) in the Fornaca Valley (Central Apennines, Italy; Ghisetti, 1987; Leah et al., 2018; Lucca et al., 2019). Coordinates: 42.432195, 13.696126. Michele Fondriest



FIGURE 1.35 Large-scale folded banded magnetite quartzite and magnetite garnet biotite schist intercalation. Tiranga hill, Pur area, Bhilwara, Rajasthan, India. See [Mukherjee et al. \(2020\)](#) for diverse other structures, most notably folds. **Ranjan Gupta**



FIGURE 1.36 Folded banded iron formation of alternate layers of ferruginous and quartzose materials. Chitradurga district, Karnataka, India. **Aabha Singh**



FIGURE 1.37 Photograph from the Chrystalls Beach Complex, coastal Otago, New Zealand, showing folded interlayered sandstones (white) and mudstones (dark gray). The rocks form part of the Otago schist, related to the Triassic–Jurassic subduction and accretion at the Gondwana–Paleopacific margin (e.g., Mortimer, 2004). The Chrystalls Beach Complex is an accretionary mélangé where stratal disruption occurred progressively from early diagenesis through to chlorite–actinolite subgreenschist facies conditions (Nelson, 1982). The fold in the photograph illustrates that more rigid sandstone layers are both disrupted by layer-parallel extension and thickened by folding and small-scale thrusts. Mudstone appears to have filled gaps in the sandstone layer by ductile flow, but tensile fractures in the sandstone attest to local brittle deformation. This mixture of continuous and discontinuous deformation is typical of this tectonic mélangé. The bulk rheology of the mélangé may therefore depend on the relative abundance of low-viscosity mudstone and more rigid sandstones; ductile deformation at the mesoscale, as seen in the photograph, likely occurs when mudstone dictates the bulk rheology, but brittle deformation may prevail if sandstone forms a rigid framework (Fagereng and Sibson, 2010). Ake Fagereng



FIGURE 1.38 Rhythmic occurrence of the relatively undeformed massive sandstone turbidite beds within the background of calcareous mudstone units (pelagic-hemipelagic sediments and “low-density” turbidites), which contain folded and closely spaced vertical joint surfaces. The flexural slip folding of joints with bedding-parallel axial surfaces is caused by compaction of the mudstones within the sedimentary diagenetic regime. The sandstone beds contain intermittent and rare bedding-perpendicular joints, which are not folded. This implies distinct postdepositional rheologic histories for mudstones and sandstone. After deposition, the sediments underwent unidirectional extension along the slope—preferably more in mudstone than in sandstone beds, thereby forming the bedding-perpendicular joint surfaces. Unlike in sandstones, the joint surfaces in mudstones subsequently were folded by further compaction. Sudipta Dasgupta and Luis A. Buatois

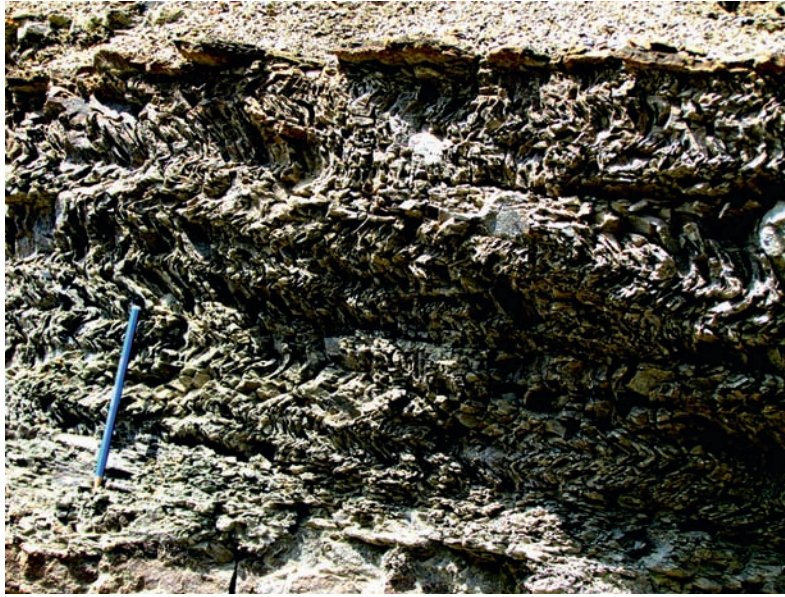


FIGURE 1.39 Closer view of the deformed mudstone. The facies-tract assemblage is possibly of an unconfined deep marine slope apron. From late Eocene–early Oligocene Ceylan Formation, Thrace Basin, Gelibolu Peninsula, Northwest Turkey. **Sudipta Dasgupta and Luis A. Buatois**



FIGURE 1.40 Angular folds (kink bands) in tourmaline-bearing garnet-mica schist. Dark green and pale brown minerals in the dark bands are of tourmaline. Small dark green crystals are the curved three-sided (basal) cross-sections of the tourmaline. The folds are asymmetric, showing larger limbs on the left side. In the hinge zones, some prismatic sections of tourmaline are slightly bent, but most of them are undeformed. Bent tourmaline crystals can be interpreted as pre- to *syn*-folding, whereas undeformed tourmaline grew at least partially after folding. Observed abundant basal sections suggest that tourmaline also grew parallel to the fold axis orientation. Section normal to the fold axis and to the foliation. Width of view 22 mm. Plain polarized light. Location: Sierra de Ambato, Catamarca Province, NW Argentina. GPS point (WGS84): S 27°38'35.6″–W 66°12'39.5″; Rock type: tourmaline-bearing garnet-mica schist; Formation name: Quebrada del Molle Metamorphic Complex; Age (relative): Ordovician; Facies/grade: greenschist facies/garnet zone. **Mariano A. Larrovere**

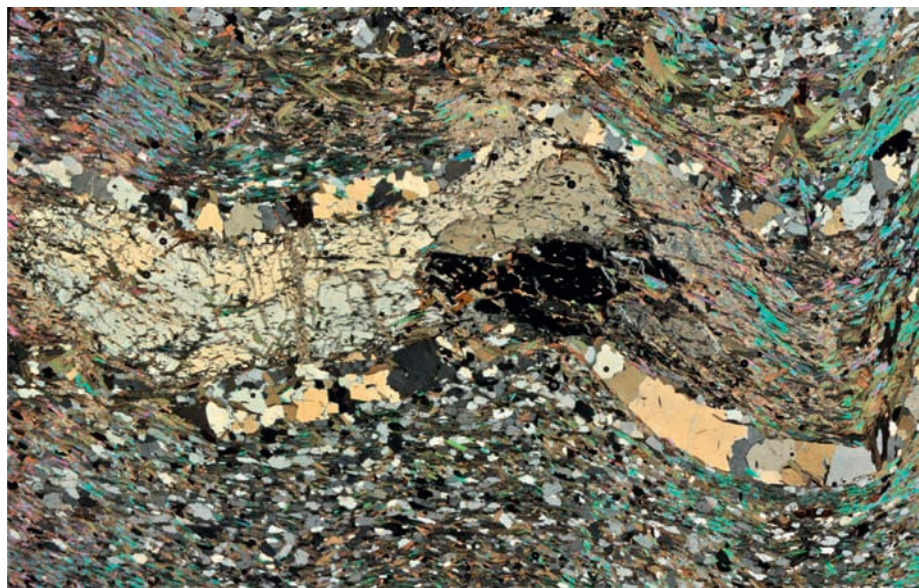


FIGURE 1.41 Microfolded porphyroblast of cordierite (in the center of the photo) in gneiss. Subgrains occur within the large elongated deformed cordierite grain. They are recognized optically by low relief boundaries and differential extinction between subgrains. Inside the cordierite crystal is observed a bent inclusion pattern marked by micas (internal foliation) that shows continuity with the folded subhorizontal gneissic foliation S_1 . The crystal of cordierite is bordered by two ribbons of recrystallized quartz that also are folded. A subvertical crenulation cleavage S_2 can be recognized. The cordierite porphyroblast may be classified as pre-tectonic with respect to S_2 because cordierite is folded and internally deformed by the same deformation phase (D_2) that generated the crenulation cleavage S_2 . On the other hand, cordierite porphyroblast is interpreted as post-tectonic with respect to the subhorizontal gneissic foliation because it includes S_1 . Section normal to the microfold axis and to the foliation. Width of view 13 mm. Cross-polarized light. Location: Sierra de Aconquija, Catamarca Province, NW Argentina. GPS point (WGS84): S 27°34'07.6"–W 66°14'20.6"; Rock type: cordierite-mica gneiss; Formation name: Quebrada del Molle Metamorphic Complex; Age (relative): Ordovician; Facies/grade: greenschist facies/medium grade. **Mariano A. Larrovere**



FIGURE 1.42 Crenulation schistosity. Crenulation schistosity of the Compton Formation in southern Québec. The first one is almost horizontal (center of the photograph) and crosscut by the second one that is almost vertical (upper left of the photograph). Reproduced from [Perrot et al. \(2020\)](#). **Morgann Perrot**



FIGURE 1.43 Crenulation cleavage. Steeply dipping crenulation cleavage (S3) with microlithons in which the folded cleavage is an older crenulation cleavage S2 foliation plane. Location: Orthogenesis (near the Gangotri area) of the Vaikrita group of the Higher Himalayan Crystalline, Garhwal region, Bhagirathi river section. Do you have any alternate logical interpretation of this snap? ([Singh, 2014](#); [Singh et al., 2012](#)). **Paramjeet Singh**

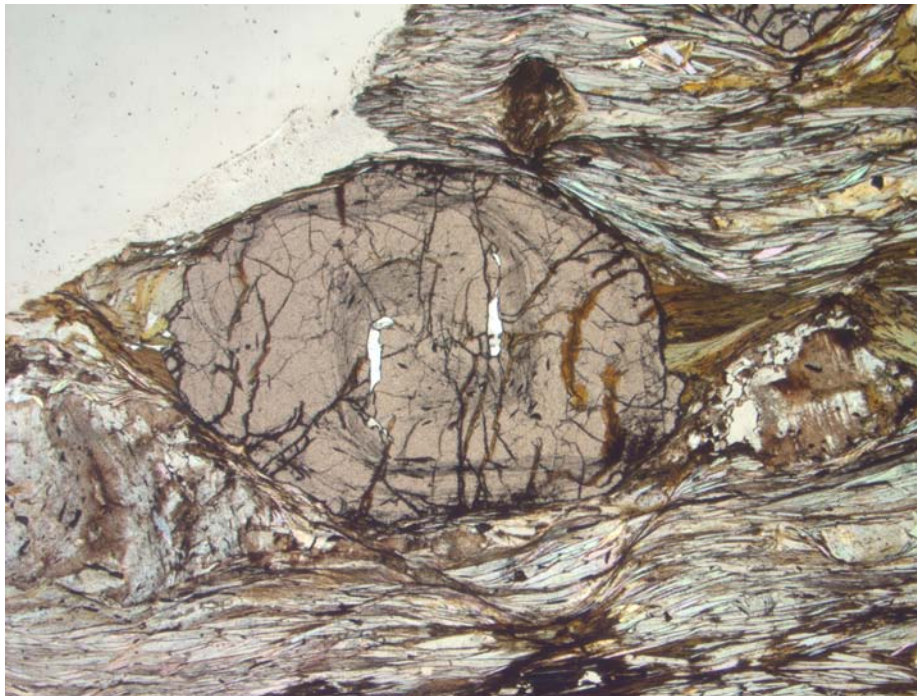


FIGURE 1.44 Weakly folded foliation near a garnet porphyroblast. Intertectonic garnet porphyroblast in oligoclase-garnet-bearing mica-schist. Sardinian Variscan basement, Medium-Grade Metamorphic Complex in the southeastern sector of the Posada Asinara shear zone (Italy). The internal foliation is defined by ilmenite and graphite. Garnet is wrapped by the mylonitic foliation mainly made by white mica and biotite. (PPL; 4×). **Petroccia Alessandro**

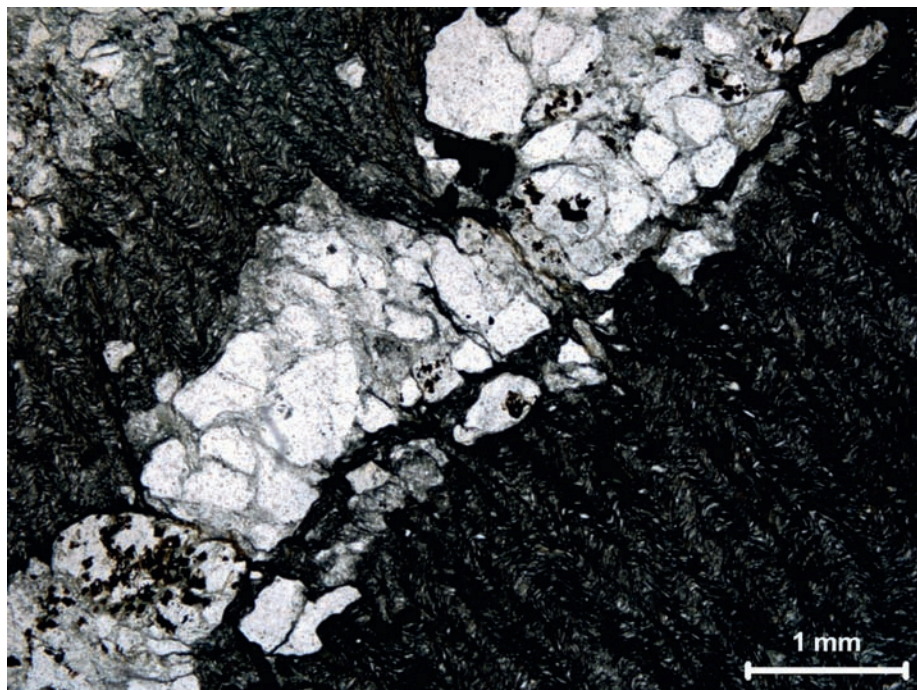


FIGURE 1.45 Crenulation cleavage. Crenulation cleavage (Hobbs et al., 1976, p. 217) in thin pelitic laminae intercalated with sandstone beds. A bedding parallel, phyllosilicate-rich fabric (due to load metamorphism) in the pelitic laminae is crenulated while the sandy laminae remain straight but cut by occasional pressure solution seams grading into crenulation cleavage seams in the pelitic laminae. Quartz grains in the sandy laminae retain their original angular to subangular shape. PPL photomicrograph, Bowmore Sandstone, Rhinns of Islay, Scotland, bar scale 1 mm. PPL, plain polarized light. **Dilip Saha**

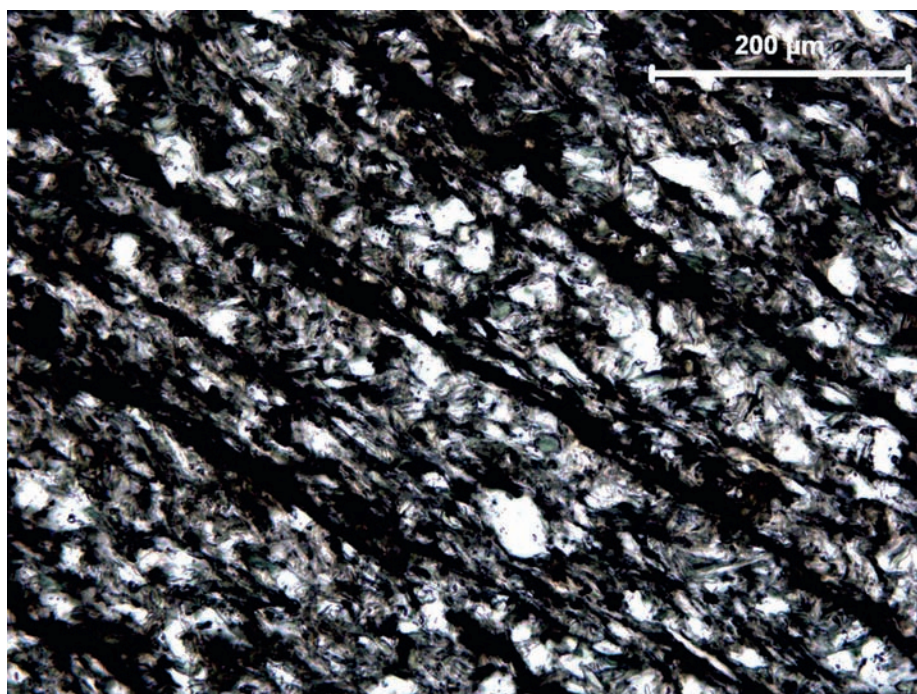


FIGURE 1.46 Disjunctive spaced cleavage in metasiltstone. Note (1) narrow cleavage seams, (2) thin dark bands (P-domain: Williams et al., 2001) dipping to the right, and (3) alternating with microlithons (Q-domain). Q-domains are characterized by randomly oriented chlorite and muscovite flakes. P-domains have tiny subparallel phyllosilicate flakes and concentration of ferruginous opaques. The distributed quartz grains also show poor shape preferred orientation. Photo in plane polarized light. Colonsay Group, western Islay, Scotland. Bar scale: 200 μm. **Dilip Saha**

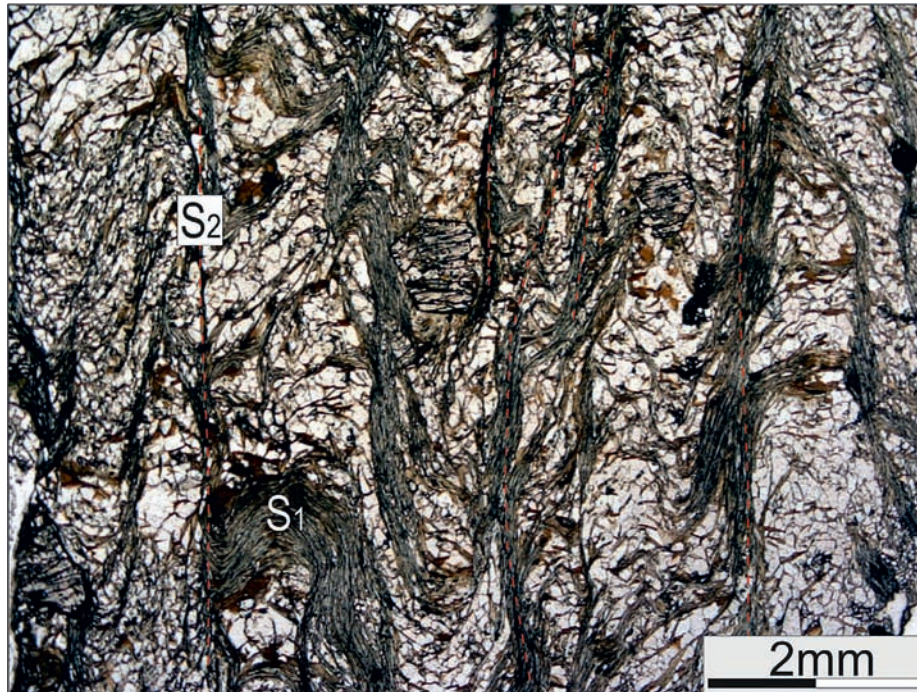


FIGURE 1.47 Crenulation cleavage (S_2) from early crenulation (S_1) that occurred as microfolds in quartz-rich microlithons. Photomicrograph under the cross-nichol of Mesoproterozoic garnetiferous mica schist, upper unit of Lesser Himalayan Crystallines, Kameng valley, Western Arunachal Himalaya showing latter schistosity. GPS location: N27°17'11.3"; E92°15'48.3" (Bell and Rudenach, 1983; Passchier and Trouw, 1996; Bikramaditya Singh and Gururajan, 2011). **Bikramaditya Singh**



FIGURE 1.48 Overprinting crenulation cleavages. The subhorizontal set in the photo (left to right) with thin, sharp, and longer seams transposes an early phyllitic cleavage (slaty cleavage) defined by the alignment of chlorite and muscovite flakes and flattened quartz grains. A still later set of crenulations affects both the phyllitic cleavage and the subhorizontal crenulation cleavage seams, leading to a second crenulation cleavage with shorter narrow seams gently dipping to the right of the photo. PPL photomicrograph, phyllites of Colonsay Group, Saligo Bay, Western Isaly, Scotland, bar scale 1 mm. PPL, plain polarized light. **Dilip Saha**



FIGURE 1.49 Crenulation cleavage. Rock type: Calc-phyllite. Structure: Crenulation cleavage. Location: Tocantinzinho river bank in the Moquéim Salient, Chapada dos Veadeiros Region, Northern Goiás State, Brazil. Facies: Lower to intermediate greenschist. Description: Penetrative crenulation cleavage on calc-phyllite producing open folds in different scales. The folds related to this cleavage range from mm to decametric in scale. **Marco Martins-Ferreira**



FIGURE 1.50 Similar folds within the Los Cabos Series quartzites (Ordovician), below the basal thrust of the Mondoñedo nappe. Folds show characteristic thickened hinges and the left limb shows top-to-right (up) shear. Left hand fold is approximately 2 m wide at the base. West Asturian Leonese Zone, Tapia de Casariego, Spain. **Amy Ellis**



FIGURE 1.51 Disturbed layer in lacustrine organic rich dolomitic lime mudstone/oil-shale. Eocene Green River Formation, Piceance Creek Basin, Colorado, United States. The deformed interval shows a lower, brittle-ductile part with a fault-propagation fold and a mixed, fragmented interval above. The pronounced difference in the style of deformation reflects the different rheological properties of the two sedimentary packages during deformation. Sediments of the lower part were in a semilithified state while the sediments above were softer. Undulation of the upper boundary might indicate deposition after the deformation event, which took place at the sediment–water interface. Deformation structures with similar characteristics have been previously described as “mixed layers” in the literature (e.g., [Marco and Agnon, 1995](#); [Rodríguez-Pascua et al., 2000](#)), showing a gradual upward transition in the style of deformation induced by seismic shaking. The depositional environment of the host sediments with a very gentle or flat lake floor also points to a tectonic origin. **Balázs Törö, Brian R. Pratt, and Sudipta Dasgupta**



FIGURE 1.52 Parasitic minor folds exhibiting an S-shaped sense of asymmetry within the overturned eastern forelimb of the NNW-SSE-trending Montagna dei Fiori anticline in the Central-Northern Apennines foreland fold-and-thrust belt, Italy. Folding involves the well-bedded pelagic limestones of the Upper Cretaceous–Eocene Scaglia Rossa Formation. The contrasting lithological response to folding is exposed: thick and stiff calcarenitic layer remains undeformed, whereas the thinly layered mudstone strata are remarkably parasitic S-shaped folded. [Calamita et al. \(1998\)](#) and [Scisciani et al. \(2002\)](#) described the structures of the Montagna dei Fiori anticline. [Calamita et al. \(2011, 2012\)](#) detailed the thrust-related folding mechanisms and examples from the Central-Northern Apennines. Location: Sant’Angelo Caves (42.752752° 13.623099°) W to the Ripe di Civitella village, province of Teramo (Italy). Width of view ~ 16 m. **Paolo Pace**



FIGURE 1.53 Chevron-like fold in amphibolite in the dismantle block. Near the center of the photograph, the limb snapped in one case. Akjoujt, Inchiri region, Western Mauritania. **Rajib Sadhu**



FIGURE 1.54 A tight isoclinal fold, with uneven thickness of limbs and hinge regions, in amphibolite. Akjoujt, Inchiri region, Western Mauritania. [Gogoi et al. \(2017\)](#) analyzed the shape of this fold using NURB curve. **Rajib Sadhu**

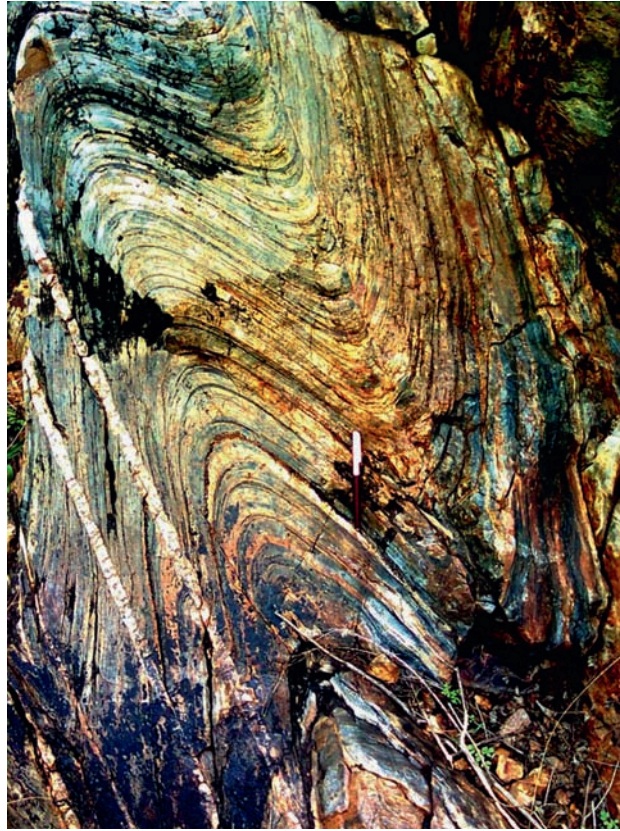


FIGURE 1.55 Intrusion of nearly straight quartz veins in the folded quartzite intercalated with mica schist. Notice the fold hinges in a few cases are thicker than the limbs. Ghatshila, Singhbhum, Jharkhand, India. See [Mukherjee et al. \(2020\)](#) for diverse other structures, most notably folds. **Ranjan Gupta**

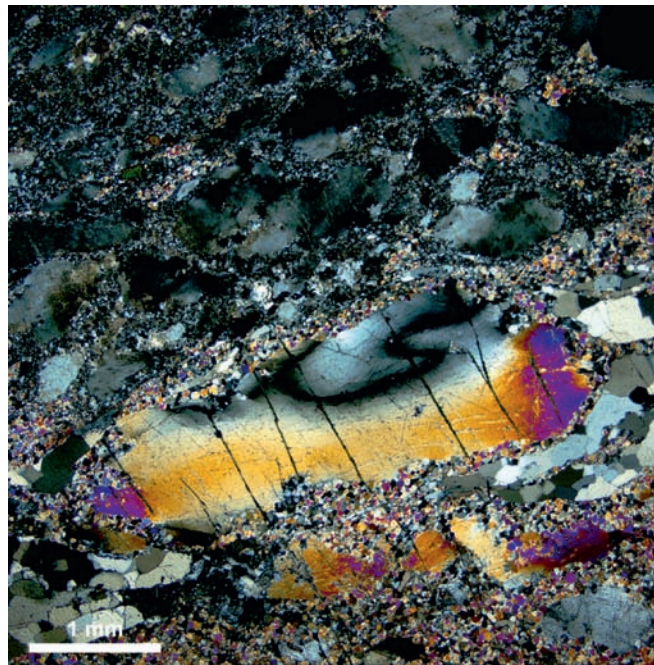


FIGURE 1.56 Cross-polarized photomicrograph of a folded scapolite porphyroclast partially wrapped by quartz ribbons and in a matrix of grain-size reduced scapolite and alkali feldspar. This grain occurs in a *syn*-deformational, late-Grenville-aged vein from the NW Adirondack Mountains (New York, Unites States). It demonstrates that although porphyroclasts are typically considered to be more competent than their surrounding matrix phases, they may accumulate significant internal strain. This is similar to folded quartz grains reported in [Mukherjee \(2010\)](#), [Mukherjee and Koyi \(2010\)](#), and [Mukherjee \(2013\)](#). The pronounced internal folding and dynamically recrystallized grain margin indicate that scapolite was only marginally more competent than alkali feldspar at the conditions of deformation experienced by this vein. **Chloë Bonamici**



FIGURE 1.57 Asymmetric folds with stretched quartz boudins in the metasedimentary rock of the Higher Himalayan Crystallines, Tawang valley, Western Arunachal Himalaya. GPS location: N27°39'30.5"; E91°52'17.2". Bikramaditya Singh



FIGURE 1.58 Tightly folded quartz vein in dolomitic host rock. Central Indian Suture Zone, Jabalpur, Madhya Pradesh, India. Jyotirmoy Paul

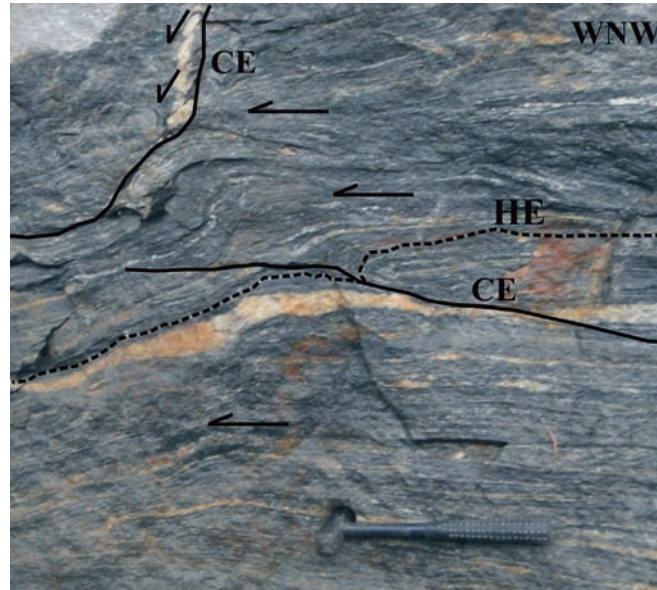


FIGURE 1.59 The Higher Himalaya gneisses near Tato, Siyom River section, West Siang district, Arunachal Pradesh. These garnetiferous gneisses have the general trend of WNW-ESE dipping at a low angle toward N. These gneisses are migmatitic near Tato and represent a high strain ductile shear zone. Flanking folds (Passchier, 2001; Mukherjee, 2014b) in these high-grade gneisses represent sinistral thrusting. The host element is the compositional layering and the cross-cutting elements (CE) are a fault in the central part while in the top left, a subvertical vein is responsible for the flanking of the host layers. The entire fold train is deflected along the axis. The thick quartz vein in the central part postdates the flanking of the host layers and thus shows zero slip. The flanking folds in the central part clearly indicate positive slip, lift, and over roll. The lower mylonitic part shows limbs of the F_1 folds stretched and boudinaged. The photograph is unique in the sense that two CEs, that is, a fault in the central part and a subvertical vein in the top left part, are both responsible for the flanking of the host fabric elements. The shear sense in the top vein is at a high angle to the senses in the central part. The thick quartz vein in the central part in a way divides the area into one part showing flanking structures while the lower part has mylonitic fabric. West Siang district, Arunachal Pradesh, India. Coordinates: N28°30'976", E94°22'642". **Tapos Kumar Goswami**

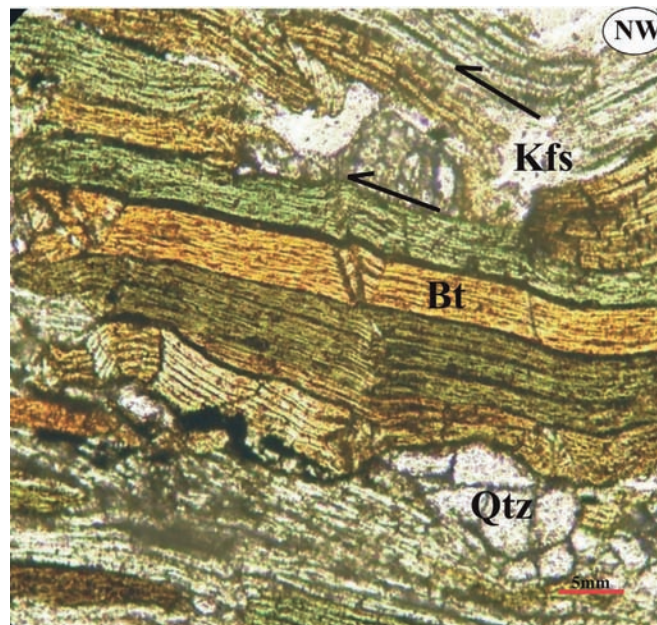


FIGURE 1.60 Micaceous Dafla sandstone of Middle Siwalik (N27°05'057", E92°35' 258"), of the Kameng River section, West Kameng district, Arunachal Pradesh, India. The bottom-most Dafla sandstone thrust over the Subansiri Formation near the Tipi. Kink bands is frequent in the Dafla sandstones. These bands in sandstones formed at relatively low temperatures and must be related to local stress. The kink bands vary from simple to very complex and verge in the same direction of the outcrop-scale folds. Phyllosilicates deform homogeneously when shear stress is applied to the basal planes (001). However, in the nonbasal planes, the applied shear stress produces kinks or fractures (Kronenberg et al., 1990; also see Van Loon et al., 1984). Syndiagenetic deformation is achieved at ~150°C (Lin, 1997). Brown and green (chloritised) mica layers in Dafla sandstone show kink bands of different styles and verge toward SE. Both mobile and fixed hinge kinking are observed in the central part. The top mica layer shows the long limb above the shorter limb and is a thrust. The left central part shows a curved kink boundary indicating differential movement of the basal plane front. **Tapos Kumar Goswami**



FIGURE 1.61 Z-type of the buckle fold of an amphibole-rich layer in metamorphosed granitic host rock. Chotonagpur Gneissic Complex, Maithon, West Bengal, India. Jyotirmoy Paul



FIGURE 1.62 Small-scale folds in banded gneiss in the hangingwall of the Main Central Thrust, Photo view toward NW. Axial trace of folds are parallel to the pen. Notice both rounded and sharp hinges of folds. Location: Unit I, Greater Himalaya, Kodari-Tatopani section, central Nepal Himalaya. For location and geology of the main central thrust in the area, see [Khanal et al. \(2014\)](#). For review of tectonics of main central thrust, [Mukherjee \(2013\)](#). Subodha Khanal



FIGURE 1.63 Crenulation cleavage in garnetiferous banded gneiss. Hangingwall of the Main Central Thrust. Penny for scale. Photo view toward NW. Location: Unit I, Greater Himalaya, Budhi-Gandaki section, Central Nepal Himalaya. **Subodha Khanal**



FIGURE 1.64 Intrafolial folds with top to the left sense of shear in the banded gneiss. Leucogranites are parallel to foliation and thin out toward the top left. Location: Unit I, Greater Himalaya, Marsyangdi section, Central Nepal Himalaya. **Subodha Khanal**



FIGURE 1.65 A gently inclined folded quartzite. Parasitic fold more prominent in the lower limb. Ajmer district, Rajasthan, India. **Moloy Sarkar**



FIGURE 1.66 Recumbent fold plunging toward E in hornblende gneiss. Upper Aravalli Group. East of Bagdunda, Udaipur district, Rajasthan, India. **Shruthi Narayanan**



FIGURE 1.67 Nonperiodic fold. Nonperiodic fold of quartzofeldspathic vein inside basalt, near Kankavli, Maharashtra, India. **Namrata Soreng**



FIGURE 1.68 Plunging fold in ferrogenous sandstone with alternate iron-enriched layer and silica layer. Axial plane dips toward left. Akjoujt, Inchiri region, Western Mauritania. **Rajib Sadhu**



FIGURE 1.69 Tight folding. Tight folds in the layered metabasites. In the bottom of the photo, mica-schist with axial planar foliation has developed. The micaschist foliation is parallel to the metabasite axial plane. Pellice Valley, Dora Maira Unit. **Petroccia Alessandro**



FIGURE 1.70 Sheath fold. Chitradurga district, Karnataka, India. **Aabha Singh**



FIGURE 1.71 A folded layer of chert with closures at two directions. Is this a sheath fold? Note layer ~ perpendicular fractures confined inside the folded chert body. Anupam Samanta



FIGURE 1.72 Superposed fold. Superposed fold in Bormes orthogneiss in Maures-Tanneron Massif (France). Petroccia Alessandro



FIGURE 1.73 Isoclinally folded chert layers with closures in two directions. In a few cases, the hinges are thicker than the limbs. Anupam Samanta



FIGURE 1.74 Field photograph shows a boudinaged sheath fold. The horizontal view is perpendicular to the mylonitic foliation with a downdip stretching lineation. The rock is a calcareous unit intercalated with quartzofeldspathic layers. The quartzofeldspathic layers show excellent development of sheath folds. A boudinage structure can also be seen in the upper quartzofeldspathic layers. The presence of boudins in these layers in a calcareous matrix indicates a strong competence contrast between them. The development of boudins in a section perpendicular to the stretching direction indicates that the deformation was of the flattening type and there is a component of compression across the shear zone. The rock is from the Phulad Shear Zone (Ghosh et al., 1999; Sengupta and Ghosh, 2004), which demarcates the western margin of the Delhi Fold Belt, Rajasthan, India. The white bold arrow indicates geographic north. The width of the photo is 23 cm. Sample location is 25°39'46.1"N, 73°48'36.3"E. Sadhana M. Chatterjee and Sudipta Sengupta



FIGURE 1.75 Doubly plunging round hinge isoclinal fold in calc-silicate. The thinned limb in the photo center possibly indicates a top-to-left shear. Note the orthogonal thickness varies along the limb. At one place, but not in every case, the hinge region is thicker than the limb. Central Indian Suture Zone. Jabalpur, Madhya Pradesh, India. **Jyotirmoy Paul**



(A)



(B)

FIGURE 1.76 Sheath folds. Sheath folds in Late Oligocene–Early Miocene sandstone and mudstone of the Misaki assemblage, Shimanto accretionary prism, Muroto Peninsula, Shikoku Island, Japan (Hibbard and Karig, 1987). The sheath folds formed during the earliest deformation phase in the prism, involving landward vergent thrusting, soon after deposition of the Misaki assemblage trench fill. These early structures were refolded during the accretion process. Subsequently, they were subjected to brittle faulting, regional flexuring, igneous intrusion, and heterogeneous rotation of earlier structures (Hibbard et al., 1992). Collectively, these late processes have been attributed to spreading ridge collision with the accretionary prism (Hibbard and Karig, 1990). The difference in the orientation of the sheath axes at the two locales shown resulted from both refolding and late-stage heterogeneous rotation. (A) Erosional section through the “toe” of a sheath fold with a steeply plunging sheath axis (parallel to a hammer handle) at Murotomisaki. (B) Erosionally dissected sheath fold on the coast south of Takaoka harbor; the trace of the sheath axis starts about 0.3 m below hammer and plunges at approximately 15 degrees to the right (north) in photo. **James Hibbard**

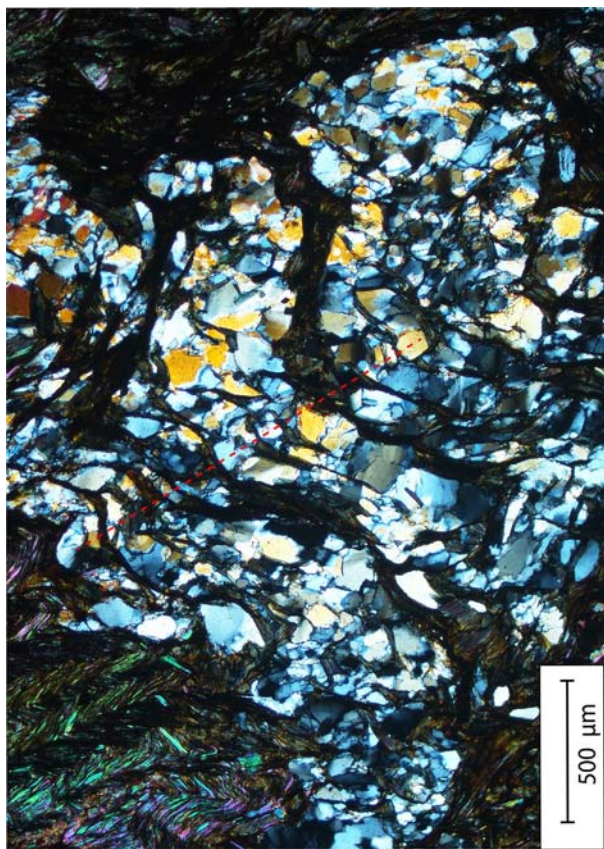


FIGURE 1.77 Fold interference. Photomicrograph of phyllonite showing a fold interference pattern defined by layers of quartz. The axial trace (red dashed line) of the second stage of folding is shown. Jahazpur, Rajasthan, India. **Hindol Ghatak**



FIGURE 1.78 Planar view of complex folding in intensely foliated high-grade quartzofeldspathic gneisses. A well-defined curvilinear hinge zone is distinct in the central part followed by complex fold styles on either side, suggesting that the rocks were sheared intensely. The variation in the hinge line indicates sheath geometry. All the folds exhibit varying plunges from near horizontal to steep values. The axial planes trend N-S and dip steeply toward E. Deformed sheath fold structures involving gabbroic rocks are also recorded in the vicinity. These structures form a part of the detachment zone located in the W part of the Kanjamalai Hills (Mukhopadhyay and Bose, 1994). High-pressure granulites have been described from the region (Saito et al., 2011; Anderson et al., 2012). The Kanjamalai Hills occur ~5 km W of Salem along the Moyar–Bhavani Shear zone, the northern boundary of the Cauvery Suture Zone, Southern Granulite Terrane (Ghosh et al., 2004). **T.R.K. Chetty**

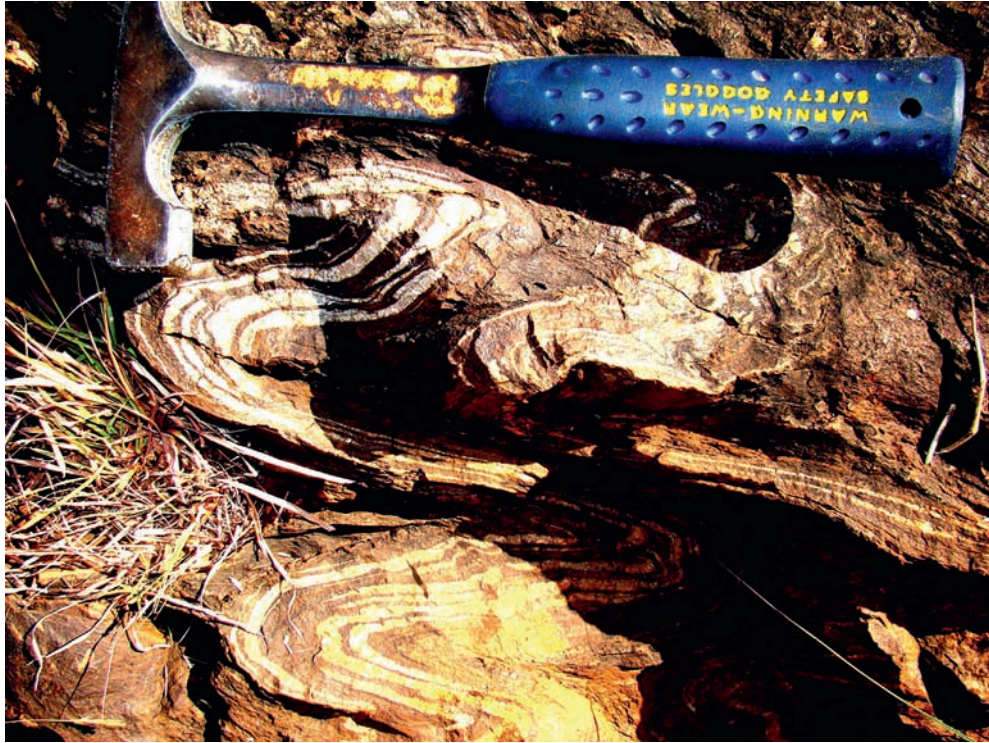


FIGURE 1.79 Neutral folding where the quartzose layers vary in thickness. The hinge area in a few cases shows M-geometry. Chitradurga district, Karnataka, India. Aabha Singh



FIGURE 1.80 Rotation of F_2 fold hinges near the Bastar Craton–Rengali Province boundary shear zone. F_2 fold hinges preserved locally in quartzofeldspathic gneisses of the Bastar Craton, and rotated into parallelism with a late S_5 shear foliation related to the contact with the Rengali Province. At a distance from the shear zone, the F_2 fold axes plunge steeply, but rotate into shallow plunges near the shear zone (the Kerajang Fault of [Crowe et al., 2003](#)). These F_2 folds are now noncylindrical, and have curved intersection lines with the S_5 shear plane. On National Highway-6, N of Padiabahal, Sambalpur district, Odisha, India. Arindam Dutta, Saibal Gupta, and M.K. Panigrahi

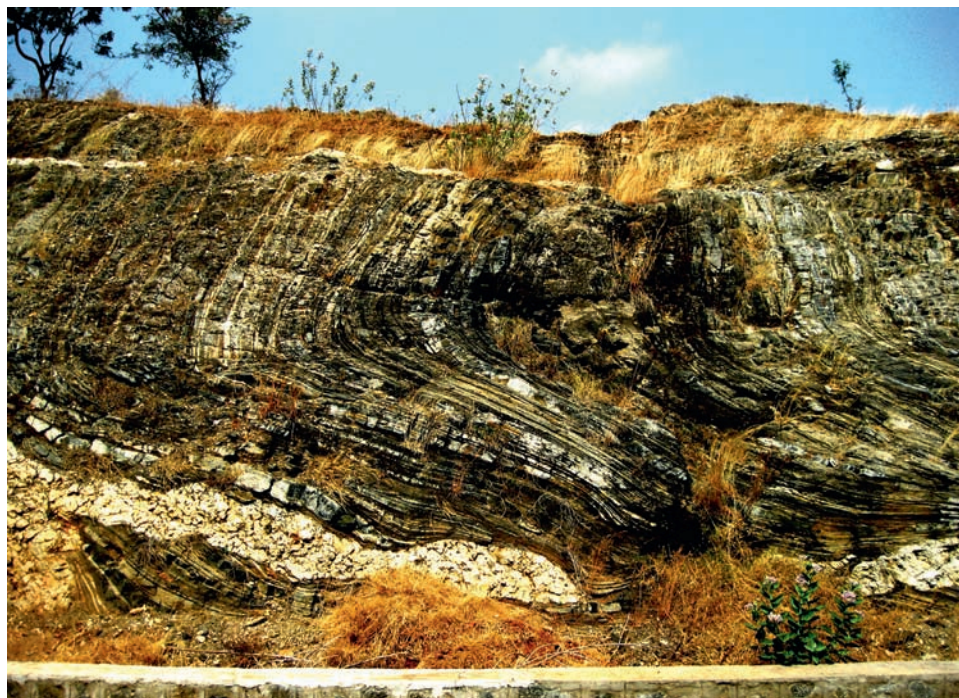


FIGURE 1.81 This ~10 m wide view shows the lower half of a major recumbent fold in a W looking sectional view across the Palghat Cauvery Shear Zone, South India. The rock types include well-foliated mafic-ultramafic rock assemblages along with thin layers of quartzofeldspathic material (Yellappa et al., 2010). The rocks show near horizontal plunges and gentle to moderate dips to north. Pegmatite veins intruded into these rocks both along and across the foliation planes. The outcrop is located near Anniyapuram along a N-S section between Namakkal and Mohanur that coincides with the S boundary zone of the Cauvery Suture Zone (Collins et al., 2014; Santosh et al., 2012). This sector forms a part of the S verging back thrust system, which has been described as a crustal scale “flower structure,” (Chetty and Bhaskar Rao, 2006a), suggesting transpression analogous to modern collisional belts. Precambrian ophiolitic rocks derived from a suprasubduction zone setting were reported from nearby areas. T.R.K. Chetty



FIGURE 1.82 Ptygmatic folds of isoclinals, round hinge, and box geometries in banded calc-silicate gneiss hosted in a recrystallized marble matrix. The calc-silicate gneiss was more viscous than the matrix. A 25 mm diameter coin for scale. N to Munsiri, India. Gogoi et al. (2017) analyzed the shape of this fold using NURB curve. Subhadip Mandal



FIGURE 1.83 Mesoscopic disharmonic folding within the eastern limb of a thrust-related anticline along the NNE-SSW-trending Valnerina Line (Tavarnelli et al., 2001), Umbria-Marche Apennines, Italy. Folding affected the well-bedded marly calcareous strata of the Upper Cretaceous–Eocene Scaglia Rossa Formation. The stunning mesoscale polyclinal fold involving the decimeter-scale calcareous strata is characterized by several nonparallel axial planes but subparallel hinge lines. The cataclastic flow of the intervening thin marly layers produced thinned limbs and a thickened hinge toward the core of the detachment folds that involve the centimeter-scale calcareous strata. Mesoscopic folds and thrust-related structures from this region of the Northern Apennines are described in Tavarnelli (1996, 1997) and Decandia et al. (2002). Location: Valnerina valley (42.784238° 12.869925°), N to the Piedipaterno village, province of Perugia (Italy). Width of view: 2.1 m. **Paolo Pace**



FIGURE 1.84 Folded quartz vein in dolomitic rock showing different geometries of hinge region. Central Indian Tectonic Zone. Jabalpur, Madhya Pradesh, India. **Jyotirmoy Paul**



FIGURE 1.85 Boudinaged mafic layer set in quartzofeldspathic paragneiss subsequently folded. From Mullet Peninsula, County Mayo, Ireland. Kieran F. Mulchrone, Patrick Meere



FIGURE 1.86 Type 3 interference pattern of folds in calc schist in plain view. South Delhi fold belt. Taleti village, Ambaji, Gujrat, India. Narayan Bose and Soumyajit Mukherjee



FIGURE 1.87 Type 3 interference pattern of folds in amphibolite. Upper Aravalli Group. Near Majam, Udaipur district, Rajasthan, India. **Shruthi Narayanan**



FIGURE 1.88 Fold interference pattern in the Variscan basement in Northern Sardinia Island (Italy). Base of the picture: ~130 cm. A thin-layered sedimentary sequence metamorphosed to greenschist facies records three-folding events with orthogonal axial planes and parallel fold axes. Both axis and axial planes are perpendicular to the picture view. The older deformation event produced the asymmetric intrafoliar fold (F1) shown in the left portion of the picture. The fold, developed in white and light-gray quartzites and quartz-rich fine paragneisses, is an isoclinal with thinned delaminated limbs and a thickened hinge. The F1 axial plane foliation, the main foliation documented in the field, is marked by a compositional layer made of muscovite- and biotite-bearing mica schists (the yellow-brownish portion) and light gray/ochre quartzites. It is deformed by a metric-size upright fold (F2) with an antiform geometry and an interlimb angle ranging from 55 to 80 degrees. The F2 subvertical axial plane is gently folded by the late deformation that produced a recumbent open fold (F3) with a subhorizontal axial plane and subhorizontal axes. The superposition of F2 on the F1 fold and those of F3 on F2 folds produce a Type 3 fold interference pattern (Ramsay and Huber, 1987). Gogoi et al. (2020) analyzed the shape of this fold using Bezier curve. **Chiara Frassi**



FIGURE 1.89 Doubly plunging fold with prominent axial depression in metasediments of the Chaibasa Formation, Tetuldanga, Ghatshila, Jharkhand, India. Rahul Kar



FIGURE 1.90 Ptygmatic folds of nonuniform geometry. The rounded hinge is much thicker than the limbs in garnetiferous mica schist, Pur, Bhilwara, Rajasthan, India. Rahul Kar



FIGURE 1.91 Type 3 fold interference with a perfect chicken neck structure. Produced by early tight reclined/inclined fold overprinted by a late set with nearly the same axial trend but with a vertical axial surface normal to the first set. Neoproterozoic dolomite of the Sirohi Group at Sivagaon, Sirohi district, Rajasthan, India. Outcrop width: ~80 cm. **Shailendra Singh**



FIGURE 1.92 Noncylindrical fold with curved axial plane. An inhomogeneous simple shear component is deciphered. Strain varies parallel to the hinge line and on the plane perpendicular to the hinge. Neoproterozoic banded calc-silicate of the Sirohi Group. Khiwandi, Pali district, Rajasthan, India. Marker pen: 15 cm. **Shailendra Singh**



FIGURE 1.93 The field photograph shows a plane noncylindrical fold with a curved hinge line in a calc-silicate mylonitic rock of the Phulad shear zone (Ghosh et al., 1999). The striping lineation (Sengupta and Ghosh, 2007) is deformed by the fold. It is perpendicular at the hinge but rotates to make a smaller angle at the limb. The Mylonitic foliation is subvertical with a northeasterly strike and downdip lineation. The width of the photo is 30 cm. The sample location is 25°36'33.1"N, 73°48'45.1"E. Sadhana M. Chatterjee and Sudipta Sengupta



FIGURE 1.94 A set of thick and thin quartzofeldspathic layers interlayered in a calcareous matrix shows complex folded structures. The locality is the Phulad shear zone, Rajasthan, India. The folds show two generations of disharmonic folding. The axial planes of the dominant folds strike NNE and there is a later set of folds with axial planes at a high angle to the dominant folds. The thin layers show pinch and swell or a boudinage structure at the outer arc of the larger folds. At the inner cores of the larger folds, the small folds are very tight or isoclinal. The arrow shows the geographic north direction. The width of the photo is 40 cm. Sample location is 25°36'29.0"N, 73°48'51.0"E. Sadhana M. Chatterjee and Sudipta Sengupta



FIGURE 1.95 Conjugate folds in Neoproterozoic marble, Sirohi Group. The subhorizontal plunge of the upright fold is at left. At right, the same fold shows a much steeper plunge. Such conjugate folds are produced in ductile shear zones. Revdar, Sirohi district, Rajasthan, India. Diameter of the lens cover: 6 cm. **Shailendra Singh**



FIGURE 1.96 Folded quartz vein within metagreywacke depicting conjugate fold geometry. Kumbhalgarh Formation, ~85 km northwest of Udaipur, Rajasthan, India. [Gogoi et al. \(2020\)](#) analyzed the shape of this fold using Bezier curve. **Swagato Dasgupta**

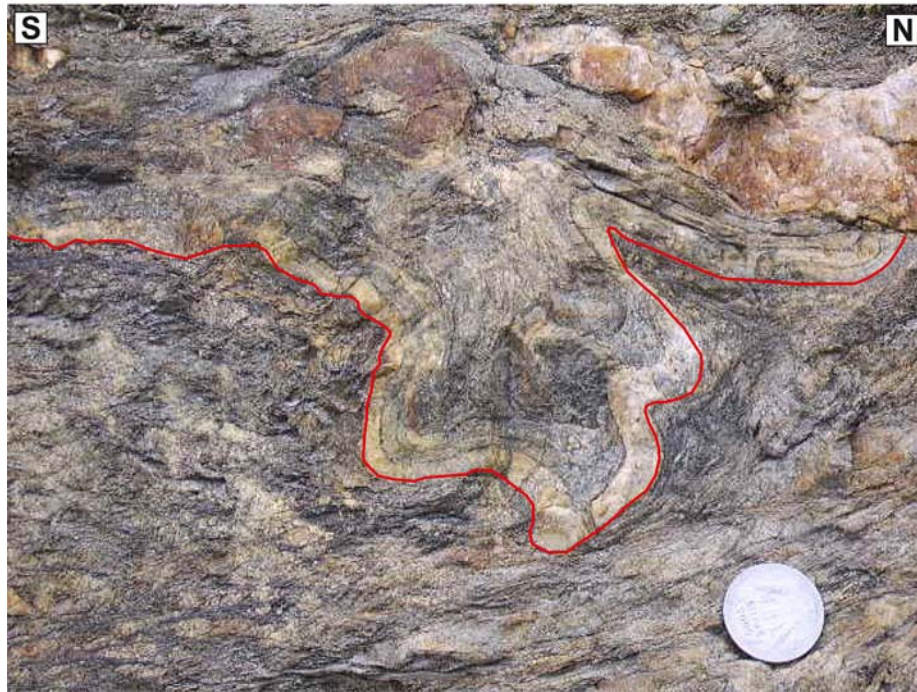


FIGURE 1.97 Ptygmatic fold. A ptygmatic fold formed at the core part of the Almora klippe at the Kumaun Himalaya (Singh, 2014; Patel et al., 2015; Singh and Patel, 2017). If the ductility contrast between the layer and the matrix is high, the matrix does not resist buckling and ptygmatic structures form. This type of fold occur in the cores of antiformal as well as synformal structures. GPS location: N 29°33.22' E 79°36.43'. **Paramjeet Singh**

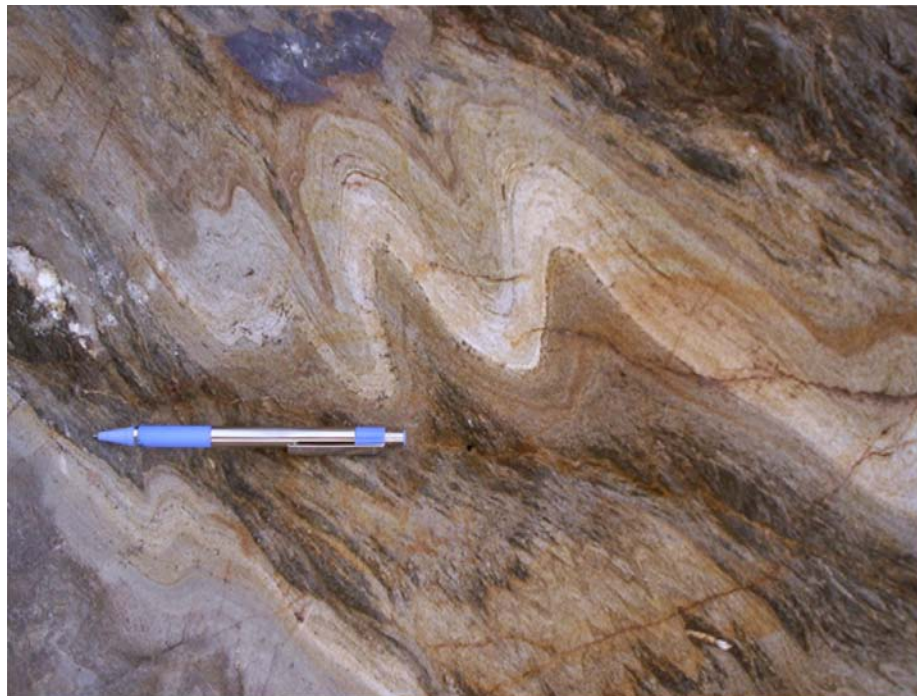


FIGURE 1.98 Asymmetric isoclinal fold. An asymmetric isoclinal fold (M-shaped) with parallel axial planes formed in the pelitic rocks near Khatyari village, Almora Syncline, Kumaun region, Uttarakhand (Singh, 2014; Patel et al., 2015; Singh and Patel, 2017). GPS location: N 29°35.40', E 79°38.30'. **Paramjeet Singh**



FIGURE 1.99 Complex disharmonic folding in lacustrine organic-rich dolomitic lime mudstone or “oil-shale” deposits of the Eocene Green River Formation of the Piceance Creek Basin, Colorado, United States. Folds are represented by close and tight folds. Deformation is situated in a brecciated oil-shale bed, over and underlain by undeformed laminated oil-shale deposits. In literature, the “streaked-and-blebby” oil shale beds range from a few centimeters up to 11 m in thickness with the flat upper and lower boundaries. They generally originate from slumps, slides, debris flows, and mass flows and were correlated over several square kilometers in the Piceance Creek Basin (e.g., [Dyni and Hawkins, 1981](#); [Johnson, 1981](#); [Tānavsuu-Milkeviciene and Sarg, 2012](#)). The formation of such folds requires nondirectional shear stresses, which might be generated within the mass-transport deposits or mass-transport complexes (MTDs or MTCs). Alternatively, considering the deposition in a very gentle/flat lake bottom, such shear stresses can also be generated by seismic shaking. Consequently, the occurrence of these deposits indicates syndimentary tectonic activity and deformation related to seismic shaking. Reproduced from Figure 12 of [Törő et al. \(2013\)](#). **Balázs Törő, Sudipta Dasgupta, and Brian R. Pratt**



FIGURE 1.100 An originally rectangular intraformational mudstone rip-up clast set in a coarse red sandstone that has been deformed into a butterfly shape. Is this a dome and basin Type-1 superposed folding? This is because the clast is less competent than the surrounding material. From Wine Strand, Ballyferriter, County Kerry, Ireland. **Kieran F. Mulchrone and Patrick Meere**



FIGURE 1.101 Elongated dome and basin structures on a subvertical (100/78S) ferruginous quartzite layer developed due to the interference of two sets of open folds. The early folds are subvertical and the later folds are subhorizontal with a gentle plunge toward the west. The structure shows the first mode of superposed buckling where the interlimb angle of the early folds was more than 135 degrees during later folding (Ghosh, 1993, p. 340, Ghosh et al., 1992, Sengupta et al., 2005). On a parallel surface (on the left side), the smaller subhorizontal later folds are more dominant and tighter. There is a set of small wrinkles (lower part of the photo) parallel to the subhorizontal folds. ~4 km from Kemmangundi, Bababudan Hills, Karnataka. The length of the pen in the lower left is 15 cm. GPS Location: N13°33′/29″ and E75°45′/27″. Sudipta Sengupta and Sadhana M. Chatterjee



FIGURE 1.102 1 to 3 cm thick folded anhydrite layers fully encased in rock salt exposed in a solution-mined cavern. At a depth of a few hundred meters, this salt mine in the Zechstein 3 sequence in Eastern Germany (ESCO salt mine Bernburg) frequently shows stacks of thin anhydrite layers that folded during salt deformation. The complex structure of folds indicates superposed folding that most likely emerges from complex salt flows. As the mechanical behavior of anhydrite during salt deformation is still poorly understood, the fold morphologies of these layers help in estimating the competence contrast between the anhydrite and the rock salt (Schmalholz and Podladchikov, 2001) as well as understanding the structure of the anhydrite layers as tracers for intrasalt deformation, also on the larger scale (see Van Gent et al., 2011; Strozzyk et al., 2012). The deformation and evolution of salts on a larger scale such as in salt domes have been modeled by many such as Mukherjee et al. (2010) and Mukherjee (2011b). Photo width: ~50 cm. Frank Strozzyk

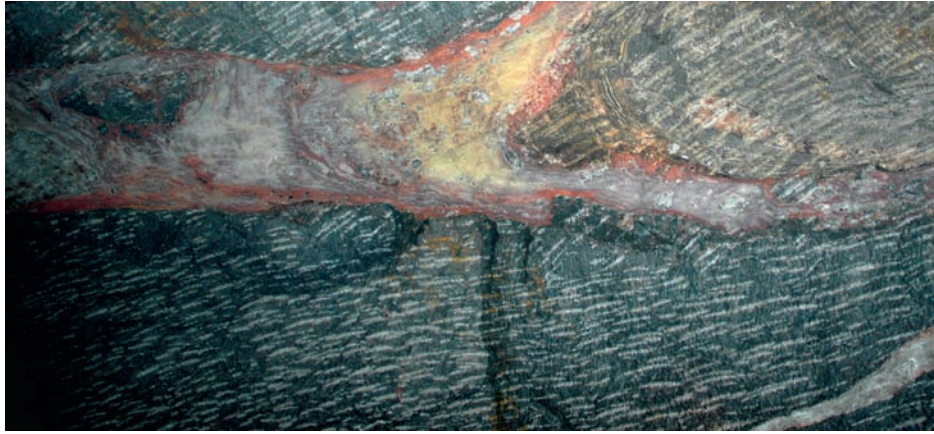


FIGURE 1.103 Red salt in fractured anhydrite. The thickness and competence contrast for layered evaporites cause brittle and ductile deformation at various scales. Compared to the folding of thin anhydrite layers embedded in salt, thick layers of anhydrite also tend to break and boudinage during salt deformation. This is from the internal part of one of the formed anhydrite blocks from the Zechstein 3 sequence in a salt mine in Eastern Germany, where the Z3 main anhydrite (dark) is several tens of meters thick and shows dominantly brittle deformation with an internal fracture system (brighter colors). The fractures are filled with fine-grained halite that shows complicated internal flow structures. The red color of the halite is a typical feature at the anhydrite-halite contact, and is most likely associated with fluid interactions between the partially overpressured anhydrite and the salt ([Hemmann, 1972](#)). Such analog examples of brittle evaporite deformation during ductile salt flows help in studying the mechanical interaction between the evaporites during deformation ([Zulauf et al., 2009](#)). This is important to understand the short- and long-term mechanics and fluid interactions of layered evaporites. These factors govern the dynamics and evolution of salt basins, which host significant volumes of oil and gas that serve as salt mines, storage caverns, and waste repository sites. Photo width: ~120 cm. **Frank Strozyk**

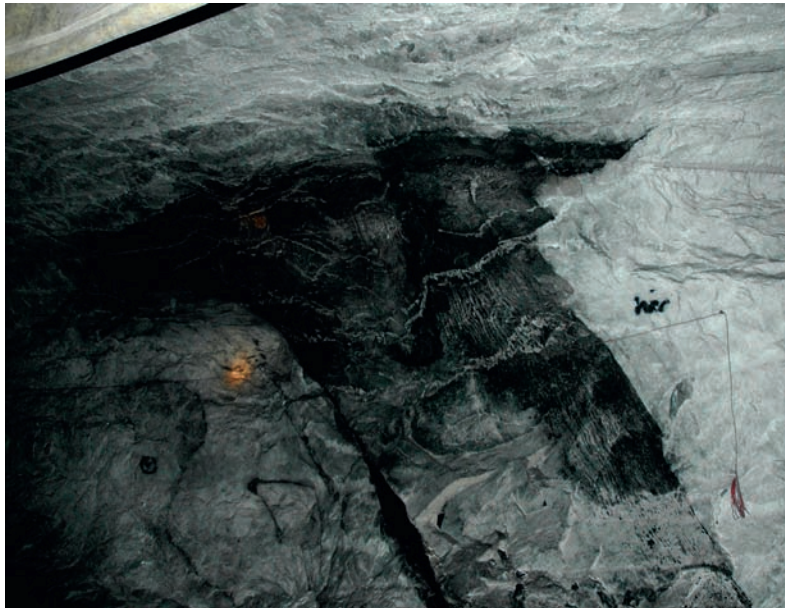


FIGURE 1.104 Anhydrite diapir in rock salt. The dark, mushroom-shaped diapir structure consists of Zechstein 3 anhydrite fully encased in halite in a salt mine in Eastern Germany. The anhydrite is layered and shows complex folding inside the diapir, which has a similar shape and internal structure to large salt diapirs. We assume that it developed coevally to the transformation of gypsum to anhydrite (see e.g., [Williams-Straud and Paul, 1997](#)), and that the quicksand-like material squeezed into the overlying rock salt. This process might have been responsible for the common observation of spatially thickened anhydrite (anhydrite “klippen”: [Zeibig and Wendzel, 2000](#)) in the Zechstein Basin. Thin, black clay layers are often associated with the main anhydrite and can be found along the stem of the diapir. Here, the clay was dragged with the gypsum during the formation of the structure and also interacted with the deforming surrounding rock salt, as indicated by a thin layer of clay tracing a very complicated, overturned structure in the salt left of the diapir stem. Such spectacular features exposed in salt mines help in estimating the relative timing and origin of the formation of intrasalt structures, and indicate that some of the structures we observe are not a product of salt tectonics, but formed during the shallow burial diagenesis of the evaporites. Width of picture: ~6 m. **Frank Strozyk**

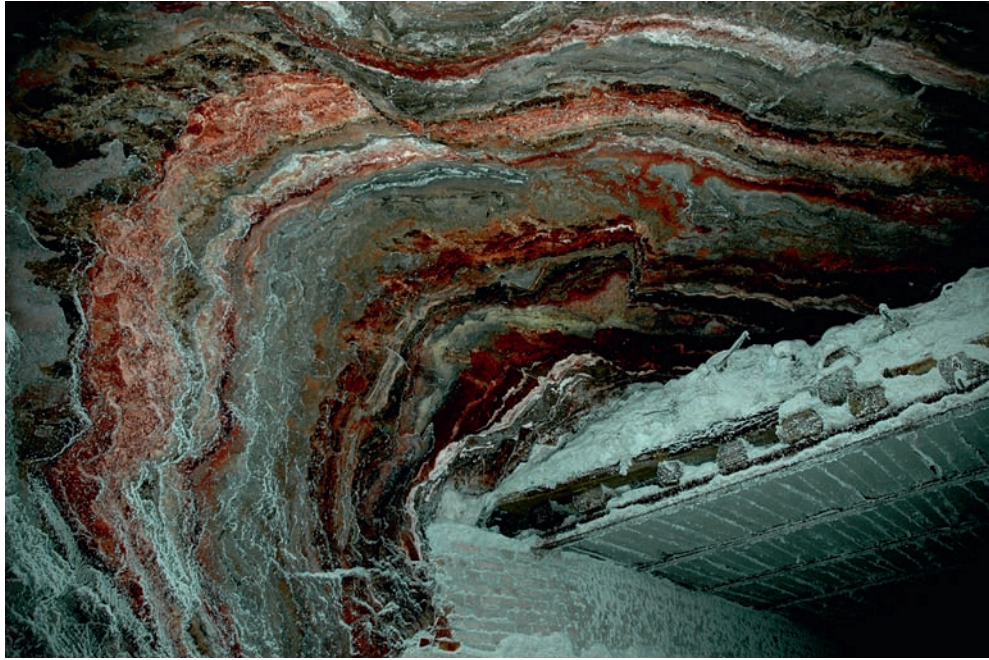


FIGURE 1.105 Structures of potassium salt. Accumulations of potassium salts, that is, carnallite, in the uppermost evaporite sequences are a common feature in German Zechstein salt mines (ESCO salt mine, Gronau, Eastern Germany). The colorful reddish to white salts alter with layers of halite and anhydrite, and form very complex structures (Urai, 1987). Larger folds of anhydrite and halite are often filled by internally complicated folds of the K-salts, which squeeze very fast and can be of highly variable thickness. However, the mechanical behavior of these evaporites during active salt deformation is still poorly understood. That also applies to their genesis and the environment of precipitation, as their fast and complex deformation overprints the original position, geometry, and extension of the layers. Finally, their hygroscopic behavior overprints features that actually formed during salt deformation. Analog and numerical models are required to study them. This would be of economic interest. Width of picture: ~3 m. **Frank Strozyk**



FIGURE 1.106 Fractured ptgmatic fold of quartz vein within granite gneiss. The fold has a thick hinge and narrowing limbs of 1C geometry. N23°50.715', E86°57.152'. India. **Ananya Basu**

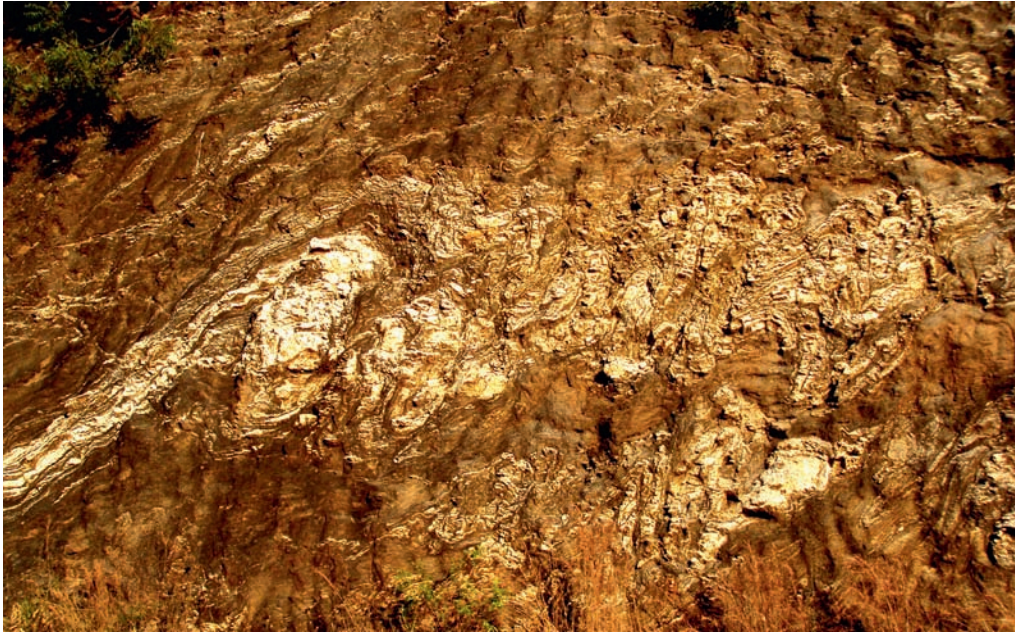


FIGURE 1.107 Complex folding with near horizontal *E-W* fold plunges derived from *N* verging thrust in a *W* looking sectional view. Fold structures are defined by cherty bands associated with highly weathered mafic-ultramafic rock assemblages. The outcrop is located along a newly dug rail cutting section between Namakkal and Mohanur and occurs along the WNW-ESE trending *S* boundary zone of the Cauvery Suture Zone, India (Chetty and Bhaskar Rao, 2006b). Interestingly, the entire assemblage represents a package of mafic-ultramafic rocks defining the back thrust system of the *E-W* trending crustal scale flower structure (Chetty and Bhaskar Rao, 2006b). Ultrahigh temperature (UHT) mineral assemblages are also reported in the vicinity (Santosh et al., 2004). These are also interpreted to have been generated through a suprasubduction zone setting representing ocean plate stratigraphy (Yellappa et al., 2012; Praveen et al., 2014). T.R.K. Chetty



FIGURE 1.108 Meso-scale structures. Tertiary shale layers uplifted and gravity slumping off the core of the Mount Sodom Salt Dome (salt exposed as the more massive light-colored material on the top of the exposure). Drape folds have near-horizontal axes. Photo taken from Road 90 between Mount Sodom and the southern Dead Sea, Israel. Jeff Greenberg



FIGURE 1.109 Type 2 interference pattern of folds in amphibolite. Upper Aravalli Group. Near Majam, Udaipur district, Rajasthan, India. Shruthi Narayanan

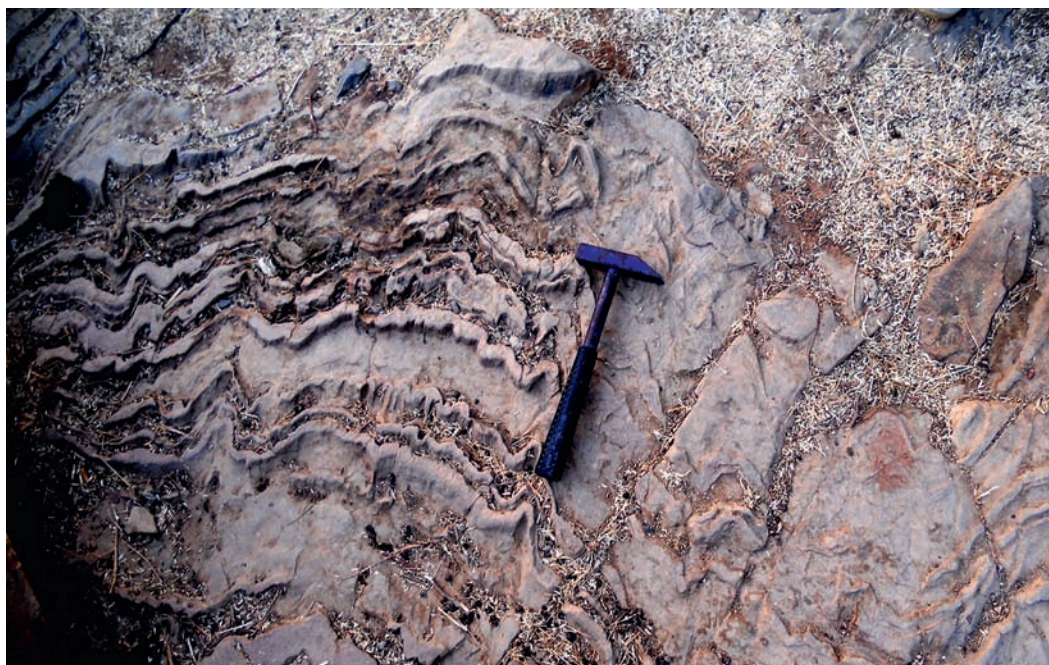


FIGURE 1.110 Two-generation folding in lower greenschist facies quartzite of the Lower to Middle Proterozoic Aravalli Supergroup. Near Zawarmala ~25 km S to Udaipur, Rajasthan, India. Limbs of the first phase folds crenulated to produce the second phase fold. The first phase fold axis parallels that of the second fold. Eirin Kar

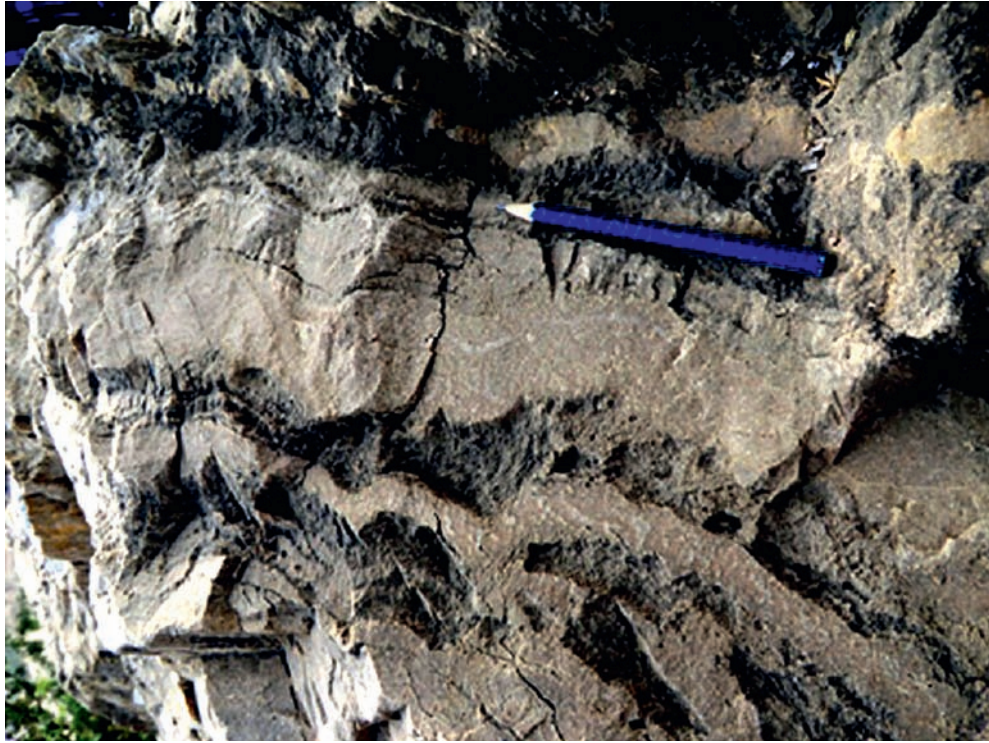


FIGURE 1.111 Type 3 interference pattern or hook-shaped pattern in the high-grade quartzite rock at the contact between the Delhi Supergroup with the Mesoproterozoic basement gneisses. Near Shrinagar ~ 15 km from Ajmer toward NE, Rajasthan, India. Eirin Kar



FIGURE 1.112 Fold interference. Tree superposed fold in migmatite. Wadi Magrish NE Sinai, Egypt. See [Eyal and Amit \(1984\)](#) for detail. Yehuda Eyal



FIGURE 1.113 Gravifossus structure in low-angle trough-cross-stratified sandstone from the late Pliocene Lower Morne L'Enfer Member, SW Trinidad (Trinidad and Tobago). Gravifossus (Van Loon, 2009) is a soft-sedimentary-deformation structure formed at the irregular interface between two fluids with different densities (unlithified sands with two different fluid pressures here), when one fluid layer accelerates into the other by the fluid dynamic Rayleigh-Taylor instability, often aided and accentuated by the passage of a seismic shock wave (Richtmyer-Meshkov instability). Montenat et al. (2007) described similar structures as thixotropic wedges, and interpreted as localized liquefaction and sediment collapse features formed by seismic shaking. The sands were deposited by the subaqueous distributary hyperpycnal channels on the outer shelf feeding the mouth-bar lobes of the paleo-Orinoco river near the shelf edge. The initial bedding surface irregularities, which led to the fluid-dynamic instabilities, were initially provided by the predatory or foraging (likely by hydraulic jetting) trace fossil created by the large vertebrates (e.g., elasmobranchs, phocids, cetaceans) on the open shelf infauna (Gingras et al., 2007; Dasgupta et al., 2016; Uchman et al., 2018; see also Fig. 1.115). Such ichnofossils, viz., *Piscichnus* isp. (e.g., below the hammer as the large-cup-shaped burrows), can be observed in this figure. Sudipta Dasgupta, Balázs Törö, and Luis A. Buatois



FIGURE 1.114 Doubly plunging fold in the Late Paleocene to Eocene sandstone along the Koshalia River section near the Koti area, Himachal Pradesh, India. Eirin Kar

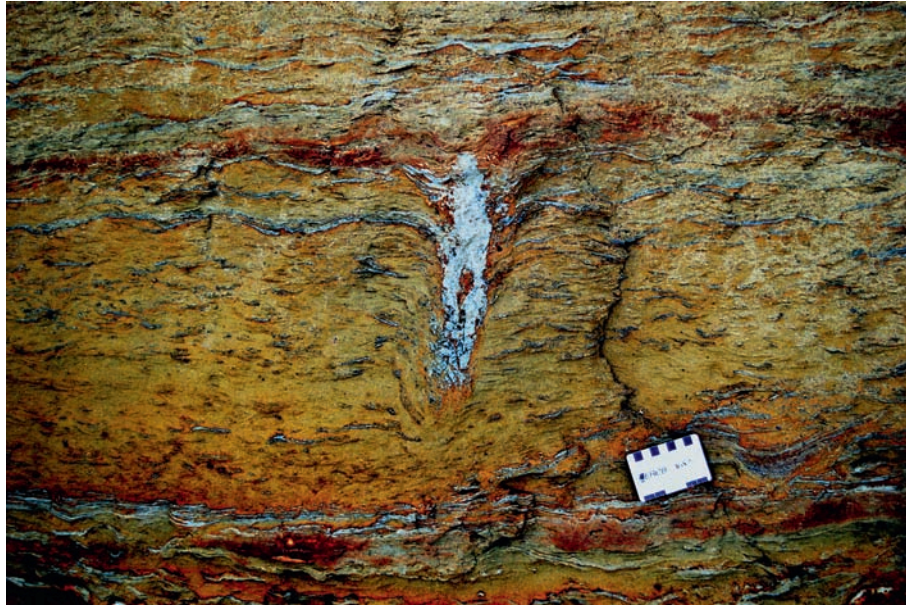


FIGURE 1.115 Photographs showing vertebrate predatory or foraging trace fossil, *Piscichnus* isp., within the flaser-bedded sand-dominated silty-sandstone heterolithic deposit from the late Pliocene Lower Morne L'Enfer Member, SW Trinidad (Trinidad and Tobago) (Gingras et al., 2007; Dasgupta et al., 2016; Uchman et al., 2018). Large vertebrates (e.g., elasmobranchs, phocids, cetaceans) predating behavior on invertebrates (e.g., crustaceans, echinoides, mollusks) by hydraulic jetting is exemplified here as evidenced by the targeted liquefaction (into a massive-looking silty sandstone mass) and the consequent brittle fragments or clasts of the surrounding organic-fragment-rich siltstone thin-beds inside the ichnofossil, particularly at the bottom of the shaft. The heterolithic sediments were deposited on the overbank of the subaqueous distributary hyperpycnal channels on the outer shelf that fed the mouth-bar lobes of the palaeo-Orinoco river close to the shelf edge. **Sudipta Dasgupta, Luis A. Buatois, and Balázs Törő**



FIGURE 1.116 Feldspathic layer in mafic mineral-rich gneiss. Are we looking at a section through a sheath fold? **Kieran F. Mulchrone and Patrick Meere**

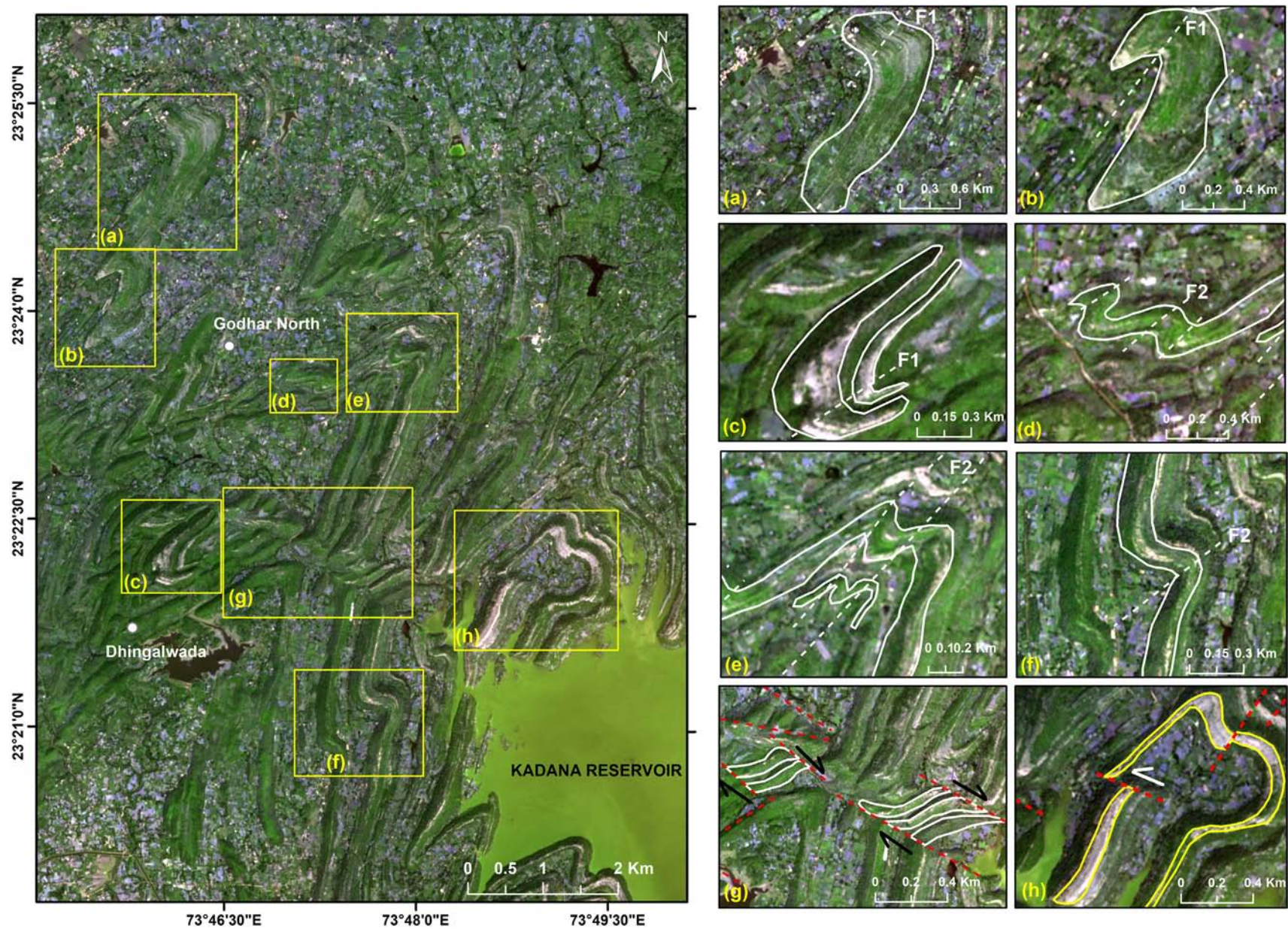


FIGURE 1.117 Polyphase megascale deformation structures: Synoptic view of quartzite-schist exposures of the Lunawada group in Gujarat, India, as seen from Sentinel-2 satellite imagery (true color composite: bands 4-3-2). (Inset) a–c, “Root-less” folds; d, Z-folds; e, M-fold; f, S-fold; g, S–C structure; h, flanking structure (white-dotted lines denote fold axis; red-dashed lines denote faults/fractures). The region falls north of Lunawada village, left embankment of Kadana reservoir in Gujarat. It is bounded by 23°20′50.10″N–23°25′39.70″N latitude and 73°44′42.04″E–73°50′39.14″E longitude. For details please see [Roy and Biswas \(2020\)](#). Reproduced with permission from Current Science journal (under Indian Academy of Science). **Ankita Biswas and Priyom Roy**



FIGURE 1.118 A fold in gray Archean gneiss. A fold in gray Archean gneiss dated at 3.5 billion years, from Swaziland. **Daniel Müller**

References

- Acharyya, S.K., Saha, P., 2008. Geological setting of the Siang Dome located at the Eastern Himalayan Syntaxis. *Himalayan Journal of Sciences* 5, 16–17.
- Adamoli, L., Bigozzi, A., Ciarapica, G., Cirilli, S., Passeri, L., Romano, A., Duranti, F., Venturi, F., 1990. Upper Triassic bituminous facies and Hettangian pelagic facies in the Gran Sasso range. *Bollettino della Società Geologica Italiana* 109, 219–230.
- Alania, V., Enukidze, O., Koiava, K., Razmadze, A., Sanishvili, A., 2008. Thrust systems and time of deformation of the Gare Kakheti foothills, eastern Georgia (Georgia). *Bollettino di Geofisica, teorica ed applicata* 49, 207–208.
- Alania, V., Chabukiani, A., Chagelishvili, R., Enukidze, O., Gogrichiani, K., Razmadze, A., Tsereteli, N., 2017. Growth structures, piggyback basins and growth strata of Georgian part of Kura foreland fold and thrust belt: implication for late alpine kinematic evolution. *Geological Society, London, Special Publications* 428, 171–185.
- Alsop, G.I., Holdsworth, R.E., 2004. Shear zone folds: Records of flow perturbation or structural inheritance? In: Alsop, G.I., Holdsworth, R.E., McCaffey, K.J.W., Hand, M. (Eds.), *Flow Processes in Faults and Shear Zones*. Vol. 224. *Geol Soc London*, pp. 177–199. *Spec Publ.*
- Anastasio, D.J., Teletzke, A.L., Kodama, K.P., Parés, J.M., Gunderson, K.L., 2020. Geologic evolution of the Peña flexure, southwestern Pyrenees mountain front, Spain. *Journal of Structural Geology* 131, 103969.
- Anderson, J.R., Payne, J.L., Kelsey, D.E., Hand, M., Collins, A.S., Santosh, M., 2012. High-pressure granulites at the dawn of the Proterozoic. *Geology* 40, 431–434.
- Banerjee, S., Bose, N., Mukherjee, S., 2019. Field structural geological studies around Kurseong, Darjeeling-Sikkim Himalaya, India. In: Mukherjee, S. (Ed.), *Tectonics and Structural Geology: Indian Context*. Springer, ISBN: 978-3-319-99340-9, pp. 421–440.
- Bell, T.H., 2010. Deformation partitioning, foliation successions and their significance for orogenesis: Hiding lengthy deformation histories in mylonites. In: Law, R.D., Butler, R.W.H., Holdsworth, R.E., Krabbendam, M., Strachan, R.A. (Eds.), *Continental Tectonics and Mountain Building: The Legacy of Peach and Horne*. Vol. 335. *Geol Soc London*, pp. 275–292. *Spec Publ.*
- Bell, T.H., Rudenach, M.J., 1983. Sequential porphyroblast growth and crenulation cleavage development during progressive deformation. *Tectonophysics* 92, 171–194.
- Bikramaditya Singh, R.K., Gururajan, N.S., 2011. Microstructures in quartz and feldspars of the Bomdila gneiss from western Arunachal Himalaya, India: implications for geotectonic evolution of the Bomdila mylonitic zone. *Journal of Asian Earth Sciences* 42, 1163–1178.
- Biswas, T., Mukherjee, S., 2020. Non-uniform B-spline curve analyses of sigmoid brittle shear Y- and ductile shear S-planes. *International Journal of Earth Sciences* (submitted).
- Bose, N., Mukherjee, S., 2019a. Field documentation and genesis of the back-structures from the Garhwal lesser Himalaya, Uttarakhand, India. In: Sharma, V.I.M., Kumar, S. (Eds.), *Crustal Architecture and Evolution of the Himalaya-Karakoram-Tibet Orogen*. 481. *Geological Society of London Special Publications*, pp. 111–125.

- Bose, N., Mukherjee, S., 2019b. Field documentation and genesis of back-structures in ductile and brittle regimes from the foreland part of a collisional orogen: examples from the Darjeeling–Sikkim lesser Himalaya, India. *International Journal of Earth Sciences* 108, 1333–1350.
- Calamita, F., Pizzi, A., Ridolfi, M., Rusciadelli, G., Scisciani, V., 1998. Il buttressing delle faglie normali sinsedimentarie pre-thrusting sulla strutturazione neogenica della catena appenninica: l'esempio della M.gna dei Fiori (Appennino Centrale esterno). *Bollettino Della Società Geologica Italiana* 117, 725–745.
- Calamita, F., Ben M'Barek, M., Di Vincenzo, M., Pelorosso, M., 2004. The Pliocene thrust system of the Gran Sasso salient (Central Apennines, Italy). In: Pasquarè, G., Venturini, C. (Eds.), *Mapping Geology in Italy*. S.EL.CA, Florence, Italy, pp. 227–234.
- Calamita, F., Esestime, P., Paltrinieri, W., Scisciani, V., Tavarnerelli, E., 2009. Structural inheritance of pre- and syn- orogenic normal faults on the arcuate geometry of Pliocene-quaternary thrusts: examples from the central and southern Apennine chain. *Italian Journal of Geosciences* 128, 381–394.
- Calamita, F., Satolli, S., Scisciani, V., Esestime, P., Pace, P., 2011. Contrasting styles of fault reactivation in curved orogenic belts: examples from the central Apennines (Italy). *Geological Society of America Bulletin* 123, 1097–1111.
- Calamita, F., Pace, P., Satolli, S., 2012. Coexistence of fault-propagation and fault-bend folding in curve-shaped foreland fold-and-thrust belts: examples from the northern Apennines (Italy). *Terra Nova* 24, 396–406.
- Calvín, P., Santolaria, P., Casas, A.M., Pueyo, E.L., 2018. Detachment fold vs. ramp anticline: a gravity survey in the southern Pyrenean front (external sierras). *Geological Journal* 53, 178–190.
- Carreras, J., Druguet, E., Griera, A., 2005. Shear zone-related folds. *Journal of Structural Geology* 27, 1229–1251.
- Chetty, T.R.K., 1996. Proterozoic shear zones in southern granulite terrain, India. In: Santosh, M., Yoshida, M. (Eds.), *Gondwana Research Group Memoir-3: The Archaean and Proterozoic Terrains in Southern India within East Gondwana*, pp. 77–89.
- Chetty, T.R.K., Bhaskar Rao, Y.J., 2006a. The Cauvery shear zone, southern granulite terrain, India: a crustal-scale flower structure. *Gondwana Research* 10, 77–85.
- Chetty, T.R.K., Bhaskar Rao, Y.J., 2006b. Constrictive deformation in transpressional regime: field evidence from the Cauvery shear zone, southern granulite terrain, India. *Journal of Structural Geology* 28, 713–720.
- Collins, A.S., Clark, C., Playas, D., 2014. Peninsular India in Gondwana: the tectonothermal evolution of the southern granulite terrain and its Gondwanan counterparts. *Gondwana Research* 25, 190–203.
- Crowe, W.A., Nash, C.R., Harris, L.B., Leeming, P.M., Rankin, L.R., 2003. The geology of the Rengali Province: implications for the tectonic development of northern Orissa, India. *Journal of Asian Earth Sciences* 21, 697–710.
- Dasgupta, S., Buatois, L.A., Zavala, C., Mángano, M.G., Törö, B., 2016. Ichnology of a subaqueously prograding clastic wedge, late Pliocene Morne L'Enfer Formation, Fullarton, Trinidad: implications for recognition of autogenic erosional surfaces and delineation of stress factors on irregular echinoids. *Palaeogeography, Palaeoclimatology, Palaeoecology* 459, 365–380.
- Dasgupta, T., Mukherjee, S., 2020. Sediment compaction and applications in petroleum geoscience. In: *Springer Series: Advances in Oil and Gas Exploration & Production*. (ISSN: 2509-372X).
- Decandia, F.A., Tavarnerelli, E., Alberti, M., 2002. Pressure-solution fabrics and their overprinting relationships within a minor fold train of the Umbria-Marche Apennines, Italy. *Bollettino Della Società Geologica Italiana* 1, 687–694.
- Deng, H., Zhang, C., Koyi, H.A., 2013. Identifying the characteristic signatures of fold-accommodation faults. *Journal of Structural Geology* 56, 1–19.
- Drury, S.A., Holt, R.W., 1980. The tectonic framework of the south Indian Craton, a reconnaissance involving Landsat imagery. *Tectonophysics* 65, T1–T15.
- Dutta, D., Mukherjee, S., 2019. Opposite shear senses: geneses, global occurrences, numerical simulations and a case study from the Indian Western Himalaya. *Journal of Structural Geology* 126, 357–392.
- Dutta D, Mukherjee S, 2020. Extrusion kinematics of UHP terrane in a collisional orogen: EBSD and microstructure-based approach from the Tso Moriri Crystallines (Ladakh Himalaya). *Tectonophysics*. <https://doi.org/10.1016/j.tecto.2020.228641> (in press).
- Dyni, J.R., Hawkins, J.E., 1981. Lacustrine turbidites in the green river formation, northwestern Colorado. *Geology* 9, 235–238.
- Eyal, Y., Amit, O., 1984. The Magrish Migmatites (Northeastern Sinai) and their genesis by metamorphic differentiation triggered by a change in the strain orientation. *Israel Journal of Earth Sciences* 33, 188–200.
- Ez, V., 2000. When shearing is a cause of folding. *Earth-Science Reviews* 51, 155–172.
- Fagereng, A., Sibson, R.H., 2010. Melange rheology and seismic style. *Geology* 38, 751–754.
- Ghisetti, F., 1987. Mechanisms of thrust faulting in the gran sasso chain, central apennines, Italy. *Journal of Structural Geology* 9, 955–967.
- Ghosh, S.K., 1993. *Structural Geology: Fundamentals and Modern Developments*. Pergamon Press, Oxford.
- Ghosh, S.K., Mandal, N., Khan, D., Deb, S.K., 1992. Modes of superposed buckling in single layers controlled by initial tightness of early folds. *Journal of Structural Geology* 14, 381–394.
- Ghosh, S.K., Hazra, S., Sengupta, S., 1999. Planar, non-planar and refolded sheath folds in Phulad shear zone, Rajasthan, India. *Journal of Structural Geology* 21, 1715–1729.
- Ghosh, J.G., de Wit, M.J., Zartman, R.E., 2004. Age and tectonic evolution of Neoproterozoic ductile shear zones in the southern granulite terrain of India, with implications for Gondwana studies. *Tectonics* 23, TC 3006.
- Gingras, M.K., Armitage, I.A., Pemberton, S.G., Clifton, H.E., 2007. Pleistocene walrus herds in the Olympic Peninsula area: trace-fossil evidence of predation by hydraulic jetting. *Palaos* 22, 539–545.
- Godin, L., Yakymchuk, C., Harris, L.B., 2011. Himalayan hinterland-verging superstructure folds related to foreland-directed infrastructure ductile flow: insights from centrifuge analogue modeling. *Journal of Structural Geology* 33, 329–342.
- Gogoi, M.P., Mukherjee, S., 2019. Synthesis of folds in 3D with Bézier surface. In: Billi, A., Fagereng, A. (Eds.), *Problems and Solutions in Structural Geology and Tectonics*. *Developments in Structural Geology and Tectonics Book Series*, vol. 5. Mukherjee, S. (Series Ed.). Elsevier, pp. 279–290. ISBN: 9780128140482.

- Gogoi, M.P., Mukherjee, S., Goswami, T.K., 2017. Analyses of fold profiles by changing weight parameters of NURB curves. *Journal of Earth System Science* 126, 98.
- Gogoi, M.P., Mukherjee, S., Goswami, T.K., 2020. Asymmetric fold profiles simulated by cubic Bezier curves. *International Journal of Earth Sciences*. <https://doi.org/10.1007/s00531-020-01945-2>.
- Gopalakrishnan, K., 1994. An Overview of Southern Granulite Terrain, India—Constraints in Reconstruction of Precambrian Assembly of Gondwanaland, Vol. 2. Oxford and IBH Publication, Gondwana Nine, pp. 1003–1026.
- Grasemann, B., Martel, S., Passchier, C., 2005. Reverse and normal drag along a fault. *Journal of Structural Geology* 27, 999–1010.
- Hardy, S., Poblet, J., 1994. Geometric and numerical model of progressive limb rotation in detachment folds. *Geology* 22, 371–374.
- Harris, L.B., 2003. Folding in high-grade rocks due to back-rotation between shear zones. *Journal of Structural Geology* 25, 223–240.
- Harris, L.B., Koyi, H.A., Fossen, H., 2002. Mechanisms for folding of high-grade rocks in extensional tectonic settings. *Earth-Science Reviews* 59, 163–210.
- Harris, L.B., Godin, L., Yakymchuk, C., 2012a. Regional shortening followed by channel flow induced collapse: a new mechanism for—dome and keel geometries in Neoarchaean granite-greenstone terrains. *Precambrian Research* 212–213, 139–154.
- Harris, L.B., Yakymchuk, C., Godin, L., 2012b. Implications of centrifuge simulations of channel flow for opening out or destruction of folds. *Tectonophysics* 526–529, 67–87.
- Hemmann, M., 1972. Ausbildung und Genese des Leinesteinsalzes und des Hauptanhydrits (Zechstein 3) im Ostteil des Subherzynen Beckens. *Ber. deutsch. Ges. Geol. Wiss. B. Min. Lagerstättenf* 16, 307–411.
- Hibbard, J., Karig, D., 1987. Sheath-like folds and progressive fold deformation in Tertiary sedimentary rocks of the Shimanto accretionary complex, Japan. *Journal of Structural Geology* 9, 845–857.
- Hibbard, J., Karig, D., 1990. Structural and magmatic responses to spreading ridge subduction; and example from southwest Japan. *Tectonics* 9, 207–230.
- Hibbard, J., Karig, D., Taira, A., 1992. Anomalous structural evolution of the Shimanto accretionary prism, Murotomisaki, Shikoku Island, Japan. *The Island Arc* 1, 133–147.
- Hobbs, B.E., Means, W.D., Williams, P.F., 1976. *An Outline of Structural Geology*. John Wiley & Sons, New York.
- Hogan, P.J., Burbank, D.W., 1996. Evolution of the Jaca piggyback basin and emergence of the external sierra, southern Pyrenees. In: *Tertiary Basins of Spain: the Stratigraphic Record of Crustal Kinematics*. vol. 6. Cambridge Univ. Press, pp. 153–160.
- Hudleston, P.J., Lan, L., 1993. Information from fold shapes. *Journal of Structural Geology* 15, 253–264.
- Hudleston, P.J., Treagus, S.H., 2010. Information from folds. A review. *Journal of Structural Geology* 32, 2042–2071.
- Johnson, R.C., 1981. Preliminary Geologic Map of the Desert Gulch Quadrangle, Garfield County, Colorado. U.S. Geological Survey Miscellaneous Field Investigations Map MF-1328, scale 1:24,000.
- Karaoui, B., 2014. Geodynamic evolution of the Bas Draâ inlier (Western Anti-Atlas, Morocco): Insights from physical volcanology, geochemistry and geochronology of the Ediacaran volcanosedimentary successions and structural analysis of Variscan deformation. *Geology departement, Moulay Ismail University*. PhD thesis.
- Khanal, S., Robinson, D.M., Mandal, S., Simkhada, P., 2014. Structural, geochronological and geochemical evidence for two distinct thrust sheets in the ‘Main Central thrust zone’, the Main Central thrust and Ramgarh–Munsiari thrust: implications for upper crustal shortening in central Nepal. In: Mukherjee, S., Carosi, R., van der Beek, P.A., Mukherjee, B.K., Robinson, D.M. (Eds.), *Tectonics of the Himalaya*. 412. Geological Society Special Publications, London, pp. 221–245.
- Kronenberg, A.K., Kirby, S.H., Pinkstone, J., 1990. Basal slip and mechanical anisotropy of biotite. *Journal of Geophysical Research* 95, 257–278.
- Leah, H., Fondriest, M., Lucca, A., Storti, F., Balsamo, F., Di Toro, G., 2018. Coseismic extension recorded within the damage zone of the Vado di Ferruccio Thrust Fault, Central Apennines, Italy. *Journal of Structural Geology* 114, 121–138.
- Lin, A., 1997. Ductile deformation of biotite in foliated cataclasis, Iida-Matsukawa fault, Central Japan. *Journal of Asian Earth Sciences* 15, 407–411.
- Llorens, M.-G., Bons, P.D., Griera, A., Gomez-Rivas, E., Evans, L.A., 2013. Single layer folding in simple shear. *Journal of Structural Geology* 50, 209–220.
- Lucca, A., Storti, F., Balsamo, F., Clemenzi, L., Fondriest, M., Burgess, R., Di Toro, G., 2019. From submarine to subaerial out-of-sequence thrusting and gravity-driven extensional faulting: gran Sasso massif, central Apennines, Italy. *Tectonics* 38, 4155–4184.
- Marco, S., Agnon, A., 1995. Prehistoric earthquake deformations near Masada, Dead Sea graben. *Geology* 23, 695–698.
- McClay, K.R., Insley, M.W., 1986. Duplex structures in the Lewis thrust sheet. Crowsnest Pass, Rocky mountains, Alberta, Canada. *Journal of Structural Geology* 8, 911–922.
- Millán Garrido, H., Pocoví Juan, A., Casas Sainz, A.M., 1995. El frente cabalgamiento surpirenaico en el extremo occidental de las Sierras Exteriores. *Revista de la Sociedad Geológica de España* 8, 73–90.
- Millán, H., Pueyo, E.L., Aurell, M., Luzón, A., Oliva-Urcia, B., Martínez Peña, M.B., Pocoví, A., 2000. Actividad tectónica registrada en los depósitos terciarios del frente meridional del Pirineo central. *Revista de la Sociedad Geológica de España* 13, 117–138.
- Mitra, S., 2002. Fold-accommodation faults. *AAPG Bulletin* 86, 671–693.
- Montenat, C., Barrier, P., Ott d’Estevou, P., Hibsich, C., 2007. Seismites: an attempt at critical analysis and classification. *Sedimentary Geology* 196, 5–30.
- Mortimer, N., 2004. New Zealand’s geological foundations. *Gondwana Research* 7, 261–272.
- Mukherjee, S., 2007. *Geodynamics, Deformation and Mathematical Analysis of Metamorphic Belts of the NW Himalaya*. (Unpublished Ph.D. thesis). Indian Institute of Technology Roorkee, pp. 1–267.
- Mukherjee, S., 2010. Microstructures of the Zaskar shear zone. *Earth Science India* 3, 9–27.
- Mukherjee, S., 2011a. Flanking microstructures of the Zaskar shear zone, west Indian Himalaya. *YES Bulletin* 1, 21–29.
- Mukherjee, S., 2011b. Estimating the viscosity of rock bodies—a comparison between the Hormuz and the Namakdan salt diapirs in the Persian Gulf, and the Tso Moriri gneiss dome in the Himalaya. *Journal of Indian Geophysical Union* 15, 161–170.
- Mukherjee, S., 2013. *Deformation Microstructures in Rocks*. Springer.

- Mukherjee, S., 2014a. Atlas of Shear-Zone Structures in Meso-Scale. Springer.
- Mukherjee, S., 2014b. Review of the flanking structures in meso- and micro-scales. *Geological Magazine* 151, 957–974.
- Mukherjee, S., Koyi, H.A., 2009. Flanking microstructures. *Geological Magazine* 146, 517–526.
- Mukherjee, S., Koyi, H.A., 2010. Higher Himalayan shear zone, Zaskar Indian Himalaya- microstructural studies and extrusion mechanism by combination of simple shear and channel flow. *International Journal of Earth Sciences* 99, 1083–1110.
- Mukherjee, S., Kumar, N., 2018. A first-order model for temperature rise for uniform and differential compression of sediments in basins. *International Journal of Earth Sciences* 107, 2999–3004.
- Mukherjee, S., Talbot, C.J., Koyi, H.A., 2010. Viscosity estimates of salt in the Hormuz and Namakdan salt diapirs, Persian Gulf. *Geological Magazine* 147, 497–507.
- Mukherjee, S., Puneekar, J.N., Mahadani, T., Mukherjee, R., 2015. Intrafolial folds- review & examples from the western Indian Higher Himalaya. In: Mukherjee, S., Mulchrone, K.F. (Eds.), *Ductile Shear Zones: From Micro- to Macro-scales*. Wiley-Blackwell, ISBN: 978-1-118-84496-0, pp. 182–205.
- Mukherjee, S., Bose, N., Ghosh, R., Dutta, D., Misra, A.A., Kumar, M., Dasgupta, S., Biswas, T., Joshi, A., Limaye, M., 2020. *Structural Geological Atlas*. Springer, ISBN: 978-981-13-9825-4.
- Mukhopadhyay, B., Bose, M.K., 1994. Transitional granulite-eclogite facies metamorphism of basic supracrustal rocks in a shear zone complex in the Precambrian shield of South India. *Mineralogical Magazine* 58, 97–118.
- Nelson, K.D., 1982. A suggestion for the origin of mesoscopic fabric in accretionary mélangé, based on features observed in the Chrystalls Beach complex, South Island, New Zealand. *Geological Society of America Bulletin* 93, 625–634.
- Nichols, G.J., 1987. The structure and stratigraphy of the Western external sierras of the Pyrenees, northern Spain. *Geological Journal* 22, 245–259.
- Oliva-Urcia, B., Casas, A.M., Pueyo, E.L., Pocoví, A., 2012. Structural and paleomagnetic evidence for non-rotational kinematics in the western termination of the External Sierras (southwestern Central Pyrenees). *Geologica Acta* 10, 125–144.
- Oliva-Urcia, B., Beamud, E., Garcés, M., Arenas, C., Soto, R., Pueyo, E.L., Pardo, G., 2016. New magnetostratigraphic dating of the Palaeogenesynthetic sediments of the west-Central Pyrenees: Tectonostratigraphic implications. In: Pueyo, E.L., Cifelli, F., Sussman, A.J., Oliva-Urcia, B. (Eds.), *Palaeomagnetism in Fold and Thrust Belts: New Perspectives*. vol. 425. Geological Society, London, pp. 127–128. Special Publications.
- Oliva-Urcia, B., Beamud, E., Arenas, C., Pueyo, E.L., Garcés, M., Soto, R., Valero, L., Pérez-Rivarés, F.J., 2019. Dating the northern deposits of the Ebro foreland basin; implications for the kinematics of the SW Pyrenean front. *Tectonophysics* 765, 11–34.
- Osanai, Y., Nogi, Y., Baba, S., Nakano, N., Adachi, T., Hokada, T., Toyoshima, T., Owada, M., 2013. Geologic evolution of the Sør Rondane Mountains, East Antarctica: collision tectonics proposed based on metamorphic processes and magnetic anomalies. *Precambrian Research* 234, 8–29.
- Passchier, C., 2001. Flanking structures. *Journal of Structural Geology* 23, 951–9962.
- Passchier, C.W., Trouw, R.A.J., 1996. *Microtectonics*. Springer-Verlag, p. 289.
- Patel, R.C., Singh, P., Lal, N., 2015. Thrusting and back-thrusting as post-emplacement kinematics of the Almora klippe: insights from low-temperature thermochronology. *Tectonophysics* 653, 41–51.
- Perrot, M., Tremblay, A., Ruffet, G., Labrousse, L., Gervais, F., Caroir, F., 2020. Diachronic metamorphic and structural evolution of the Connecticut Valley–Gaspé trough, Northern Appalachians. *Journal of Metamorphic Geology* 38, 3–27.
- Praveen, M.N., Santosh, M., Yang, Q.Y., Zhang, Z.C., Huang, H., Singaneni, S., Sajinkumar, K.S., 2014. Zircon U–Pb geochronology and Hf isotope of felsic volcanics from Attappadi, India: implications for Neoproterozoic convergent margin tectonics. *Gondwana Research* 26, 907–924.
- Pueyo, E.L., Oliva-Urcia, B., Sánchez-Moreno, E.M., Arenas, C., Silva-Casal, R., Calvín, P., Santolaria, P., García-Lasanta, C., Oliván, C., Compared, F., Casas, A.M., Pocoví, A., 2020. The geometry and kinematics of the southwestern termination of the Pyrenees; a fieldguide to the Sto. Domingo anticline. In: Mukherjee, S. (Ed.), *Structural Geology & Tectonics Field Guidebook*. Springer.
- Ramsay, J.G., 1967. *Folding and Fracturing of Rocks*. McGraw Hill, New York. Pp. 117, 352, 390, 413, 414.
- Ramsay, J.G., Huber, M.I., 1987. *The Techniques of Modern Structural Geology*. In: *Folds and Fractures*. vol. 2. Academic Press, London, Orlando, San Diego, New York, Austin, Boston, Sydney, Tokyo, Toronto. 391 pp.
- Rodríguez-Pascua, M.A., Calvo, J.P., De Vicente, G., Gómez-Gras, D., 2000. Soft-sediment deformation structures interpreted as seismites in lacustrine sediments of the Prebetic zone, SE Spain, and their potential use as indicators of earthquake magnitudes during the late Miocene. *Sedimentary Geology* 135, 117–135.
- Roy, P., Biswas, A., 2020. Unique polyphase deformational structures of Lunawada metasedimentary rocks identified from remote sensing imagery. *Current Science* 119 (4), 600–603.
- Saito, Y., Tsunogae, T., Santosh, M., Chetty, T.R.K., Horie, K., 2011. Neoproterozoic high pressure metamorphism from the northern margin of the Palghat–Cauvery suture zone, southern India: petrology and zircon SHRIMP geochronology. *Journal of Asian Earth Sciences* 40, 268–285.
- Santosh, M., Tsunogae, T., Koshimoto, S., 2004. First report of sapphirine-bearing rocks from the Palghat–Cauvery shear zone system, southern India. *Gondwana Research* 7, 620–626.
- Santosh, M., Maruyama, S., Sato, K., 2009. Anatomy of a Cambrian suture in Gondwana: Pacific-type orogeny in southern India? *Gondwana Research* 16, 321–341.
- Santosh, M., Xiao, W.J., Tsunogae, T., Chetty, T.R.K., Yellappa, T., 2012. The Neoproterozoic subduction complex in southern India: SIMS zircon U–Pb ages and implications for Gondwana assembly. *Precambrian Research*, 190–208.
- Satolli, S., Speranza, F., Calamita, F., 2005. Paleomagnetism of the gran Sasso range salient (central Apennines, Italy): pattern of orogenic rotations due to translation of a massive carbonate indenter. *Tectonics* 24, TC 4019.
- Schmalholz, S.M., Podladchikov, Y.Y., 2001. Strain and competence contrast estimation from fold shape. *Tectonophysics* 340, 195–213.
- Scisciani, V., Tavarnelli, E., Calamita, F., 2002. The interaction of extensional and contractional deformations in the outer zones of the central Apennines, Italy. *Journal of Structural Geology* 24, 1647–1658.

- Séguret, M., 1972. Etude tectonique des nappes et séries décollées de la partie centrale du versant sud des Pyrénées (Ph.D. thesis). Caractère synsédimentaire, rôle de la compression et de la gravité. University of Montpellier.
- Sengupta, S., Ghosh, S.K., 2004. Analysis of transpressional deformation from geometrical evolution of mesoscopic structures from Phulad shear zone, Rajasthan, India. *Journal of Structural Geology* 26, 1961–1976.
- Sengupta, S., Ghosh, S.K., 2007. Origin of striping lineation and transposition of linear structures in shear zones. *Journal of Structural Geology* 29, 273–287.
- Sengupta, S., Ghosh, S.K., Deb, S.K., Khan, D., 2005. Opening and closing of folds in superposed deformations. *Journal of Structural Geology* 27, 1282–1299.
- Singh, P., 2014. Exhumation history of the Higher and Lesser Himalayan crystallines in the Kumaon-Garhwal region, NW-India: As revealed from Fission Track Thermochronology. Unpublished Ph.D. thesis, Department of Geophysics, Kurukshetra University Kurukshetra.
- Singh, P., Patel, R.C., 2017. Post-emplacement exhumation history of Almora klippe of Kumaon-Garhwal Himalaya, NW-India as revealed by Fission track thermochronology. *International Journal of Earth Sciences* 106, 2189–2202.
- Singh, P., Patel, R.C., Lal, N., 2012. Plio-Pleistocene in-sequence thrust propagation along the Main Central Thrust zone (Kumaon-Garhwal Himalaya, India): new thermochronological data. *Tectonophysics*. <https://doi.org/10.1016/j.tecto.2012.08.015>.
- Strozyk, F., van Gent, H., Urai, J.L., Kukla, P.A., 2012. 3D seismic study of complex intra-salt deformation: An example from the Zechstein 3 stringer in the western Dutch offshore. In: Alsop, G.I., Archer, S.G., Hartley, A.J., Grant, N.T., Hodgkinson, R. (Eds.), *Salt Tectonics, Sediments and Prospectivity*. vol. 363. Geological Society, London, pp. 489–501. Special Publications.
- Tānavsuu-Milkeviciene, K., Sarg, F.J., 2012. Evolution of an organic-rich lake basin—stratigraphy, climate and tectonics: Piceance Creek basin, Eocene Green River formation. *Sedimentology* 59, 1735–1768.
- Tavernelli, E., 1996. The effects of pre-existing normal faults on thrust ramp development: an example from the northern Apennines, Italy. *Geologische Rundschau* 85, 363–371.
- Tavernelli, E., 1997. Structural evolution of a foreland fold-and-thrust belt: the Umbria-Marche Apennines, Italy. *Journal of Structural Geology* 19, 523–534.
- Tavernelli, E., Decandia, F.A., Renda, P., Tramutoli, M., Gueguen, E., Alberti, M., 2001. Repeated reactivation in the Apennine-Maghrebide system, Italy: A possible example of fault-zone weakening? In: Holdsworth, R.E., Strachan, R.A., Magloughlin, J.F., Knipe, R.J. (Eds.), *The Nature and Tectonic Significance of Fault Zone Weakening*. vol. 186. Geological Society, London, pp. 273–286. Special Publication.
- Teixell, A., García-Sansegundo, J., 1995. Estructura del sector central de la Cuenca de Jaca (Pirineos meridionales). *Revista de la Sociedad Geológica de España* 8, 215–228.
- Ternet, Y., Baudin, T., Laumonier, B., Barnolas, A., Gil-Peña, I., Martín-Alfame, S., 2008. Mapa Geológico de los Pirineos a E. 1: 400.000. IGME–BRGM, Madrid-Orleans.
- Törő, B., Pratt, B.R., Renaut, R.W., 2013. Seismically Induced Soft-sediment Deformation Structures in the Eocene Lacustrine Green River Formation (Wyoming, Utah, Colorado, USA) – a Preliminary Study. *Geo Convention 2013: Integration*, Calgary (Poster abstract).
- Toyoshima, T., Owada, M., Shiraishi, K., 1995. Structural evolution of metamorphic and intrusive rocks from the central part of the Sør Rondane Mountains, East Antarctica. *Proceedings of the NIPR Symposium on Antarctic Geosciences* 8, 75–97.
- Toyoshima, T., Osanai, Y., Baba, S., Hokada, T., Nakano, N., Adachi, T., Otsubo, M., Ishikawa, M., Nogi, Y., 2013. Sinistral transpressional and extensional tectonics in Dronning Maud Land, East Antarctica, including the Sør Rondane Mountains. *Precambrian Research* 234, 30–46.
- Uchman, A., Torres, P., Johnson, M.E., Berning, B., Ramalho, R.S., Rebelo, A.C., Melo, C.S., Baptista, L., Madeira, P., Cordeiro, R., Avila, S.P., 2018. Feeding traces of recent ray fish and occurrences of the trace fossil *Piscichnus waitemata* from the Pliocene of Santa Maria Island, Azores (Northeast Atlantic). *Palaos* 33, 361–375.
- Urai, J.L., 1987. Development of microstructure during deformation of carnallite and bischofite in transmitted light. *Tectonophysics* 135, 251–263.
- Van Gent, H., Urai, J.L., de Keijzer, M., 2011. The internal geometry of salt structures—a first look using 3D seismic data from the Zechstein of the Netherlands. *Journal of Structural Geology* 33, 292–311.
- Van Loon, A.J., 2009. Soft-sediment deformation structures in siliciclastic sediments: an overview. *Andean Geology* 15, 3–55.
- Van Loon, A.J., Brodzikowski, K., Gotowala, R., 1984. Structural analysis of kink bands in unconsolidated sands. *Tectonophysics* 104, 351–374.
- Wang, S., Mo, Y., Phillips, R.J., Wang, C., 2014. Karakoram fault activity defined by temporal constraints on the Ayi Shan detachment, SW Tibet. *International Geology Review* 56, 15–28.
- Williams, M.L., Scheltema, K.E., Jercinovic, M.J., 2001. High-resolution compositional mapping of matrix phases: implications for mass transfer during crenulation cleavage development in the Moretown formation, western Massachusetts. *Journal of Structural Geology* 23, 923–939.
- Williams-Straud, S.C., Paul, J., 1997. Initiation and growth of gypsum piercement structures in the Zechstein Basin. *Journal of Structural Geology* 19, 897–907.
- Yellappa, T., Chetty, T.R.K., Tsunogae, T., Santosh, M., 2010. The Manamedu complex: geochemical constraints on Neoproterozoic suprasubduction zone ophiolite formation within the Gondwana suture in southern India. *Journal of Geodynamics* 50, 268–285.
- Yellappa, T., Santosh, M., Chetty, T.R.K., Kwon, S., Park, C., Nagesh, P., Mohanty, D.P., Venkatasivappa, V., 2012. A Neoproterozoic dismembered ophiolite complex from southern India: geochemical and geochronological constraints on its suprasubduction origin. *Gondwana Research* 21, 246–265.
- Yin, A., 2006. Cenozoic tectonic evolution of the Himalayan orogen as constrained by along-strike variation of structural geometry, exhumation history, and foreland sedimentation. *Earth-Science Reviews* 76, 1–131.
- Zeigbig, S., Wendzel, J., 2000. Exploration of anhydrite wall and klippe structure for an optimized extraction of rock salt in the K+S salt mine Bernburg (Northern Germany). In: *World Salt Symposium*. vol. 1. Elsevier, Amsterdam, pp. 193–198.
- Zulauf, G., Zulauf, J., Bornemann, O., Kihm, N., Peinl, M., Zanella, F., 2009. Experimental deformation of a single-layer anhydrite in halite matrix under bulk constriction. Part 1: geometric and kinematic aspects. *Journal of Structural Geology* 31, 460.

Chapter 2

Ductile shear zones

Tabular or sheetlike and planar or curvilinear zones in which rocks are more highly strained than rocks adjacent to the zone are called ductile shear zones (Davis et al., 2012; also see Mukherjee and Biswas, 2014, 2015). The identification and study of ductile shear zones (Figures 2.1–2.73) are important because major plate boundaries are defined by such shear zones (Regenauer-Lieb and Yuen, 2003). We need to study such zones because along them, partially molten rocks can flow (review by Clark et al., 2011). Second, viscous dissipation related to such zones has been investigated (Nabelek et al., 2011). No slip boundary condition was assumed classically to explain the kinematics of ductile shear zones (Ramsay, 1980; Mukherjee, 2012; etc). However, recently, the slip boundary condition has become more recognized (Frehner et al., 2011; Mulchrone and Mukherjee, 2016, 2020). The ductile shear sense/sense of movement from such zones can be deciphered mainly from asymmetric sigmoid, parallelogram and lenticular clasts as well as intrafolial folds (Lister and Snoke, 1984; ten Grotenhuis et al., 2003; Mukherjee, 2011a,b, 2013a,b,c, 2014a,b,c; Bhadra and Gupta, 2015). See Passchier and Trouw (2005) for a review on ductile shear zones, and Mukherjee and Mulchrone (2013) and Mulchrone and Mukherjee (2015) for the shear heat pattern in these zones. In addition to such shear sense indicators, this chapter also presents near symmetric clasts that form possibly within shear zones but that do not give the shear sense (e.g., Mukherjee, 2017). See Mukherjee et al. (2020) for shear fabrics from other terrains. Interestingly, Figure 2.38 describes cleavage refraction. On this topic, see the recent work of Bose et al. (2020). Fig. 2.32 presents a bookshelf glide. See Fig. 7i2 and its caption in Dutta and Mukherjee (2019) for the shear sense assigned in that figure with white half arrows. For new works on bookshelf glide, see Mukherjee (2018) and Mukherjee and Khonsari (2018).



FIGURE 2.1 Domino-style normal faults with a strike slip component, dipping 50 degrees toward N60°–64°E (rake 70°W). Upper Pliocene–Lower Pleistocene polymictic volcanic breccias. A transtension component with western extension is likely due to the parallelism of the Cordillera with the NW-trending Middle America trench located ~160 km to the W. The Cordillera de Tilarán is an andesitic extinct volcanic range, a paleoarc genetically associated with the Costa Rica subduction zone. Most of the ongoing and recent maximum and minimum horizontal stresses are generated there. Campos de Oro Arriba (10°22′4.09″N – 84°54′57.77″ W), Guanacaste Province, Costa Rica. See Dabrowski and Graseman (2014) as the latest paper on a domino-type structure. **Guillermo Alvarado Induni**



FIGURE 2.2 Ductile to brittle deformation of the Livada Detachment. NE-SW field view of the Livada Detachment surface (dipping ~10–15 degrees toward the left) separating the lower Mykonos granitoids (apparently massive, in the lowermost portion of the picture) from the upper Upper Cycladic metabasites intruded by cm to m thick aplites (central and upper part of the picture), from Mykonos Island, Greece. The granitoids are intensely deformed, resulting in a mylonitic foliation roughly parallel to the detachment plane. The metabasites instead show a mylonitic foliation only in the first 6–8 m above the contact, rapidly passing to massive metabasites (upper left corner of the picture). Metabasites and aplite dikes are dominated by ductile-to-brittle features such as 1–5 m thick S-C-C' structures (central part of the picture), and the 10–30 cm scale shear band boudins (lower left) indicate a top-to-left (NE) shear consistent with that obtained from the Mykonos mylonite granitoids. Width of view: ~22 m. Coordinates: 37°28'59.61"N–25°24'23.54"E. **Raffaele Gazzola, Chiara Frassi, and Giovanni Musumeci**



FIGURE 2.3 Spectacular dextral shear zone affecting high-grade schists developed during the Hercynian Orogeny. Mobile phone for scale. Cap de Creus, Catalunya, Spain. Coordinates: 42°19'31.6"N, 3°18'06.3"E. Eloi Carola and Irene Cantarero



FIGURE 2.4 Extensional shear bands. A limestone breccia with a reddish matrix consisting of marl and calcarenite is a very characteristic stratigraphic horizon of the Julian Alps, marking the onset of flysch sedimentation in front of the rising Alpine orogen in the Late Cretaceous (e.g., [Miklavič and Rožič, 2008](#)). Here, subhorizontal bedding planes are displaced by numerous normal faults and shear planes that dip toward the left. The outcrop is positioned immediately left of a km-scale normal fault with a similar dip and orientation. Fault planes with up to several meters of offset are clearly brittle in character (see e.g., a large dissected boulder in the upper-central part of the picture), but prevailing are numerous discontinuous shear bands that offset and curve the bedding sigmoidally. While such shear bands commonly develop in higher-grade rocks, they are rarely observed in unmetamorphosed sediments. Their development may have been facilitated by the highly heterogeneous composition of the rock, where large rigid clasts localized deformation within the fine-grained matrix. This outcrop is the only known example of such a deformation in the Julian Alps. Rock type: mud-supported blocky breccia, Upper Flyschoid Formation, Late Cretaceous. Location: Kozjak gorge, Julian Alps, Slovenia. Coordinates: 46°15'50"N, 13°36'30"E. **Marko Vrabec**



FIGURE 2.5 Shear band. Rock type: Paragneiss. Structure: Shear band. Location: São Luis dos Campos Belos, Arenópolis Magmatic Arc, Western Goiás State, Brazil. Facies: Intermediate amphibolites. Description: Shear bands (right-lateral shear) cutting and folding orthogneissic banding. **Marco Martins-Ferreira**

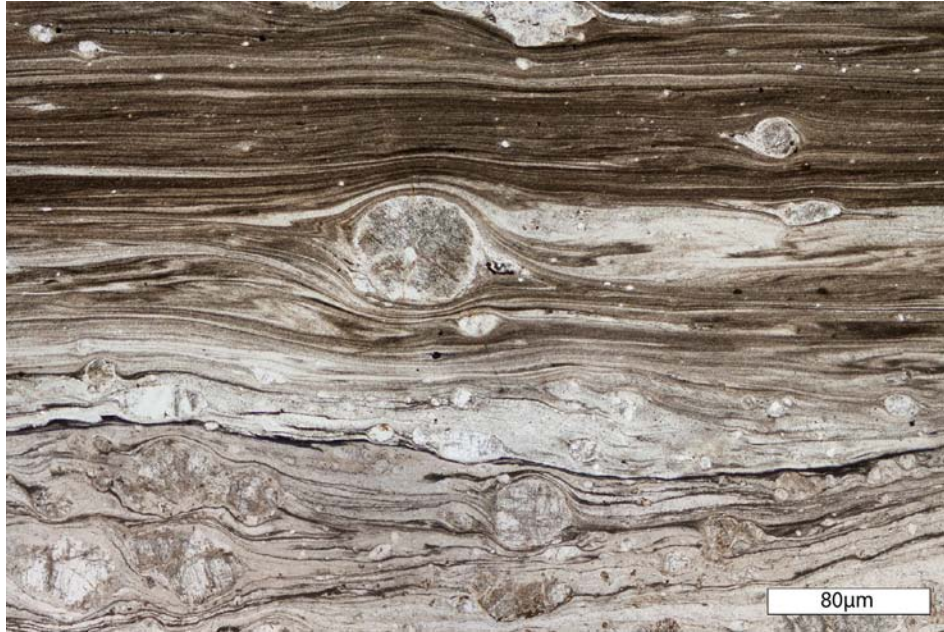


FIGURE 2.6 Ductile deformation of the Livada Detachment. Photomicrograph showing mylonite (lower portion) and ultramylonite (upper portion) bands developed in the Mykonos granitoids at the floor of the Livada Detachment exposed at Fokos Bay, Mykonos Island, Greece. Section showing the XZ plane, plane-polarized light. The main foliation is parallel to the long side of the photograph. In the mylonite, it is highlighted by quartz ribbons and dark thin films of fine-grained biotite and oxides wrapping feldspar grains. They are rounded or elongated with the long axis parallel to the main foliation. They generally show σ -type geometry with asymmetric tails of recrystallized quartz. In the ultramylonite, porphyroclasts with a scarce mantle may show weak stair-stepping (the small δ -type porphyroclast in the upper left corner) or quarter folds (the big one in the center). Kinematic indicators point to a top-to-left sense of shear. Coordinates: 37°28'49.35"N; 25°24'43.78"E. Chiara Frassi, Raffaele Gazzola, and Giovanni Musumeci



FIGURE 2.7 Post- D_3 sigmoidal quartz vein in amphibolite, Bastar Craton, Sambalpur, India. The regional amphibolite facies foliation (S_3), represented by fine segregations of hornblende and plagioclase-rich layers, is crosscut by a post- D_3 quartz vein. S_3 was crenulated, and the vein was folded during subsequent D_4 and D_5 deformation. Top-to-right shear. On National Highway-6 near Padiabahal, Sambalpur district, Odisha, India. Arindam Dutta, Saibal Gupta, and M.K. Panigrahi

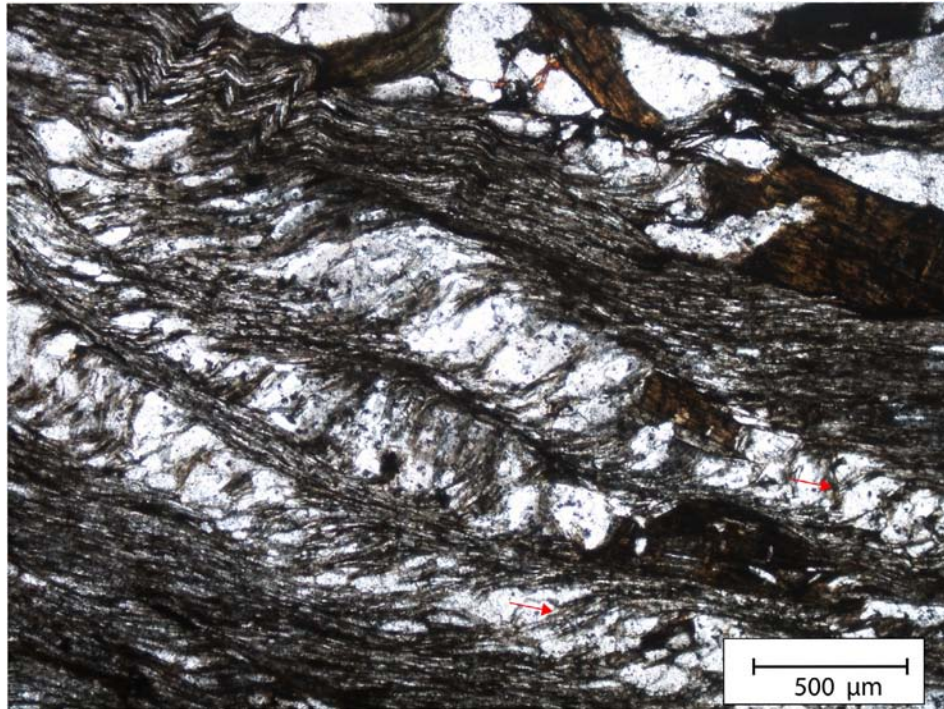


FIGURE 2.8 S-C fabric. S-C fabric within quartz mica schist indicates top-to-right shear. The C plane is defined by micaceous minerals while the S plane is defined by sigmoidal quartz grains and biotite (red arrows). Jahazpur, Rajasthan, India. **Hindol Ghatak**



FIGURE 2.9 Sheared quartz vein. Top-to-south fore-shear shown by the asymmetric quartz vein, near the Jutogh Thrust near Kullu Town, Himachal Pradesh (Singh et al., 2020). GPS location: N31°58.73', E77°07.14' **Paramjeet Singh**

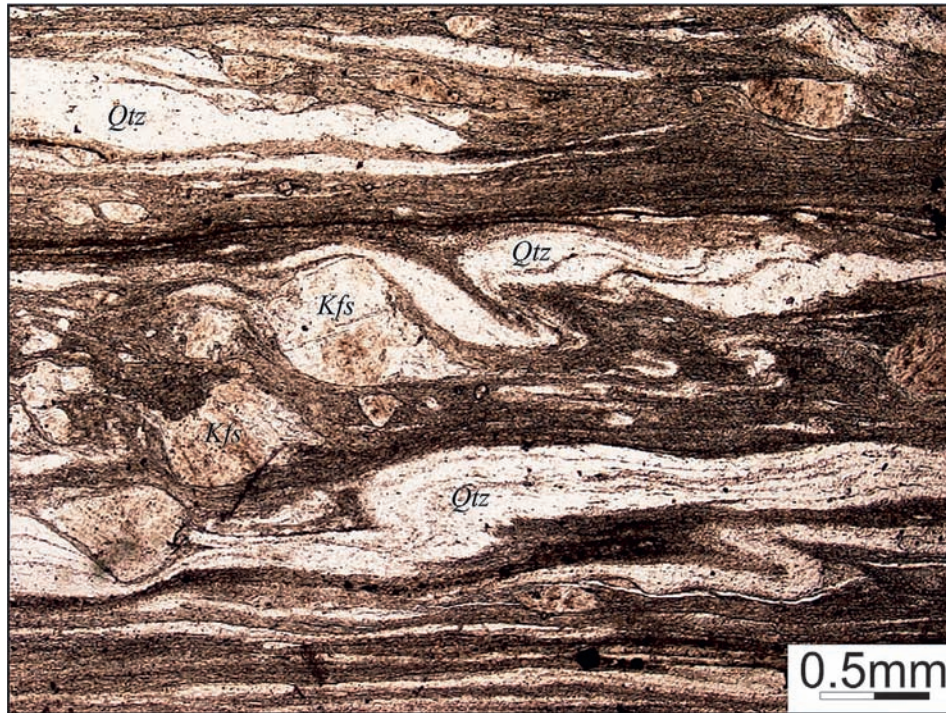


FIGURE 2.10 Photomicrograph under the plane polarized light of the Paleoproterozoic S-type Lesser Himalayan Granitoids from the Kameng valley of the Western Arunachal Himalaya showing asymmetric microfolds defined by quartz (Qtz) with a pressure shadow around the k-feldspar (kfs) porphyroblast. Quartz shows intrafolial folding (Vernon, 2004; Bikramaditya Singh, 2010; also see Mukherjee, 2007, 2010a,b; Mukherjee and Koyi, 2010a,b; Mukherjee, 2013a,b; Mukherjee et al., 2015). GPS Location: 27°07'47.2"N; 92°32'53.0"E. Bikramaditya Singh



FIGURE 2.11 Asymmetric quartz shadow. Eye-catching example of asymmetric quartz shadow around a staurolite porphyroblast defining a sigma-structure and a dextral slip. Maures-Tanneron Massif, France. Petroccia Alessandro



FIGURE 2.12 Chlorite strain shadows. Asymmetric chlorite strain shadows around a garnet porphyroblast in albite-garnet-bearing mica-schists. Sardinian Variscan basement, Medium-Grade Metamorphic Complex in the southeastern sector of the Posada Asinara shear zone (Italy). Dextral slip (PPL; 4X). **Petroccia Alessandro**



FIGURE 2.13 Ductile sheared quartz vein shows a top-to-right shear. The sigmoid-shaped vein indicates the ductile shear S-fabric. **Anupam Samanta**



FIGURE 2.14 Foliation parallel train of boudins in schistose quartzite. The large sigmoid quartz boudin, in the center, is necked at the margins. Top-to-right shear is indicated. A symmetric lenticular/rhombic boudin in the same train: no shear sense indicated. Photographed perpendicular to foliation. 14 mm pen for scale. Berinag Quartzite, Sutlej Valley, Himachal Pradesh, NW India. **Subhadip Mandal**



FIGURE 2.15 A relatively large feldspar σ -type porphyroclast. Top-to-right shear. The outcrop parallels the XZ section. The rock is a metagranite, part of the mylonitic zone, which is formed along the contact between the Rila-Rhodope batholith and the surrounding metamorphic “frame.” West Rhodope Mountains–Southwest Bulgaria, near the village of Kovachevitsa. **Svetoslav Bontchev**



FIGURE 2.16 A top-to-left sheared sigmoidal quartz lens in the garnet bearing schist. Location: Unit I, Greater Himalaya, Marsyangdi section, Central Nepal Himalaya. Subodha Khanal



FIGURE 2.17 Mylonite with a big delta mantled porphyroblast of K-feldspar in a matrix of quartz, mica, and feldspar. Mylonite is derived from a porphyritic granite characterized by large K-feldspar phenocrysts (up to 20 cm long). Medium-grade conditions can be inferred from the recrystallization of the K-feldspar along the rims of the porphyroblast. Shear sense is dextral as indicated by the stair stepping to the right across the delta structure. Section subparallel to the lineation and normal to the foliation. Width of view: 154 mm. Location: Sierra de Velasco, La Rioja Province, NW Argentina; GPS point (WGS84): S 28°36'26.2"–W 67°10'38.5"; Rock type: Mylonite; Formation name: Ortogneiss Antinaco (TIPA Shear Zone); Age (relative): Post-Lower Ordovician/Pre-Carboniferous; Facies/grade: medium grade. **Mariano A. Larrovere**



FIGURE 2.18 Quartzite veinlet as a crosscutting element within host calc schist rock. Dragging effect of the foliated layer near the quartzite also found at both its margins. Competency contrast probably played a significant role in generating the sigmoid shape of the quartzite body. Top-to-left ductile shear. Taleti Village area: (Latitude: $24^{\circ} 21.792'N$ Longitude: $72^{\circ} 54.640'E$), near Ambaji (Gujrat), India. **Rajkumar Ghosh**



FIGURE 2.19 Sigmoidal-shaped ductile sheared quartz vein within metagreywacke showing sinistral shear sense associated with en-echelon shear fractures. Kumbhalgarh Formation, ~85 km northwest of Udaipur, Rajasthan, India. **Swagato Dasgupta**



FIGURE 2.20 A type 1 flanking structure within the calc-schist. Quartz vein crosscutting element top-to-left sheared. At bottom right, the tail of the sheared quartzite body boudinaged. Taleti Village: (Latitude: $24^{\circ} 21.792'N$ Longitude: $72^{\circ} 54.640'E$), Ambaji, Gujrat, India. See [Passchier \(2001\)](#), [Mukherjee \(2007, 2011a, 2013a, 2014a,b\)](#), [Mukherjee and Koyi \(2009\)](#) and [Koyi et al. \(2013\)](#) for details of flanking structures. **Rajkumar Ghosh**



FIGURE 2.21 Around m-scale delta-type asymmetric-feldspar clast. See [Mukherjee \(2010a,b\)](#) for the general term “fish” to describe such structures. Asymmetric tails containing quartz of much reduced grain size indicate top-to-left shear. Chitrial granite; Place: Chitrial Village, Nalgonda, India. Delta structures are usually found under microscales from ductile shear zones. Very rarely are they found in the mesoscale as well (e.g., Figure 4 in [Mukherjee \(2013b\)](#)). See [Bose et al. \(2018\)](#) for the role of grain size in deformation. **Rajkumar Ghosh**

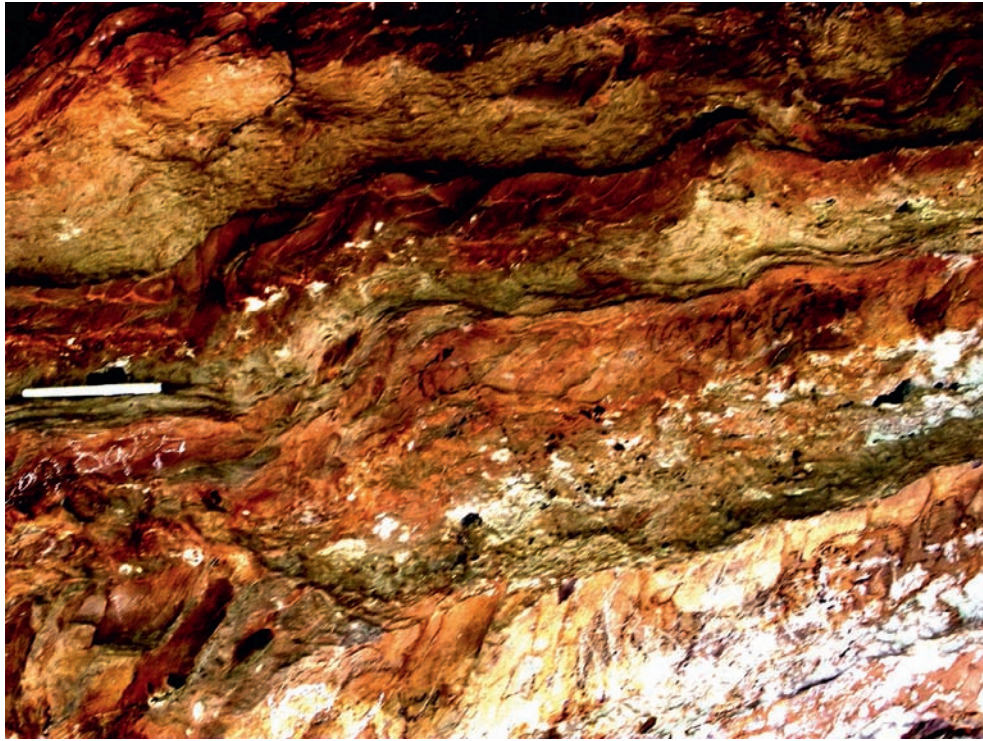


FIGURE 2.22 Top-to-right/west sheared intercalations of quartzites and phyllites showing antiformal thrust stacks at the Udayagiri Durgam Hill, Nellore Schist Belt, Kondamadipalle village ($14^{\circ}53'37.54''\text{N}$, $79^{\circ}16'23.20''\text{E}$), Nellore District, Andhra Pradesh, India. Sankha Das

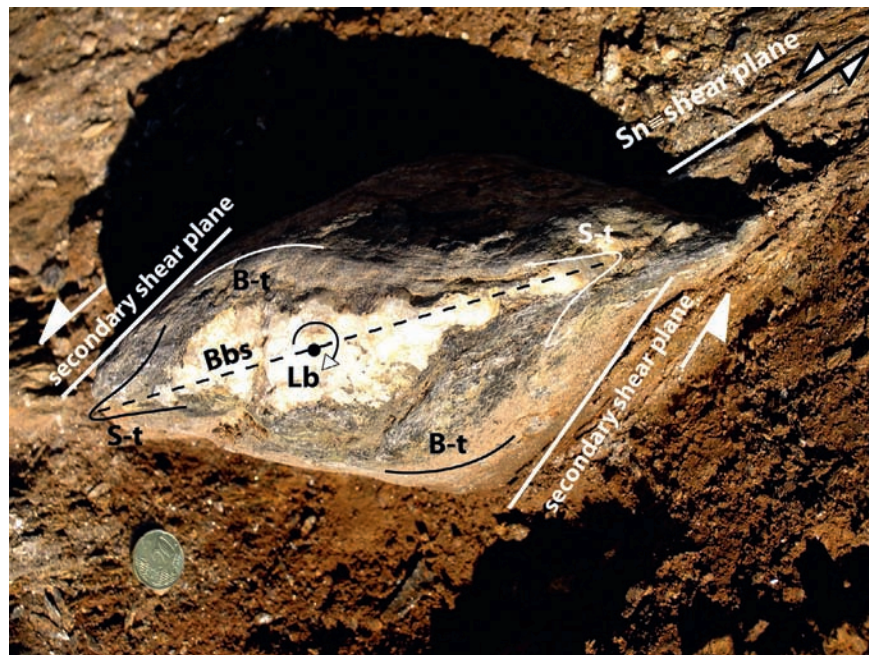


FIGURE 2.23 A classic shearband boudin generated by the deformation of a thicker tabular competent body (quartz vein) within a less competent matrix. This quartz vein does not exhibit internal folding. The methodology of analysis of shearband boudins proposed by Pamplona and Rodrigues (2011) includes geometrical parameters that allow a better characterization of this kind of geological body: Bbs-orientation of the boudin symmetry plane, Lb-boudin axis: defined by the intersection points between the opposite sharp tips (S-t) and the secondary synthetic shear plane; the blunt tip (B-t) that is the zone of the boudin surface that corresponds to the development of a convexity at the interface boudin/matrix with a secondary synthetic shear plane. Criteria to kinematic interpretation as a bulk sinistral shear zone using shearband boudin parameters: Bbs rotates dextral (antithetic) relative to the foliation plane (Sn); when looking parallel to Bbs, at a sharp tip of the boudin, toward the interior of the boudin, the B-t is on the left. Photo scale is given by the coin (diameter–22.25 mm). Outcrops of Salgosa Sector (NW of Portugal, 4642140N 524687E, WGS84). See Pamplona and Rodrigues (2011) and Pamplona et al. (2014) for details. Shearbands/secondary shears are considered readily by structural geologists as evidence of general shear deformation (Mukherjee and Koyi, 2010b; Mukherjee, 2013c). Jorge Pamplona, Benedito Calejo Rodrigues, and Carlos Fernández



FIGURE 2.24 Incipient heterogeneous ductile shear zone localized on a precursor fracture. The discrete fracture is still clearly visible in the shear zone core. The new foliation in the shear zone is well defined by the elongation of the deformed pseudomorphs after the original magmatic biotite. Precursor fractures can run for tens of meters and typically have a consistent stepping geometry (left stepping for dextral overprinting shear zones and vice versa), suggesting that the fractures developed in a kinematic framework similar to the subsequent ductile shear. The metamorphic minerals biotite and garnet concentrated in the fracture are also consistent with Alpine upper amphibolite facies conditions during ductile shear. The sense of shear is dextral. This and the three following photographs are from the Neves area of the Tauern window in the Eastern European Alps. Superb exposure is provided by the recent retreat of the Mesule glacier, exposing a perfectly polished and subhorizontal pavement at the foot of the glacier, at ~2600 m above sea level. The investigated shear zones are subvertical, with a flat-lying mineral stretching lineation so that the horizontal surface provides a profile section. Shear zones are developed in a pre-Alpine pluton of dominantly granodioritic composition, which was metamorphosed during Alpine time under upper amphibolite facies conditions. The shear zones developed at near-peak Alpine metamorphic conditions. Details of the location, regional geology, and a more extensive description of the structures are available in [Mancktelow and Pennacchioni \(2005\)](#), [Pennacchioni and Mancktelow \(2007\)](#), and [Mancktelow and Pennacchioni \(2013\)](#). Coin (one euro) for scale. Neil Mancktelow and Giorgio Pennacchioni



FIGURE 2.25 More advanced development of a localized heterogeneous shear zone. Here, the initial fracture is no longer visible but the outcrop pattern of these ductile shear zones on the meter to tens of meters scale still mimics the original fracture pattern. Dextral shear. Coin (one euro) for scale. Neil Mancktelow and Giorgio Pennacchioni



FIGURE 2.26 A pair of incipient localized dextral shear zones developed to either side of a precursor fracture. The slip occurs both on the central fracture and on the flanking pair of heterogeneous shear zones. Coin (one euro) for scale. Neil Mancktelow and Giorgio Pennacchioni



FIGURE 2.27 Typical paired shear zones developed approximately symmetrically to either side of an initial fracture. The fracture itself has filled to form an epidote-garnet vein, and fluid-rock interaction to either side of the fracture has produced a bleached zone enriched in plagioclase and epidote and depleted in biotite. The paired shear zones flank this bleached zone and must have developed after the altered zone reached its current width, rather than during its progressive development and broadening. Similar paired shear zones develop at the boundary of relatively strong layers such as aplite dykes within the granodiorite. This suggests that paired shear zones develop by reactivating boundaries of stronger layers (e.g. the bleached halo here). Sinistral shear. Coin (one euro) for scale. Neil Mancktelow and Giorgio Pennacchioni

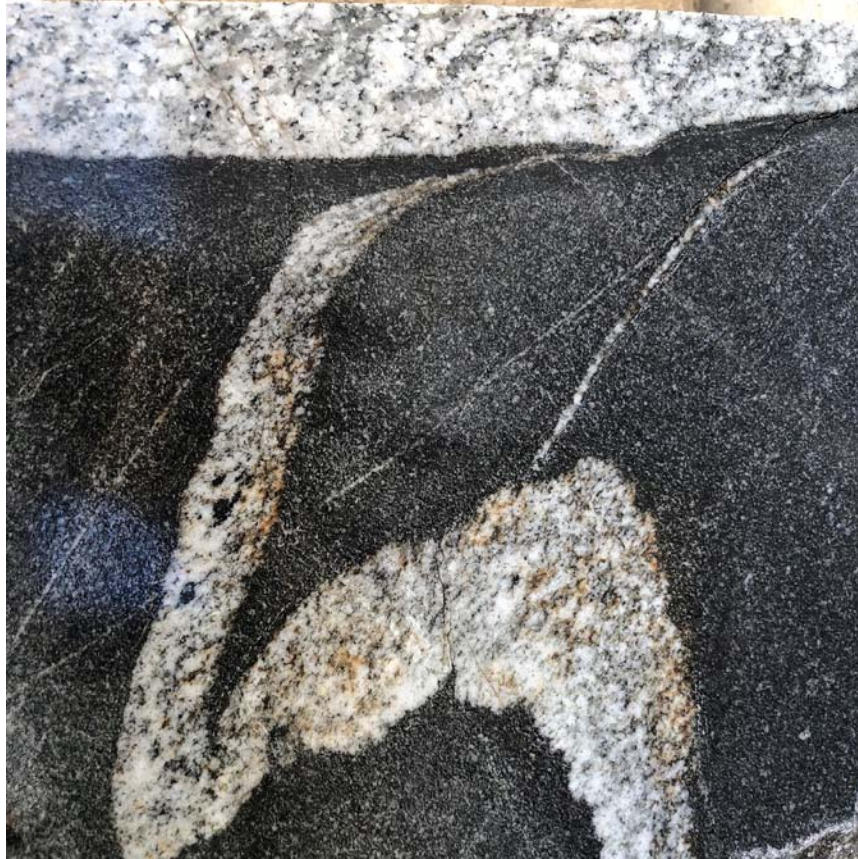


FIGURE 2.28 Structure related to dyke. Schistose quartz-andesite dike (black) in sharp contact with Umm-Maghra granodioritic gneiss (white) country rock. The dike is intruded by a vein sourced in the granodiorite, seen at the upper part of the dike wall. Later right-lateral shear along the dike walls folded the vein, along with the development of axial plane gneissosity, thinning of the fold limb near the dike wall, and thickening at the fold hinge. Intrusion of the andesite dike took place prior to final solidification of the granodiorite when it was still a crystal mush. Wadi Umm-Maghra NE Sinai, Egypt. Readers are encouraged to look for an alternate logical interpretation of the structural geology of the snap. See Eyal (1980) for detail. **Yehuda Eyal**

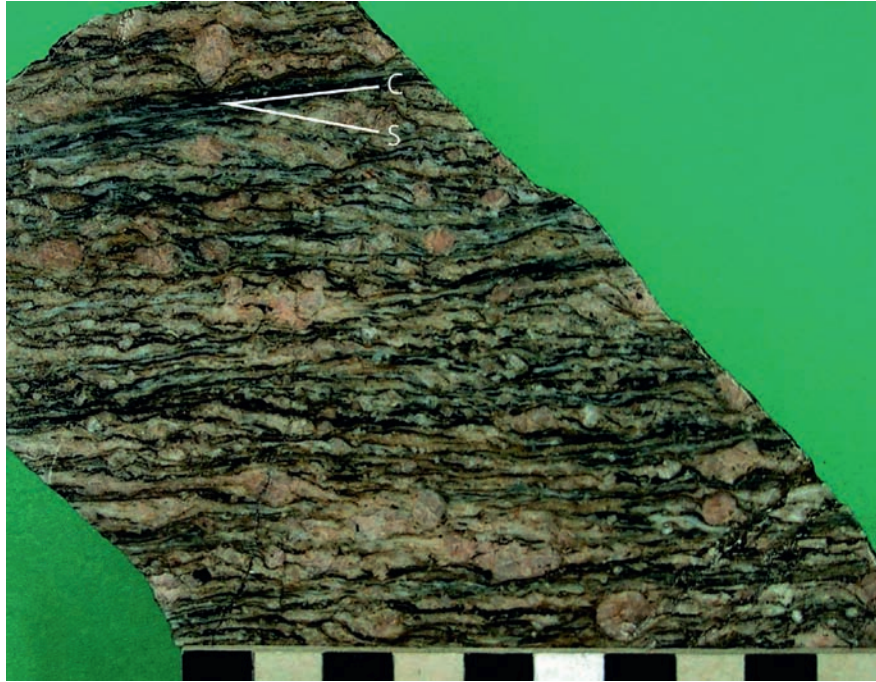


FIGURE 2.29 A polished slab of granite mylonite from the Shirakami Mountains of N Japan ($40^{\circ}27'27.7''\text{N}$, $139^{\circ}57'7.8''\text{E}$). This slab was cut parallel to the lineation and perpendicular to the foliation. Porphyroclasts of K-feldspar develop with pressure shadows. The foliation defined by elongated aggregates of fine-grained biotite (dark parts) and quartz ribbons (pale gray lenticular parts) is clear on the slab. Shear bands (C-planes) develop oblique to the main foliation (S-plane): sinistral ductile shear. Scale bar: 10 cm. The granite mylonite originated from the biotite granite of the Shirakami-dake Granites. Its K-Ar hornblende and biotite ages are ~ 90 Ma (Fujimoto and Yamamoto, 2010). Mylonitization occurred ~ 90 Ma under upper greenschist to amphibolite facies condition. This mylonite zone in the Shirakami Mountain is a possible northern extension of the shear zone–Tanagura Tectonic Line, which is a possible NE extension of the Median Tectonic Line (Takahashi, 2002). Therefore, the mylonite zone is one of the key areas to study the Cretaceous tectonics of E Asia. **Yutaka Takahashi**



FIGURE 2.30 Boudinaged quartz veins within banded magnetite quartzite and magnetite garnet-biotite schist intercalation. Top-to-right ductile shear and synthetic secondary shear present. Tiranga hill, Pur area, Bhilwara, Rajasthan, India. See Mukherjee and Koyi (2010b) for microboudins. **Ranjan Gupta**

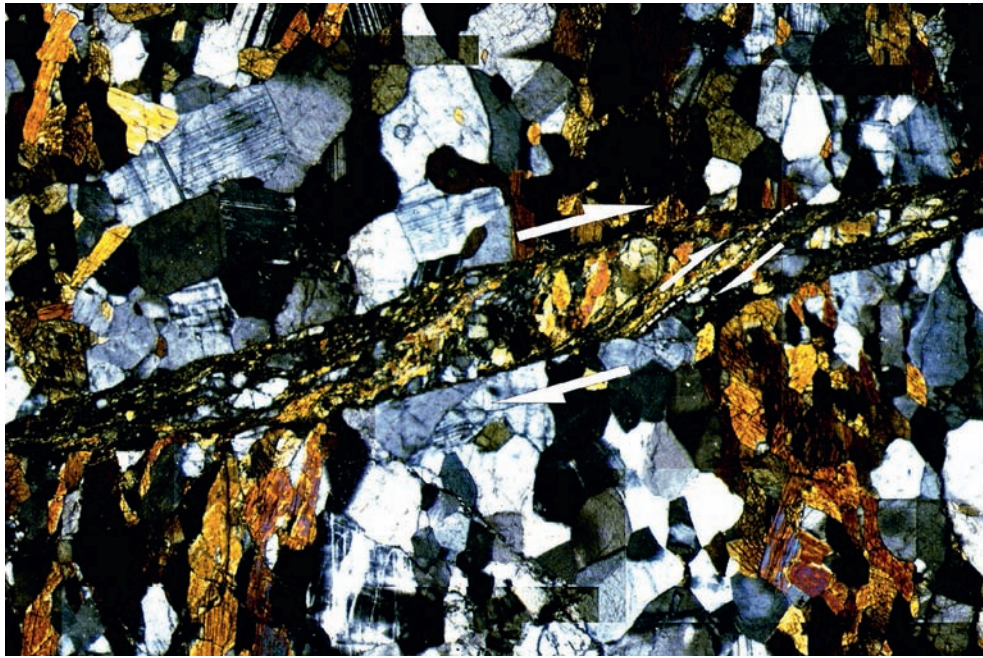


FIGURE 2.31 Photomicrograph shows a duplex structure in a strike slip fault system. Shear planes in the microduplex are defined by fine amphibole grains and are marked by the broken white line. The white arrows indicate the sense of shear movement. The rock is granodiorite from the Kajalbas area (hanging wall side) nearly a km east of the Phulad Shear Zone (Ghosh et al., 1999; Sengupta and Ghosh, 2004) of the Southern Delhi Fold Belt, Rajasthan, India. The rock shows a prominent foliation parallel to the mylonitic foliation of the shear zone and is dissected by late brittle-ductile shear bands. Photo in cross-polarized light. The width of the photo is 40 mm. The sample location is 25°38'58.2"N, 73°49'48.9"E. Sadhana M. Chatterjee and Sudipta Sengupta



FIGURE 2.32 The photomicrograph shows a plagioclase feldspar porphyroclast in the fine-grained recrystallized matrix of quartz, feldspar, and calcite. The sample is a quartzofeldspathic mylonite. The feldspar porphyroclast in the center is divided into four pieces by grain-scale faults and shows a typical bookshelf sliding or fragmented domino-type feature (Trouw et al., 2010). The fractures in the feldspar megacryst are at an angle with the general mylonitic foliation. The sense of slip along the fractures (shown by small white arrows) is sympathetic to the dextral shear direction of the mylonite (shown by larger arrows). However, the grain shows antithetic rotation indicating transpressional deformation (compare with Figure 21.13B of Ghosh (1993), p. 521). The megacryst in the upper right side shows horizontal and vertical fractures. There is no slip along these fractures. Photo in cross-polarized light. Sample location: 25°36'33.1"N, 73°48'45.1"E, from the Phulad Shear Zone, Rajasthan, India (Sengupta and Ghosh, 2004). Sudipta Sengupta and Sadhana M. Chatterjee

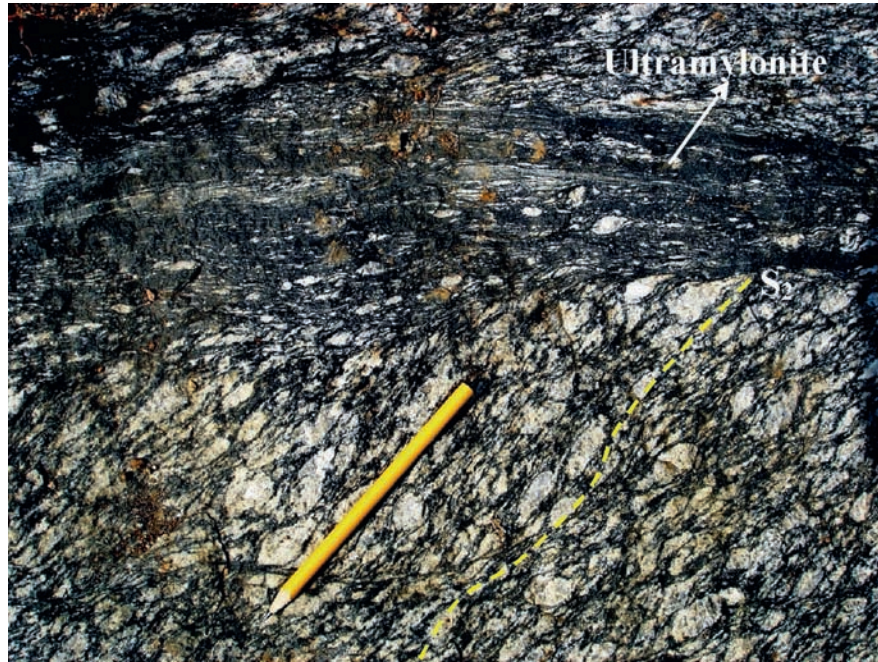


FIGURE 2.33 Post D_2 , syn- D_4 ultramylonite shear zone in augen gneiss, Bastar Craton, Sambalpur, India. The gneissic foliation (S_2) was dextrally sheared and transposed by a late ultramylonitic, amphibolite facies shear zone (dark gray). The ultramylonitic shear foliation, with $81/83^\circ\text{N}$ attitude, is synchronous with the Eastern Ghats Boundary Fault (Bhadra et al., 2004; Biswal et al., 2000, 2007; Dobmeier and Raith, 2003). S of Sambalpur town, Odisha, India. Arindam Dutta, Saibal Gupta, and M.K. Panigrahi

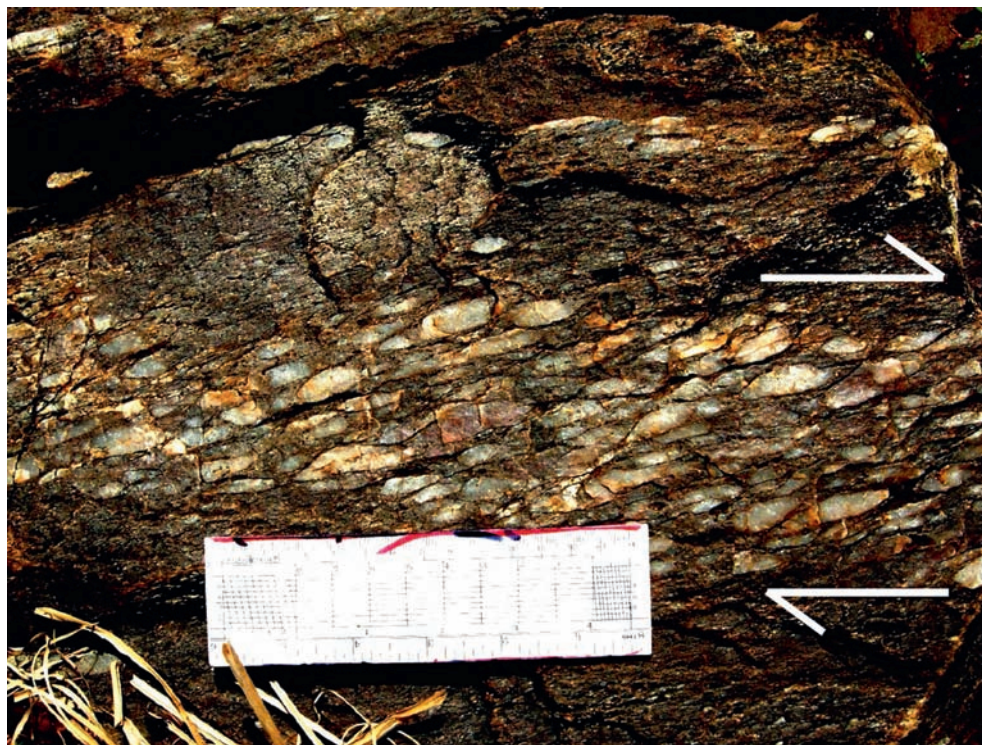


FIGURE 2.34 Asymmetric quartz porphyroclasts in sheared quartzofeldspathic gneiss indicate an apparent dextral shear. The steeply SW dipping mylonitic foliation parallels the WNW-ESE trending Kerajang Fault that separates the Rengali Province from the Eastern Ghats Mobile Belt (Crowe et al., 2003; Dutta et al., 2010) along National Highway-6, E of Jamankira, Odisha, India. Arindam Dutta, Saibal Gupta, and M.K. Panigrahi



FIGURE 2.35 Top-to-SW sheared sigmoid quartz veins. Event of extension followed by ductile shear. Centimeter-scale product of Himalayan compression. Lesser Himalaya, 31°14.578'N, 76°58.96'E, Mangu village, district: Solan, Himachal Pradesh, India. **Tuhin Biswas**



FIGURE 2.36 Photograph of a dilational jog within the Chrystalls Beach Complex, Otago, New Zealand. The Chrystalls Beach Complex is an accretionary mélangé comprising lenses of sandstone, chert, and minor basalt within a cleaved mudstone matrix containing an anastomosing vein network. This sheared rock assemblage forms part of the Otago schist, and was metamorphosed at subgreenschist facies during the Triassic-Jurassic subduction under the Gondwana margin (Hada et al., 2001). The photograph is taken looking W at a subvertical face. Thus the dilational jog indicates top-to-north shear (top-to-right in the figure). This is also typical of the mélangé as a whole. The tensile veins within the jog and the enveloping slickenfiber-coated shear surfaces are nearly orthogonal, intersecting at an angle of ~80 degrees. The presence of tensile veins implies that fluid pressure exceeded the least compressive stress, at least locally within the jog. In addition, the high angle between the shear and extension fractures requires high fluid pressure and low frictional resistance along the shear surfaces for their continued reactivation (Fagereng et al., 2010). Internally, the slickenfiber shear veins (as seen on the left in the photograph) comprise shear surfaces at a low angle to the vein margin, separated by incrementally grown quart layers. These shear surfaces were therefore active episodically, possibly governed by fluid pressure cycling, leading to the episodic growth of dilational jogs (Fagereng et al., 2011). This “dilational hydro-shear” may be analogous to repeating, low stress-drop, microearthquakes observed in actively deforming accretionary complexes. **Ake Fagereng**

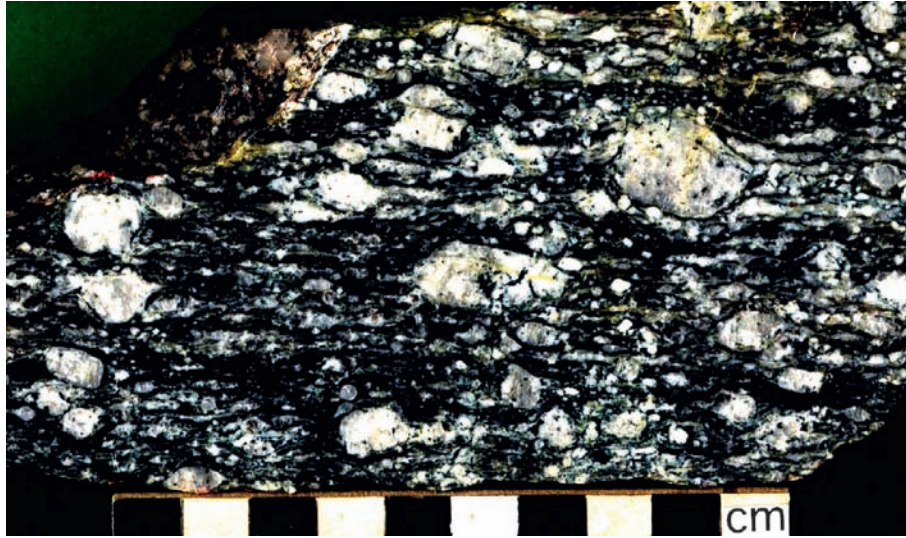


FIGURE 2.37 A polished slab of the augen gneiss/granite mylonite in the Funatsu Shear Zone within the Hida Belt of Southwest Japan ($36^{\circ}38'34.8''\text{N}$, $137^{\circ}33'40.3''\text{E}$) (Harayama et al., 2000). This slab was sectioned parallel to lineation and perpendicular to foliation. Porphyrocrasts of K-feldspar are characteristic with anisotropic pressure shadows: dextral sheared. Foliations defined by elongated aggregates of fine-grained biotite (dark parts) and quartz ribbons (pale gray lenticular parts) are clear on the nearly horizontal surface. Scale bar: 10 cm. The Funatsu Shear Zone is a late Triassic dextral ductile shear zone in the Hida Belt, which is a possible NE extension of the Cheongsan Shear Zone in the Korean Peninsula (Takahashi et al., 2010). Yutaka Takahashi

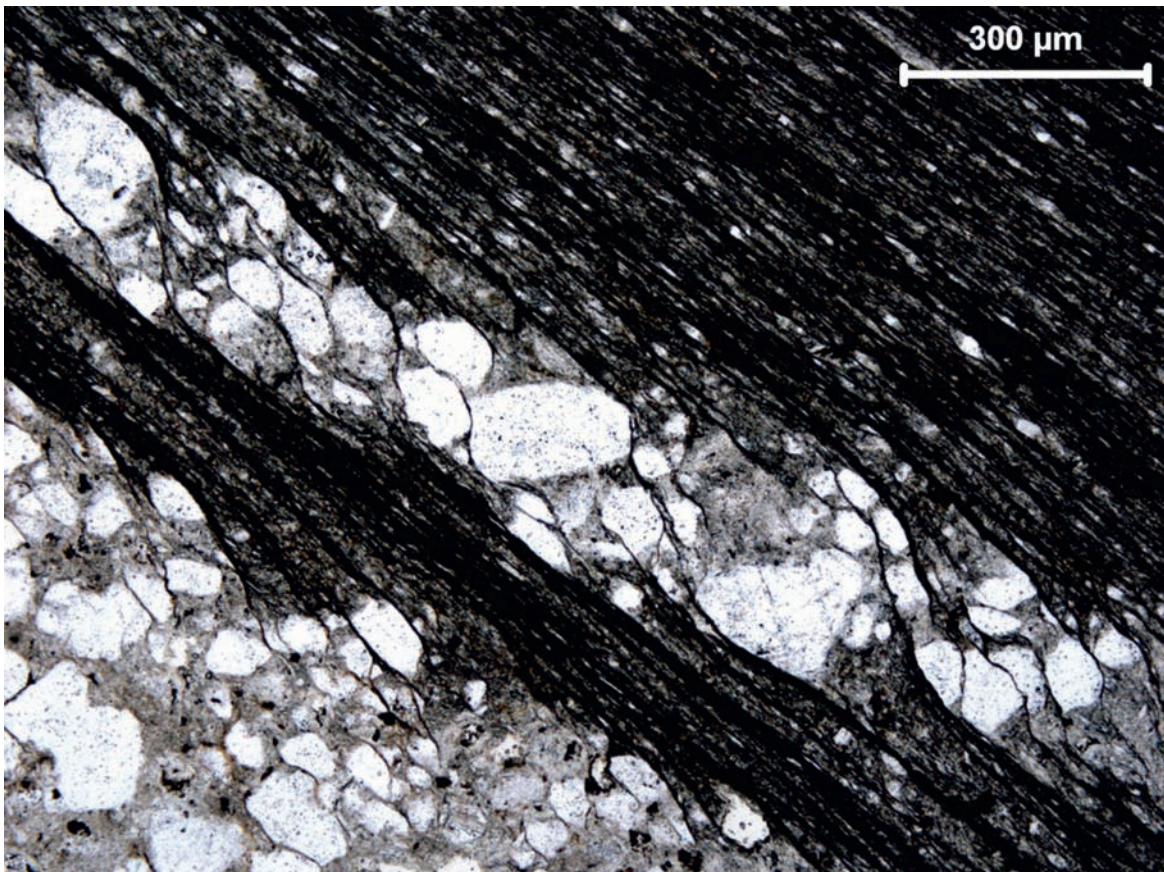


FIGURE 2.38 Cleavage refraction across heterolithic sandstone-shale. Gently dipping, close-spaced disjunctive cleavage to penetrative slaty cleavage (Engelder and Marshak, 1985) in pelitic laminae refracts to steeper spaced cleavage in the psammitic laminae. The cleavage seams, darker bands, are associated with pressure solution (Rutter, 1983) as evidenced by the sharp truncation of detrital quartz grain margins. Note that cleavage spacing in the psammitic laminae is controlled by the size of the quartz clasts, which show little intracrystalline deformation. Photo in plane-polarized light. Kurnool Group rocks. Palnad, Southern India. Bar scale: 300 μm . Dilip Saha



FIGURE 2.39 Sigmoid brittle P-planes bound by Y-planes in mafic schist: top-to-right shear. Foliation boudins below. 4 mm pen for scale. Rampur meta-basalt, Inner Lesser Himalaya, Sutlej Valley, Himachal Pradesh, India. **Subhadip Mandal**

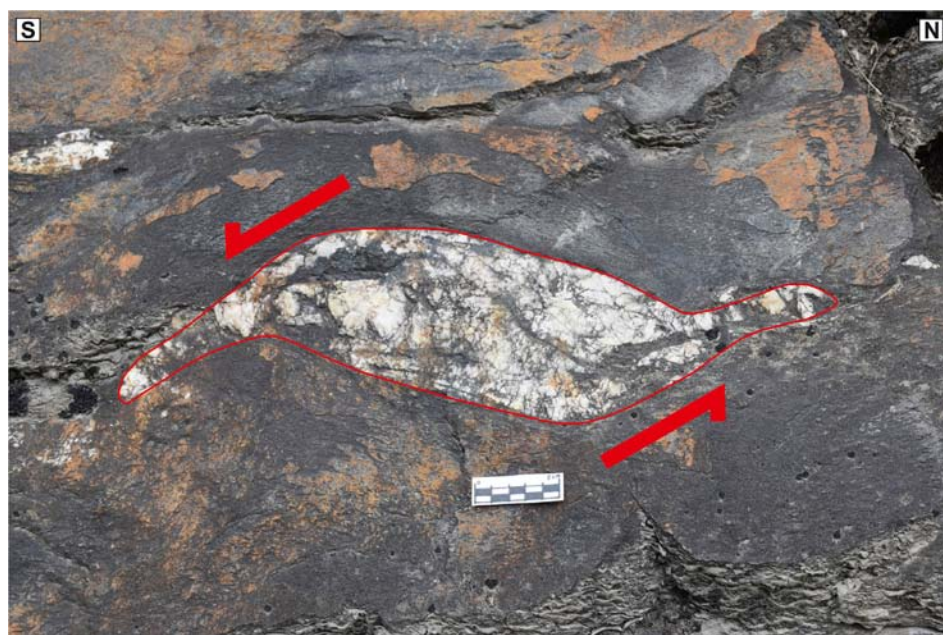


FIGURE 2.40 Ductile shear sense indicator. The sense of asymmetry of sigma (σ) type “tails” of quartz object in the gneiss rocks and show top-to-south shear (look at Mukherjee, 2011 b, Mukherjee et al., 2015; [Passchier and Trouw, 2005](#); Singh et al., 2020). GPS location is N31°58.73', E77°07.14'. Kullu area, Himachal Pradesh, India. **Paramjeet Singh**



FIGURE 2.41 **Shear structure.** Rock type: Paragneiss. Structure: Shear structure. Location: São Luis dos Campos Belos, Arenópolis Magmatic Arc, Western Goiás State, Brazil. Facies: Intermediate amphibolites. Description: Kinematic indicators of left-lateral shear marked by sigmoid granitic neosomes developed during partial melting (anatexis) in paragneiss. **Marco Martins-Ferreira**

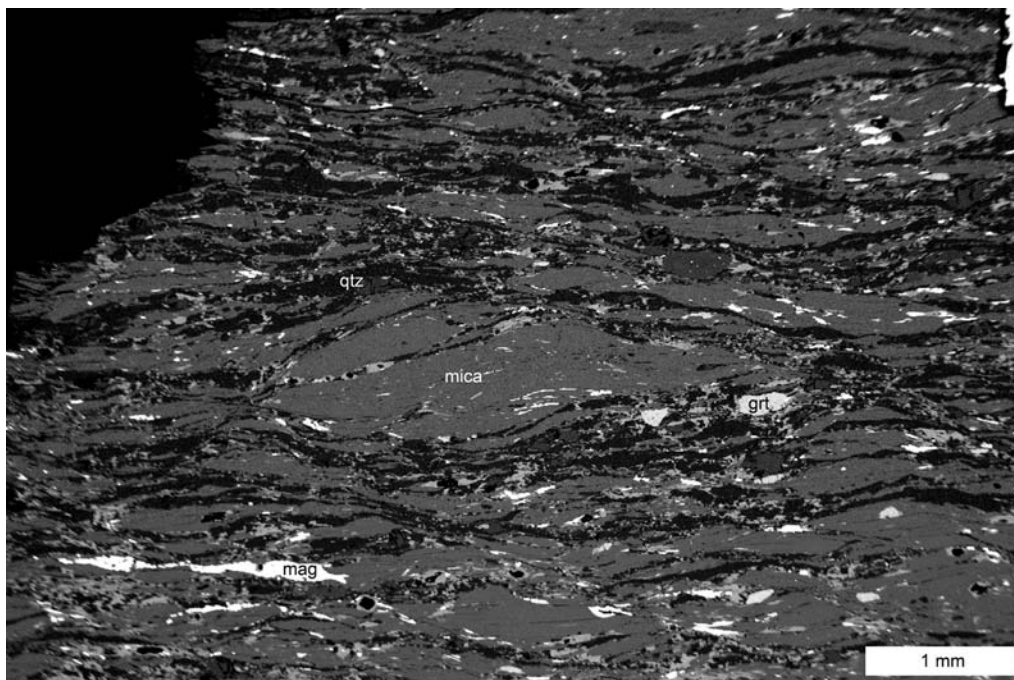


FIGURE 2.42 Scanning electron microscope image of a lower eclogite facies mylonitic garnet-micaschist of the Upper Seve nappe with kinematically grown magnetite (mag) in a quartz (qtz)-mica-feldspar-matrix with mica fish indicating top-to-right sense of shear (i.e. hinterland-directed) on top of an extrusion wedge in the central Scandinavian Caledonides (Grimmer et al., 2015; Kontny et al., 2012). Note also developed synthetic shear bands. **Jens Carsten Grimmer**

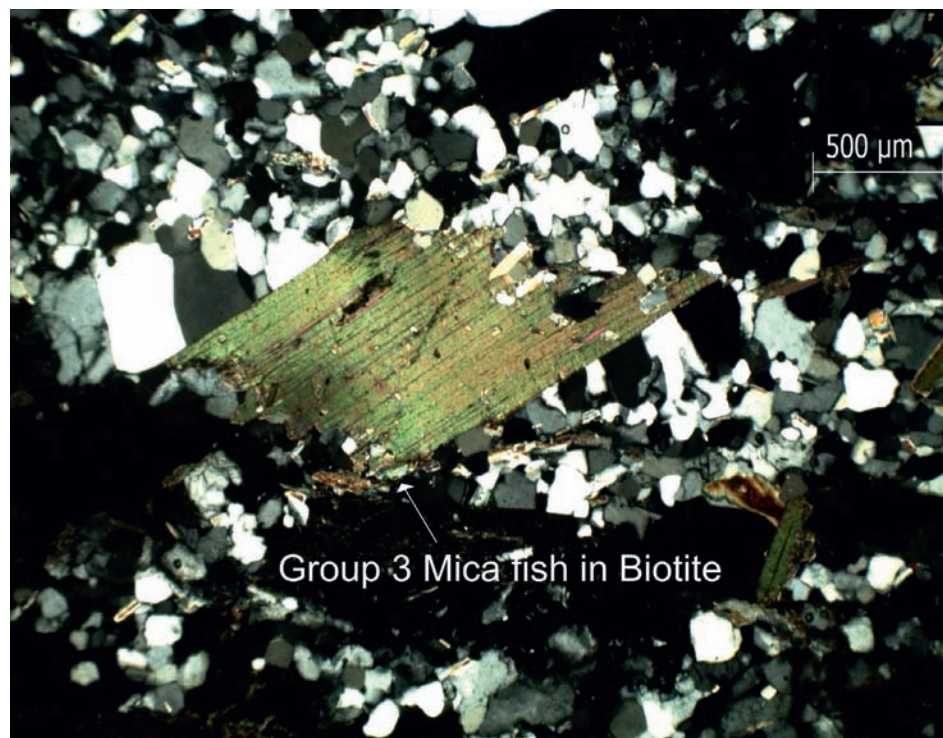


FIGURE 2.43 Mylonitized micaschist shows a top-to-right sheared biotite “fish.” Cleavage planes are at an angle to the ductile shear. Therefore it is an r-parallelogram fish of Mukherjee (2011b). As per a different classification scheme, this is a Group 3 fish (ten Grotenhuis et al., 2003). See Mukherjee (2012) for simple shear mechanism. Natyal (23°05′39.51″N-73°42′06.63″E), Kadana Formation, Lunawada Group, Gujarat, India. Aditya Joshi, M.A. Limaye, and Bhushan S. Deota



FIGURE 2.44 Asymmetric sheared granite pebble in mylonitic garnet-micaschists of the Middle Allochthon Seve Nappe Complex indicates foreland-directed (top-to-left) tectonic transport on top of the (not exposed) Ammannäs Complex (Grimmer et al., 2011). Jens Carsten Grimmer



FIGURE 2.45 Sigma clasts, S-C structures in soft sediment. Microstructures in ~1 m thick clastic infill of a steeply dipping synsedimentary fault displaced Mesozoic rocks. Compositional bands in clastic infill parallel the fault. The major structures: calcite shear veins correspond to stacked slickenside fibers that occur along minor faults within the infill and parallel to the main fault. Calcite fibers alter with millimeter-thick bands of clastic sediment (quartz and chert grains, clays with iron impregnation). Sigma clasts with calcitic tails indicate top-to-left shear. The quartz grains within the sigma clasts are intensely fractured and extended by calcite veinlets, which are also consistent with sinistral shear. In the lower part, parallel iron-impregnated dark clay bands correspond to S-foliation planes and merge with C-shear surfaces parallel to calcitic shear veins. Thus, the ductile S-C structure (Platt and Vissers, 1980) is defined. All these features are geometrically similar to structures found in crystal-plastically deformed metamorphic rocks. However, the sediment infill and host rocks are unmetamorphosed and were never buried below 2 km. The interpretation is that the structures formed in an unconsolidated state of the clastic infill during the burial path of the sediment. The whole deformed zone is crosscut by the youngest parallel set of calcite veinlets, which could form after the complete diagenesis of the shear zone rocks. Middle Eocene sandstone, siltstone. Location: Vöröshíd quarry, Tardos village, Gerecse Hills, Hungary. Coordinates: 47°41'48.47"N, 18°26'56.25"E. **László Fodor**



FIGURE 2.46 A top-to-left ductile sheared sigmoid quartz lens in kyanite-garnet gneiss, hanging wall rock of the Main Central thrust. Location: Unit I, Greater Himalaya, Kali-Gandaki section, Central Nepal Himalaya. **Subodha Khanal**



FIGURE 2.47 Ductile deformation of the Livada Detachment. Field view of the Mykonos granitoids affected by the extremely partitioned shearing of the Livada Detachment, Metalleia, Mykonos Island, Greece. In the lower portion of the photograph, the mylonitic foliation is marked by very fine-grained recrystallized quartz (the black thin layers dipping toward the right) deflected by cm thick high-strain shear zones (2–4 cm thick dark layer gently dipping toward the left in the center of the picture). The deflection of foliation indicates a top-to-east (NE) shear. Width of view: ~ 45 cm. Coordinates: 37°28′21.63″N; 25°26′45.71″E. Chiara Frassi, Raffaele Gazzola, and Giovanni Musumeci

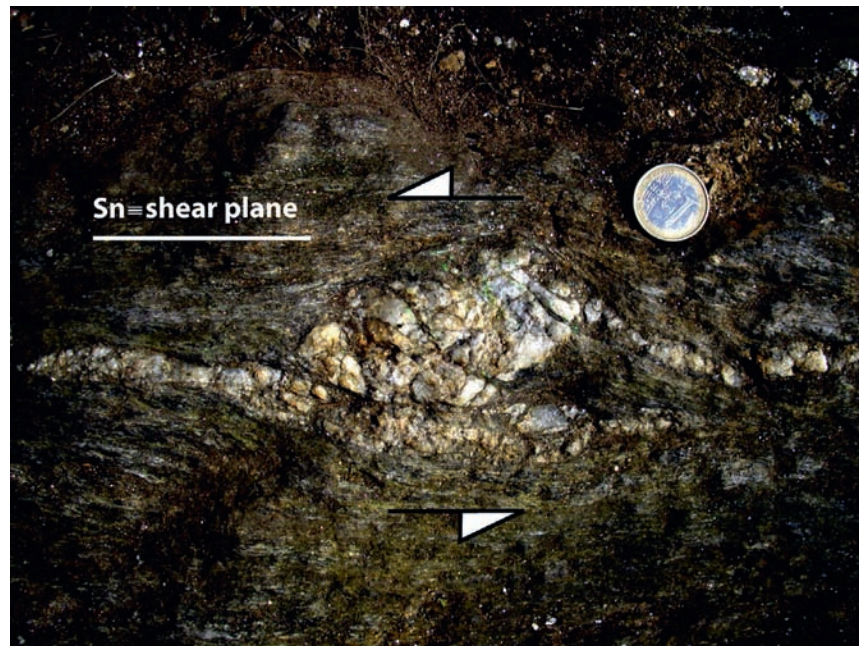


FIGURE 2.48 The continuous flattening of a folded package, rather than the developing of new shear structures, develops a false sigma feature called fold-boudin. Folding starts with the buckling of quartz veins with the axial plane oblique to the shear plane. Then the axial plane rotates and the fold tightens. At this stage, the position of the hinges still records an asymmetric distribution relative to the shear plane. This fold train exhibits apparently antithetic kinematics relative to the shear plane given by its external morphology. The key structure to an appropriate kinematic interpretation is the internal symmetry of the folds. After the folds tighten, the fold train starts to behave as one single unit that rotates due to the flow vorticity. The diameter of the coin as a marker is 23.25 mm. Outcrops of Salgosa Sector (NW of Portugal, 4642140N 524687E, WGS84). See Pamplona and Rodrigues (2011) and Pamplona et al. (2014) for details. Jorge Pamplona, Benedito Calejo Rodrigues, and Carlos Fernández

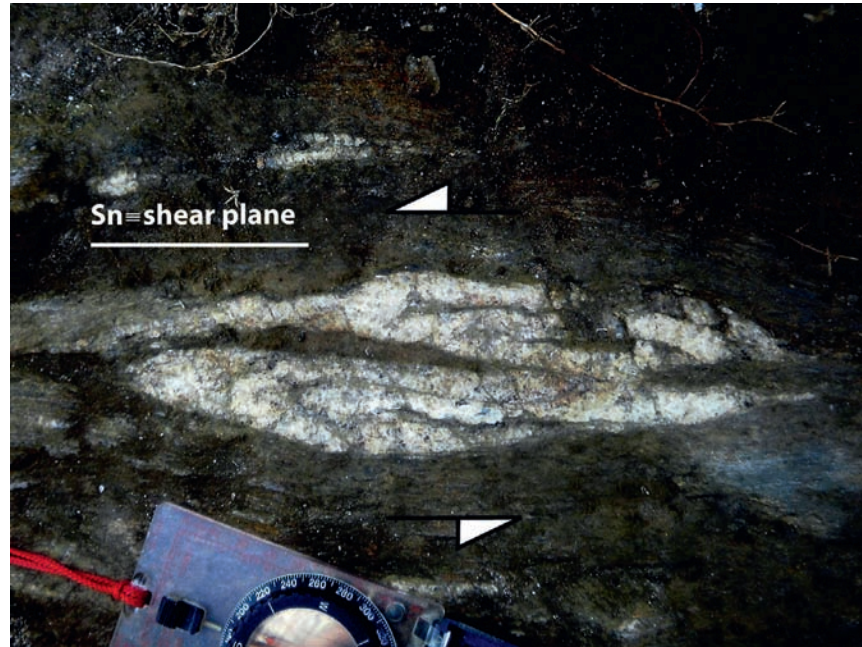


FIGURE 2.49 The evolutive sequence of fold-boudin generates a thick compact, parallel-sided body designed by a stacked-fold-boudin. The hinges and axial planes of folds tend to parallel the shear plane. At this and the previous stage, it is possible to find remains of an old ductile matrix (amphibolitic facies of quartz micaschist) interbedded with quartz fold flanks. The condition to achieve this evolutionary level is verified when the inhibition of shear rupture predominates, which develops a localized central folding on the vein, generating a fold-boudin with two narrow and opposite tails. Photo scale is given by the compass. Outcrops of Salgosa Sector (NW of Portugal, 4642140N 524687E, WGS84). See Pamplona and Rodrigues (2011) and Pamplona et al. (2014) for details. Jorge Pamplona, Benedito Calejo Rodrigues, and Carlos Fernández



FIGURE 2.50 When stacked-folds-boudins are fully developed, the geologic body—originally a thinner vein—acquired the critical thickness that developed the shearband boudin. The internal structure is composed by a successive package of folds flanks while the external morphology shows typical shear band structures like a sigmoid with the tips bound by opposite secondary shear planes. Photo scale is given by the compass. Outcrops of Salgosa Sector (NW of Portugal, 4642140N 524687E, WGS84). See Pamplona and Rodrigues (2011) and Pamplona et al. (2014) for details. Jorge Pamplona, Benedito Calejo Rodrigues, and Carlos Fernández



FIGURE 2.51 Top-to-S/SW ductile sheared parallelogram/sigmoid mud unit inside sandstone. Competency contrast between sandstone and mud controlled the shape of the mud unit (like Treagus and Lan, 2003). Mohand, Siwalik Himalaya, Roorkee-Dehradun transect, Uttarakhand, India. **Tuhin Biswas and Soumyajit Mukherjee**

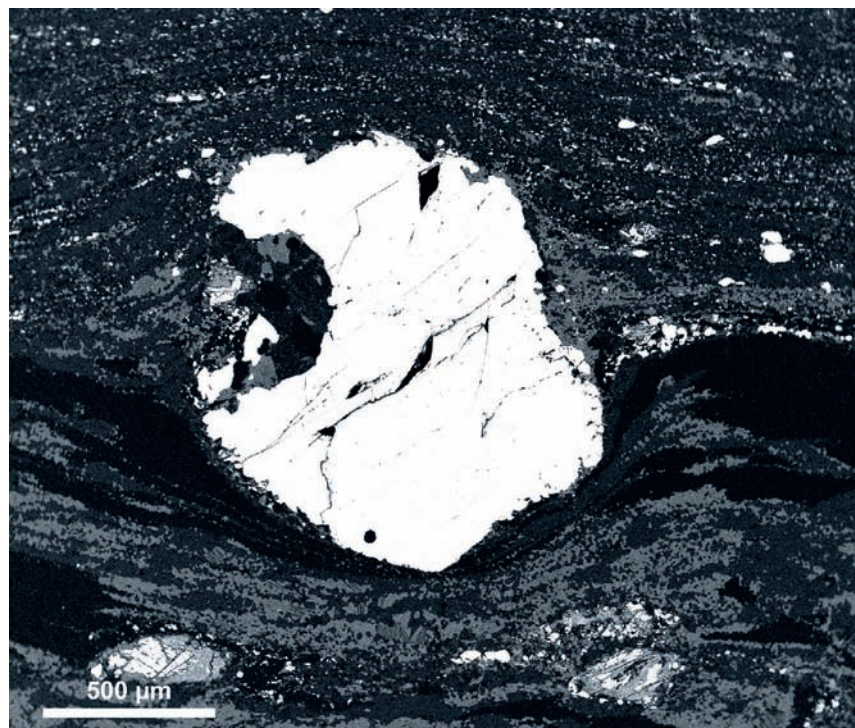


FIGURE 2.52 Backscattered electron image of a titanite porphyroblast in an ultramylonitic shear zone. The shear zone is developed in a coarse-grained metasyenite from the boundary between the Adirondack Highlands and the Adirondack Lowlands (New York, United States). The rounded porphyroblast is consistent with the rotation of the porphyroblast relative to the grain-size reduced matrix. The embayment within the porphyroblast contains coarser matrix grains that were apparently protected from further grain-size reduction within the strain shadow of the surrounding titanite. Foliation is defined by the very fine-scale compositional layering that formed by the extreme attenuation of individual dynamically recrystallized quartz, alkali feldspar, and augite grains. The matrix in the upper half of the image has undergone greater attenuation and/or a greater degree of phase mixing during shearing than the matrix in the lower half of the image. Coarse feldspar grains in the nearby unsheared metasyenite are perthitic, but dynamic recrystallization separated the exsolved domains into individual sodic or potassic matrix grains in the shear zone. The darkest gray in the image is quartz while the intermediate grays are potassic and sodic feldspars. The image plane is perpendicular to foliation; no lineation is observed in the outcrop or hand sample. **Chloë Bonamici**

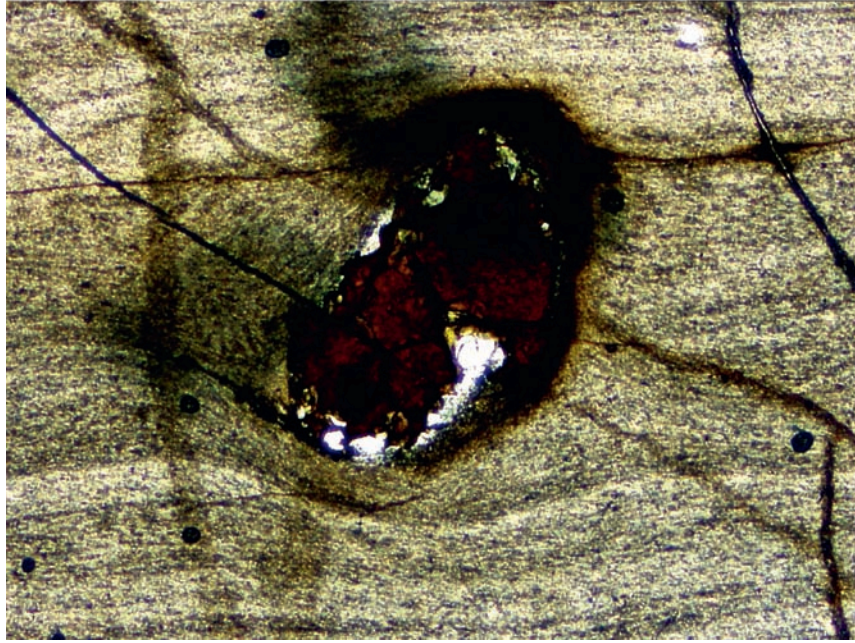


FIGURE 2.53 Delta-like structure in an ultramylonitic peridotite. The partially recrystallized porphyroblast is composed of spinel. The wings consist of very fine spinel grains and they are very thin. Plane-polarized light. Location: Archipelago of Saint Peter and Saint Paul (Brazil). Width of view: 2.5 mm. Suellen Olívia Cândida Pinto, Leonardo Evangelista Lagoeiro, Luiz Sérgio Amarante Simões, and Paola Ferreira Barbosa

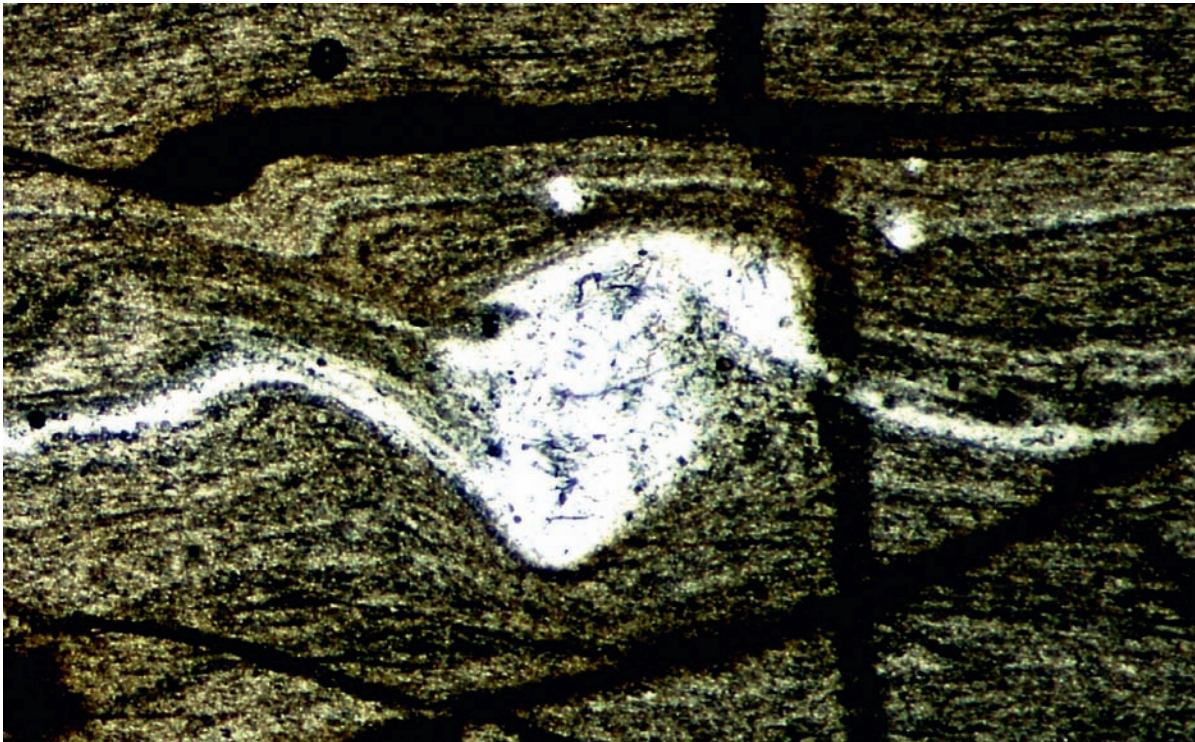


FIGURE 2.54 Delta (δ) microstructure of olivine. A porphyroblast of forsterite within peridotite has asymmetric wings of fine recrystallized grains. The core is recrystallized almost entirely. The wings are of the delta type: top-to-left sheared. The asymmetric fold in the NW quadrant too provides a consistent shear sense. Plane-polarized light. Location: Archipelago of Saint Peter and Saint Paul (Brazil). Width of view: 0.25 mm. Suellen Olívia Cândida Pinto, Leonardo Evangelista Lagoeiro, Luiz Sérgio Amarante Simões, and Paola Ferreira Barbosa

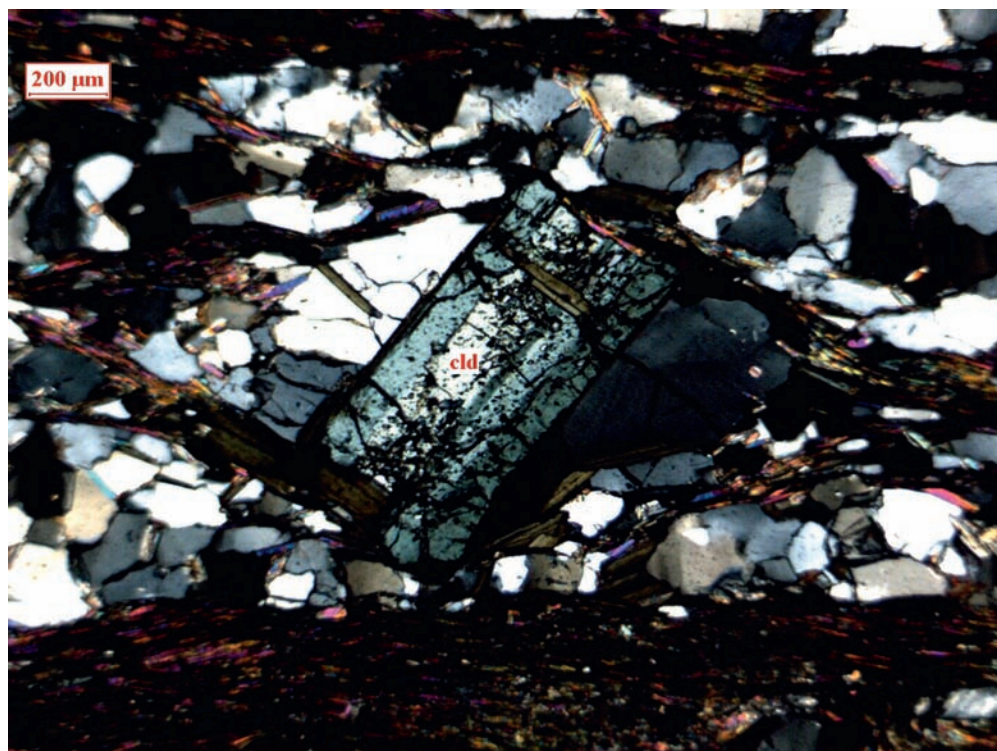


FIGURE 2.55 Top-to-right ductile sheared syntectonic microscopic porphyroblast of chloritoid (cld) under cross-polars. Asymmetric pressure shadow of quartz around the porphyroblast bound by mica grains. Middle greenschist facies metamorphosed Proterozoic chloritoid bearing garnet-muscovite schist, Udayagiri Group, Nellore schist belt. Arlapadia village (15°02'08"N, 79°16'02"), Prakasam District, Andhra Pradesh, India. Sankha Das



FIGURE 2.56 Top-to-right ductile sheared microscopic garnet with spiral, early foliations (S-internal: Si) within the core. See Mukherjee (2014c) for a review of inclusion minerals. The rim is almost free of inclusions. This indicates that the grain grew in two stages. After its initial syntectonic growth, the garnet grain grew again in a posttectonic phase. Middle greenschist facies metamorphosed Proterozoic chloritoid bearing garnet-muscovite schist, Udayagiri Group, Nellore schist belt. Arlapadia village (15°02'08"N, 79°16'02"), Prakasam District, Andhra Pradesh, India. Sankha Das



FIGURE 2.57 Top-to-right ductile sheared syntectonic microscopic garnet under plane-polarized light. Middle greenschist facies metamorphosed Proterozoic chloritoid bearing garnet-muscovite schist, Udayagiri Group, Nellore schist belt. West of Peddarajupalem Village (15°06'38.00"N, 79°15'44"E) Prakasam District, Andhra Pradesh. **Sankha Das**

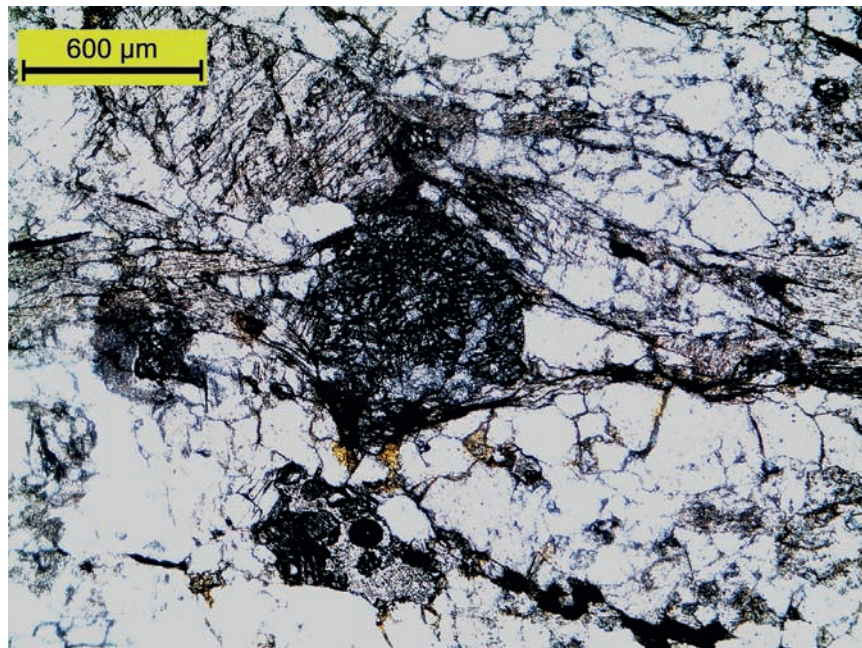


FIGURE 2.58 Fractured garnet porphyroblast showing phi-structure and intertectonic deformation. No shear sense indicated. Plane-polarized light. Photo width: 1.5 mm. Tso Moriri Crystallines, Ladakh, India. **Kankajit Maji**



FIGURE 2.59 Symmetric phi-structure. Symmetric phy-structure shown by a clast of feldspar in the granitic rock of the Higher Himalayan Crystalline. Section parallel to the stretching lineation and normal to the foliation showing no stair-stepping (Singh et al., 2020). Location: N32°16.22', E77°10.54' near the Shanag village in the Manali area of Himachal Pradesh (Singh et al., 2012). **Paramjeet Singh**

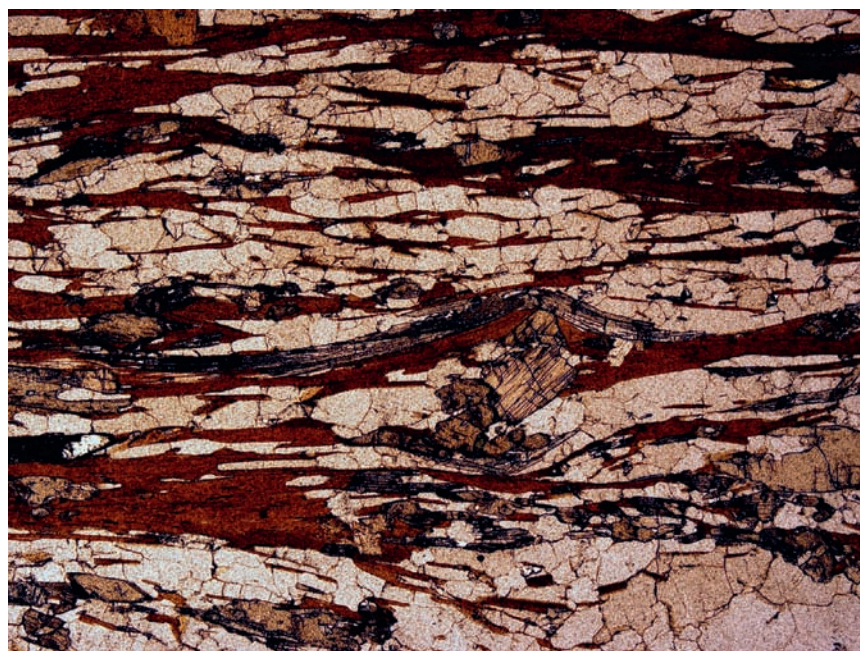


FIGURE 2.60 Photomicrograph of biotite + kyanite-bearing micaschists from the Num orthogneiss in the Makalu valley (East Nepal). Plane-polarized light, width of view c. 4 mm. The main foliation, oriented parallel to the long side of the picture, is highlighted mainly by a strong shape-preferred orientation of polycrystalline quartz ribbons, kyanite crystals (with high relief and light gray-yellowish color), and less than 1 mm thick biotite layers. Quartz grains have (< 500 μm) and show a weak shape-preferred orientation (generally parallel or at very low angle to the main foliation), weak undulatory extinction, and straight to interlobate grain boundaries suggesting a high-temperature dynamic recrystallization mechanism (Grain Boundary Migration) probably associated with annealing. Biotite crystals have no evidence of retrograde replacement. Kyanite crystals show inequigranular grain size (ranging from 1 mm to < 100 μm) and {100} and {001} sections oriented parallel and orthogonal to the main foliation, respectively. In particular, in the center of the picture, a large kyanite crystal showing the euhedral basal section is wrapped by the main foliation made of biotite and strongly elongated kyanite crystal that shows an aspect ratio of c. 20:1 and a well-developed cleavage system. Although geometric relationships could indicate two different generations of kyanite (pre- and syn-foliation), the bending of the elongated crystal may be also explained considering a differential growth velocity between {100} and {001} (basal) crystal sections during the same synkinematic metamorphic blastesis. **Chiara Frassi**

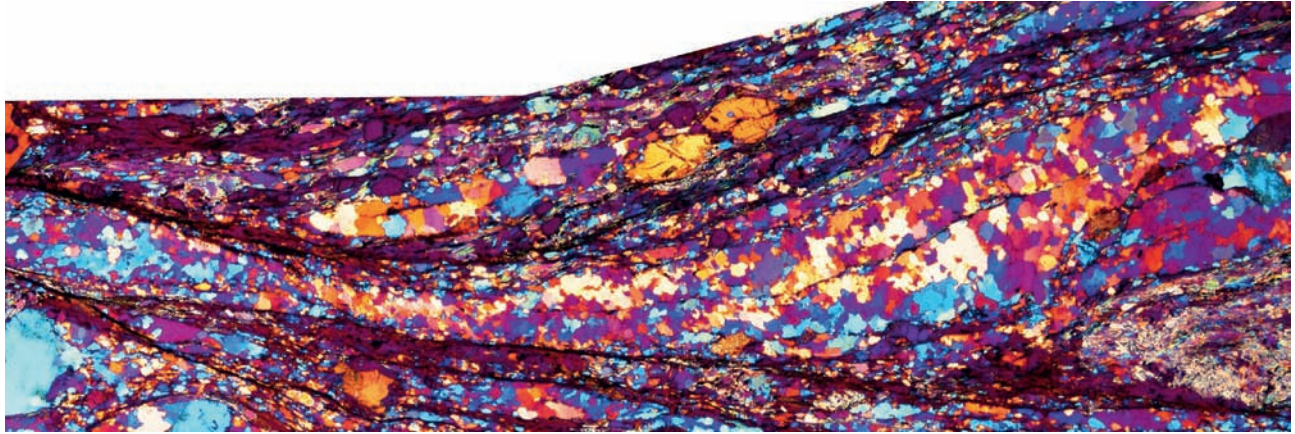


FIGURE 2.61 Photomicrograph of an asymmetric quartz ribbon from the mylonitic micaschists in the Variscan basement on Northern Sardinia Island (Italy). The picture is viewed with the lambda plate under crossed polarizer light. Width of view c. 7 mm. The main mylonitic foliation is defined by quartz, fine-grained garnet, feldspar, and very thin layers of muscovite and biotite aggregates (the irregular layers with a dark red-violet color). A < 1 cm thick shear zone (upper left to lower right) deforms the main foliation and a mm thick quartz ribbon suggests a dextral sense of shear. In the left and right portions of the ribbon, the quartz shows interlobate grain boundaries and seriate grain size indicating a grain boundary migration recrystallization mechanism. Within the shear zone in the thinner portion of the ribbon, the quartz grains are small, equigranular, and slightly elongated, indicating that intracrystalline deformation probably occurred by subgrain rotation recrystallization. The strong crystal preferred orientation and the well-defined grain shape foliation suggest a sense of shear opposite to that inferred by other microstructures (including the asymmetry of the quartz ribbon itself). This opposite kinematics can be interpreted as the result of rigid body rotation on quartz grains affected by low-velocity intracrystalline deformation. **Chiara Frassi**

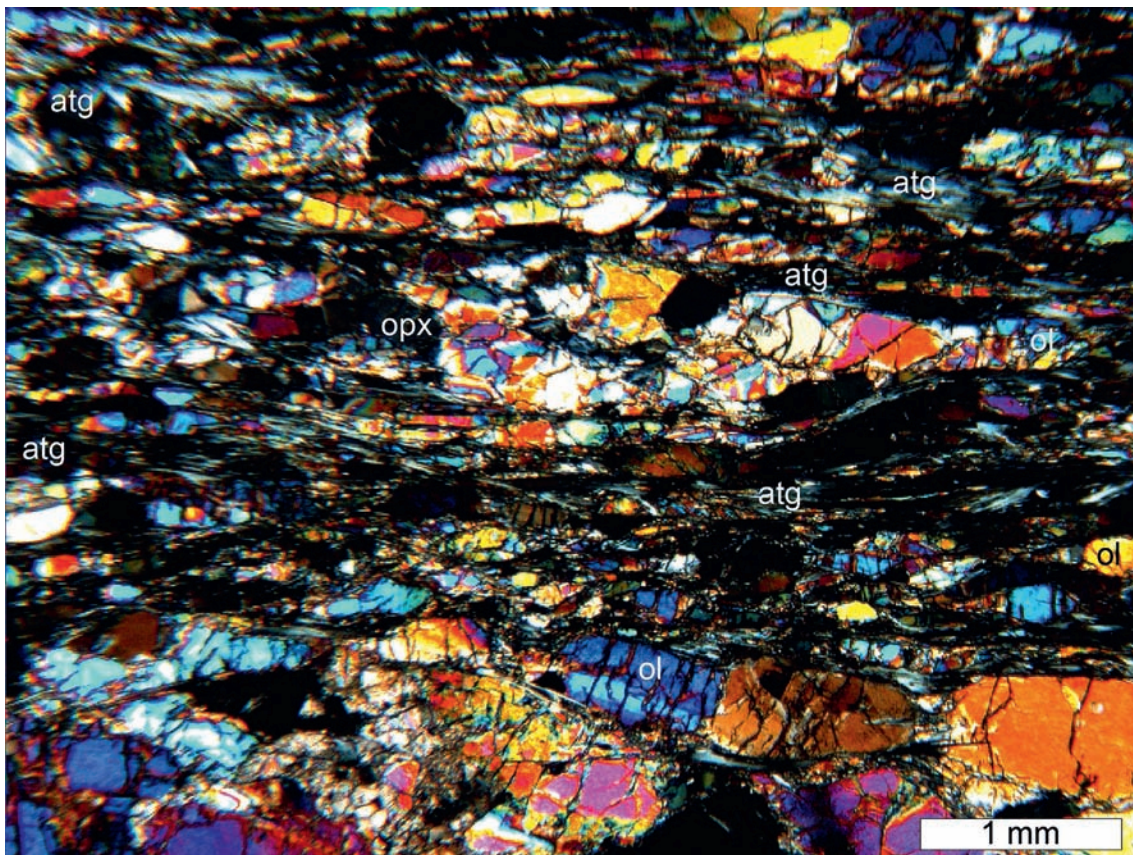


FIGURE 2.62 S-C-fabrics in antigorite (atg) mylonite and asymmetric sheared composite olivine-pyroxene (ol, opx) clasts indicate top-to-right tectonic transport. Cross-polars. Seve Nappe Complex, Central Scandinavian Caledonides, Sweden. **Jens Carsten Grimmer**



FIGURE 2.63 Photomicrograph of mylonitic peridotite cropping out in northwestern Elba island (Italy). Plane-polarized light, width of view *c.* 4 mm. The main foliation, oriented parallel to the long side of the picture, is marked by a strong shape-preferred orientation of olivine (the high-relief colorless minerals with microfractures orthogonal to the main foliation), spinel (the dark brown elongated minerals), and amphibole with a minor amount of phlogopite, pyroxene, and plagioclase. The foliation is the result of a progressive shearing developed during Mesozoic mantle exhumation. The earlier metamorphic paragenesis is defined by olivine (Fo₇₀₋₈₀), magnesium-aluminum spinel, rare anorthite (the bright colorless elongated crystal in the central lower portion of the picture), phlogopite, and very small orthopyroxene crystals (10–30 μ m). Olivine crystals generally show an elongated shape (see the olivine ribbon in the lower right portion of the picture). However, the olivine porphyroblast in the center-left portion of the picture shows a very small aspect ratio and sigma-type geometry with asymmetric tails, indicating a top-to-right sense of shear. The tails are made of strongly elongated olivine and amphibole crystals grew during the second metamorphic event. The amphibole (Mg-hornblende/tremolite) is highlighted by yellowish to pale brown acicular to fibrous crystals. Finally, small amphiboles with a gedrite-anthophyllite composition (see the small colorless rhombohedral crystals crosscutting the main foliation) grew during the Late Miocene contact metamorphism related to the emplacement of the Mt. Capanne intrusion. **Chiara Frassi, Giovanni Musumeci, and Francesco Mazzarini**

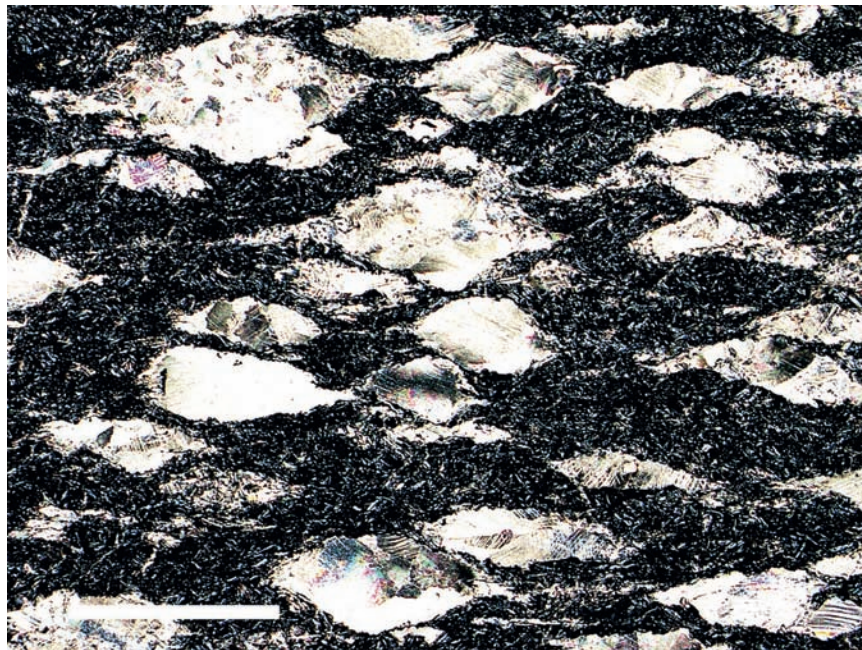


FIGURE 2.64 A thin section of basic lava containing deformed amygdules. The sample was taken from the Manba Unit at a Jurassic accretionary complex in the Northern Chichibu Belt, Central Japan (Shimizu and Yoshida, 2004). The section was cut normal to the foliation and parallel to the lineation. Cross-polarized light. Scale bar: 3 mm. The amygdules are filled with calcite and show many features of intracrystalline plasticity such as deformation twins, wavy extinction, and subgrain formation. The deformed amygdules have lenticular shapes due to precipitation and the overgrowth of calcite grains in the extensional direction. **Ichiko Shimizu**

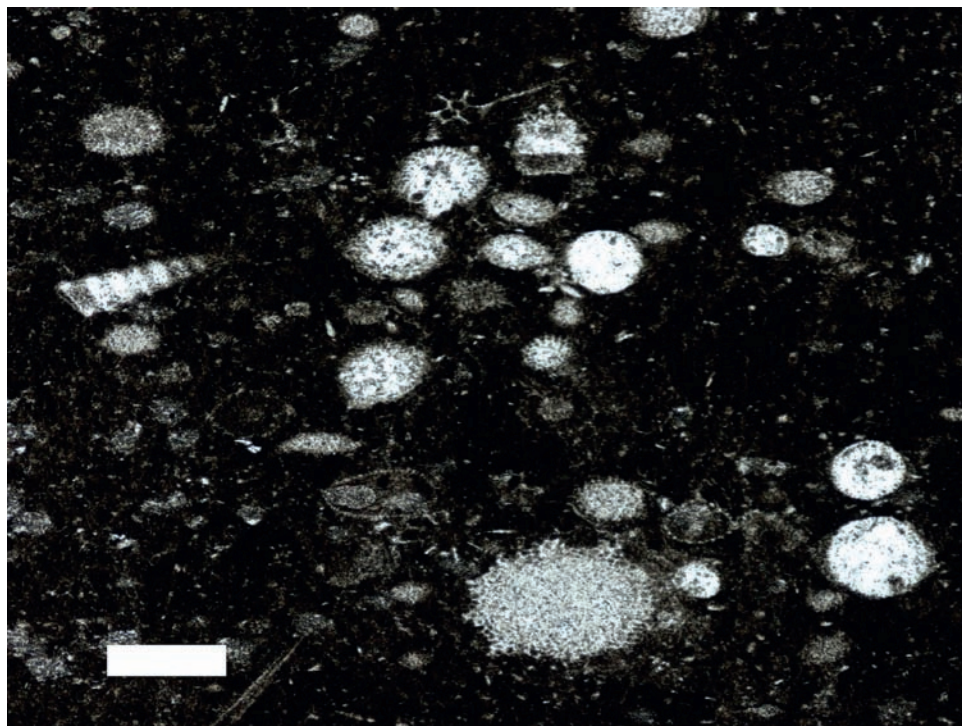


FIGURE 2.65 Deformed radiolarian fossils in black shale from a Jurassic accretionary complex (the Manba Unit) in the Northern Chichibu Belt, Central Japan (Shimizu, 1988). The section was cut normal to the foliation. Plane-polarized light. Scale bar: 200 μm . The shapes of the initially spherical radiolarian fossils are a direct indicator of strain ellipses. A corn-like radiolarian fossil (Nassellaria), hexagonal skeletons, and radial needles are also observed. Angular changes in these structures can also be used to quantify finite strain. Ichiko Shimizu

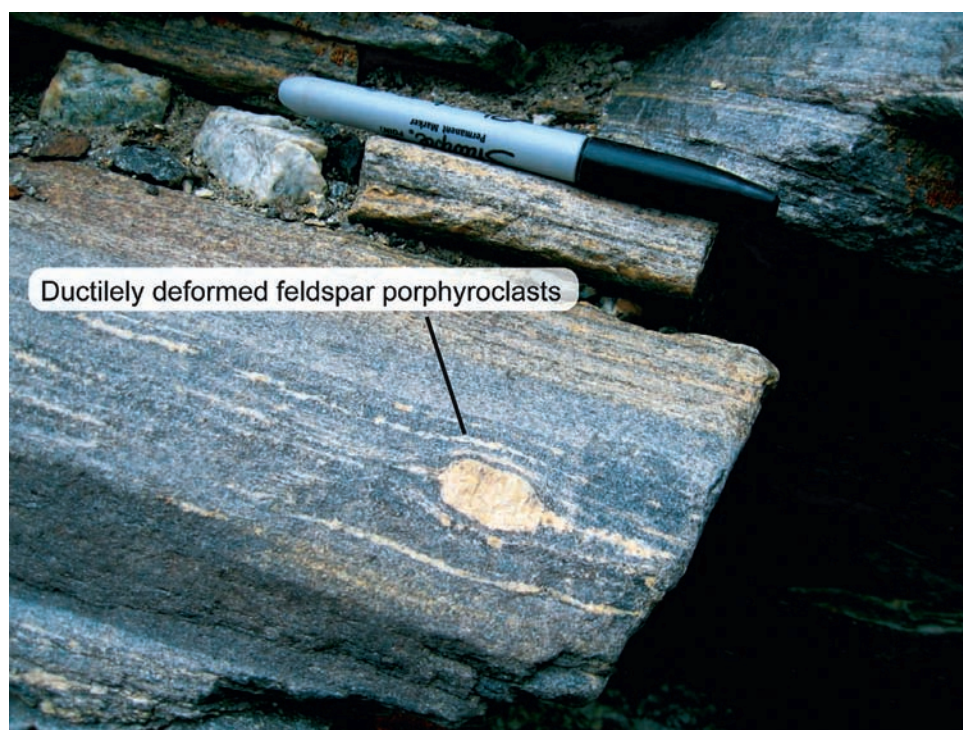


FIGURE 2.66 Shear fabrics display a ductile deformed lenticular feldspar porphyroblast. No shear sense indicated. Mylonitic foliation dips toward the right. Ayishan detachment, West Tibet. Ran Zhang

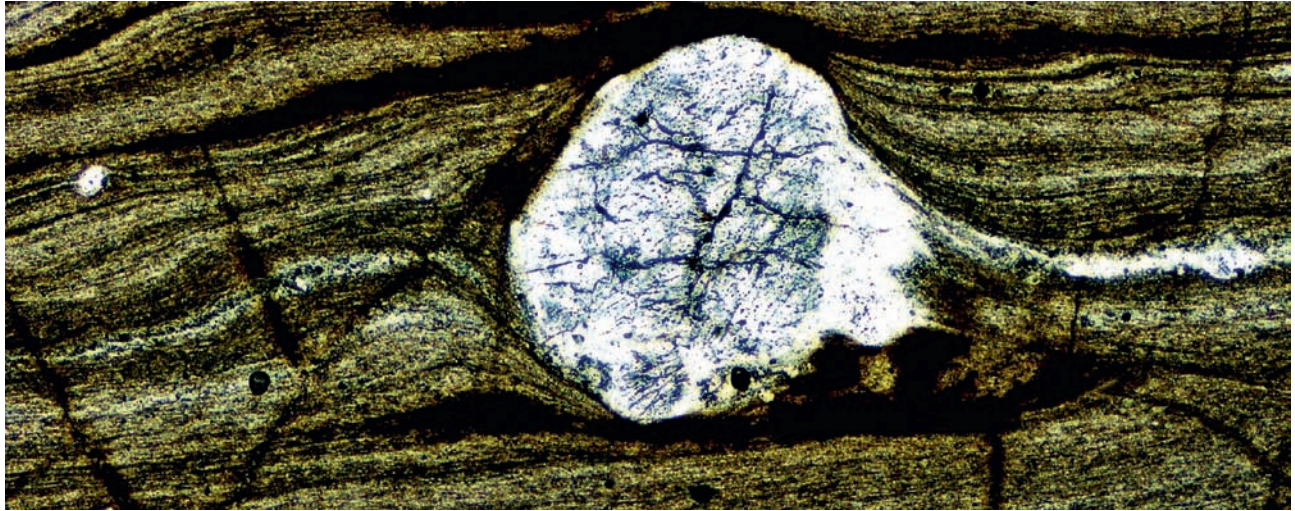


FIGURE 2.67 Winged δ -microstructure of olivine. The olivine grain deformed crystal-plastically under mantle condition in an ultramylonitized peridotite. The rocks crop out in a set of small islands in the Brazilian equatorial margins, the Archipelago Saint Peter and Saint Paul (ASPSP). The islands are one of the rare expositions of mantle rocks above sea level. They are located along the active segment of the Saint Paul Transform Fault, in the Atlantic Mid Ocean ridge. The Olivine Forsterite is the main mineral in these rocks. In addition, clasts of orthopyroxene and spinel are found. The matrix consists of a very fine-grained crystal of forsterite and spinels. The microstructures consist of subgrains, deformation lamellae, and undulose extinction. Postmylonitization fractures may also crosscut both the clast and matrix and normally are filled with magnetite and serpentine. Adjacent to the clast, recrystallized olivine developed as asymmetric wings. Wing asymmetry indicates a top-to-left shear. Location: ASPSP (Brazil). Plane-polarized light. Width of view 1.0 mm. **Suellen Olívia Cândida Pinto, Leonardo Evangelista Lagoeiro, Luiz Sérgio Amarante Simões, and Paola Ferreira Barbosa**

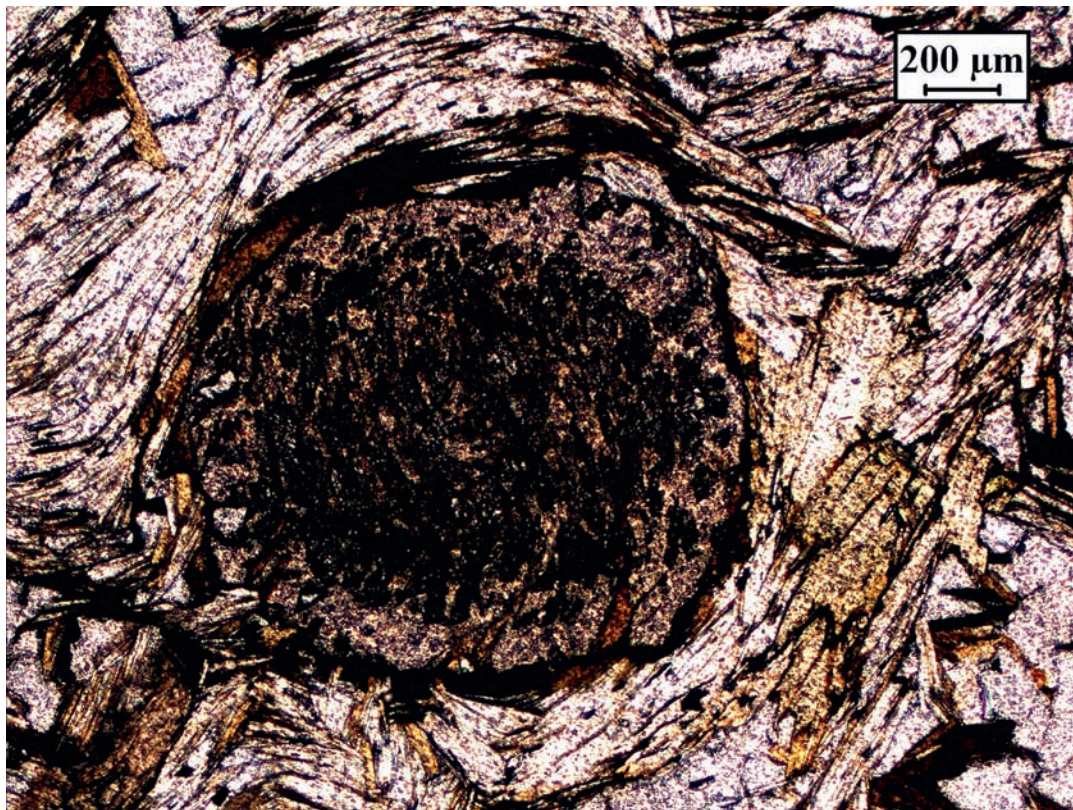


FIGURE 2.68 Syntectonically grown garnet with a sigmoid inclusion pattern. Top-to-left sheared? Garnet-biotite schist of the Proterozoic Daling Group. North to Gangtok, Sikkim, India. **Atanu Mukherjee**



FIGURE 2.69 Ductile shear zone. Ductile shear zone affecting high-grade schists and pegmatites developed during the Hercynian Orogeny. Stretching and thinning of the pegmatite body at the core of the shear zone where ultramylonites also formed. Lens cap: 70 mm diameter. Cap de Creus, Catalunya, Spain. Coordinates: 42°19'32.1"N, 3°18'01.2"E. **Eloi Carola and Irene Cantarero**



FIGURE 2.70 Mylonitic shear zone. A mylonitic shear zone cutting blue Archean gneiss dated at 3.35 billion years, from Swaziland. **Daniel Müller**

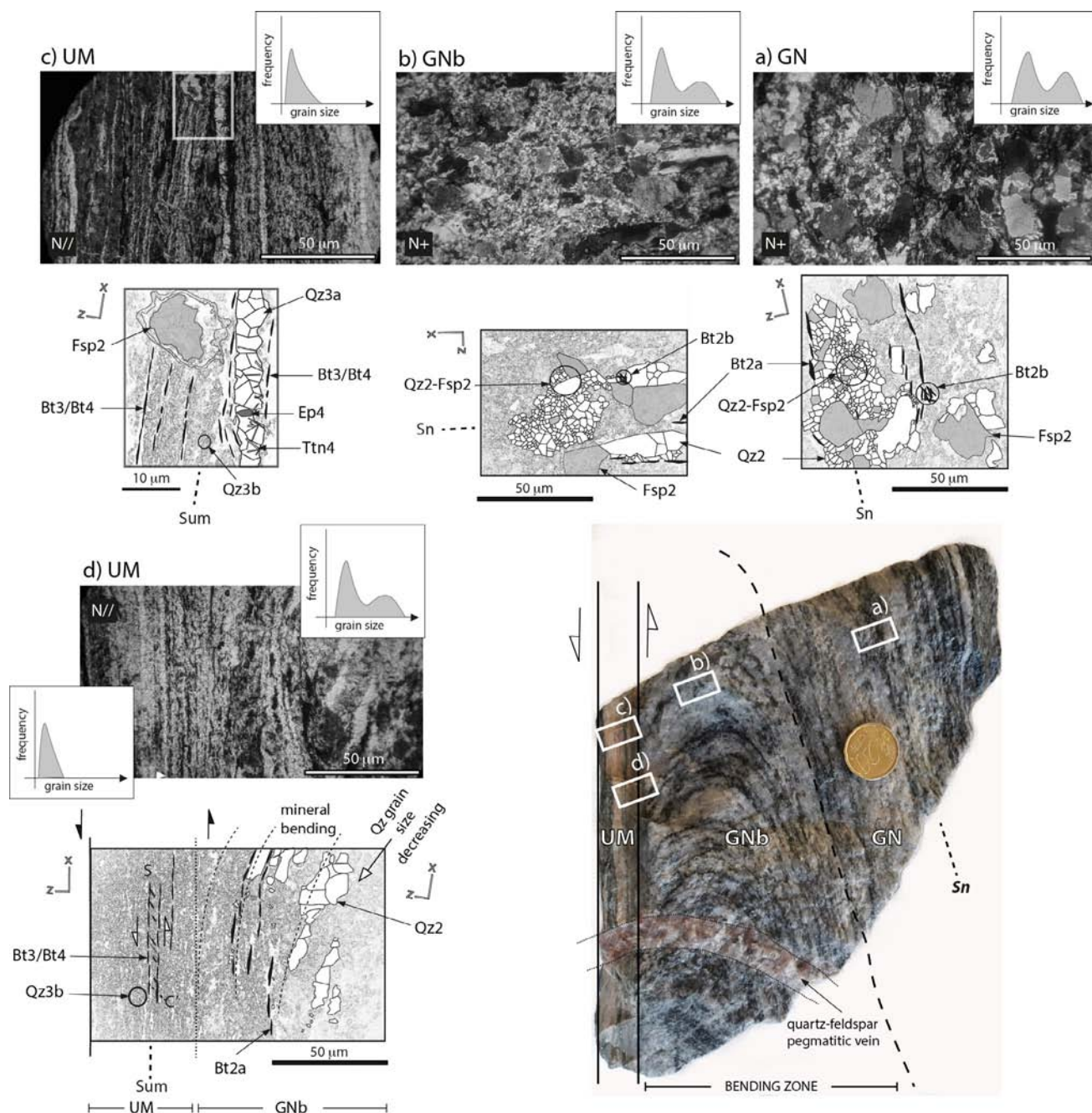


FIGURE 2.71 Ultramylonitic zone in medium-high temperature gneiss. Sheared amphibolitic gneiss. The amphibolitic gneiss belongs to the Lower Group of the Lower Arcaic on the “Greenstone Belt” of the Lufico-Cabinda zone—Angola, SW Africa. The gneiss (GN) develops typical gneiss banding (Sn) on amphibolitic facies PT conditions. Locally, shear corridors occur at all scales, generating Sn bending zones (GNb) in a sudden transition to an ultramylonitic zone (UM). This ultramylonite represents an almost complete recrystallization of the original gneiss (GN). The entire deformation zone is affected by regional greenschist retrogradation. (a) GN—The gneiss (GN) is composed of quartz-feldspathic and micaceous domains, characterized by a granoblastic texture. The quartz-feldspathic levels are dominated by quartz monomineralic aggregates that are relatively coarse and inequigranular (Qz2) exhibiting regular boundaries with a tendency to form 120 degree triple junctions. Quartz occurs at ~60%. The minor mineral component is feldspar-Kf and plagioclase (Fsp2), which is embedded in a quartz-feldspar polycrystalline aggregate (Qz2-Fsp2), highlighting the metamorphic gneissic foliation. The micaceous domains are constituted by biotite defining microshear plans (Bt2a) that mark the gneissic foliation (Sn). Biotite also appears in polycrystalline aggregates (Bt2b). (b) GNb—The gneiss registers qualitative textural changes on the bending zone—ultramylonite limit (bending zone gneiss-GNb), which is characterized by a slightly granular dimension reduction of quartz (Qz2). Biotite (Bt2a) occurs predominantly to define microshear zones that accentuate the bending that has affected this zone. There is a mechanical rotation of all microstructures in GNb, without developing an Sn + 1 foliation. (c, d) UM—The transition between the gneiss bending zone (GNb) and the ultramylonite zone (UM) at a large scale is sharp. However, at the microscale, this transition is continuous without the presence of any mechanical rupture interface. The granular size of the gneiss (Qz2-Fsp2 of GNb) decreases toward the ultramylonite boundary. The curvature of the gneissic bending is marked by the biotitic domain (Bt2a) that ends in an evident parallelism with the ultramylonite planar microstructures: biotite in microshear planes (Bt3); ultramylonite foliation (Sum), and quartz ribbons (Qz3a). Quartz ribbons are limited to the ultramylonite zone. This zone is also characterized by a microgranular quartz—cryptocrystalline lookalike—(Qz3b) and polycrystalline quartz ribbons (Qz3a) (Boullier and Bouchez, 1978; polycrystalline ribbon type 4) with epidote (Ep4), acicular titanite (Ttn4), and rare anhedral feldspar (Fsp2). The cryptocrystalline quartz domains involve the feldspar clasts, indicating a high viscosity contrast between these two mineral components. The late stage quartz-feldspar pegmatitic vein crosscut all previous structures. *Notes:* 1—Assemblage of metamorphic protolyte (relicts of magmatic quartz—Qz1 and relicts of magmatic Kf—Fsp1) do not occur in this sample. 2—Metamorphic gneissic assemblage: Quartz aggregates (Qz2); Quartz-feldspar (mainly Kf and Ab-plagioclase) aggregates (Qz2-Fsp2); Biotite in microshear plans (Bt2a) // foliation; Biotite in polycrystalline aggregates (Bt2b). 3—Ultramylonite assemblage: Quartz ribbon (Qz3a); Cryptocrystalline quartz (Qz3b); Recrystallized biotite (Bt3). 4—Retrometamorphic assemblage: chloritized biotite (Bt4); Epidote (Ep4); Titanite (Ttn4). 5—Indices: 1, 2, and 3 indices stand for magmatic, metamorphic, and ultramylonitic phases, respectively; 4 stands for the retrometamorphic assemblage. **Benedito C. Rodrigues and Jorge Pamplona**



FIGURE 2.72 Soft-sediment deformation at the roof of the brittle Mykonos Detachment. Polygenic conglomerate of the Miocene Sedimentary Unit with several elongated clasts showing an asymmetric sigmoid shape and small fine-grained tails indicating a top-to-left shear (e.g., the reddish and the light grey clast in the central parts of the photograph), from Mykonos Island, Greece. The clasts show a strong shape preferred orientation with the long axis dipping toward the right. In the matrix, mm to cm thick yellow layers mark the C and the C' planes. NE-SW view orientation. Width of view: ~90 cm. Coordinates: 37°28'27.87"N; 25°27'2.17". **Raffaele Gazzola, Chiara Frassi, and Giovanni Musumeci**

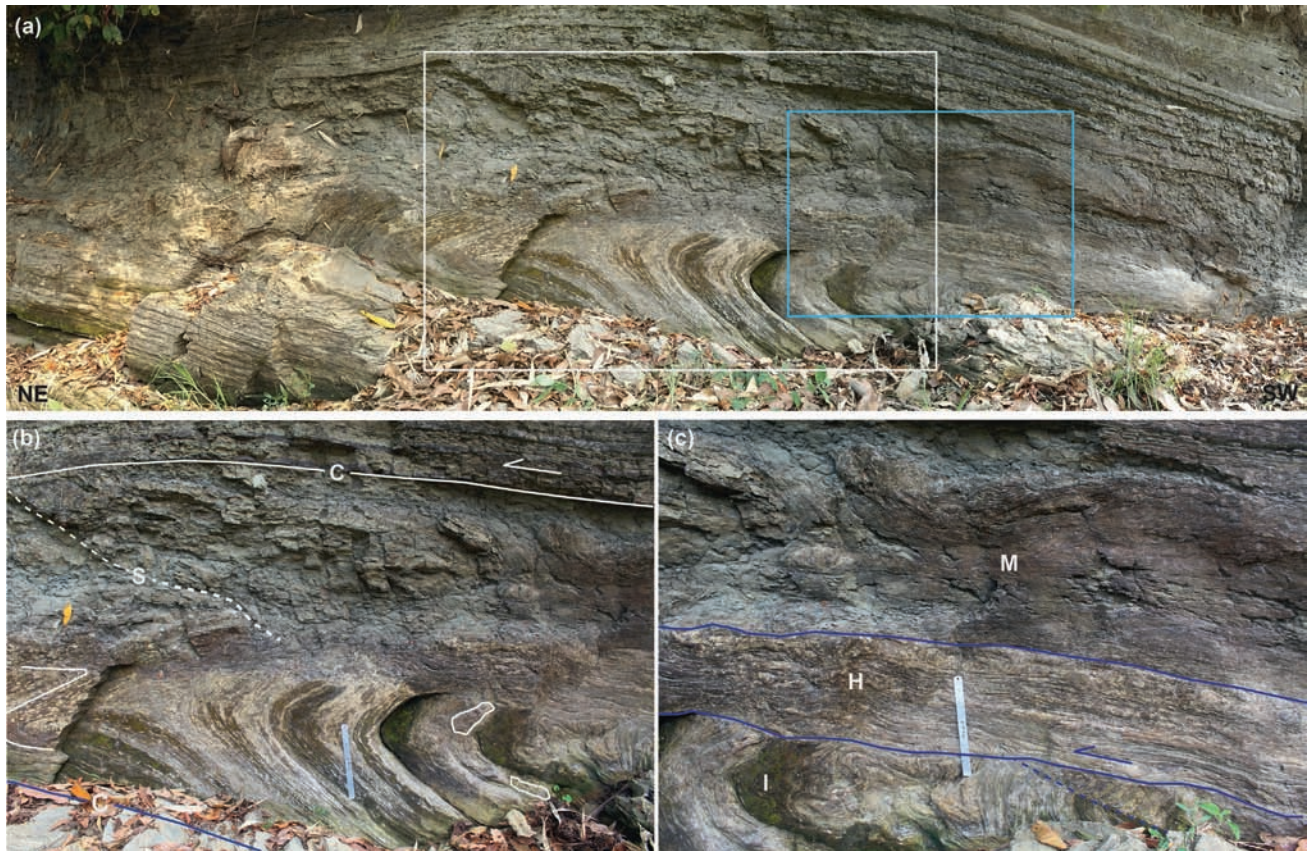


FIGURE 2.73 Passive shear folding, Gobamura-Belasari Anticline, CTFB, Bangladesh. Ductile deformed passive shear folding in the Tertiary sedimentary rock of the Chittagong-Tripura Fold Belt (CTFB), Bangladesh. (a) Fold developed in the Mid-Miocene to Late-Miocene Boka Bil Formation in the west flank of the NNW-SSE oriented Gobamura-Belasari Anticline along the Kaptai Lake section (latitude: 22.709250 degrees, longitude: 92.244639 degrees). This anticline is a part of the series of (sub)parallel anticline of the Chittagong-Tripura Fold Belt (CTFB), Bangladesh. The area started deforming since Early Pliocene (Hossain et al., 2019, 2020). Current eastward convergence/shortening rate is $\sim 5 \text{ mm year}^{-1}$ (Maurin and Rangen, 2009). The axial plane of the anticlines strikes 338–350 degrees, dips 70–78 degrees toward NE, and have 75–95 degrees interlimb angle. White and blue rectangles: locations of the figures (b) and (c), respectively. (b) Recumbent shear fold in the thinly bedded silty-shale with calcareous sandstone band (Boka Bil Formation). NE-SW exposure. White lines: upper and the lower boundaries of the shear zone. The attitude of the upper and the lower underformed shale beds are 215 degrees/23 degrees and 220 degrees/25 degrees, respectively. Noncoaxial deformation passively folded the Tertiary Boka Bil Formation due to eastward convergence of the thick sedimentary pile of the Indian Plate, which is subducting beneath the Burmese Plate. The Z-vergence (white color) of the asymmetric fold indicates top-to-the-left shear. The deformation structure can be approximately considered to be an S-C structure in which the intrafolial fold is caught between two C-planes (Fossen, 2016). White outlines on the lower left corner: broken blocks of calcareous sandstone band within the ductile deformed shale rock mass. (c) Three distinct deformation gradations observed from top to bottom of the shear zone. Broken line: minor thrust-shear band within the shear zone. M, moderately deformed; H, highly deformed; I, intensely deformed. **Md. Sakawat Hossain**

References

- Bhadra, S., Gupta, S., 2015. Reworking of a basement-cover interface during terrane boundary shearing: an example from the Khariar basin, Bastar Craton, India. In: Mukherjee, S., Mulchrone, K.F. (Eds.), *Ductile Shear Zones: From Micro- to Macro-scales*. Wiley-Blackwell, ISBN: 978-1-118-84496-0, pp. 164–181. ISBN.
- Bhadra, S., Gupta, S., Banerjee, M., 2004. Structural evolution across the Eastern Ghats Mobile Belt–Bastar Craton boundary, India: hot over cold thrusting in an ancient collision zone. *Journal of Structural Geology* 26, 233–245.
- Bikramaditya Singh, R.K., 2010. Geochemistry and mineral chemistry of granitoids of lesser himalayan crystallines, Western Arunachal Himalaya: implication for petrogenesis. *Journal of the Geological Society of India* 75, 618–631.
- Biswal, T.K., Jena, S.K., Datta, S., Das, R., Khan, K., 2000. Deformation of the terrane boundary shear zone (Lakhna shear zone) between the Eastern Ghats Mobile Belt and the Bastar Craton, in the Balangir and Kalahandi districts of Orissa. *Journal of the Geological Society of India* 55, 367–380.
- Biswal, T.K., DeWaele, B., Ahuja, H., 2007. Timing and dynamics of the juxtaposition of the Eastern Ghats Mobile Belt against the Bhandara Craton, India: a structural and zircon U–Pb SHRIMP study of the fold-thrust belt and associated nepheline syenite plutons. *Tectonics* 26, TC 4006.
- Bose, N., Dutta, D., Mukherjee, S., 2018. Role of grain-size in phyllonitisation: Insights from mineralogy, microstructures, strain analyses and numerical modeling. *Journal of Structural Geology* 112, 39–52.

- Bose, N., Dutta, D., Mukherjee, S., 2020. Refraction of micro-fractures due to shear-induced mechanical stratigraphy in a low-grade meta-sedimentary rock. *Journal of Structural Geology* 133, 103995.
- Boullier, A.-M., Bouchez, J.-C., 1978. Le quartz en rubans dans les mylonites. *Bulletin Société Géologique de France* 7, 253–262.
- Clark, C., Fitzsimons, I.C.W., Healy, D., et al., 2011. How does the Continental crust gets really hot? *Elements* 7, 235–240.
- Crowe, W.A., Nash, C.R., Harris, L.B., Leeming, P.M., Rankin, L.R., 2003. The geology of the Rengali Province: implications for the tectonic development of Northern Orissa, India. *Journal of Asian Earth Sciences* 21, 697–710.
- Dabrowski, M., Graseman, B., 2014. Domino boudinage under layer-parallel simple shear. *Journal of Structural Geology* 68, 58–65.
- Davis, G.H., Reynolds, S.J., Kluth, C.F., 2012. *Structural Geology of Rocks and Regions*. Wiley, New York.
- Dobmeier, C., Raith, M., 2003. Crustal architecture and evolution of the Eastern Ghats Belt and adjacent regions of India. In: Yoshida, M., Windley, B.F., Dasgupta, S. (Eds.), *Proterozoic East Gondwana: Supercontinent Assembly and Breakup*. 206. Special Publications, Geological Society of London, pp. 145–168.
- Dutta, D., Mukherjee, S., 2019. Opposite shear senses: geneses, global occurrences, numerical simulations and a case study from the Indian Western Himalaya. *Journal of Structural Geology* 126, 357–392.
- Dutta, A., Gupta, S., Panigrahi, M.K., 2010. The southern Rengali province—a reworked or exotic terrane? *Indian Journal of Geology* 80, 81–96.
- Engelder, T., Marshak, S., 1985. Disjunctive cleavage formed at shallow depths in sedimentary rocks. *Journal of Structural Geology* 7, 327–343.
- Eyal, Y., 1980. Synplutonic dikes in the Wadi Um-Mara Area, Sinai. *Tectonophysics* 67, 35–44.
- Fagereng, A., Remitti, F., Sibson, R.H., 2010. Shear veins observed along planar anisotropy at high angles to greatest compressive stress. *Nature Geoscience* 3, 482–485.
- Fagereng, A., Remitti, F., Sibson, R.H., 2011. Incrementally developed slickenfibres—geological record of repeating low stress-drop seismic events? *Tectonophysics* 510, 381–386.
- Fossen, H., 2016. *Structural Geology*, second ed. Cambridge University Press.
- Frehner, M., Exner, U., Mancktelow, N.S., Grujic, D., 2011. The not-so-simple effects of boundary conditions on models of simple shear. *Geology* 39, 719–722.
- Fujimoto, Y., Yamamoto, M., 2010. On the granitoids in the Shirakami mountains and correlation to the Cretaceous to Paleogene granitoids distributed in the Northeast Japan. *Earth Science* 64, 127–144 (in Japanese with English abstract).
- Ghosh, S.K., 1993. *Structural Geology: Fundamentals and Modern Developments*. Pergamon Press, Oxford, p. 598.
- Ghosh, S.K., Hazra, S., Sengupta, S., 1999. Planar, non-planar and refolded sheath folds in Phulad shear zone, Rajasthan, India. *Journal of Structural Geology* 21, 1715–1729.
- Grimmer, J.C., Greiling, R.O., Gerdes, A., 2011. The Ammarnäs complex in the central Scandinavian Caledonides: an allochthonous basin fragment in the Sveconorwegian foreland. *Terra Nova* 23, 270–279.
- Grimmer, J.C., Glodny, J., Drüppel, K., Greiling, R.O., Kontny, A., 2015. Early- to mid-Silurian extrusion wedge tectonics in the central Scandinavian Caledonides. *Geology* 43, 347–350.
- Hada, S., Ito, M., Landis, C.A., Cawood, P., 2001. Large-scale translation of accreted terranes along continental margins. *Gondwana Research* 4, 628–629.
- Harayama, S., Takahashi, Y., Nakano, S., Kariya, Y., Komazawa, M., 2000. Geology of the Tateyama District. With Geological Sheet Map at 1: 50,000. Geological Survey of Japan, p. 218 (Japanese with English abstract 6 p).
- Hossain, M.S., Khan, M.S.H., Chowdhury, K.R., Abdullah, R., 2019. Synthesis of the tectonic and structural elements of the Bengal Basin. In: Mukherjee, S. (Ed.), *Tectonics & Structural Geology: Indian Context*. Springer International Publishing AG, Cham. https://doi.org/10.1007/978-3-319-99341-6_6.
- Hossain, M.S., Xiao, W., Khan, M.S.H., Chowdhury, K.R., Ao, S., 2020. Geodynamic model and tectono-structural framework of the Bengal Basin and its surroundings. *Journal of Maps* 16, 445–458. <https://doi.org/10.1080/17445647.2020.1770136>.
- Kontny, A., Engelmann, R., Grimmer, J.C., Greiling, R.O., Hirt, A., 2012. Magnetic fabric development in a highly anisotropic magnetite-bearing ductile shear zone (Seve Nappe Complex, Scandinavian Caledonides). *International Journal of Earth Sciences* 101, 671–692.
- Koyi, H.A., Schmeling, H., Burchardt, S., Talbot, C., Mukherjee, S., Sjöström, H., 2013. Shear zones between rock units with no relative movement. *Journal of Structural Geology* 50, 82–90.
- Lister, G.S., Snoke, A.W., 1984. S-C mylonites. *Journal of Structural Geology* 6, 617–638.
- Mancktelow, N.S., Pennacchioni, G., 2005. The control of precursor brittle fracture and fluid-rock interaction on the development of single and paired ductile shear zones. *Journal of Structural Geology* 27, 645–661.
- Mancktelow, N.S., Pennacchioni, G., 2013. Late magmatic healed fractures in granitoids and their influence on subsequent solid-state deformation. *Journal of Structural Geology* 57, 81–96.
- Maurin, T., Rangin, C., 2009. Structure and kinematics of the Indo-Burmese Wedge: recent and fast growth of the outer wedge. *Tectonics* 28, TC2010.
- Miklavič, B., Rožič, B., 2008. The onset of Maastrichtian basinal sedimentation on Mt. Matajur, NW Slovenia. *RMZ-Materials and Geoenvironment* 55, 199–214.
- Mukherjee, S., 2007. Geodynamics, deformation and mathematical analysis of metamorphic belts of the NW Himalaya. Unpublished Ph.D. thesis Indian Institute of Technology Roorkee, pp. 1–267.
- Mukherjee, S., 2010a. Structures at meso- and micro-scales in the Sutlej section of the Higher Himalayan Shear Zone in Himalaya. *e-Terra* 7, 1–27.
- Mukherjee, S., 2010b. Microstructures of the Zaskar shear zone. *Earth Science India* 3, 9–27.
- Mukherjee, S., 2011a. Flanking microstructures of the Zaskar shear zone, West Indian Himalaya. *YES Bulletin* 1, 21–29.
- Mukherjee, S., 2011b. Mineral fish: their morphological classification, usefulness as shear sense indicators and genesis. *International Journal of Earth Sciences* 100, 1303–1314.
- Mukherjee, S., 2012. Simple shear is not so simple! Kinematics and shear senses in Newtonian viscous simple shear zones. *Geological Magazine* 149, 819–826.

- Mukherjee, S., 2013a. Deformation Microstructures in Rocks. Springer.
- Mukherjee, S., 2013b. Higher Himalaya in the Bhagirathi section (NW Himalaya, India): its structures, backthrusts and extrusion mechanism by both channel flow and critical taper mechanism. *International Journal of Earth Sciences* 102, 1851–1870.
- Mukherjee, S., 2013c. Channel flow extrusion model to constrain dynamic viscosity and Prandtl number of Higher Himalayan Shear Zone. *International Journal of Earth Sciences* 102, 1811–1835.
- Mukherjee, S., 2014a. Atlas of Shear Zone Structures in Meso-scale. Springer.
- Mukherjee, S., 2014b. Review of flanking structures in Meso- and Micro-scales. *Geological Magazine* 151, 957–974.
- Mukherjee, S., 2014c. Mica inclusions inside host mica grains from the Sutlej section of the Higher Himalayan Crystallines, India: Morphology and Constrains in Genesis. *Acta Geologica Sinica* 88, 1729–1741.
- Mukherjee, S., 2017. Review on symmetric structures in ductile shear zones. *International Journal of Earth Sciences* 106, 1453–1468.
- Mukherjee, S., 2018. Moment of inertia for rock blocks subject to bookshelf faulting with geologically plausible density distributions. *Journal of Earth System Science* 127, 80.
- Mukherjee, S., Biswas, R., 2014. Kinematics of horizontal simple shear zones of concentric arcs (Taylor–Couette flow) with incompressible Newtonian rheology. *International Journal of Earth Sciences* 103, 597–602.
- Mukherjee, S., Biswas, R., 2015. Biviscous horizontal simple shear zones of concentric arcs (Taylor Couette flow) with incompressible Newtonian rheology. In: Mukherjee, S., Mulchrone, K.F. (Eds.), *Ductile Shear Zones: From Micro- to Macro-scales*. Wiley-Blackwell, ISBN: 978-1-118-84496-0, pp. 59–64. ISBN.
- Mukherjee, S., Khonsari, M.M., 2018. Inter-book normal fault-related shear heating in brittle bookshelf faults. *Marine and Petroleum Geology* 97, 45–48.
- Mukherjee, S., Koyi, H.A., 2009. Flanking microstructures. *Geological Magazine* 146, 517–526.
- Mukherjee, S., Koyi, H.A., 2010a. Higher Himalayan Shear Zone, Sutlej section: structural geology and extrusion mechanism by various combination of simple shear, pure shear and channel flow in shifting modes. *International Journal of Earth Sciences* 99, 1267–1303.
- Mukherjee, S., Koyi, H.A., 2010b. Higher Himalayan Shear Zone: Zaskar Indian Himalaya-Microstructural studies and extrusion mechanism by a combination of simple shear and channel flow. *International Journal of Earth Sciences* 99, 1267–1303.
- Mukherjee, S., Mulchrone, K.F., 2013. Viscous dissipation pattern in incompressible Newtonian simple shear zones: an analytical model. *International Journal of Earth Sciences* 102, 1165–1170.
- Mukherjee, S., Puneekar, J.N., Mahadani, T., Mukherjee, R., 2015. Intrafolial folds-review and examples from the western Indian Higher Himalaya. In: Mukherjee, S., Mulchrone, K.F. (Eds.), *Ductile Shear Zones: From Micro- to Macro-scales*. Wiley-Blackwell, pp. 182–205. ISBN: 978-1-118-84496-0.
- Mukherjee, S., Bose, N., Ghosh, R., Dutta, D., Misra, A.A., Kumar, M., Dasgupta, S., Biswas, T., Joshi, A., Limaye, M., 2020. *Structural Geological Atlas*. Springer, ISBN: 978-981-13-9825-4. ISBN:.
- Mulchrone, K.F., Mukherjee, S., 2015. Shear senses and viscous dissipation of layered ductile simple shear zones. *Pure and Applied Geophysics* 172, 2635–2642.
- Mulchrone, K.F., Mukherjee, S., 2016. Kinematics and shear heat pattern of ductile simple shear zones with ‘slip boundary condition’. *International Journal of Earth Sciences* 105, 1015–1020.
- Mulchrone, K.F., Mukherjee, S., 2020. Numerical modelling and comparison of the temporal evolution of mantle and tails surrounding rigid elliptical objects in simple shear regime under stick and slip boundary conditions. *Journal of Structural Geology* 132, 103968.
- Nabelek, P.I., Hofmeister, A.M., Whittington, A.G., 2011. The influence of temperature-dependent thermal diffusivity on the conductive cooling rates of plutons and temperature-time paths in contact aureoles. *Earth and Planetary Science Letters* 317, 157–164.
- Pamplona, J., Rodrigues, B.C., 2011. Kinematic interpretation of shearband boudins: new parameters and ratios useful in HT simple shear zones. *Journal of Structural Geology* 33, 38–50.
- Pamplona, J., Rodrigues, B.C., Fernández, C., 2014. Folding as precursor of asymmetric boudinage in shear zones affecting migmatitic terranes. *Geogaceta* 55, 15–18.
- Passchier, C.W., 2001. Flanking structures. *Journal of Structural Geology* 23, 951–962.
- Passchier, C.W., Trouw, R., 2005. *Microtectonics*, second ed. Springer, Berlin. Chapter 5, Shear zones, 336 p.
- Pennacchioni, G., Mancktelow, N.S., 2007. Nucleation and initial growth of a shear zone network within compositionally and structurally heterogeneous granitoids under amphibolite facies conditions. *Journal of Structural Geology* 29, 1757–1780.
- Platt, J.P., Vissers, R.L.M., 1980. Extensional structures in anisotropic rocks. *Journal of Structural Geology* 2, 397–410.
- Ramsay, J.G., 1980. Shear zone geometry: a review. *Journal of Structural Geology* 2, 83–99.
- Regenauer-Lieb, K., Yuen, D.A., 2003. Modeling shear zones in geological and planetary sciences: solid-and fluid-thermal-mechanical approaches. *Earth-Science Reviews* 63, 295–349.
- Rutter, E.H., 1983. Pressure solution in nature, theory and experiment. *Journal of the Geological Society, London* 140 (5), 725–740.
- Sengupta, S., Ghosh, S.K., 2004. Analysis of transpressional deformation from geometrical evolution of mesoscopic structures from phulad shear zone, Rajasthan, India. *Journal of Structural Geology* 26, 1961–1976.
- Shimizu, I., 1988. Ductile deformation in the low-grade part of the Sanbagawa metamorphic belts in the northern Kanto Mountains, Central Japan. *Journal of Geological Society of Japan* 94, 609–628.
- Shimizu, I., Yoshida, S., 2004. Strain geometries in the Sanbagawa metamorphic belt inferred from deformation structures in metabasite. *Island Arc* 13, 95–109.
- Singh, P., Patel, R.C., Lal, N., 2012. Plio-Pleistocene in-sequence thrust propagation along the Main Central Thrust zone (Kumaon-Garhwal Himalaya, India): new thermochronological data. *Tectonophysics*. <https://doi.org/10.1016/j.tecto.2012.08.015>.

- Singh, P., Singhal, S., Das, A.N., 2020. U–Pb (zircon) geochronologic constraint on tectono-magmatic evolution of Chaur granitoid complex (CGC) of Himachal Himalaya, NW India: implications for the Neoproterozoic magmatism related to Grenvillian orogeny and assembly of the Rodinia supercontinent. *International Journal of Earth Sciences* 109, 1–18.
- Takahashi, Y., 2002. Granitic mylonites situated around the Shirakami Mountains, Northeast Japan. *Earth Science* 56, 215–216. In Japanese.
- Takahashi, Y., Cho, D.L., Kee, W.S., 2010. Timing of mylonitization in the Funatsu Shear Zone within Hida Belt of southwest Japan: Implications for correlation with the shear zones around the Ogcheon Belt in the Korean Peninsula. *Gondwana Research* 17, 102–115.
- ten Grotenhuis, S.M., Trouw, R.A.J., Passchier, C.W., 2003. Evolution of mica fish in mylonite rocks. *Tectonophysics* 372, 1–21.
- Treagus, S., Lan, L., 2003. Simple shear of deformable square objects. *Journal of Structural Geology* 25, 1993–2005.
- Trouw, R.A.J., Passchier, C.W., Wiersma, D.J., 2010. *Atlas of Mylonites and Related Microstructures*. Springer.
- Vernon, R.H., 2004. *A Practical Guide to Rock Microstructure*. Cambridge University Press, p. 610.

Chapter 3

Brittle faults

Brittle shear zones/fault zones are usually defined by curved brittle P-planes bound by usually straight Y-planes (Passchier and Trouw, 2005). These shears may affect a narrow zone within the rock bodies (Misra et al., 2015). Brittle sheared lenses of rocks vary in geometry, and the P-planes may curve only near the Y-planes (Mukherjee, 2014a,b). Fault gouge zones sometimes contain P-planes that help to deduce the shear sense. Fault planes/Y-planes may contain slickensides. See Doblas (1998) for detail of slickenside types and their reliable use in shear sense determination (also see Vanik et al., 2018; Shaikh et al., 2020). This is despite Tjia (1964) questioning the reliability of slickensides as shear sense indicators. Deformational structures and especially faulted units within soft-sedimentary structures are quite common (Byrne, 1994) (Figures 3.1–3.101). In collisional tectonic regimes, brittle faults can form either in an in-sequence or in an out-of-sequence manner (Mukherjee, 2015). See Mukherjee et al. (2020) for shear fabrics from other terrains.

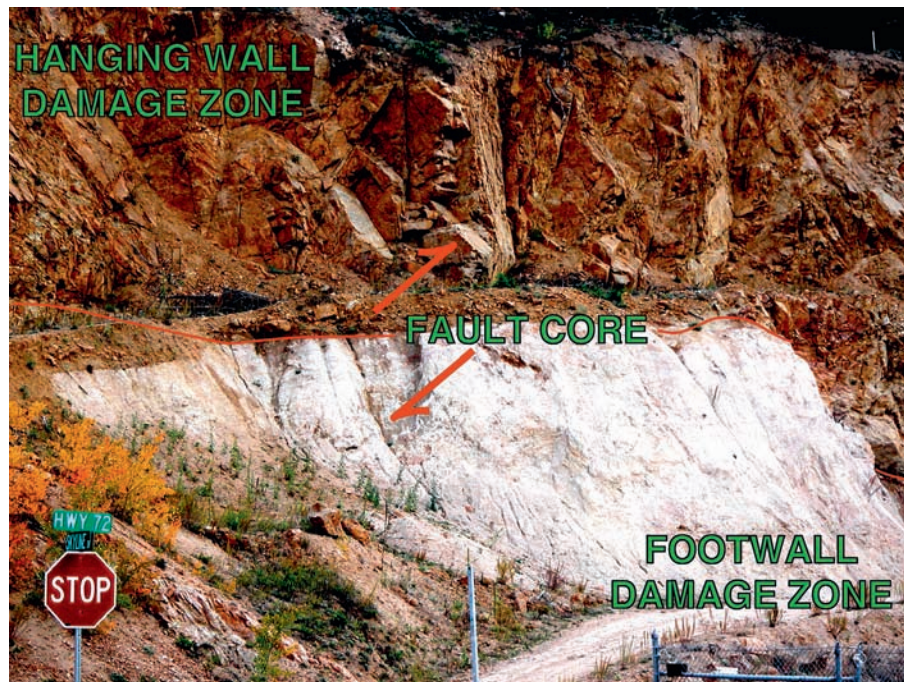


FIGURE 3.1 Road-cut exposure of the Coal Creek fault zone, central eastern Front Range, Colorado, United States (39°54'14"N, 105°20'46"W). This reverse fault zone occurs within the 1.7 Ga Boulder Creek granodiorite batholith and hosts a ~620 m west directed slip. The exposure shows a discrete, clay-rich gouge fault core and a surrounding damage zone (cf. Caine et al., 1996). The damage zone is characterized by relatively low-temperature hydrothermal alteration concentrated mainly in hanging wall fractures juxtaposed against the pervasively and moderately altered clay-rich, white footwall. See Caine et al. (2010) for details. **Jonathan Caine**

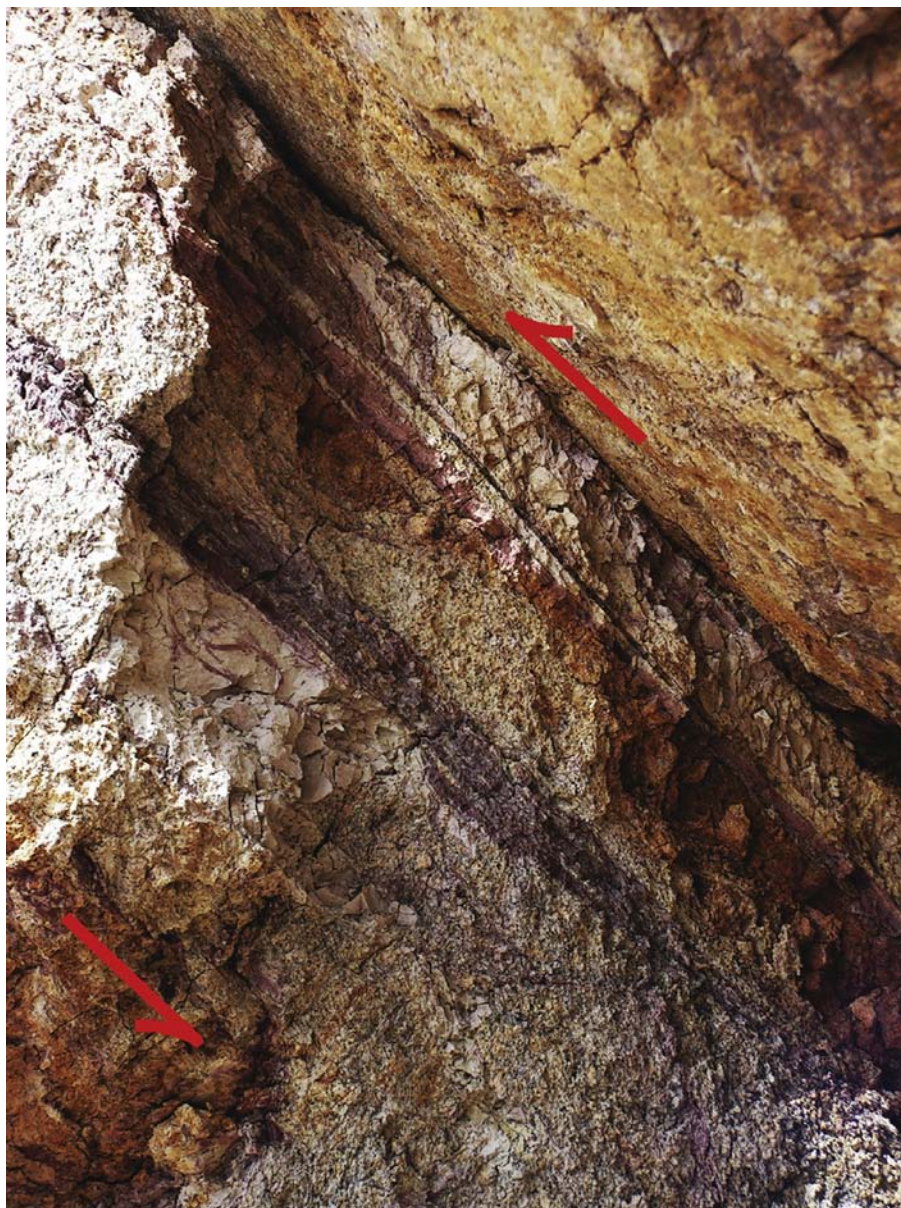


FIGURE 3.2 Fault core of the Coal Creek fault zone (see [Figure 3.1](#)). Outcrop detail of the sharp, polished, and striated principal slip surface hanging wall contact with the clay-rich gouge fault core. The gouge is composed of foliated, fault parallel white and red clay-rich gouge seams 1–3 cm thick. **Jonathan Caine**

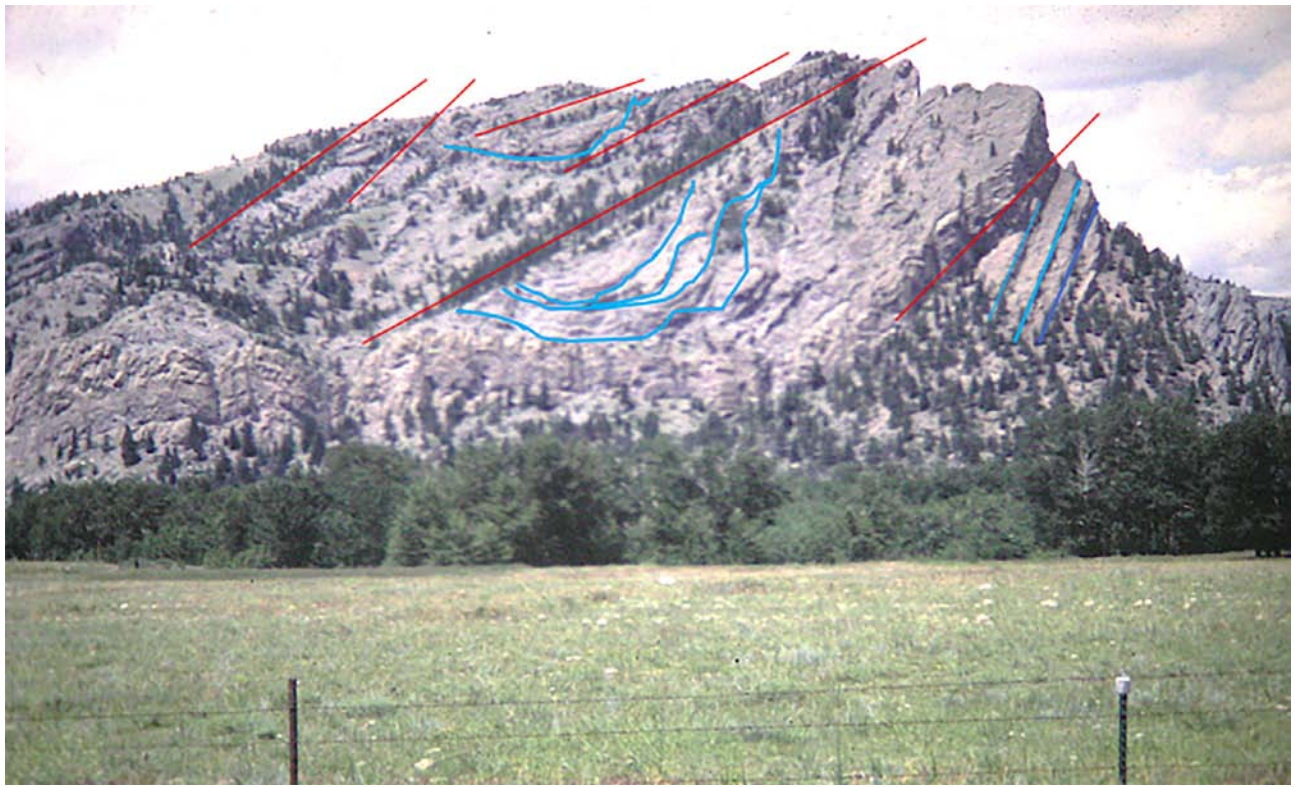
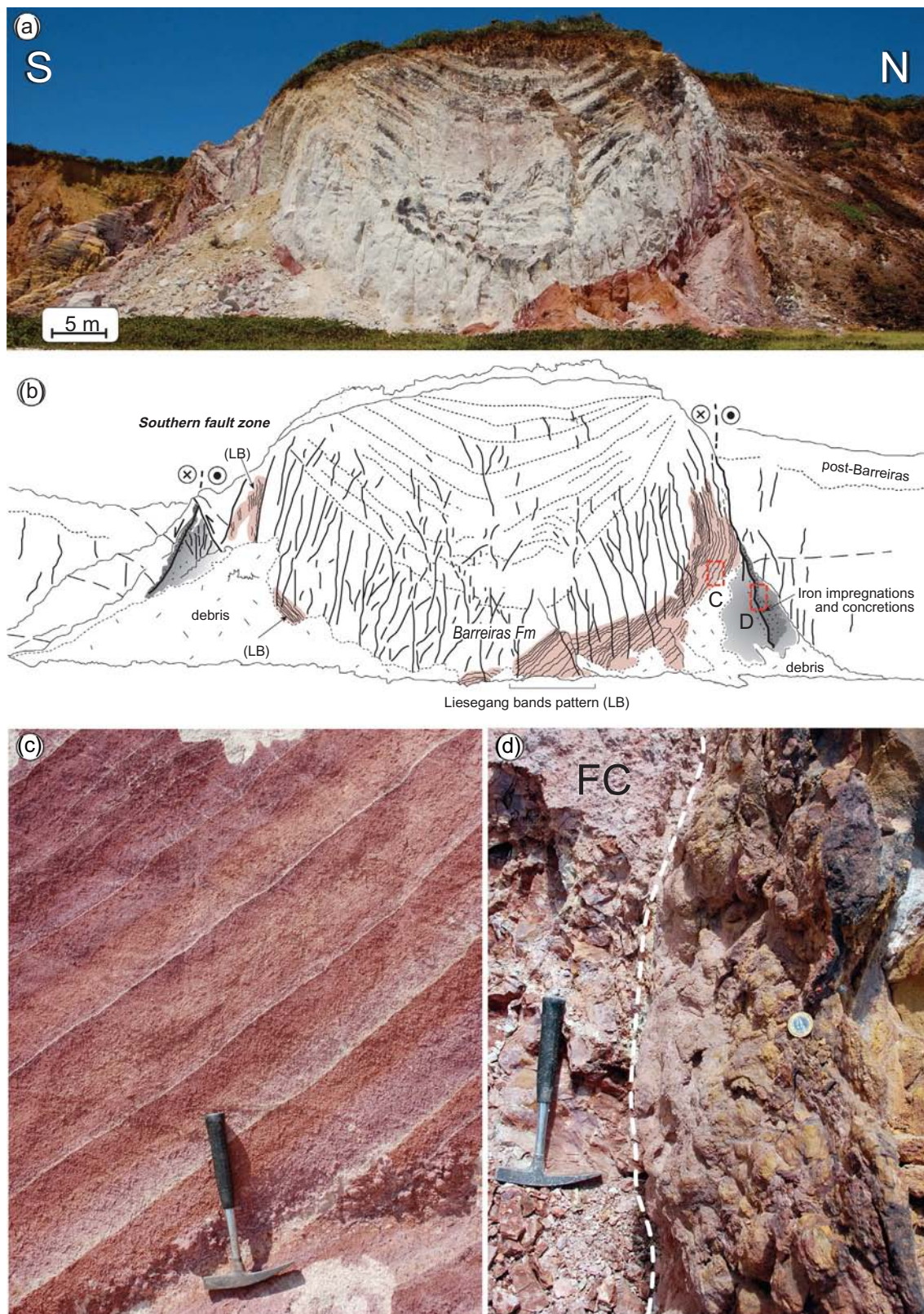


FIGURE 3.3 Stacked thrust sheet. Hillside exposure of stacked thrust sheets north of Nye, Montana. Faults dip southward back toward the source of the Laramide crystalline basement uplift of the Archean Beartooth Block, including the Stillwater layered igneous complex. Red lines coincide with thrust planes and blue curves-lines are shown to indicate bedding, folded, or nearly planar. Thrusted units are Paleozoic limestones, primarily of the Devonian-Mississippian Madison Formation. **Jeff Greenberg**



FIGURE 3.4 Extensional fault affecting the Jurassic succession made up of limestones and black shales with a cm-scale throw. Stratabound fractures in the harder limestone levels. San Andres, Cantabria, Spain. Coordinates: 42°54'30.0"N, 4°05'43.6"W). **Eloi Carola and Irene Cantarero**



Balsamo & Bezerra, 2020

FIGURE 3.5 Strike-slip faulting and iron oxide deposits. (A) Photomosaic showing the studied outcrop in the Paraíba Basin, NE Brazil, characterized by a gentle syncline bounded by two normal faults that reactivated with right-lateral transpression, compatible with the recent stress field in the region (Bezerra et al., 2014). Faults affect both the Mio-Pliocene Barreiras Formation sandstone and the post-Barreiras Quaternary sediments. (B) Line drawings of the outcrop showing the main structural features (northern and southern fault zones) and the structurally controlled iron oxide deposits in the form of (i) Fe-oxide concretionary bodies developed out of the fault-bounded syncline, and (ii) Fe-oxide concentric Liesegang bands patterning within the syncline. (C) Detail of Liesegang band pattern within the syncline, developed under a diffusive mass transfer in the fault-bounded compartment. (D) Detail of m-scale iron oxide concretionary bodies developed at the boundary between the low-permeable fault core and the high-permeable external damage zone, likely under an advective fluid flow. Both Liesegang bands and Fe-oxide concretions are affected by late-stage fracturing and, in places, bleaching localized along fractures. Details in Balsamo et al. (2013). LB: Liesegang bands; FC: fault core. **Fabrizio Balsamo and Francisco H.R. Bezerra**



FIGURE 3.6 Hanging-wall meso-scale buttressing. A hanging-wall meso-scale buttressing (sensu Butler, 1989) structural assemblage across a preexisting normal fault within the Montagna dei Fiori shortcut anticline, central Apennines of Italy (Calamita et al., 2017). The photo is a remarkable example of hanging-wall buttressing developed due to the presence of weaker Cretaceous-Miocene hemipelagic marls juxtaposed onto the stronger, massive Jurassic platform limestones in the footwall. Minor low-angle reverse faults (thrusts and back-thrusts) displace the high-angle prethrusting normal fault plane, giving rise to local younger-on-older relationships. S-C fabrics show the overprinting relationships between the extant normal faults and contractional structures within the damage zone of the fault. Tight and angular folds may develop as a consequence of the competence contrast between the involved lithologies (Calamita et al., 2017). Location: ~3 km west to the Ripe di Civitella Village (42°44'30.26"N 13°36'24.30"E WGS84). Width of view: ~ 1 m. **Paolo Pace and F. Calamita**



FIGURE 3.7 Compactive shear bands, 1. Outcrop-scale compactive shear bands (CSB, black arrowheads) with cataclasis (Aydin, 1978) associated with calcite-cement nodules (CN) in arkose sandstones. When CSBs occur in cluster, a zone of CSB (ZB) is formed. The assemblage CSB nodules are more resistant to erosion than the poorly cemented host rock (HR) (Del Sole et al., 2020a,b). Typical branching structures such as eye (ES) and a ramp can be recognized. Dotted white lines: bedding. Hammer for scale (33 cm long). **Leonardo Del Sole and Marco Antonellini**

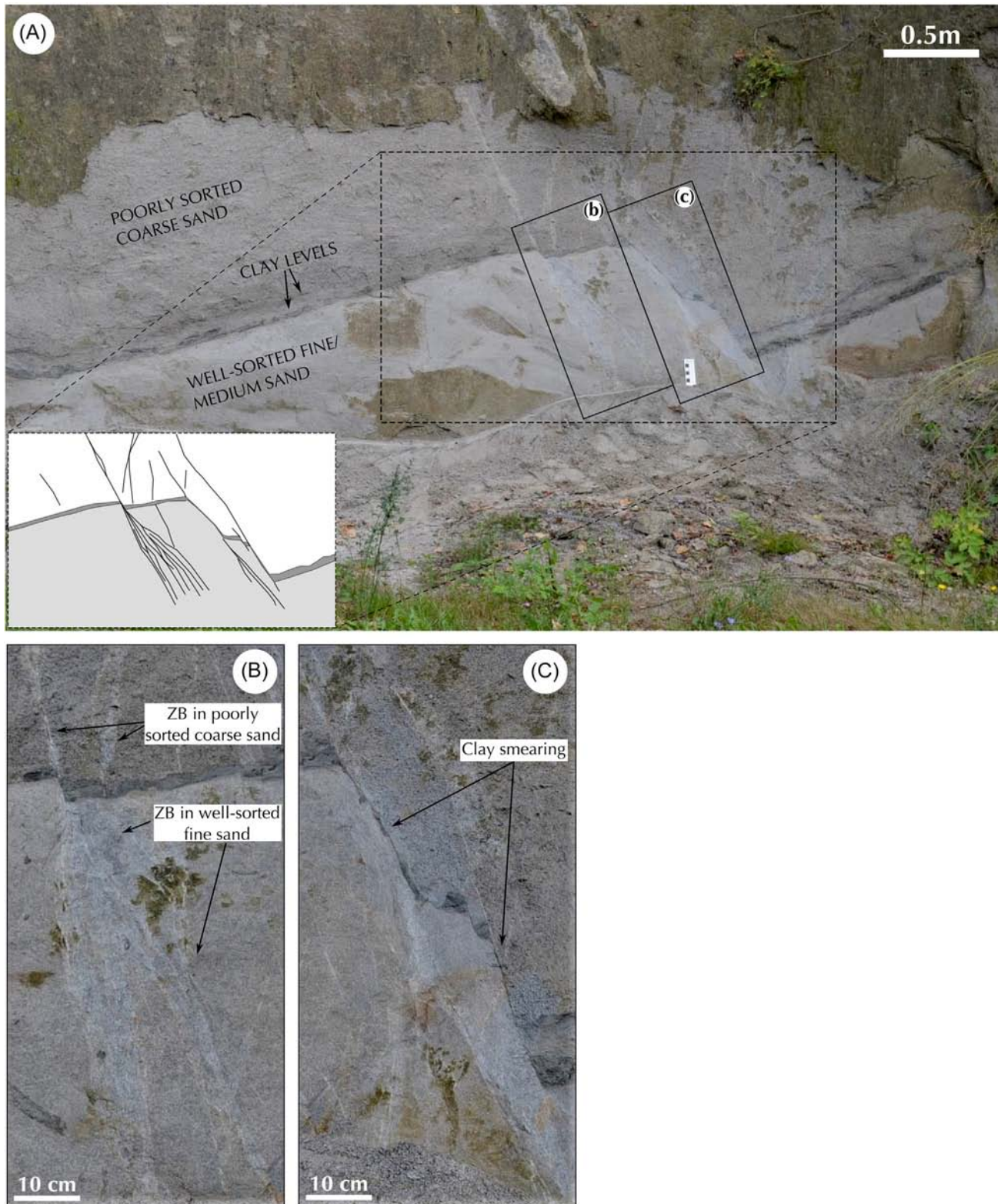


FIGURE 3.8 Compactive shear bands, 2. Rock properties control normal fault zone characteristics. (a-b) In poorly sorted low porosity and clay-rich arkose sandstone, the deformation is localized, the volumes where strain localization occurs are narrow, and the CSBs tend to be straight and develop along a single strand that accommodates all displacement. In well-sorted high porosity and fine-grained sandstones, the deformation is more distributed, the area of strain localization is wide, the CSB splits in several wavy and anastomosing segments, and each segment accommodates part of the total displacement (Antonellini and Mollema, 2002). (c) Cataclastic deformation is accompanied by a shale smear of thin dark-colored shale levels. **Leonardo Del Sole and Marco Antonellini**

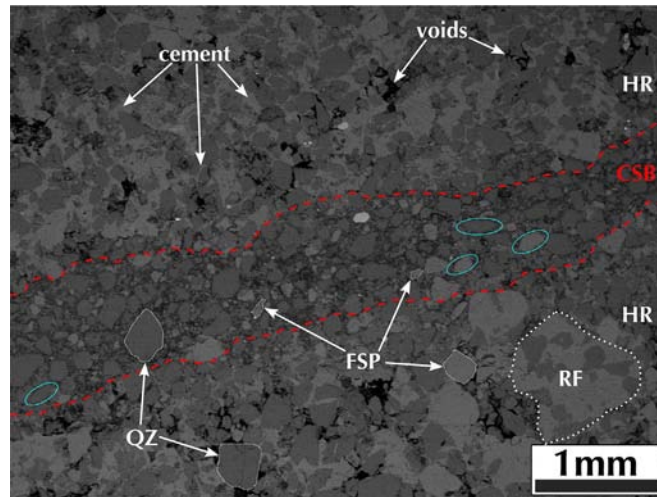


FIGURE 3.9 Compactive shear bands, 3. In cataclastic CSBs, grain crushing is the main microstructural deformation mechanism. CSBs are characterized by a reduction of grain size and porosity through grain crushing, compaction, and reorganization of grains by boundary sliding and rotation (grains aligned along the CSB, light-blue ellipses). The CSB core is characterized by a wide grain-size distribution with a few large, rounded, and nearly undisturbed sand-size grains (mostly quartz, QZ) surrounded and cushioned by an angular fine-grained matrix (mostly feldspars, FSP) with little pore spaces. RF: rock fragment. CSB could be surrounded by a thin zone of compaction. **Leonardo Del Sole and Marco Antonellini**

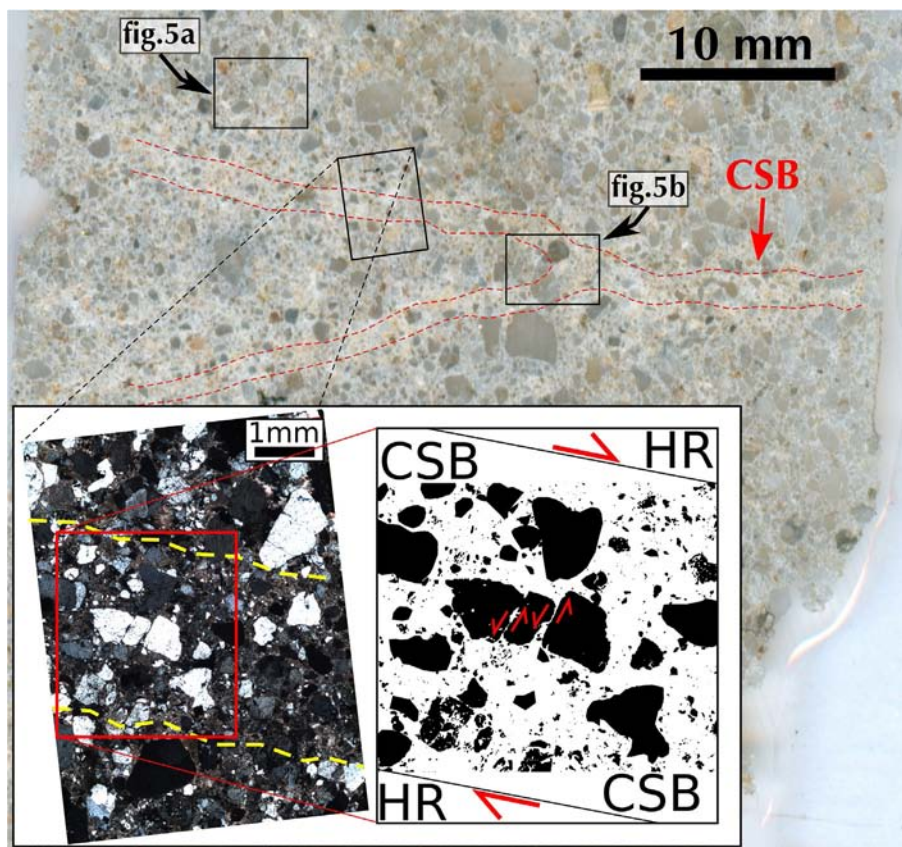


FIGURE 3.10 Compactive shear bands, 4. Thick (~ 2 mm) CSB trace in a thin-section scan. Branching structures (i.e., ramp structures) can be recognized also at the microscale (black-box: Figure 5B). The inset shows the CSB microstructure in cross-polarized light and the major elements are outlined. Notice the bookshelf sliding-like structure (Ghosh, 1993) or domino-type fragmented grain (Trouw et al., 2010), where a framework grain slices up by parallel high-angle shear fractures. The sense of slip (red arrows) along the grain-scale faults is antithetic (left-lateral), with reference to the shear sense of CSB (right-lateral). The angle between the CSB's plane and the grain-scale faults is ~60–70 degrees. **Leonardo Del Sole and Marco Antonellini**

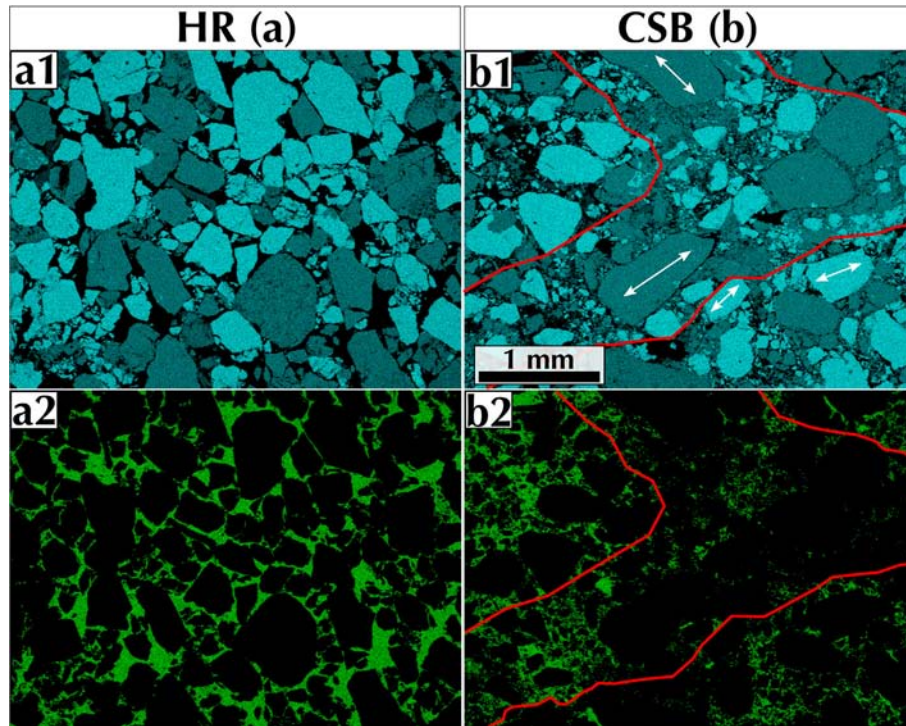


FIGURE 3.11 Compactive shear bands, 5. SEM-EDS element distribution maps for (a) HR and (b) CSB. Maps a1 and b1 show the silica (Si): quartz (light blue) and feldspars (gray). Maps a2 and b2 show the calcium (Ca): Ca-cement within the pores. The combined effect of cataclasis and compaction within the CSB (b1, b2) degrades the porosity by grain size and sorting reduction, packing increase, and grain rearrangement with respect to the HR (a1, a2). After band localization, the cementation almost fills up the pores and forms the nodules (Del Sole and Antonellini, 2019). **Leonardo Del Sole and Marco Antonellini**

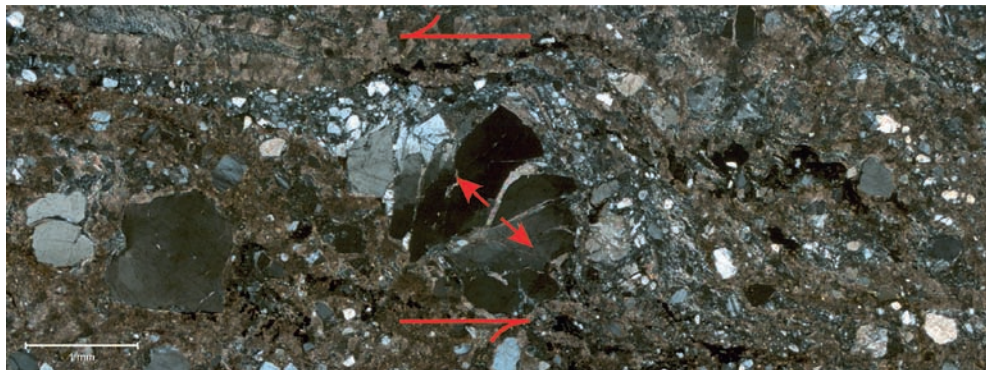


FIGURE 3.12 Polarized light micrograph of the red gouge from the Coal Creek fault zone (see Figure 3.2). A relatively large quartz grain with asymmetric, granular “tails” shows kinematic compatibility with the outcrop-scale indicators of contractional slip and is interpreted as evidence for cataclastic flow. The large central quartz grain also shows extensional fractures opened in a kinematically compatible direction and filled by calcite, suggesting syntectonic fluid flow. The thin section is cut perpendicular to the plane of the fault and parallel to the slip. **Jonathan Caine**

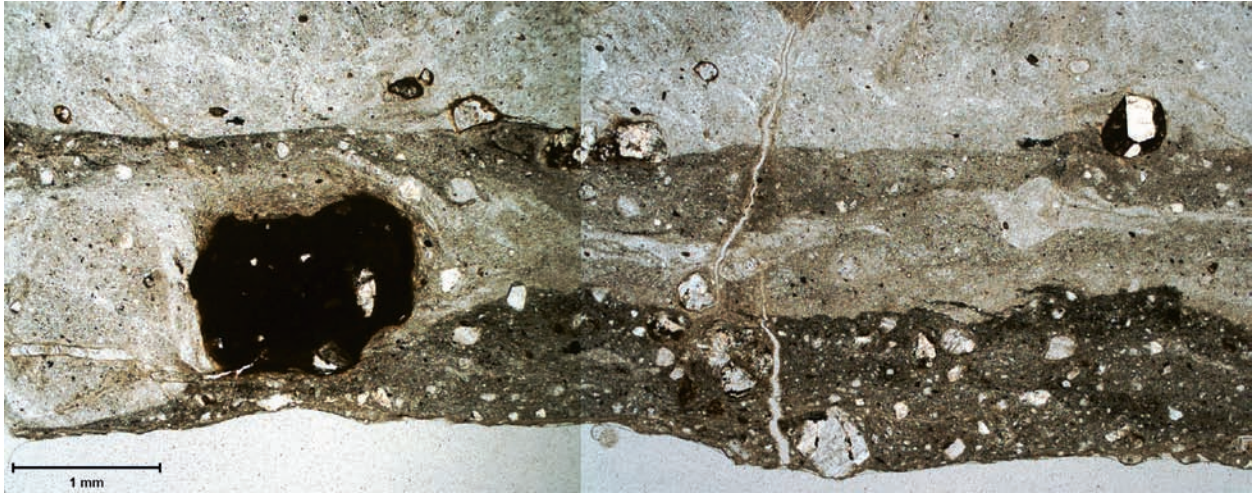


FIGURE 3.13 Plain light micrograph of white and red clay-rich gouge from the Coal Creek fault zone (see [Figure 3.2](#)). Clays envelop rounded quartz, feldspar, and lithic grains interpreted as evidence for episodic, cataclastic flow. The thin section is cut perpendicular to the plane of the fault and parallel to the slip. **Jonathan Caine**



FIGURE 3.14 Fault zone of the Raša fault. Location: Senadole, Slovenia; WGS 84 coordinates: 45°43'00" N, 14°00'15" E; Rock type: bedded micritic limestone, Sežana formation, Late Cretaceous; Field of view: approx. 20m. The Raša fault is a regional-scale seismically active fault with dextral to dextral-reverse kinematics inferred from fault-slip data and earthquake focal mechanisms ([Poljak et al., 2000](#)). A highway roadcut provides excellent exposure of its fault zone, which is here more than 100m wide. The photograph shows the fault core (the right half of the picture) including the fault gouge and the principal slip plane with well-developed slickensides (center). The damage zone to the left is pervasively fractured and veined to the extent that the originally subhorizontal bedding is completely obliterated. **Jonathan Caine**



FIGURE 3.15 Shear zone and mineralization. Cu-mineralized vertical shear zone cutting the Cryogenian granodiorite, Saghro inlier, Eastern Anti-Atlas, Morocco (El Ouardi et al., 2016). The ore body is an N155-trending lenticular structure with gangue minerals, mainly quartz and carbonate. The wall rock is mylonitized and the host rocks are stretched and flattened parallel to the quartz lenses. Photographed by Prof. Karaoui Brahim (Moulay Ismail University). **Zakarya Yajoui**



FIGURE 3.16 Mesoscopic conjugate set of normal faults seen in a WNW-ESE section developed within a thinly laminated sandstone-shale sequence of Early Cretaceous Lower Bhuj succession. Connotes extensional tectonic setting. The fault planes strike NE-SW, and dip steeply ~ 70 degrees. The slip is greater on the fault toward the right of the section, which displaces the earlier formed fault to the left. The right side of the photo is the west direction. Width of the section: ~ 1.5 ft. On Kodki Road, Latitude $23^{\circ}14'37.1''$ N, Longitude $69^{\circ}34'59''$ E, near Bhuj city, Gujarat, India. **Mainak Choudhuri**



FIGURE 3.17 Nonparallel faults. Nonparallel faults slipped a quartz vein within granodiorite, near the Singhbhum Shear Zone. Near Dudh River, Narwa, Ghatsila, India. Mery Biswas



FIGURE 3.18 Subvertical brittle shear Y-planes bound tangentially curved brittle P-planes, observed in a subvertical section. The tip of the pen indicates a sense of shear. Psammitic schist. 2419.903 N, 72 51.496 E. South Delhi Fold Belt. Near Rewari Dhamsala, Ambaji, Gujarat, India. See [Mukherjee and Koyi \(2010a,b\)](#), [Mukherjee \(2010a,b, 2012a,b, 2013a,b,c\)](#), [Misra et al. \(2014\)](#) etc. for more such features, and [Mukherjee \(2017\)](#) for vertical tectonics. Narayan Bose and Soumyajit Mukherjee

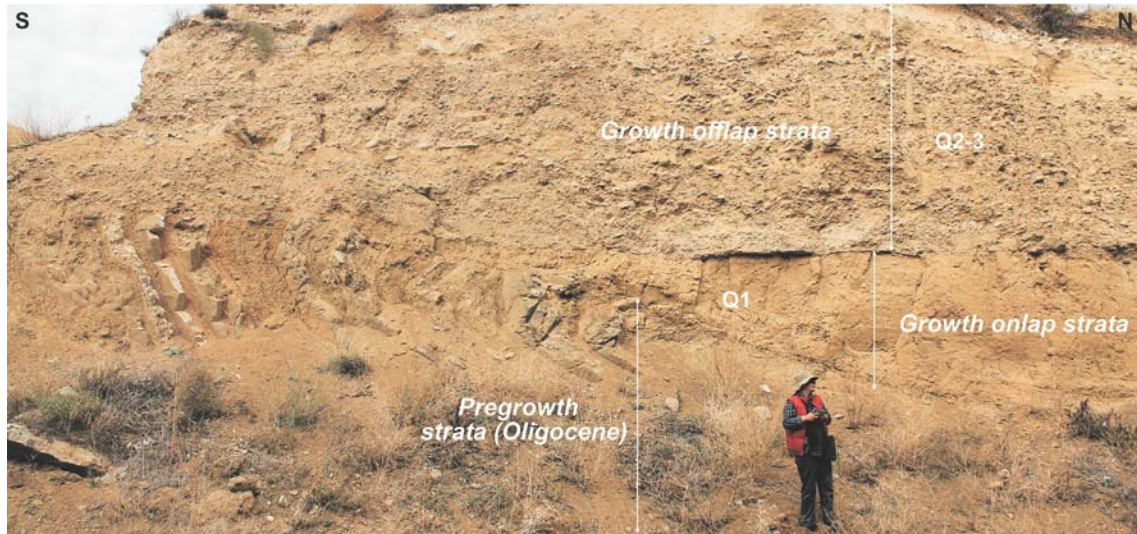


FIGURE 3.19 Fault-propagation fold and growth strata. The photograph of the fault-propagation fold shows the geometry of the hangingwall structure with the *syn*-folding growth stratal sequence. The genesis of the fold is related to the out-of-syncline thrust within the Ormoiani syncline (Alania et al., 2017). Pregrowth Oligocene strata are overlain by Quaternary alluvial fan gravels, sands, and clays. The growth unconformity of the back-limb shows flat clays unconformably on top of Oligocene sandstone and shale beds. The growth strata geometry of the growth fold is related to the progressive limb-rotation model (Hardy and Poblet, 1994). Location: 41°46.75' N, 44°041.646' E. Near Tbilisi, frontal part of the eastern Achara-Trialeti fold-and-thrust belt, Georgia. Victor Alania, Onise Enukidze, and Nino Sadradze



FIGURE 3.20 Breakthrough fault-propagation fold. The fold is developed within limestones of the Upper Cretaceous age. This is similar to the model described by Suppe and Medwedeff (1990). Location: 42°10.529' N, 44° 40.614' E. Near v. Ananuri, South zone of the Greater Caucasus orogen. Victor Alania



FIGURE 3.21 Double wedge thrust. The thrust system is developed within the turbidites and shales of the Upper Eocene age. Location: $41^{\circ}39.531'N$; $44^{\circ}36.607'E$. Near v. Kiketi, central part of the eastern Achara-Trialeti fold-and-thrust belt, Georgia. **Victor Alania and Nino Sadradze**



FIGURE 3.22 Tri-shear fault-propagation fold. The fold is developed within limestone rocks of the Upper Cretaceous age. Location: $41^{\circ}50'14.34''N$, $44^{\circ}34'24.39''E$. Frontal part of the eastern Achara-Trialeti fold-and-thrust belt, Near v. Kavtiskhevi, Georgia. **Victor Alania, Zoé Candaux, Onise Enekidze, and Nino Sadradze**



FIGURE 3.23 Normal fault. The fault is developed within the Oligocene strata. The formation of normal faults in the Oligocene time probably should be related to the thermal sag of the Achara-Trialeti extensional basin (Alania et al., 2020). Location: 41°43'47.53"N, 44°44'23.81"E. Near Tbilisi, Georgia. **Victor Alania and Onise Enukidze**



FIGURE 3.24 Normal fault within a thrust-sheet. The fault is developed within the Upper Cretaceous strata of the Dzegvi-Kavtiskhevi thrust sheet. Location: 41°51'11.17"N, 44°17'22.93"E. Near v. Kavtiskhevi, frontal part of the eastern Achara-Trialeti fold-and-thrust belt. **Victor Alania, Zoé Candaux, Rusudan Chagelishvili, and Nino Sadradze**

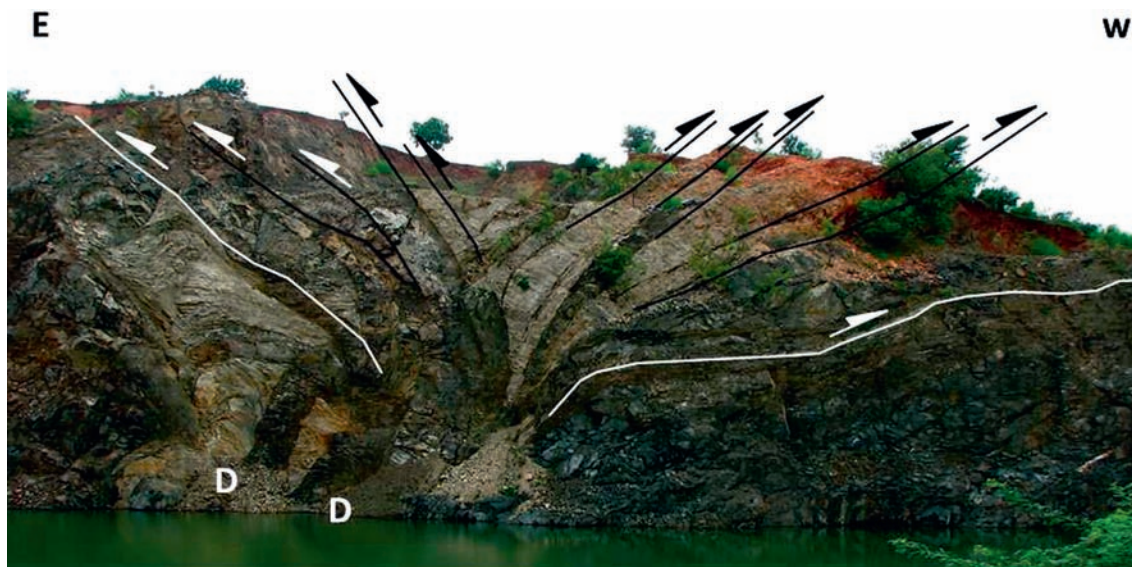


FIGURE 3.25 A rare positive flower structure in the Precambrian quartzites (white) and metabasalts (black) in an abandoned quarry near Rajupalem, Andhra Pradesh, India. The thrust verging toward W (white line) also shows a ramp-flat-ramp geometry. There are two dykes indicated by “D.” Transpression probably during Pan-African orogeny (El-Wahed and Kamha, 2010). Refer to Babar et al. (2017) and Misra and Mukherjee (2017), for other dyke-related deformation issues. In Dasgupta and Mukherjee (2017), figure A5 presents a probable flower structure. Width of view: ~150 m. Location: 14°0’37.96”N, 79°50’9.74”E. Achyuta Ayan Misra

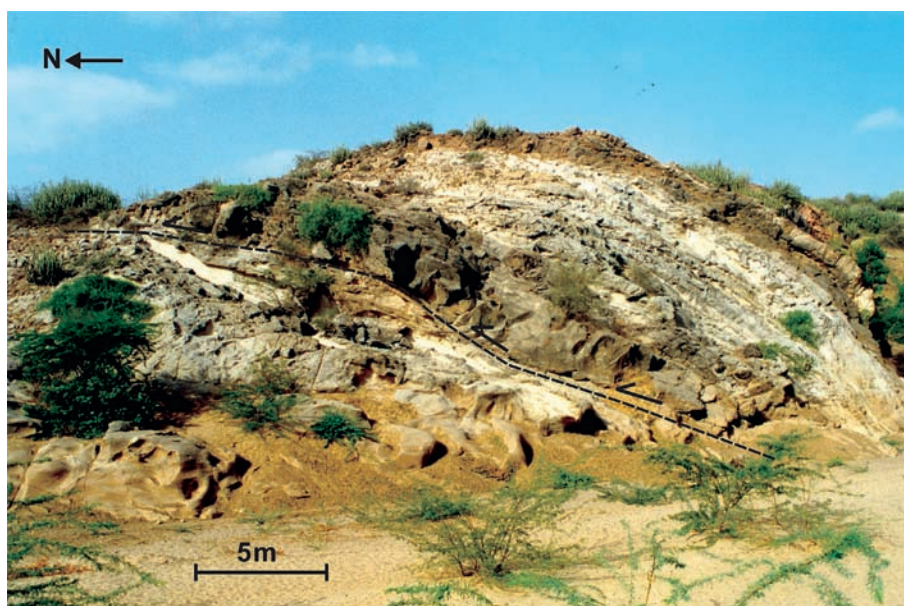


FIGURE 3.26 Curvilinear fault-bend folding of the Bhuj Sandstone at Lakhond in the Kachchh district of Gujarat, India. The river that flows north has incised the exposure. Folding of the E-W striking beds is on account of the contraction (structural inversion) phase experienced by the Kachchh basin. George Mathew and Dnyanada Salvi



FIGURE 3.27 Fault-propagation fold. Fault-propagation folds are folds forming ahead of a propagating fault tip. Generally, thrust fault breaks through the fault-propagation fold if these faults keep accumulating displacement. This results in drag folds along the fault, which can be used to determine fault kinematics. An example from the Valsugana Thrust cutting Lower Jurassic carbonate rocks belonging to the Calcarei Grigi Group (Southern Alps, Italy). Thick white lines highlight thrust trace; instead, thin white lines mark bedding. Photo taken from Monte Pizzon (Agordino, Dolomites). **Simone Masoch**

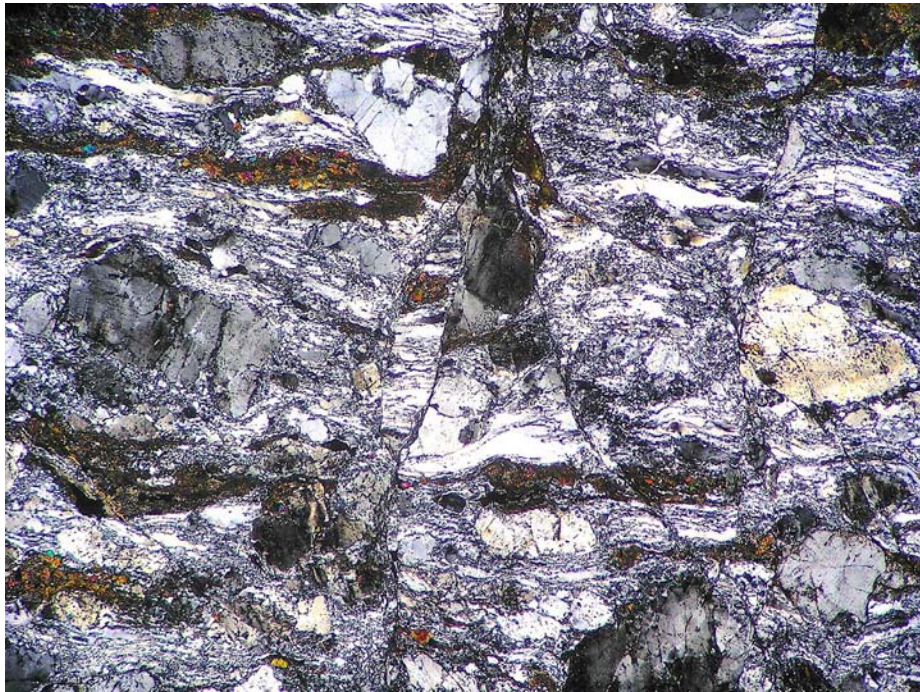


FIGURE 3.28 Semi-brittle microfaults. Cross-polarized thin section of mylonite from the Hayesville Fault in southwestern North Carolina. 5 mm horizontal dimension. Porphyroclasts and quartz ribbons are truncated with some recognizable offset-transposition along semibrittle microfaults. **Jeff Greenberg**

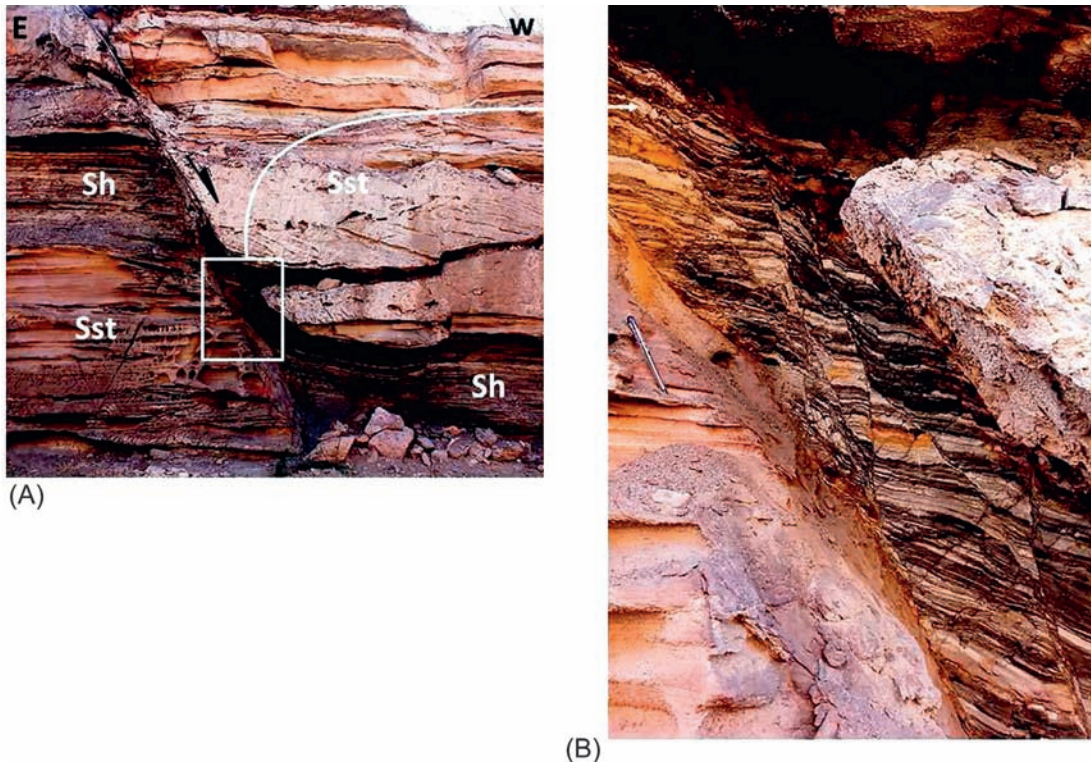


FIGURE 3.29 (a) A normal fault and (b) zoomed in showing the smear in the fault zone/overlap zone in a sand-shale sequence in the Cretaceous Bhuj Formation near Kodki village, E of Bhuj, Gujarat, India. The shale trapped and smeared in the overlap zone is characterized by smaller faults. Location: 23°14'37.59"N, 69°35'0.07"E. Achyuta Ayan Misra



FIGURE 3.30 Coalescing thrust-related folds. Coalescing thrust-related folds along the salient apex zone of the curve-shaped Gran Sasso thrust system. The Gran Sasso is a NE-verging curved thrust system in the outer Central Apennines of Italy. This mountain range exhibits remarkable morphological relief associated with a strong structural elevation (Calamita et al., 2004; Cardello and Doglioni, 2014). Thrust-related folding involved the Triassic-Miocene platform and slope-to-basin carbonate successions, which are juxtaposed over Messinian-Lower Pliocene foredeep siliciclastic deposits (Ghisetti and Vezzani, 1991). The photo portrays a spectacular view of the salient apex zone, exposed on the Mt. Camicia north face, where the upper thrust ramp surface and the related fault-bend fold are antiformally folded and overturned by a fault-propagation fold developed in the footwall. The footwall fault-propagation fold is tight and exhibits a subhorizontal E-W-trending axial surface involving the Upper Jurassic-Cretaceous succession. The coalescing interference fold pattern is therefore represented by the upper hanging wall fold-bend fold folded by the lower footwall fault-propagation fold in the salient apex zone, suggesting a synchronous in-sequence emplacement between fault-bending and fault-propagation folding (Pace and Calamita, 2015). Location: 2 km west of the Castelli village province of Teramo (42°28'6.83"N 13°43'7.62"E WGS84). Paolo Pace and F. Calamita

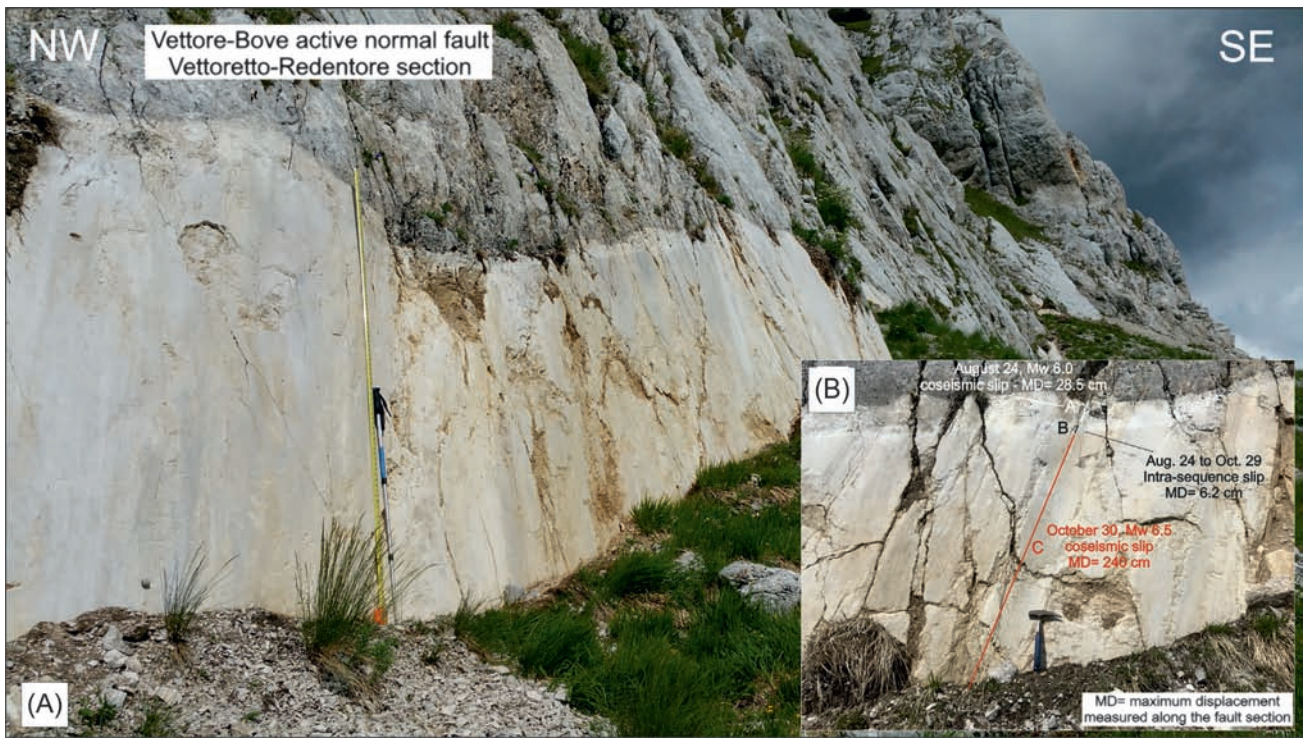


FIGURE 3.31 Field evidence of subsequent slip events of the 2016 Central Italy seismic sequence. (a) Image of the VBF fault scarp near the “Scoglio dell’Aquila” site showing the “composite free face” that was exhumed during the entire seismic sequence, Mt Vettore–Mt Bove normal Fault (VBF, Italy). The free face consists of three adjacent bands (photo b) produced by different exposure periods of the unearthened rocks: (A) upper band, showing the coseismic slip caused by the Aug. 24, Mw 6.0 foreshock; (B) intermediate thin and whitish band showing the intrasequence after-slip that occurred between Aug. 24 and Oct. 29, 2016; (C) Lower thicker band showing coseismic deformation caused by the Mw 6.5 mainshock. Field mapping performed on Oct. 27–28, 2016, showed that this segment of the VBF was not reactivated at the surface by Oct. 26 Mw 5.9 earthquake, allowing to exclude that the band B represents coseismic slip. A temporal constraint to the bands was provided by permanent strain-markers drawn on the fault planes during field surveys to record the position of the topography at the fault hanging wall (site location and details in [Brozzetti et al., 2019](#)). **Francesco Brozzetti, D. Cirillo, F. Ferrarini and G. Lavecchia**



FIGURE 3.32 Antiformal stack duplex, Lesser Himalayan rocks exposed in the NE syntaxial zone of Arunachal Himalaya, India. Arrows represent thrust slices. The exposed duplex lies within a smaller antiformal structure toward the foreland bound at its N by Miri Thrust and S by the Main Boundary Thrust. The major crustal scale antiformal, called the “Siang Antiform,” bound this smaller antiformal that is represented by the Gondwana Group of rocks. Location: 28°8′57.85″N, 95°13′23.41″E. Scale: Person (circled) height: 170 cm. **George Mathew and Dnyanada Salvi**



FIGURE 3.33 Brittle deformation of the Mykonos Detachment. Field view of the fault core of the Mykonos Detachment belonging to the North Cycladic Detachment System (Cape Evros, Mykonos Island, Greece). The main detachment fault plane gently dips toward the bottom left (NE), and bears down-dip slickenside striae on the glossy surface. In the background, up to a m-thick fault gouge is marked by a very fine-grained yellowish-greenish phyllosilicate-rich matrix wrapping cm to 30cm-sized sigmoid clasts of mylonite metabasite (dark green) and granitoid (light gray), indicating a top-to-left (north) shear. In the uppermost portion of the photograph is the basal contact of the gouge with the overlying conglomerates of the Miocene Sedimentary Unit. Width of view: ~ 2.5 m. Coordinates: 37°28'26.82"N; 25°27'25.23"E. **Giovanni Musumeci, Raffaele Gazzola, and Chiara Frassi**



FIGURE 3.34 Fault breccia. Fault breccia along with a dense network of veins (mainly calcite) in a weathered section in the Deccan trap. This shear zone is 4.5 to 5 m in width. Here, open fractures and joints later on were filled by the secondary material such as calcite, generating a dense network of veins. Angular and sharp lithoclasts of basaltic rock occur, which suggests that those can be megabreccia. Southeastern Saurashtra, Gujarat, western India, near a tributary of the Shetrunji river. **Tarun Solanki**



FIGURE 3.35 Uniform set of small-scale faults in a confined interval of parallel laminated lacustrine micrites. Eocene Green River Formation, Fossil Basin, Wyoming, United States. Faults die out both upward and downward, and a deformed interval is bound by dark-brown (higher organic content), undisturbed laminated sediments. This indicates that deformation only affected the rheologically susceptible sediments at the time. Slight changes in the thickness of the overlying sediments might indicate that deformation occurred before the deposition of the overlying sediments. The light colour of the faulted sediments indicates low organic content, which might be responsible for contrasting lithological properties, and the formation of brittle deformation structures in the deposits. Faults might be related either to compaction-related extensional forces or seismic shocks. Reproduced from Figure 6 of [Törő et al. \(2013\)](#). Balázs Törő, Brian R. Pratt, and Sudipta Dasgupta



FIGURE 3.36 A synsedimentary normal fault produced by the gravitational effect. Mudstone and graywacke. From the W side of the Rakhavdav complex, Udaipur district, Rajasthan, India. Moloy Sarkar



FIGURE 3.37 Field photographs (a) and (b) demonstrate the range in thickness that can be observed in pseudotachylytes (PSTs). Both images are of high-pressure (1.8–2.6 GPa) PST fault veins from the Schistes Lustres Complex, Cape Corse, Corsica ([Austrheim and Andersen, 2004](#); [Andersen and Austrheim, 2006](#); [Ravna et al., 2010](#)) (a) Shows an ultramafic PST vein approximately 35 cm thick hosted by peridotite wall rock. (b) Shows a much thinner fault vein (~2 mm thick) from the same area; it is hosted by a blueschist facies metagabbro wall rock ([Andersen and Austrheim, 2006](#)). Top-to-right shear sense displayed. **Natalie Deseta**



FIGURE 3.38 Sheared dyke. Ductile deformation observed in N–S oriented dyke due to the presence of an E–W trending dextral strike slip fault into the Shetrunji River basin, Saurashtra, Gujarat state, western India. **Tarun Solanki**



FIGURE 3.39 Meso-scale fault. Meso-scale fault in a boulder, Anbar Village, Peshawar Basin, Pakistan. **Muhammad Awais**



FIGURE 3.40 Drag folding related with faulting. Mesoscopic scale S-shaped drag folds and fault in the Paleocene Patala Formation, Kala-Chitta Range, Pakistan. **Muhammad Awais**



FIGURE 3.41 Centimeter-scale top-to-NW brittle reverse fault within a quartzite clast. The fault zone is ~1 cm thick. Mohand, Siwalik Himalaya, Roorkee–Dehradun transect, Uttarakhand, India. [Srivastava and John \(1999\)](#) reported the same shear sense from sandstones from this terrain. **Tuhin Biswas**



FIGURE 3.42 Fascinating development of Y- and P-brittle shear planes within a single quartzite clast within a sandy matrix. Top-to-NNE (down) brittle shear indicated by small sigmoid P-planes. Near Mohand, Siwalik Himalaya, Roorkee–Dehradun transect, Uttarakhand, India. **Tuhin Biswas**



FIGURE 3.43 Plan view of a sinistral strike-slip faulted pebble. SSW geographical direction is toward the right. $30^{\circ}14.027'N$, $77^{\circ}56.871'E$. Near Mohand, Roorkee–Dehradun transect, India. If one can locate points on the faulted clasts that were in contact before faulting, one can apply the fault slip model of Mukherjee (2019). See Dutta et al. (2019) for the tectonics of this region. **Dripta Dutta**



FIGURE 3.44 Subvertical fault plane cuts across the quartzite pebble within a conglomerate bed, Siwalik Supergroup. Top-to-SW (up) shear. Tiny slip visible for the clast at the right side to the pen. Latitude: $30.2339^{\circ}N$, Longitude: $77.9438^{\circ}E$. Near Mohand, Roorkee–Dehradun transect, India. **Dripta Dutta**



FIGURE 3.45 SE-dipping subparallel curved fault planes within a single quartzite pebble. Siwalik Supergroup conglomerate. Long axis of the pebble: 14 cm. Near Mohand, Roorkee–Dehradun transect, Uttarakhand, India. Consult [Mukherjee and Agarwal \(2018\)](#), [Mukherjee and Tayade \(2019\)](#) and [Mukherjee and Chakraborty \(2020\)](#) for the kinematics of the curved faults. **Dripta Dutta**



FIGURE 3.46 A N-dipping subvertical fault plane cut across quartzite pebble. Siwalik Supergroup conglomerate. Such a faulting indicates possibly an isostatic adjustment (such as [Mukherjee, 2017](#)). Top-to-S (up) brittle shear. Near Mohand, Roorkee–Dehradun transect. 30°14.038'N, 77°56.9'E. Uttarakhand, India. **Dripta Dutta**

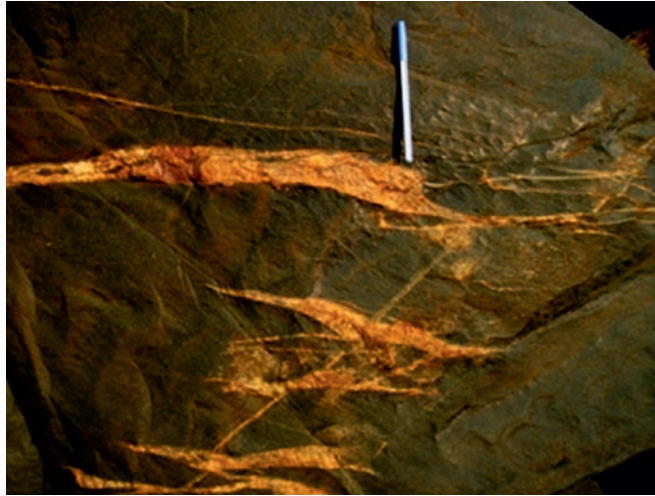


FIGURE 3.47 En echelon veins. The quartz vein appears as a set of short, parallel, mineral-filled lenses within the dolerite dyke. This structure is useful in determining slip sense (Rothery, 1988). Ghatshila, Jharkhand, India. Sanjukta De



FIGURE 3.48 Along-dip segmented normal fault and fault-related fold in Jurassic sequence. Three fault segments dissect the condensed pelagic Jurassic sequence: one single planar plane in the lower part, two in the Tölgyhát Formation, one above the lower segment and one to the left (Sasvári et al., 2009). This disposition is typical for along-dip segmented normal faults (Childs et al., 1996; Rykkelid and Fossen, 2002). Between segments, the deformation was accommodated in the thin marlstone unit. The upper marlstone layers show folding between fault segments. The lower gray clay layers are boudinaged/pinched along the lower fault segment. Note that the hanging wall part is present in the shadow of the marlstone layers. This different behavior could occur because of the contrasting rheology of the deforming rocks. The segmented fault can have a Middle Jurassic age (Bathonian, 168–166 Ma) because at least one upper segment is covered by Middle to Late Jurassic (Callovian–Oxfordian) radiolarite beds (Fodor et al., 2013). This early formation time matches the folding of the Toarcian unit, which deformed before complete diagenetic cementation, still in a semiplastic stage. The E-W trending fault accommodated a minor extension of a downbending side of a foreland basin opposite to the growing Dinaridic orogen (Fodor et al., 2013). Blue rucksack: ~50 cm. Early Jurassic limestone, late Early Jurassic (Toarcian) marlstone-claystone, Middle Jurassic nodular limestone of Tölgyhát Formation. Location: Tölgyhát quarry, Lábatlan village, Gerecse Hills, Hungary. Coordinates: 47°43'20.92"N, 18°30' 45.80"E. László Fodor

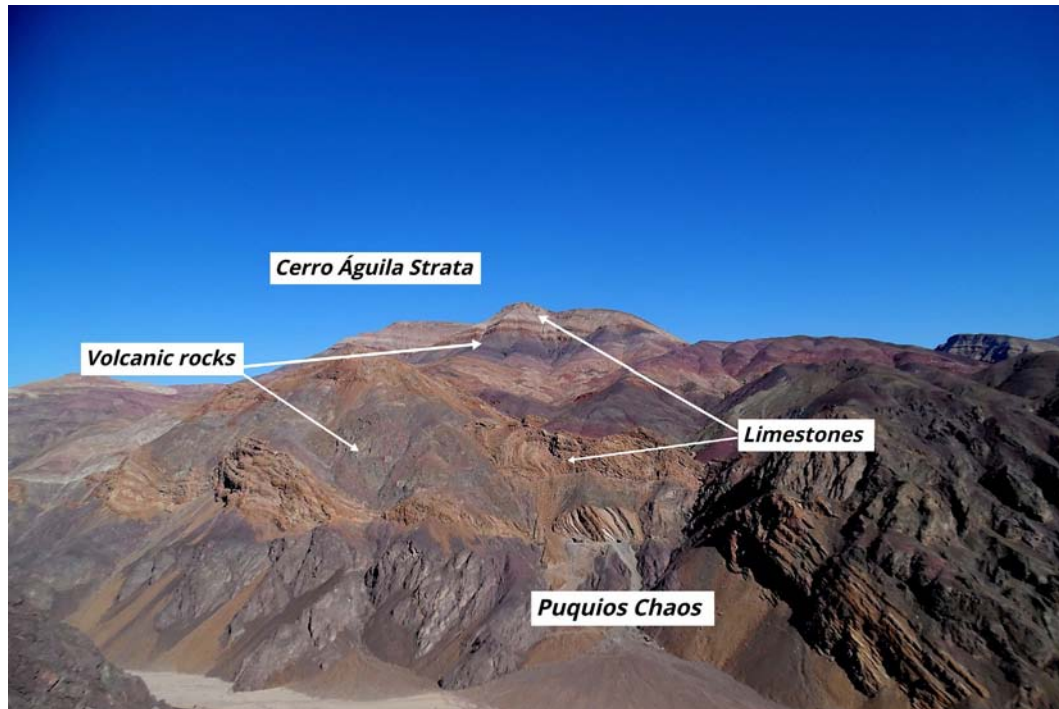


FIGURE 3.49 Boudinaged, folded, and faulted limestones blocks. View from the 31CH in Quebrada Paipote to the northeast Copiapó (Chile), the boudinaged, folded, and faulted limestone blocks of the Puquios chaos stand out at the forefront. At the top of the hill, the allochthon IV shows the original succession of volcanic rocks at the base and limestones toward the top that constitute the Cerro Águila strata. Reproduced from [Reinoso et al. \(2020\)](#). Felipe Reinoso



FIGURE 3.50 Boudinaged limestone block. View of the blocks of bioclastic limestones that appear as large boudined bodies in a volcanic matrix. The Puquios Chaos can be defined as a mélangé unit according to the mesoscopic mixing between calcareous and volcanic units. Reproduced from [Reinoso et al. \(2020\)](#). Felipe Reinoso

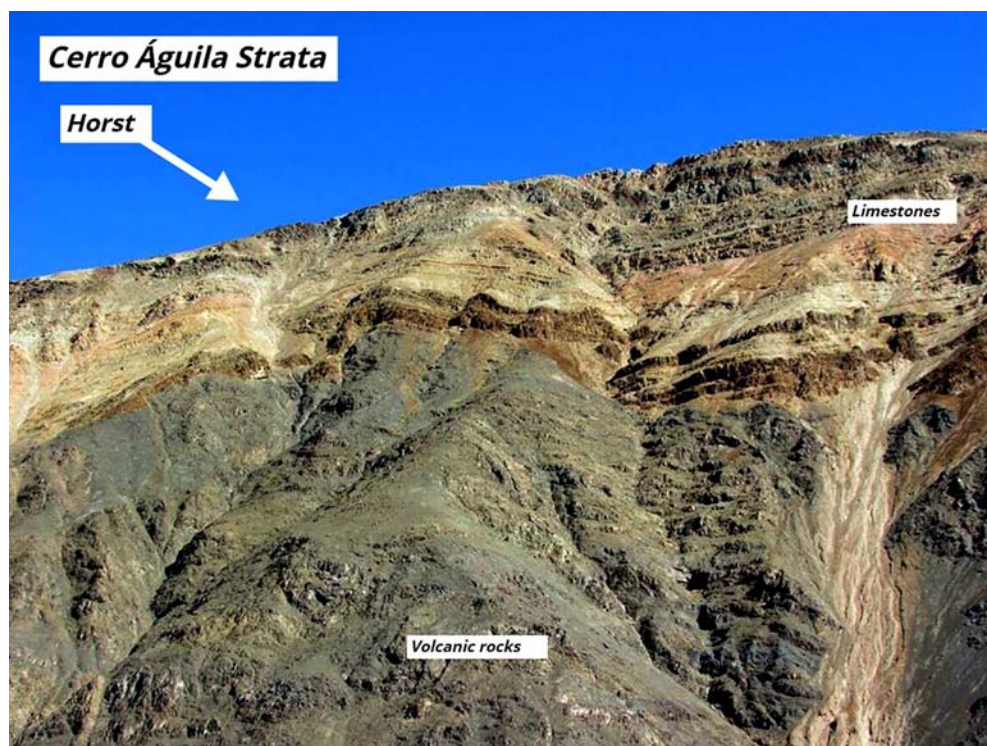


FIGURE 3.51 Horst-graben structure. N-S view shows the Horsts and grabens in the Cerro Águila strata limited by extensional structures rooted in the main Puquios detachment normal faults (dipping ~60 degrees) with fewer low-angle detachments that present larger displacement. Reproduced from [Reinoso et al. \(2020\)](#). **Felipe Reinoso**

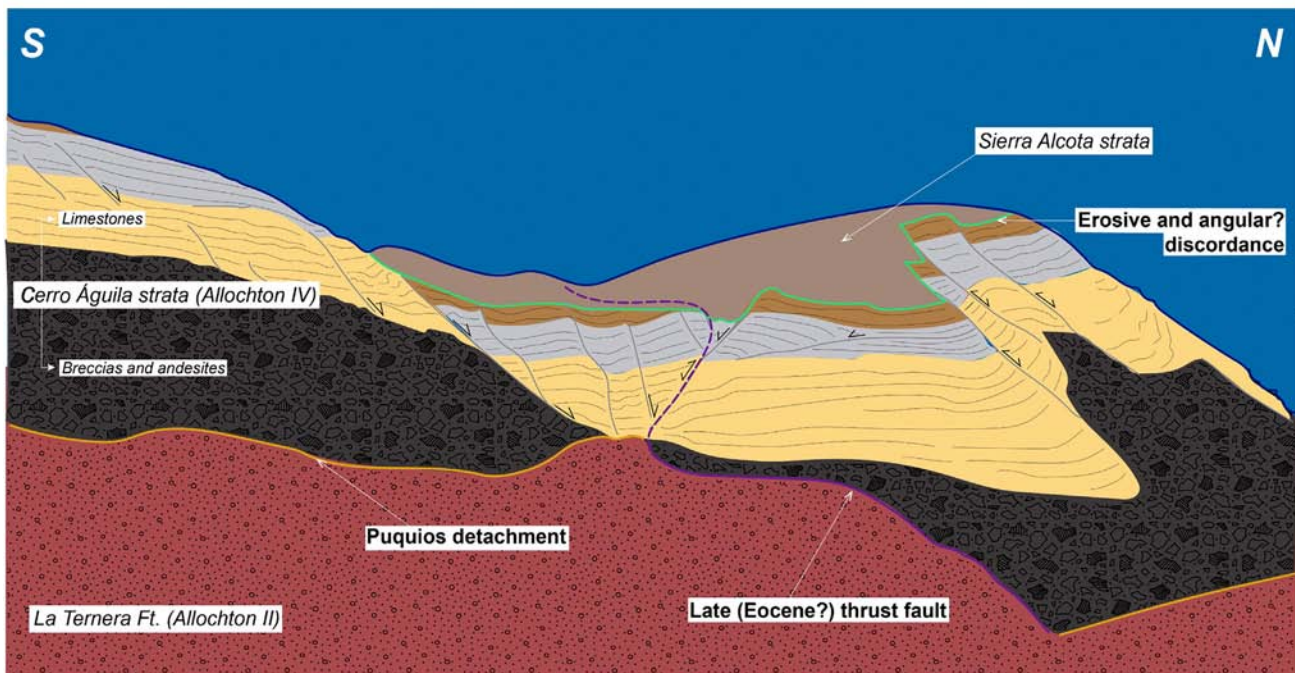


FIGURE 3.52 Synthetic and antithetic normal faults. N–S view of the Cerro Águila strata showing a set of synthetic and antithetic normal faults that affected the original succession. This extensional fault system in the Allochthon IV is related with descriptions of regional extensional structures in the Sierra de Fraga-Puquios (Atacama region, northern Chile). Reproduced from [Reinoso et al. \(2020\)](#). **Felipe Reinoso**

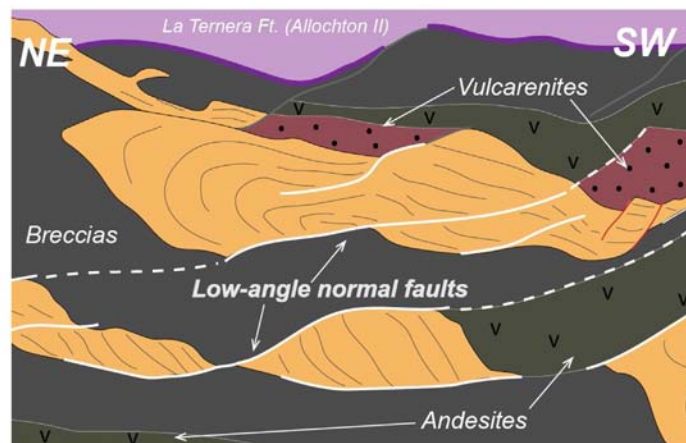


FIGURE 3.53 The Puquios tectonic unit. Front view of the Puquios tectonic unit in the Precordillera of the Atacama region ($\sim 27^\circ\text{S}$), which is considered by several authors as a unique tectonic unit in the world and has been related to the activity of low-angle detachments that characterized the extensional tectonics in the middle of the Cretaceous. **Felipe Reinoso**



FIGURE 3.54 Faulted vein. Rock type: Orthogneiss. Structure: Fault. Location: São Luis dos Campos Belos, Arenópolis Magmatic Arc, Western Goiás State, Brazil. Facies: Intermediate amphibolites. Description: Granite vein (aplite) faulted during reactivation of orthogneissic banding. Note how the displacement varies between the different gneissic bands. **Marco Martins-Ferreira**



FIGURE 3.55 Top-to-SW brittle sheared or reverse faulted sandstone. Deciphered from slip of brown bedding planes as markers. Near the pen marker, one more thinner marker set seen. Mohand, Siwalik Himalaya, Roorkee–Dehradun transect, Uttarakhand, India. **Tuhin Biswas**

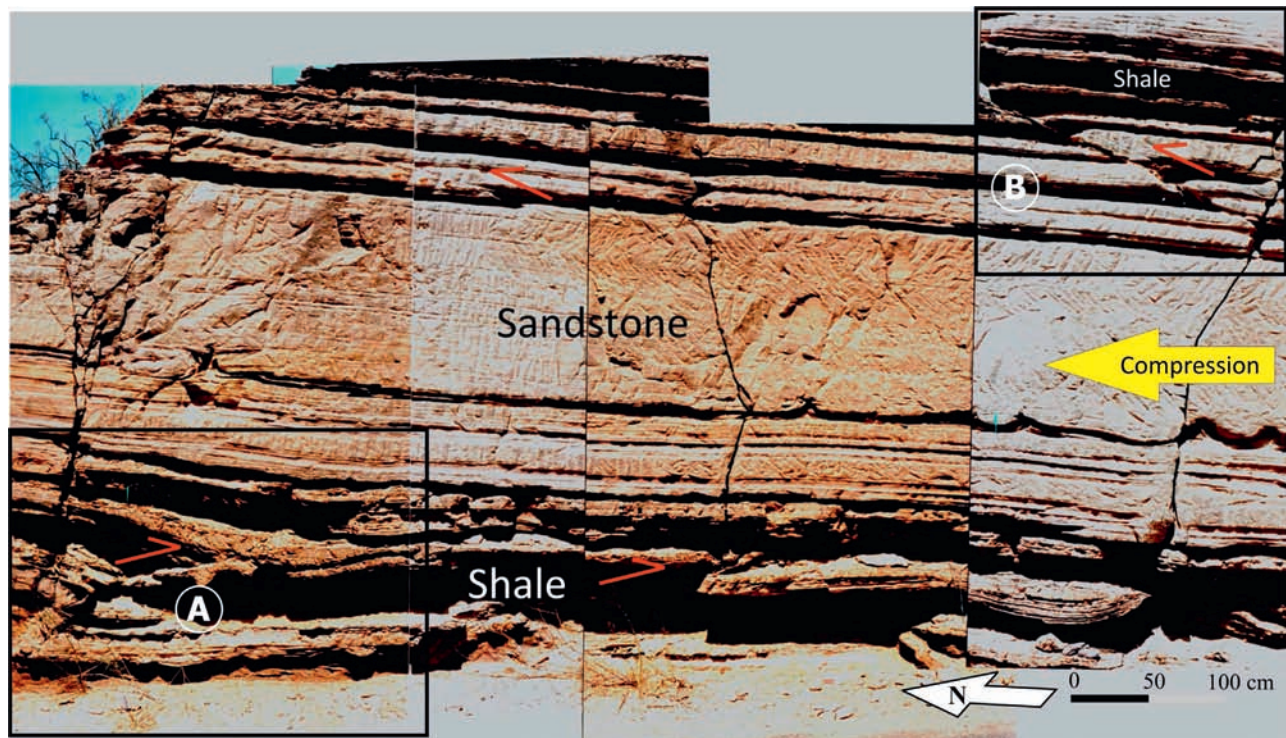


FIGURE 3.56 Kachchh Peninsula in Western India constitutes an active “fold-and-thrust” tectonic belt ([Karanth and Gadhavi, 2007](#)). A curious structural feature is recorded in a road cutting near Nadapa (Latitude: 23°19'N Longitude: 69°52'E), about 5 km north of Bhuj in a lithologically heterogeneous succession of a thick bed of sandstone overlain as well as underlain by thin beds of shale belonging to the Jhuran Formation (Upper Jurassic). The pile of sediments subjected to compression exhibits the development of folding and faulting in ductile shale layers on either side of the competent sandstone with an opposite sense of vergence of folding and displacement. While the shale layers below the thick sandstone bed show northerly verging folds and north dipping fault planes, the ductile layers above the sandstone reveal an opposite sense of folding and faulting. Based on [Teisseyre's analysis \(1959\)](#), analogous movements have been suggested by [Jaroszewski \(1984\)](#). Jaroszewski further strengthens his views quoting the results of the experiments conducted by B. Willis and R. Willis. Along with several structural features such as low-angle reverse faults, fault-bend folds, bending moment faults, and drainage reversals, the present described feature supplements northerly directed compressive movements giving rise to a “fold-and-thrust” tectonic belt in the region of Kachchh. An opposite sense of relative displacements in thin incompetent-shale layers on either side of a sandstone bed. **R.V. Karanth and M.S. Gadhavi**



FIGURE 3.57 Brittle-ductile composite thrust shear zone. Brittle-ductile composite thrust shear zone fabric developed along a lateral thrust ramp of the Coscerno-Rivodutri Thrust (Tavarnelli, 1994; Barchi and Lemmi, 1996) in the Umbria-Marche Apennines of Central Italy. Along the Coscerno-Rivodutri Thrust, Lower Jurassic massive platform carbonates of the Calcare Massiccio Formation emplace onto Upper Eocene–Oligocene marls interbedded with limestone and calcarenite horizons of the Scaglia Cinerea Formation. Syn-kinematic deformation and shearing along the Coscerno-Rivodutri Thrust occurred at a shallow crustal depth (2–3 km) under nonmetamorphic conditions ($T < 100^{\circ}\text{C}$), as described by Tesei et al. (2013). The snap portrays a remarkably well-developed, cm to mm-spaced pressure-solution cleavage (S) that pervasively affects the Scaglia Cinerea Formation in the footwall of the considered lateral thrust ramp of the Coscerno-Rivodutri Thrust. The upper thrust surface and the S-fabrics developed within the lateral thrust ramp are displaced by foreland-dipping, mesoscopic normal faults. These faults are listric, producing a high-angle cut-off when propagating within the massive Lower Jurassic Calcare Massiccio Formation in the thrust hanging wall, and rapidly flatten over a footwall splay thrust within the marly Eocene–Oligocene Scaglia Cinerea detachment layer located in the uppermost part of the thrust footwall. Meso-scale pervasive, closely spaced folded S-cleavage surfaces with axial planes slightly dipping toward the foreland are developed in the footwall of the listric normal faults. The composite shear zone fabric is interpreted to be related to *syn*-to-late-thrusting normal faulting overprinting the early thrust and related thrust shear zone within a foreland-directed gravitational collapse (Pace et al., 2017). Location: 2 km west of the Monteleone di Spoleto town, province of Perugia ($42^{\circ}38'54.16''\text{N}$ $12^{\circ}55'28.39''\text{E}$ WGS84). Width of view is approximately 170 cm. **Paolo Pace, E. Tavarnelli, and F. Calamita**



FIGURE 3.58 Tension gashes. Right-lateral en-échelon tension gashes of quartz. They developed in a shear zone within a brittle-ductile deformation system. These veins are hosted within an Ediacaran andesite rock. This picture was taken in the Tassafte mining area, Saghro inlier, eastern Anti-Atlas, Morocco (Yajoui, 2019). **Zakarya Yajoui**



FIGURE 3.59 Superposed tectonics. Superimposed tectonics: the first phase (yellow) demonstrates sinistral strike-slip structures infilled by the first generation of quartz; the second phase (orange) represents the second generation of quartz that has infilling sigmoidal structures in dextral movement; and the third phase (dark brown) is characterized by the deposit of oxides and carbonates in conjugated normal faults. These structures were observed in the late Proterozoic turbidite, Skoura inlier, Central High Atlas, Morocco. Photographer: Karaoui Amar (Moulay Ismail University). We invite the reader to send us any alternate logical interpretation! **Zakarya Yaioui**



FIGURE 3.60 En-échelon tension gash. Triassic formation, Eastern High Atlas, Morocco. Photographed by Prof. Karaoui Brahim (Moulay Ismail University). Photographed by Prof. Karaoui Brahim (Moulay Ismail University). **Zakarya Yaioui**

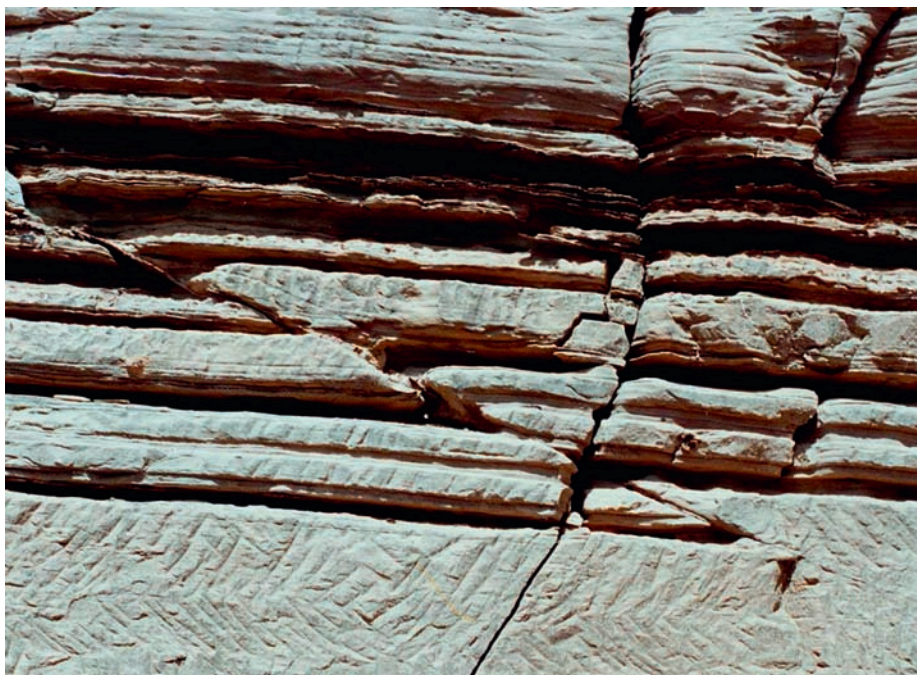


FIGURE 3.61 Zoomed part from a portion of Fig. 3.56. R.V. Karanth, M.S. Gadhavi



FIGURE 3.62 Zoomed part from a portion of Fig. 3.56. R.V. Karanth, M.S. Gadhavi



FIGURE 3.63 Imbricate thrusts possibly constitute an accretionary wedge. Siwalik Himalayan sandstone of Dhokpathan Formation. Bagh Rao nala section Haridwar district, Uttarakhand, India. Outcrop width ~ 200 cm. **Shailendra Singh**

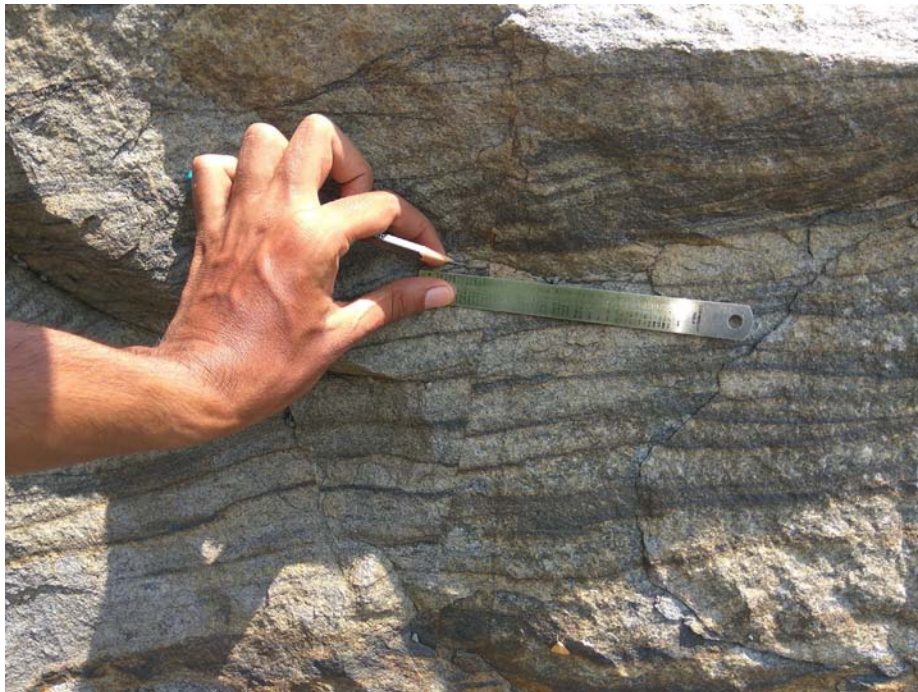


FIGURE 3.64 Reverse fault. High-dipping reverse faults in quartzite. Rock Garden, Malvan, Maharashtra, India. **Namrata Soreng**

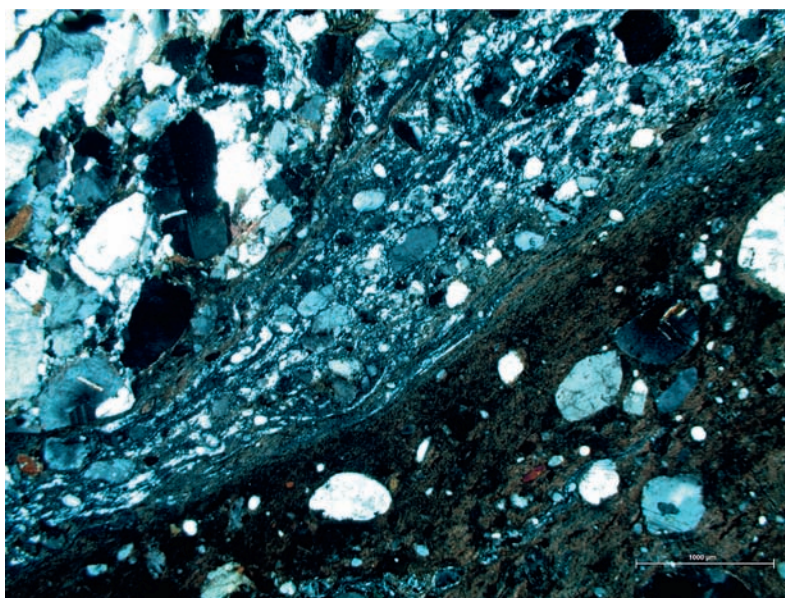


FIGURE 3.65 Granodiorite of the Eagle Wash Intrusive Complex with mylonitic to cataclastic shear zones formed by rapid exhumation and cooling during detachment faulting (Pease and Argent, 1999; Pease et al., 1999). Note the fine-grained biotite matrix (lower right corner) grades into mylonitic ductile shear as the original igneous fabric of the granodiorite is approached at the upper left. The dynamic recrystallization of quartz in the mylonitic shear zone is indicated by fine-grained ribbons, undulose extinction, and parallel and elongate subgrains; it indicates $> 350^{\circ}\text{C}$ temperature (Simpson, 1985; Hirth and Tullis, 1994). Sacramento Mountains, California, Southwest United States. Coordinates: N3853884, E710016. **Victoria Pease**



FIGURE 3.66 En-echelon vein. Rock type: Ankerite in calc-phyllite. Structure: En-echelon vein. Location: Road cut from Alto Paraíso de Goiás to Colinas do Sul, Goiás state, Brazil. Facies: Low to intermediate greenschist. Description: En-echelon veins filled by ankerite mineral (calcium, iron, magnesium, manganese carbonate) and rotated by right-lateral shear sense in calc-phyllite lens from the Rosário Formation, Traíras Group, Veadeiros Supergroup (Martins-Ferreira et al., 2018a,b). **Marco Martins-Ferreira**

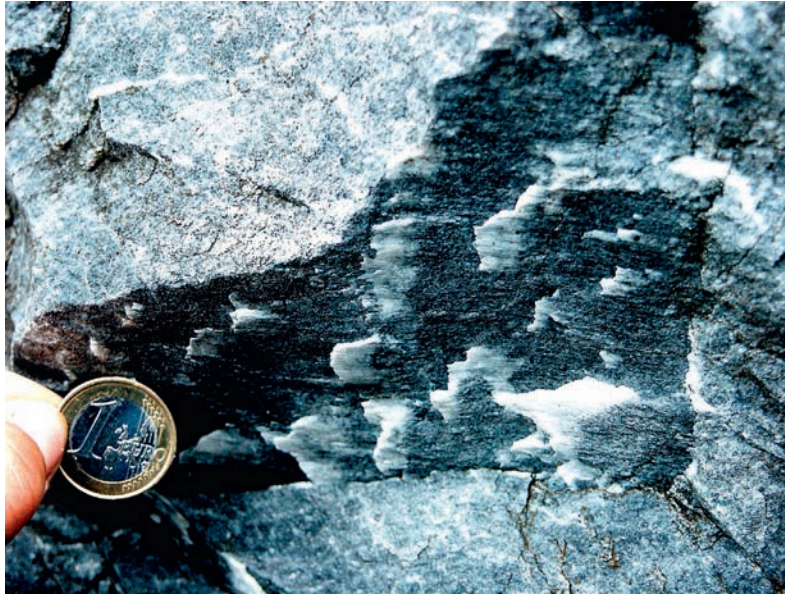


FIGURE 3.67 Brittle tectonics is a powerful tool for studying rock characteristics in the field. The results of a brittle deformation are tension or shear fractures and faults. On the basis of fracture orientation and indicators of the movements along the planes, it is possible to determine the stress conditions when fractures (re)activated. Kinematic indicators on the fault surface decode slip sense (Doblas, 1998). The mineral accretion calcite steps (mineral fibers displayed on the fault plane in the figure) are commonly used as slickenside indicators (Novakova, 2010). Here, the mineral steps identify right lateral movement along the fault plane. From an abandoned quarry near the village Vapenna, Rychleby Mts., Czech Republic, Europe, Devonian crystalline limestones of Branna Group. GPS coordinates: N50°16'41", E017°05'32". **Lucie Novakova**



FIGURE 3.68 A fault slickenside containing calcite slickenfibers. Depending on conditions during brittle deformation, mineral fibers such as calcite here may grow at a low angle on the rough fault planes on the facets that tend to open during slip. Mineral slickenfibers are asymmetric features that indicate slip sense: the congruous steps face toward the slip direction (Hancock, 1985; Petit, 1987). This picture specifically shows a synfolding fault slip (after Navabpour et al., 2007; with permission from Elsevier). The fault plane is subvertical and sinistrally offsets the inclined strata. The plunge of striae is less than the dip of the bedding plane, which is obvious at the bottom left. This indicates that the slip was synfolding after the strata tilted (Angelier, 1984). In this process, probably the fault plane also tilted. This is similar to a few flanking structure mechanisms (see Mukherjee, 2014a,b). The picture spans ~15 cm width, from a NW-SE-trending fault plane in the Zagros Mountains, within the Late Cretaceous marl of the Gurpi Formation, W of Shiraz, Iran. **Payman Navabpour**



FIGURE 3.69 A vertical fault with slickenside indicates oblique stylolites, also called slickolites. Depending on the conditions in brittle deformation, soluble rock minerals, such as carbonates in this case, may dissolve from rough fault planes from facets involved with contraction during the fault slip to create oblique stylolites as pressure-solution seams. Oblique stylolites are asymmetric features that reveal slip sense, with the picks of stylolites at a low angle to the fault plane pointing the slip direction as incongruous steps (Hancock, 1985). This picture shows a strike-slip fault slickenside with horizontal striae, specifically (personal observation). The fault plane is at a right angle to the horizontal bedding plane of the local strata and indicates a dextral slip. Picture spans ~15 cm width. Photographed by N. Kasch from an NNW-SSE-trending fault plane in the Thuringian Forest, within the mid-Triassic shell-bearing limestone of the Muschelkalk lithostratigraphic unit, Germany. **Payman Navabpour**



FIGURE 3.70 Picture presents a fault slickenside that contains striae of tectonic grooves. Tectonic grooves result from scratching of the fault plane by the opposite block. This creates linear tool marks. Depending on the conditions, tectonic grooves may indicate asymmetric geometries that can be used as kinematic indicators for slip sense (Hancock, 1985; Petit, 1987). This photograph shows crosscutting striae on a vertical fault slickenside (after Navabpour et al., 2007; with permission from Elsevier). The steeply dipping striae are subparallel to local bedding and are cut by the gently dipping striae, indicating a dextral shear. This feature shows successive striae on a fault plane (Angelier, 1984), indicating a progressive counter-clockwise rotation around a horizontal axis perpendicular to the fault plane. At places, a gradual change from the first to the second striae is obvious. The picture spans ~15 cm width, and is taken from an E-W-trending fault plane in the Zagros Mountains, within the Late Cretaceous marl of the Gurpi Formation, NW of Shiraz, Iran. **Payman Navabpour**



FIGURE 3.71 A fault slickenside presents striae of erosive tectonic tools. These tools are hard asperities of rock, such as garnet here, located between two faulted blocks or along a potential shear plane. During the slip on the fault plane, the asperities that are fixed within one block scratch the opposite block to create tectonic grooves, but at the same time they save rock materials behind them to leave linear rods in the direction of slip. As long as these asperities are preserved, the asymmetric geometry of the erosive tool marks can be used as a kinematic indicator for slip sense (Hancock, 1985; Petit, 1987). This picture indicates a normal fault slickenside, with downward linear rods of the saved rock materials behind the garnet grains. The picture spans ~15 cm width from an SE-dipping high-angle fault plane in the Zagros Mountains, within the Late Cretaceous marl of the Gurpi Formation, NW of Shiraz, Iran. Payman Navabpour

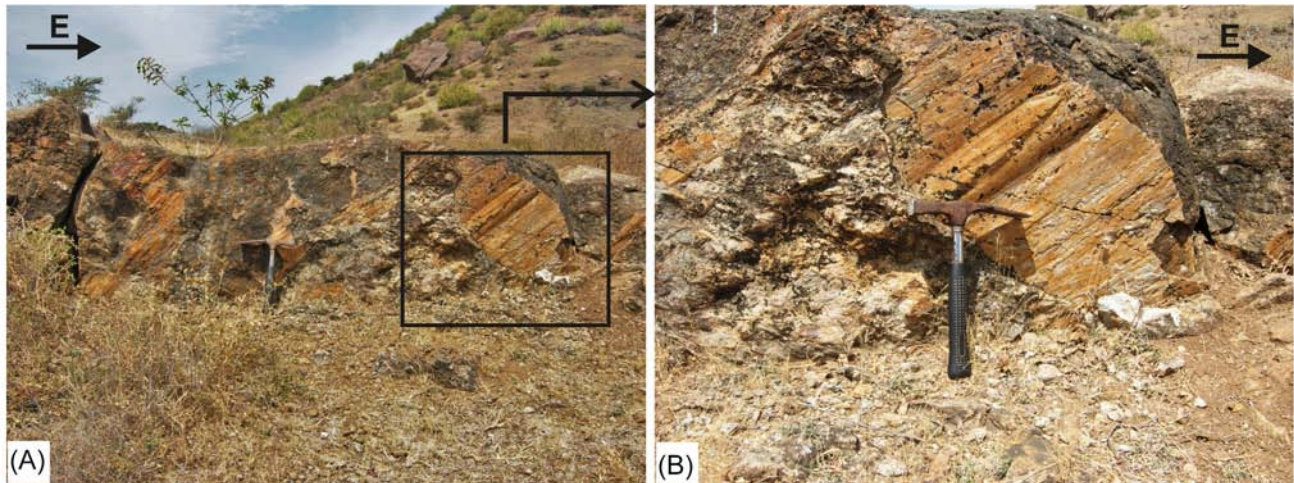


FIGURE 3.72 Brittle faults and lineations-1. The Katar Fault Plane showing prominent plunging/oblique striations, at Katar village near Rajula, Saurashtra, Gujarat, India. The vertical fault plane strikes E-W, dipping ~89 degrees. (a) The fault offsets the NE trending trapean ridge seen in the background. (b) Close-up image of the undulating fault plane surface with prominent slickensides. Hammer length 25 cm. Reproduced from Vanik et al. (2018). Naimisha Vanik, D. M. Maurya, Soumyajit Mukherjee, Mohammedharoon Shaikh, and L. S. Chamyal



FIGURE 3.73 Brittle shear planes-1. P- and Y- brittle shear planes trending NE on the horizontal plane of the highly fractured basaltic rock along the Katar Fault, Katar village, Saurashtra, Gujarat, India. P- planes form a sigmoid shape with mineral veins near the edges. The sigmoid shear planes merging with each other show sinistral slip. Pen length 14.6 cm. Reproduced from [Vanik et al. \(2018\)](#). Naimisha Vanik, D. M. Maurya, Soumyajit Mukherjee, Mohammedharoon Shaikh, and L. S. Chamyal



FIGURE 3.74 Brittle shear planes-2. Brittle shear zone indicated by Y- and P- planes observed on an NE-SW trending dyke near Katar village, Saurashtra, Gujarat. Multiple wavy and sigmoidal P-planes are observed on a vertical surface. Such brittle shear planes are observed all along the ridge near Katar village, Gujarat India. Hammer length 25 cm. Reproduced from [Vanik et al. \(2018\)](#). Naimisha Vanik, D. M. Maurya, Soumyajit Mukherjee, Mohammedharoon Shaikh, and L. S. Chamyal

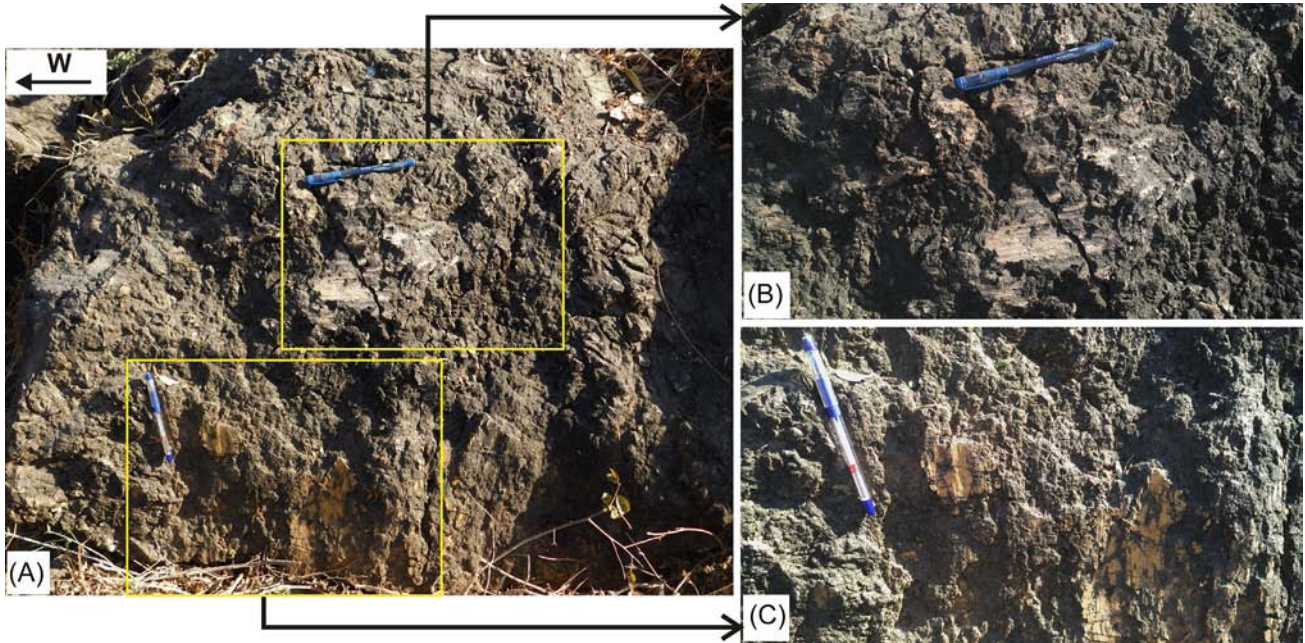


FIGURE 3.75 Reactivated brittle fault. Evidence of multiple reactivations along the Katar Fault, Katar village, Gujarat India. (a) Highly sheared brittle subvertical fault plane with two types of striations near Katar village, Saurashtra, Gujarat, India. (b) Close view of horizontal striations. (c) Close view of vertical striations. Pen length 14.6 cm. Reproduced from [Vanik et al. \(2018\)](#). Naimisha Vanik, D. M. Maurya, Soumyajit Mukherjee, Mohammedharoon Shaikh, and L. S. Chamyal



FIGURE 3.76 Listric fault. A curvi-planar fault plane with two trends 1 and 2 of oblique striations near Katar village, Saurashtra, Gujarat. The striations plunge and the trend is variable. Pen length 14.3 cm. Reproduced from [Vanik et al. \(2018\)](#). Naimisha Vanik, D. M. Maurya, Soumyajit Mukherjee, Mohammedharoon Shaikh, and L. S. Chamyal



FIGURE 3.77 Polished fault surface (slickenside or fault mirror), with well-developed striation that indicates vertical movement. At the top and left side of the image, a brown fault gauge is also visible. Sandstone from a complex volcano-sedimentary terrain (former island arch). Sredna Gora Mountain, West-Central Bulgaria. **Svetoslav Bontchev**



FIGURE 3.78 Slickensides on the fault plane of amphibolite gneiss. These lineations are developed nonuniformly over the fault plane. Maithon, West Bengal, India. Lineations related to fault planes are quite important in paleostress studies (e.g., [Shaikh et al. 2020](#)). **Ananya Basu**

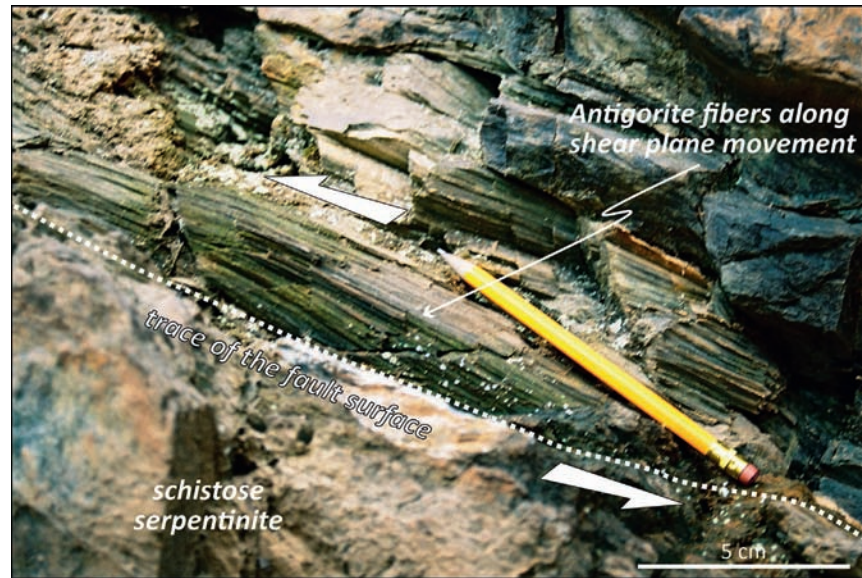


FIGURE 3.79 Serpentine slip fibers. Antigorite fibers grown along a reverse fault zone in serpentinite, Susa Valley, Western Alps, Italy. The fibrous morphology (i.e., the length is at least three times the width) and crystallization of the antigorite are due to fluid-assisted shearing. The fibrous minerals are disposed parallel to the shear surface and can be interpreted as slip fibers (Ramsay and Huber, 1983). The studied rocks are part of the Liguro-Piemontese oceanic domain of the Western Alps (Polino et al., 1990). These ophiolitic units have been involved in the subduction/exhumation cycle during orogenic construction (Agard et al., 2009) and they are affected by ductile-to-brittle deformation fabrics, locally hosting fibrous mineralization (e.g., Compagnoni and Groppo, 2006). Gianluca Vignaroli and Federico Rossetti



FIGURE 3.80 Lineation. Rock type: Orthogneiss. Structure: Lineation. Location: São Luis dos Campos Belos, Arenópolis Magmatic Arc, Western Goiás State, Brazil. Facies: Intermediate amphibolites. Description: Stretched quartz forming a mineral lineation (parallel to pencil) on leucocratic orthogneiss bands. Consult Doblas (1998) to classify this lineation. Marco Martins-Ferreira

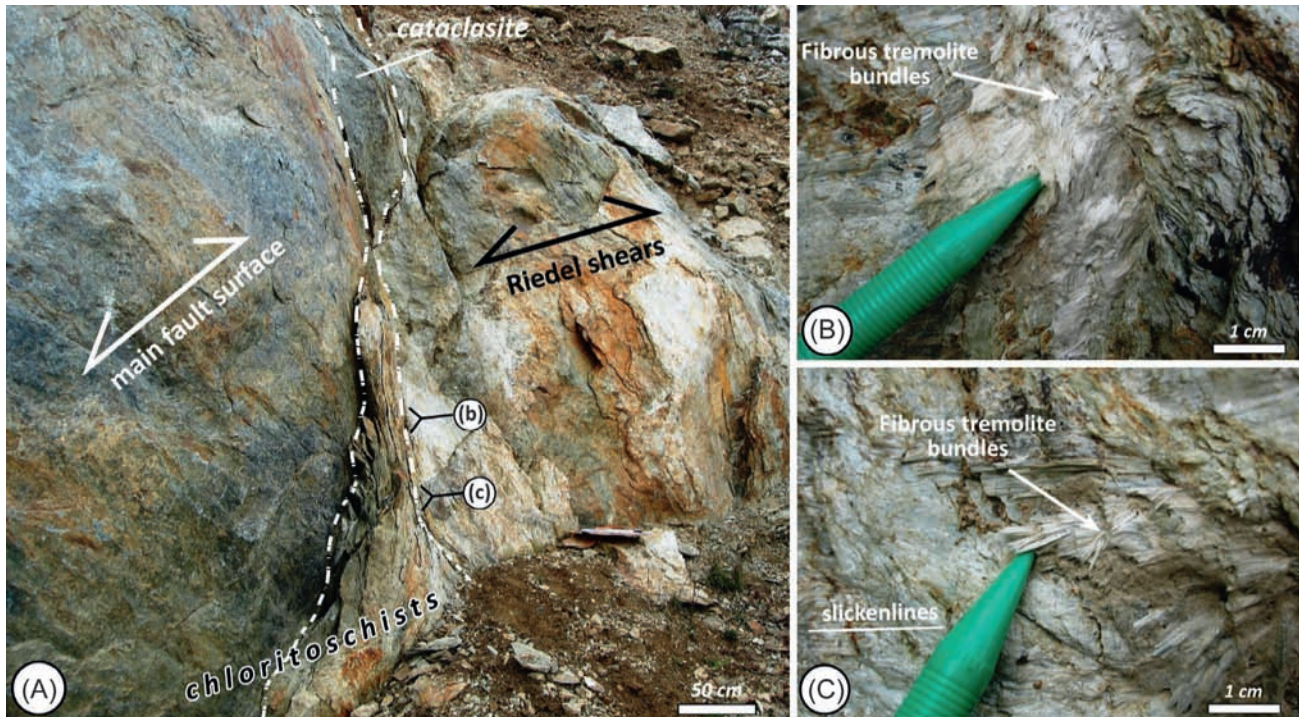


FIGURE 3.81 The structural control on asbestos mineralization in mafic rocks. (a) Chloritose schists affected by strike-slip faulting, Voltri Massif (Ligurian Alps, Italy). The fault zone consists of a decimeter-thick cataclastic band parallel to the main fault surface. Synthetic Riedel shear planes intersect at a low angle to the main fault surface and attest dextral kinematics (e.g., Petit, 1987). Asbestos mineralization occurs within the fault damage zone, localized where the main fault interferes with the Riedel shears. (b), (c) Detail of asbestos mineralization that decorates the Riedel shears. Asbestos mineralization consists of up to 2 cm long tremolite fibers, commonly elongated parallel to the fault slickenlines. The Voltri Massif is an ophiolitic domain located at the Alps-Apennines junction in Northern Italy. It includes subduction-related exhumed high-pressure (variably retrogressed blueschist-to-eclogite) units (Vanossi et al., 1984). During the exhumation of the high-pressure units, ductile-to-brittle deformation structures developed, and hosted composite mineralogical assemblages associated with retrogressive metamorphism (Federico et al., 2007; Vignaroli et al., 2010). Fibrous mineralization usually occurs in semibrittle and brittle deformation structures. **Gianluca Vignaroli and Federico Rossetti**

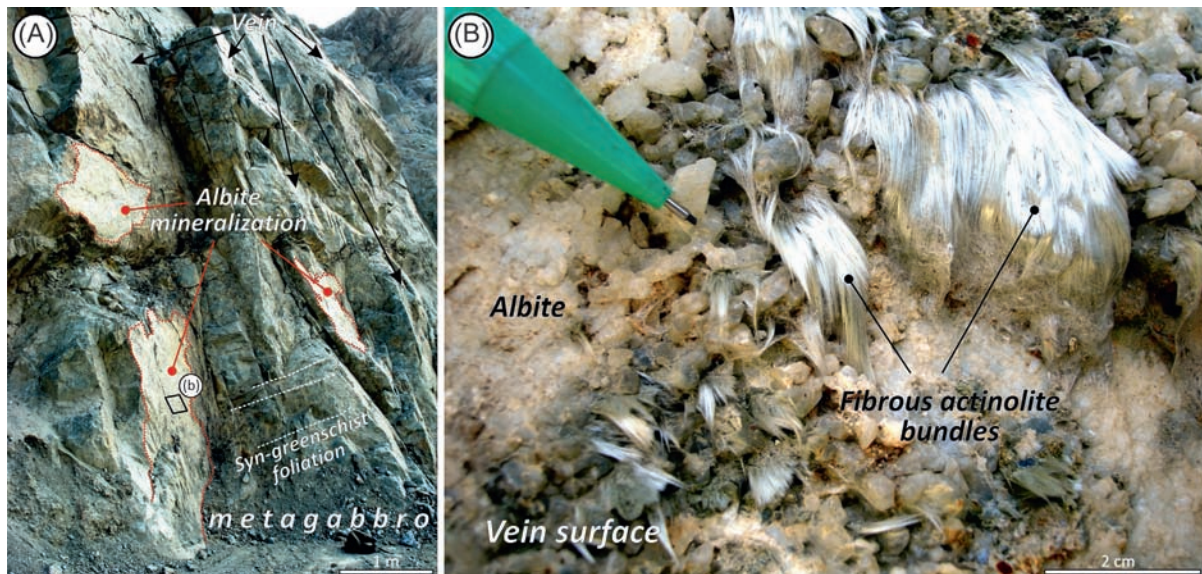


FIGURE 3.82 Structurally controlled fluid-flow and asbestos mineralization. (a) Subvertical vein system that cuts across the syn-greenschist foliation in metagabbros, Voltri Massif (Ligurian Alps, Italy). The veins are made up of albite with subordinate actinolite amphibole. (b) Detail of the vein surface where fibrous actinolite crystallizes. Fiber growth occurs in square centimeter bundles. This example documents the percolation of mineralizing fluids assisted by a structurally controlled permeability network. Metamorphic veins with fibrous minerals are described commonly in ophiolitic rocks (Hoogerduijn Strating and Vissers, 1994; Karkanis, 1995; Andreani et al., 2004). These tensional fractures can be thought of as dilatation sites where fibrous mineral forms along with fluid circulation and confined chemical mass transfer within the vein width (Barker et al., 2006). For references on the regional geology, see the previous caption. **Gianluca Vignaroli and Federico Rossetti**

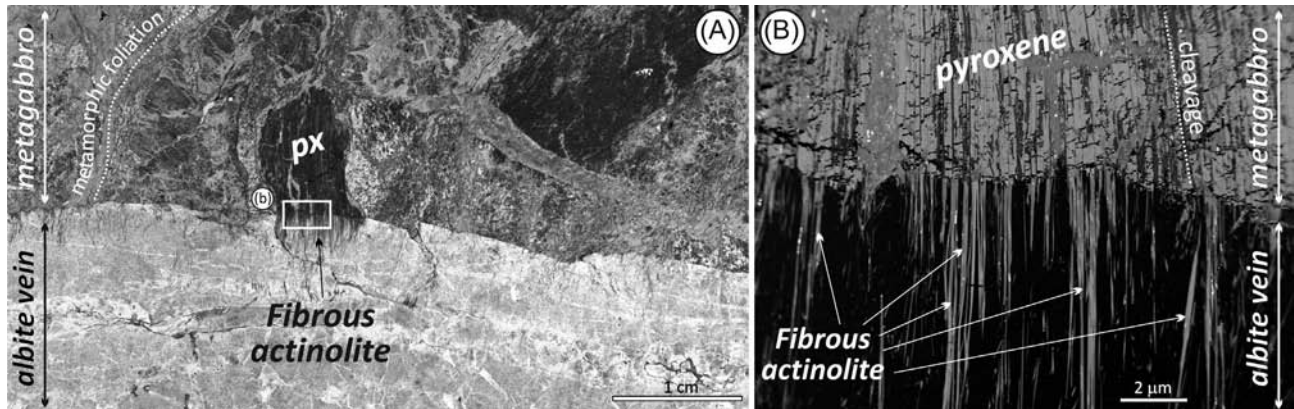


FIGURE 3.83 The structural control on asbestos mineralization at the microscale. (a) Detail of the sharp boundary between the metagabbro host rock and the albite-actinolite vein shown in [Figure 3.82](#). The vein shows antitaxial growth ([Passchier and Trouw, 2005](#)). The pyroxene (px) grain from the metagabbro is truncated at the vein-wall interface. Half a centimeter long fibers of actinolite concentrate along the pyroxene-vein interface. (b) This backscattered electron image is a detail of the textural relationships between pyroxene and fibrous actinolite. Fiber occurrence parallel to the internal cleavage of the pyroxene suggests a textural control of the pyroxene lattice during the actinolite overgrowth. Fibrous actinolite is one of the six asbestos minerals regulated by the normative ([World Health Organization, 1986](#)). The asbestos hazard in the natural environment is connected to the rock fabric heterogeneities (ductile-to-brittle deformation localization, metamorphism/metasomatism, and structurally controlled fluid flow) developed in response to the regional tectonics ([Vignaroli et al., 2011](#)). **Gianluca Vignaroli and Federico Rossetti**

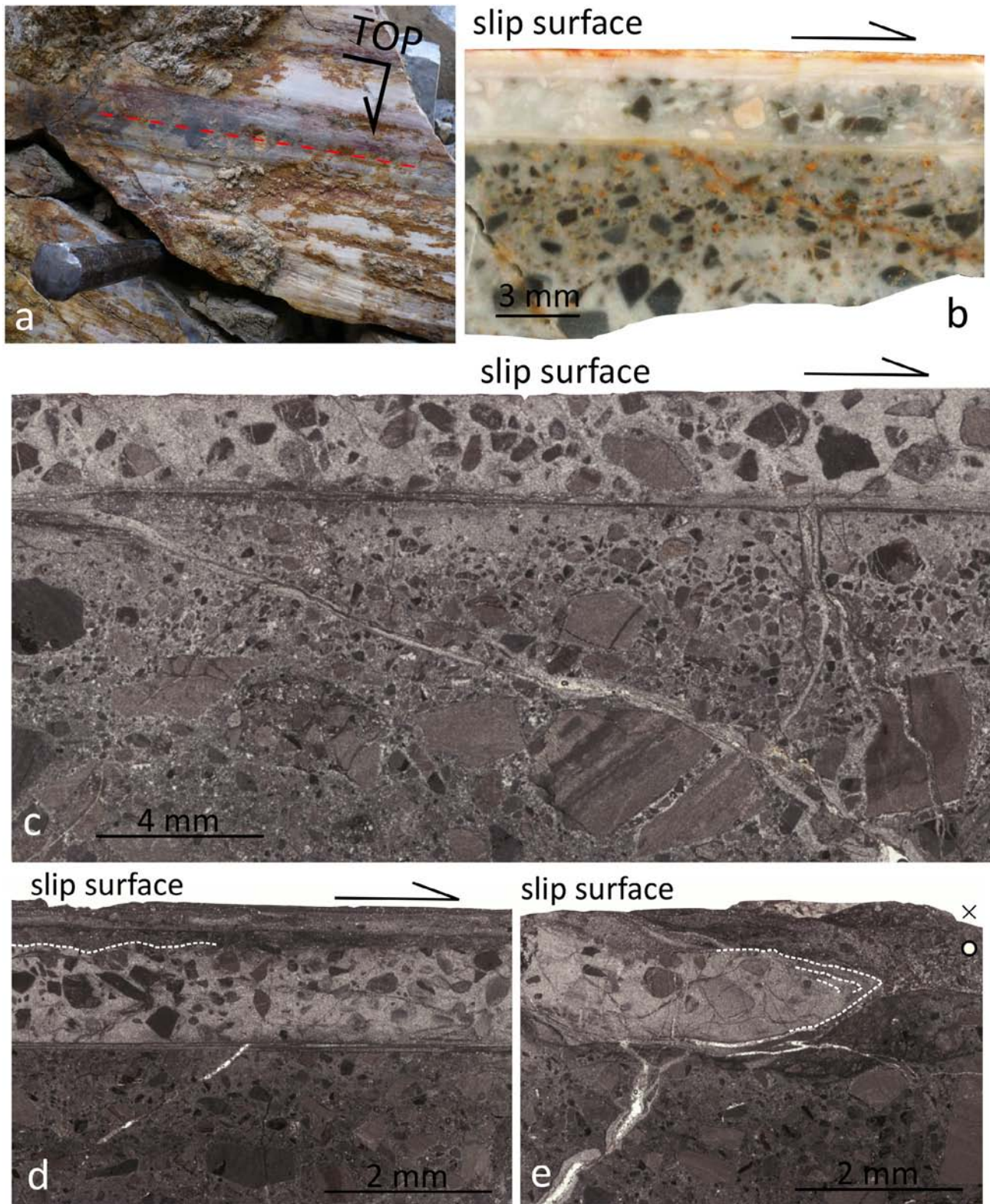


FIGURE 3.84 Fluidization features. Fluidization features in (a) Fault surface of a subsidiary strike-slip fault cutting dolostones within the Borcola Pass Fault Zone (Southern Alps, Italy) (Fondriest et al., 2012). The fault surface displays strike-slip grooves, truncated clasts, and patches of cataclastic material cemented on the top. (b) Section across the fault surface shown in (a). The fault rock is a cohesive cataclasite to ultracataclasite (the clast size is reduced toward the slip surface) arranged in subparallel layers. A whitish cataclastic layer is recognizable near the slip surface. (c-e) Optical transmission microscopy scans of the fault rock in (b) in directions parallel (c-d) and perpendicular (e) to the fault slip. The whitish cataclastic layer truncates the fault rock below and is characterized by (i) dolostone clasts suspended within a euhedral dolomite cement, (ii) well-sorted clast size with the lack of small particles, (iii) injection veins, and (iv) irregular to cusped-lobate and intrusive boundaries with the surrounding layers (see dashed white lines). These microstructures have been interpreted in relation to a fluidization event associated with ancient earthquake ruptures along the Borcola Pass Fault Zone. Coordinates: 45.838444, 11.207412. **Michele Fondriest**

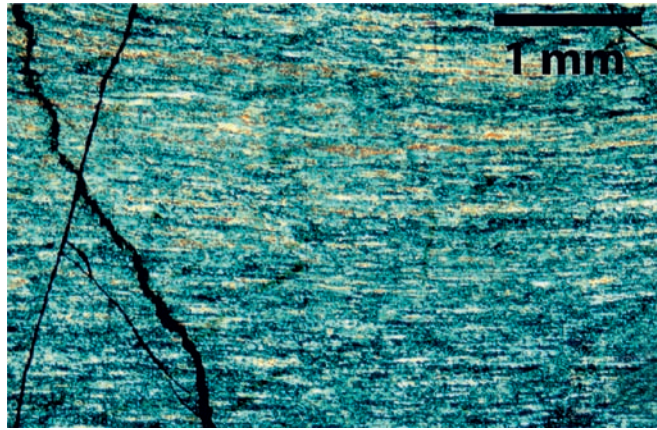


FIGURE 3.85 Microstructural evidence for repeated cycles of coseismic damage and viscous flow at the frictional to viscous transition in an ancient strike-slip fault. Large-displacement continental strike-slip faults are characterized by a core of ultrafine-grained rocks surrounded by a “damage zone” of fractured rocks that can extend laterally outward for hundreds of meters. A notable characteristic of these faults is the extensive occurrence of the so-called “pulverized” rocks that exhibit intragranular cracking and fragmentation down to the micron scale. A fundamental question is how deep do these damage zones extend into the crust, and how do their physical characteristics change with depth (Mooney et al., 2007; Tullis et al., 2007)? The Paleozoic Norumbega Fault System in Maine, United States, is known to be one of the best ancient analogs for the San Andreas Fault currently exposed on Earth’s surface (Ludman and West Jr, 1999; Sibson and Toy, 2006). The Norumbega is exposed at a range of depths along its length, and in Central Maine, the mylonites along different fault strands preserve spectacular evidence for repeated coseismic brittle damage followed by viscous flow, representing the frictional to viscous transition. We conclude from our studies of these rocks that damage zones extend throughout the seismogenic zone, but are difficult to detect geophysically and also by optical methods at depth owing to rapid microcrack healing and interseismic viscous flow. Some microstructural evidence is visible optically, but most of it can only be observed using cathodoluminescence (CL) and electron backscatter diffraction analyses. Figures 3.85 and 3.86 from the Sandhill Corner shear zone (Price et al., 2012) illustrate the efficacy of CL imaging in extracting a detailed microstructural history that is not visible optically. Optical (a: cross-polarized light) and CL (b) images of a shattered plagioclase grain. Optically, the grain shows at least three generations of crosscutting quartz-filled cracks and patchy extinction. The CL image reveals remarkable complexity that is not visible optically. The dark patches are extensive tensile microcrack networks in plagioclase. A dense network of quartz-filled cracks overprints them. Plagioclase fragments are as fine as 1 μm . **Scott Johnson**

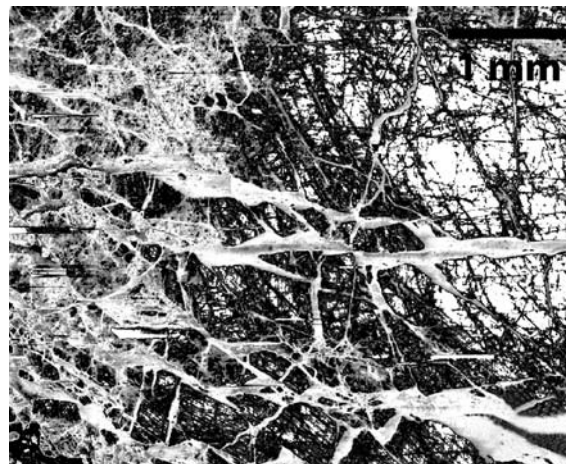


FIGURE 3.86 Microstructural evidence for repeated cycles of coseismic damage and viscous flow at the frictional to viscous transition in an ancient strike-slip fault. Large-displacement continental strike-slip faults are characterized by a core of ultrafine-grained rocks surrounded by a “damage zone” of fractured rocks that can extend laterally outward for hundreds of meters. A notable characteristic of these faults is the extensive occurrence of the so-called “pulverized” rocks that exhibit intragranular cracking and fragmentation down to the micron scale. A fundamental question is how deep do these damage zones extend into the crust, and how do their physical characteristics change with depth (Mooney et al., 2007; Tullis et al., 2007)? The Paleozoic Norumbega Fault System in Maine, United States, is known to be one of the best ancient analogs for the San Andreas Fault currently exposed on Earth’s surface (Ludman and West Jr, 1999; Sibson and Toy, 2006). The Norumbega is exposed at a range of depths along its length, and in Central Maine, the mylonites along different fault strands preserve spectacular evidence for repeated coseismic brittle damage followed by viscous flow, representing the frictional to viscous transition. We conclude from our studies of these rocks that damage zones extend throughout the seismogenic zone, but are difficult to detect geophysically and also by optical methods at depth owing to rapid microcrack healing and interseismic viscous flow. Some microstructural evidence is visible optically, but most of it can only be observed using cathodoluminescence (CL) and electron backscatter diffraction analyses. Figures 3.85 and 3.86 from the Sandhill Corner shear zone (Price et al., 2012) illustrate the efficacy of CL imaging in extracting a detailed microstructural history that is not visible optically. Optical (a: cross-polarized light) and CL (b) images of a shattered plagioclase grain. Optically, the grain shows at least three generations of crosscutting quartz-filled cracks and patchy extinction. The CL image reveals remarkable complexity that is not visible optically. The dark patches are extensive tensile microcrack networks in plagioclase. A dense network of quartz-filled cracks overprints them. Plagioclase fragments are as fine as 1 μm . **Scott Johnson**

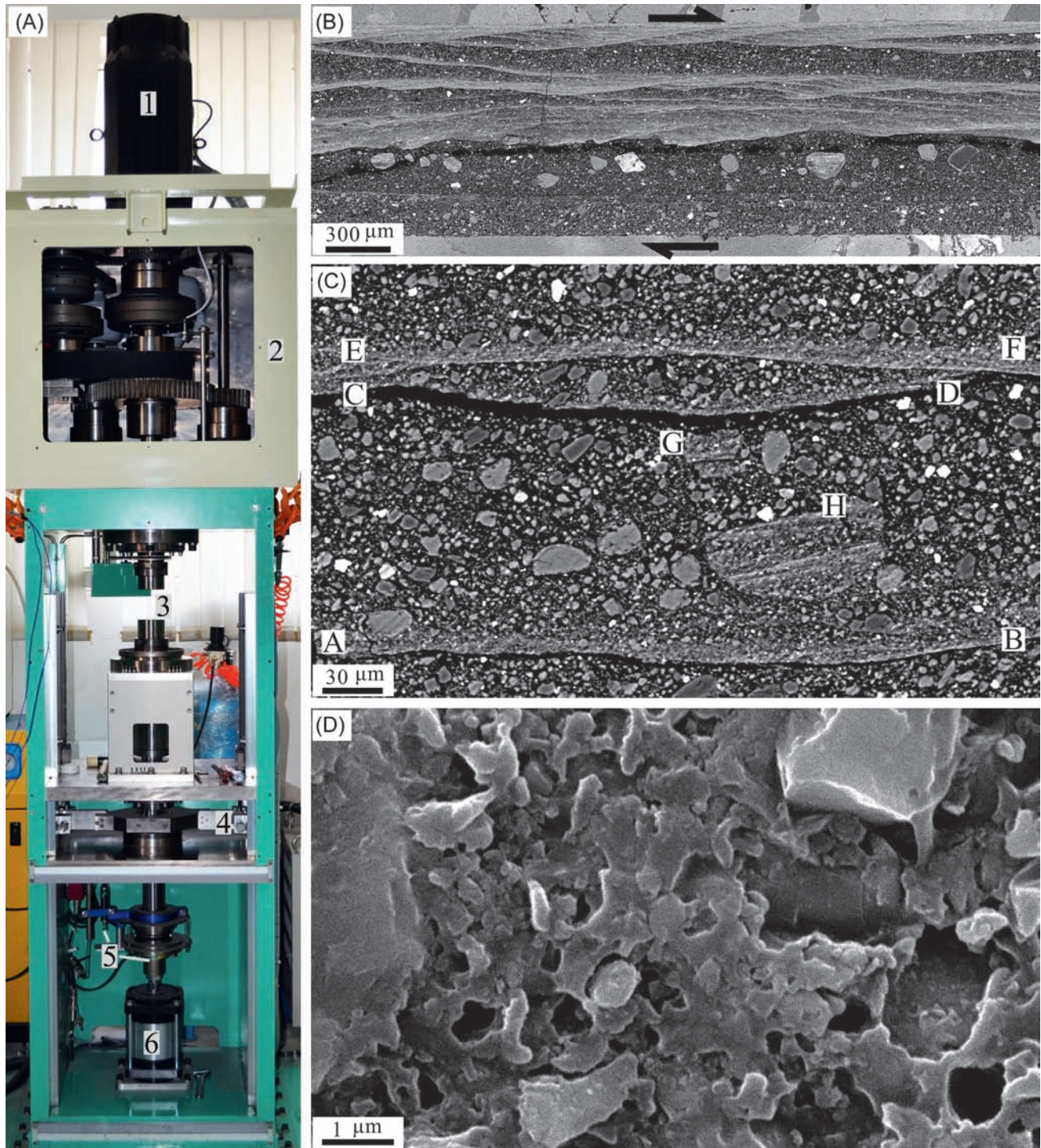


FIGURE 3.87 Overlapped slip-zone structures in experimental fault gouge. Reproducing seismic fault motion in a laboratory has received attention in the last two decades. Our institute installed a low to high velocity friction apparatus (a) that produces plate to seismic velocities (60 mmyr^{-1} to a few m s^{-1}). The apparatus consists of (1) a servomotor, (2) a gear/belt system for changing velocity, (3) holders of a pair of cylindrical specimens, (4) a torque gauge, (5) axial-force and displacement transducers, and (6) a bellow cylinder for applying the axial force. Sometimes very complex slip-zone structures such as those formed in an experimentally deformed gouge have been noted. (b): Gouge was collected from the Pingxi fault zone in the Longmenshan fault system that caused the 2008 Wenchuan earthquake and was deformed with room humidity at a slip rate v of 1.4 ms^{-1} and a normal stress σ_N of 0.8 MPa (Yao et al., 2013). The gouge consists of highly deformed slip zones that appear white on the photograph and a weakly deformed gouge. Crosscutting relations are recognized clearly along the Riedel shears within the gouge. Many of those slip zones are characterized by asymmetric grain-size distributions with ultrafine grains at the bottom that coarsen gradually upward (see three slipping zones AB, CF, and EF in (c) from the same gouge.) The middle slip zone is truncated by the upper slip zone at point F, and two fragments of slip zones are scattered at points G and H. Ultrafine-grained zones often consist of sintered grains with some pores (e.g., quartz gouge in (d) deformed at $v=1.3 \text{ ms}^{-1}$ and $\sigma_N=3.1 \text{ MPa}$; Togo and Shimamoto, 2012). A highly sheared gouge is strong, and a slip zone can shift to a less-deformed weaker gouge once the gouge is welded or hardened by compaction. This develops complex slip-zone structures. We suggested that welding or compaction of a gouge can be a mechanism for the growth of a gouge zone in natural fault zones (Shimamoto and Togo, 2012). Shengli Ma, Lu Yao, Tetsuhiro Togo, and Toshihiko Shimamoto

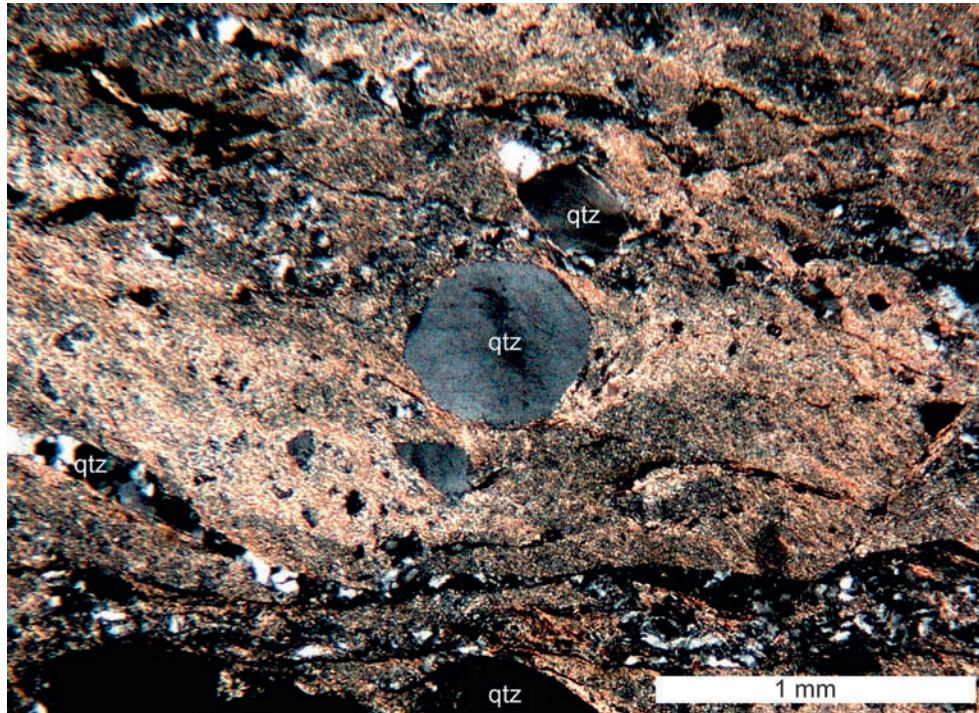


FIGURE 3.88 Sigma-structure in ultracataclastic, fine-grained matrix of quartz and clay around quartz-clast indicates foreland-directed (top-to-right) tectonic transport. Lower Allochthon, Central Scandinavian Caledonides. See [Greiling et al. \(1998\)](#) for detail. Jens Carsten Grimmer



FIGURE 3.89 Brittle-ductile thrust shear zone related to the NNE-SSW-trending Olevano-Antrodoco-Sibillini oblique thrust ramp, Central-Northern Apennines, Italy. The foliated cataclasite is organized in a planar S-fabric ([Calamita et al., 2012](#)). The penetrative subhorizontal closely spaced pressure-solution S-cleavage affects the marly calcareous Eocene–Oligocene Scaglia Cinerea Formation cropping out in the footwall of the thrust ramp. Conjugate high-angle extensional shear planes occur within the thrust shear zone and are related to extensional crenulation cleavage as per [Calamita et al. \(2012\)](#). Details about the brittle-ductile thrust shear zones in the Central-Northern Apennines can be found in [Calamita et al. \(1991\)](#), [Tavarnelli \(1999\)](#), and [Calamita et al. \(2012\)](#). Location: Valle Scura Valley (42.490855° 13.049969°), W to the Sigillo village, Province of Rieti (Italy). Width of view: 70 cm. Paolo Pace



FIGURE 3.90 Synlithification faults in Cretaceous clastics. In the gray marl, the centimeter-thick sandstone layers commonly contain a set of small, parallel displacement zones, which cannot be followed up to the next sandstone bed. Within the sandstone, the fault planes are frequently not discrete surfaces and are macroscopically invisible. They either do not continue in the intercalating marlstone or occur as closed fractures. In addition, displacement lines at the upper and lower boundaries of the sandstone bed are not always aligned but are en-echelon along the dip direction. This can be interpreted as along-dip segmented fractures. Displacement can be smaller at the upper than at the lower bedding plane. All these deformation features developed when sandstone beds consolidated/cemented partly and were in a plastic state so they are synlithification faults. The deformation can be regarded as a first step for boudinage. Deformation occurred during the Early Cretaceous progressive burial. Compaction affected the conjugate fracture set and increased their angle to the obtuse angle. Postdeformation cementation sealed the early displacement features. The deformation is related to an Early Cretaceous foreland basin formation (Tari, 1994; Fodor et al., 2013). Green eraser: ~ 2 cm. Early Cretaceous (Valanginian) marlstone, sandstone (Fogarasi, 1995). Location: Bersek quarry, Lábatlan village, Gerecse Hills, Hungary. Coordinates: 47°43'20.33"N, 18°31'29.13"E. László Fodor



FIGURE 3.91 The outcrop exposes one of the main faults of the active Hronov-Poříčí Fault Zone, Czech Republic. It is a ~70 km long intra-plate zone recently responsible for earthquakes up to $M \sim 4.7$ (Woldřich, 1901; Špaček et al., 2006). Red-brown Permian conglomerates and breccias of the Trutnov Formation on the right side form a hanging wall of the fault zone. Conglomerates are overlain unconformably by ochre to dark gray Cretaceous sandstones and siltstones of the Peruc-Korycany Formation, cropping out on the left side of the wall (see Novakova, 2014). The dip of both the Permian and Cretaceous sediments is steep (up to 89 degrees SW) due to the close vicinity of the main fault line. The Hronov-Poříčí Fault Zone represents a main reverse fault accompanied by parallel/oblique normal or reverse faults (Valenta et al., 2011). GPS coordinates: N50°32'14", E016°02'31". Lucie Novakova



FIGURE 3.92 This view from Point Keen above Kaikoura (South Island, New Zealand) displays a set of anastomosed sinistral faults. These relatively small faults are related to the main Hope Fault. The Hope Fault is currently the most active structure of the Marlborough Fault System with a right-lateral slip rate of 20–40 mm/yr (Cowan, 1991). The Northern Canterbury basin and range topography are a consequence of spreading deformation associated with the Australian-Pacific plate boundary (Rattenbury et al., 2006). GPS coordinates: S42°25'26", E173°43'01". Lucie Novakova

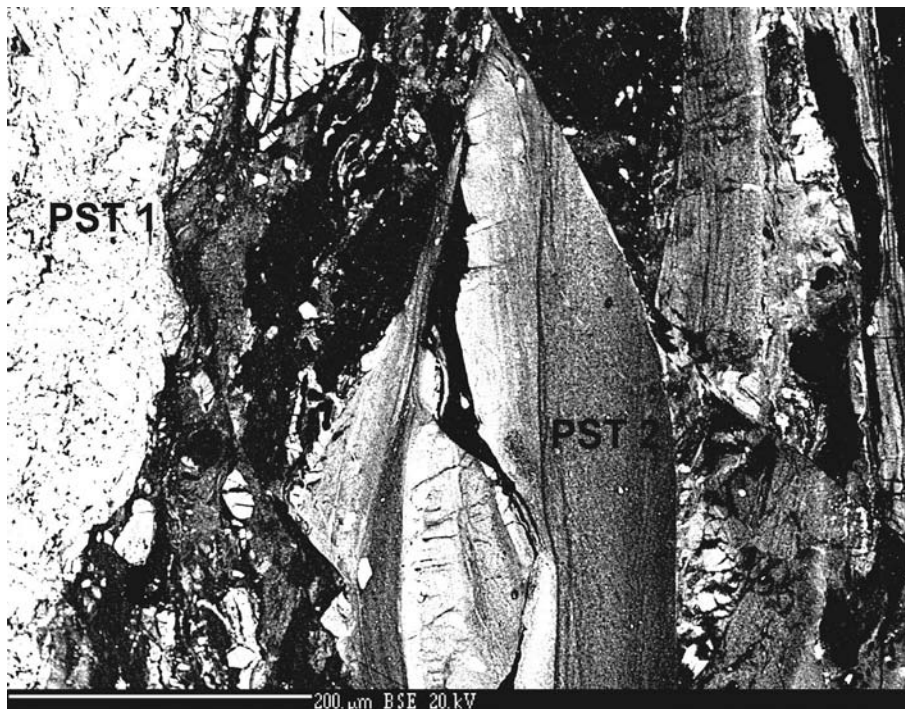


FIGURE 3.93 Multiple generations of pseudotachylite. This back-scattered electron image shows an Eocene blueschist facies, peridotite-hosted pseudotachylite (PST). At least three generations of faulting whereby the earliest generation of pseudotachylite (PST 1) has been cross-cut by two later generations (PST 2 and PST 3; Sibson, 1975; Spray, 1992; Swanson, 1992). PST 2 is microfaulted, implying the PST had time to solidify between pseudotachylite melt generations. The dark gray PST 3 remains glassy and has entrained chunks of the previous PST generations. This PST is situated in the exhumed ophiolite complex: Schistes Lustres, Cape Corse, Corsica (Andersen and Austrheim, 2006). Natalie Deseta

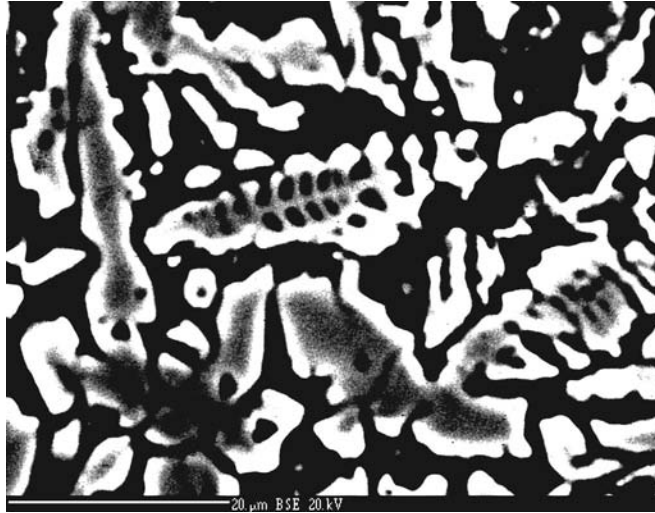


FIGURE 3.94 High-Al Omphacite. The first documented occurrence of omphacite hopper crystals quenching directly from a pseudotachylytic melt, suggesting high-pressure (1.8–2.6 GPa) and high-temperature ($>1350^{\circ}\text{C}$) conditions of formation (Andersen and Austrheim, 2006; Ravna et al., 2010). These mafic pseudotachylytes are hosted by blueschist-eclogite-lawsonite facies metagabbro from the exhumed Schistes Lustrés Ophiolite Complex, Cape Corse, Corsica. These omphacites contain an average of 15 wt% Al_2O_3 and a ~ 20 mol% Ca-Eskola component (Smyth, 1980; Katayama et al., 2000; Deseta et al., 2014). This high-temperature occurrence of omphacite is important as it confirms that these pseudotachylytes formed under high-pressure conditions. **Natalie Deseta**



FIGURE 3.95 Imbricate thrust structure in flysch. This spectacularly exposed structure is located in the most external part of the Dinaric fold-thrust belt in the Istria peninsula (Placer et al., 2010). The floor detachment runs ~ 1 m above prominent sandstone beds at the foot of the cliff. The isolated position of this duplex within the undisturbed flysch sequence, and the markedly plastic behavior of the sandstone layers during deformation, indicated by tight drag folds in the footwall of imbricate thrusts, suggest that the structure might have originated due to soft-sediment slumping rather than tectonic deformation. Rock type: thin-bedded sandstone, marlstone, and mudstone, Dinaric foreland flysch, Eocene. Location: San Simon bay, Adriatic coast, Slovenia. Coordinates: $45^{\circ}32'00''\text{N}$, $13^{\circ}38'25''\text{E}$. **Marko Vrabec**

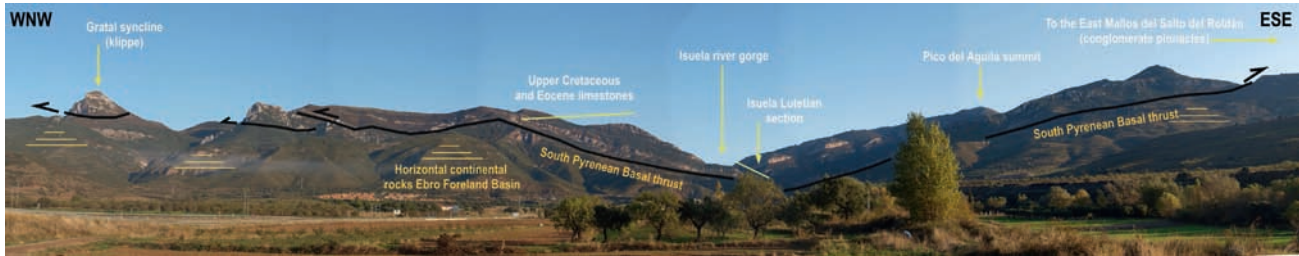


FIGURE 3.96 The External Sierras Front (Southern Pyrenees) in the Isuela Section. The South Central Pyrenean basal thrust crops out near the city of Huesca (Aragón) in the transverse of the Isuela River. There, a complex break-back thrusting sequence ends up with a large-scale ramp (30 degree north dipping) visible from the A23/E07 highway, thrusting over the horizontal Miocene deposits of the Ebro Foreland Basin (where the picture was taken). [Bose and Mukherjee \(2019a,b\)](#) recently reviewed back-thrusting mechanisms from different orogens. The so-called External Sierras in this position evolved during Bartonian times (coeval with the movement of the Gavarnie basement thrust) and produced a complex submarine imbricate system responsible for the well-known structures as the Pico del Aguila anticline (whose core-summit is visible in the picture). The oldest structures crop out in the footwall of the basal thrust in the Isuela gorge where a tectonic window allows observing them as well as the detachment of the deformation in the Muschelkalk facies. Some klippe, like the Gratal syncline, are witnesses for the geometry of the footwall of the basal thrust ([Millán, 1996](#); [Casas and Pardo, 2004](#)). The kinematics of the thrust front are fully recorded by outstanding syntectonic sedimentation. Besides, both the hanging wall and footwall sedimentary piles have been dated by magnetostratigraphic sections. In the hanging wall, the Lutetian Guara Fm. ([Rodríguez-Pintó et al., 2012](#); [Silva-Casal et al., 2019](#)), the Bartonian-Priabonian Arguis Marls Fm ([Hogan and Burbank, 1996](#); [Pueyo et al., 2002](#); [Kodama et al., 2010](#)), and the Rupelian and Chattian continental Campodarbe Fm ([Hogan and Burbank, 1996](#)). On the other hand, the Ebro Foreland Basin deposits (from Oligocene to Miocene) are dated to the West ([Oliva-Urcia et al., 2016, 2019](#); [Anastasio et al., 2020](#)). The excellent outcrop conditions, the preserved syntectonic records, and the enviable chronostratigraphic frames makes the External Sierras a unique natural laboratory to study deformation processes in fold and thrust belts. **Emilio Pueyo**

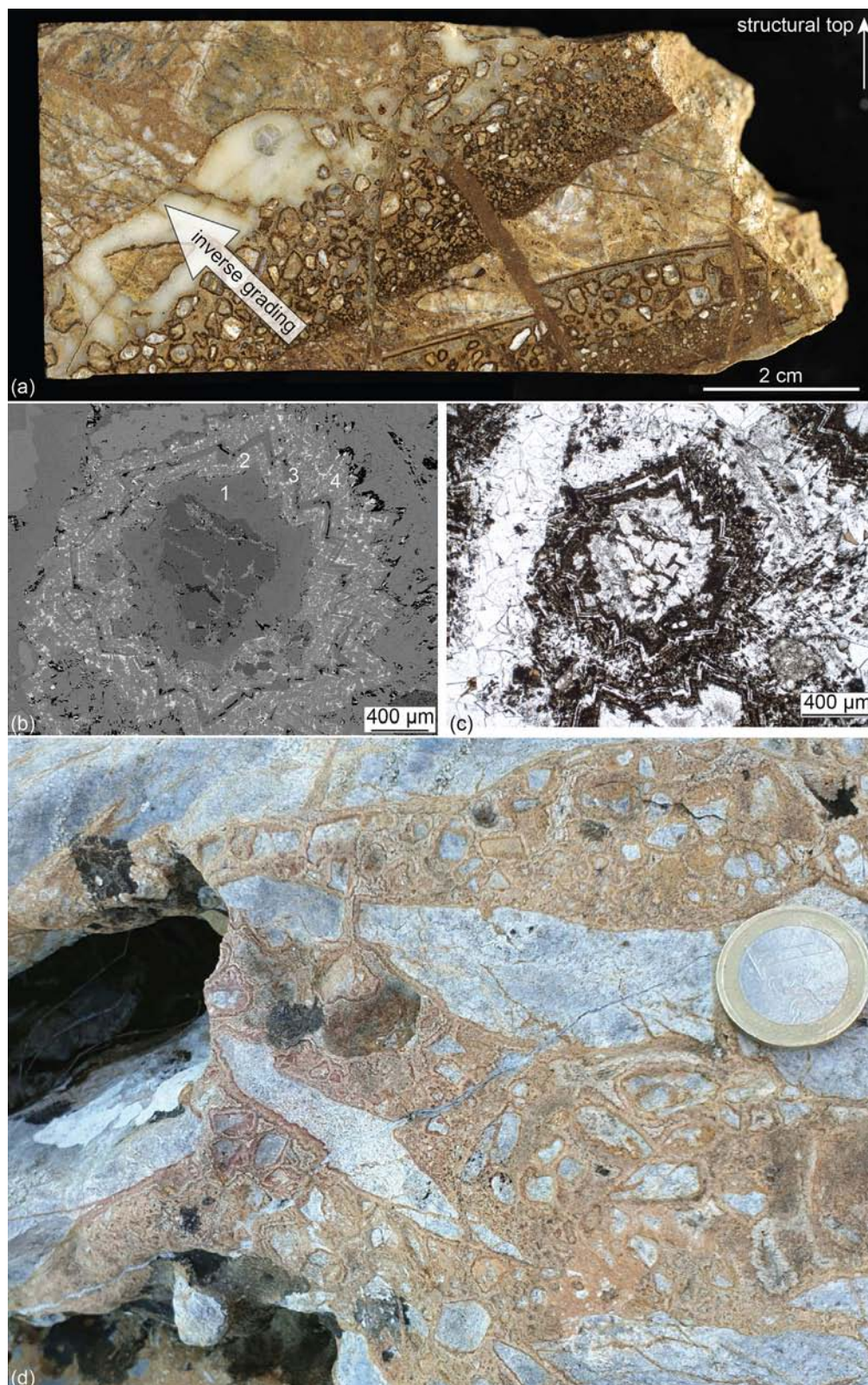


FIGURE 3.97 Breccia. Cockade breccias are a relatively common fault product of shallow-crustal hydrothermal systems and consist of up to 10 cm-sized core clasts wrapped by concentric bands of cement. The formation of cockade breccias requires (i) the presence of pore space among the core clasts, and (ii) the ingress of fluids among the core clasts leading to the precipitation of the concentric bands of cement. Several mechanisms could lead to their formation (review in [Frenzel and Woodcock, 2014](#)) and a few are associated with seismic faulting (e.g., [Berger and Herwegh, 2019](#); [Cox and Munroe, 2016](#); [Masoch et al., 2019](#)). (a) Polished sample with multiple veins filled with cockade breccias found in Miocene in age transtensional faults from the Col de Teghime area (Alpine Corsica, France; [Masoch et al., 2019](#)). Core clasts consist of quartzite fragments. The core clasts have inverse grading (i.e., the smallest at the bottom, the largest at the top), and are separated by concentric bands of reddish- to brown-colored carbonate-rich cement. (b) SEM-BSE image of a cockade (i.e., core clast + concentric rims). The core clast made of quartzite fragment is wrapped by four concentric rims composed mainly of euhedral carbonate minerals. From the core clast outward, the rim-forming minerals are: (1) saddle dolomite, (2) Mg-calcite with goethite and anatase microcrystals partially filling cleavage-parallel cavities, (3) saddle dolomite, and (4) Mg-calcite. (c) Under the optical microscope in parallel-polarized light, the dolomite-built rims are transparent while the hydroxide- and oxide-rich rims are brown in color. (d) Cockade breccias found near Cima Orcaio (Alpine Corsica, France). Core clasts consist of up to 4 cm-sized quartzite fragments. A one euro coin for scale. **Simone Masoch, Michele Fondriest, and Giulio Di Toro**



FIGURE 3.98 Domino structures. Small-scale domino structures associated to compaction within bituminous dolostones (Dolomie Bituminose formation—Upper Triassic; [Adamoli et al., 1990](#)) of the Fornaca Valley (Central Apennines, Italy; [Ghisetti, 1987](#); [Leah et al., 2018](#); [Lucca et al., 2019](#)). **Michele Fondriest**

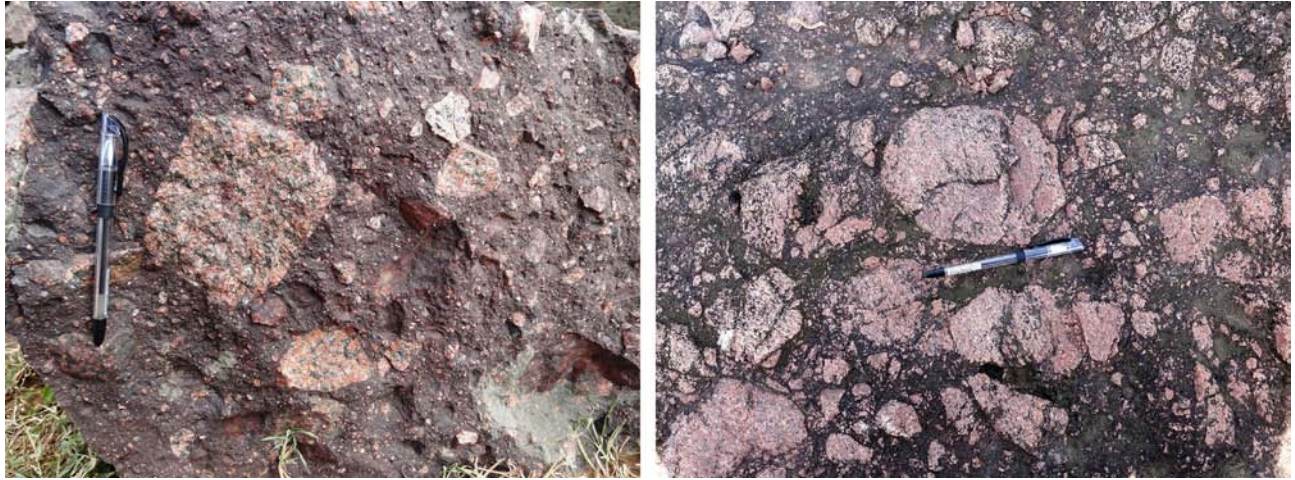


FIGURE 3.99 Granite breccias. Granite breccia from the Dhala impact structure, Shivpuri district, Madhya Pradesh, India. This type of breccia consists of extensively fractured/brecciated, angular to subangular granite/granitoid clasts (> 90%), and other xenolithic components such as granite gneiss, calc-silicate rocks, felsic volcanics, vein quartz, and dolerite dyke set within purple/chocolate brown colored pulverized granitic groundmass. The size of these clasts may vary from a few mm up to few cm, rarely occur as meter. Maniar and north of Pagra villages, respectively, Shivpuri district, Madhya Pradesh, India. **Arindam Dutta, Debjani Raychaudhuri, Aparajita Bhattacharya, and Anindya Bhattacharya**

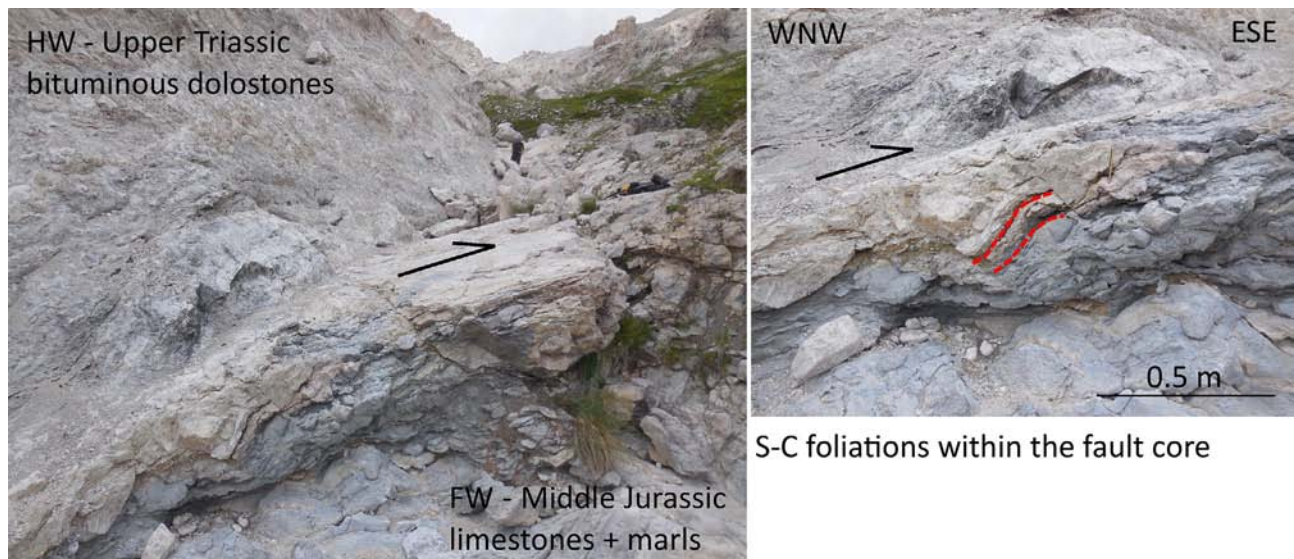


FIGURE 3.100 Thrust zone structures. The Vado di Ferruccio Thrust puts in contact intensely fractured bituminous dolostones (Dolomie Bituminose Formation–Upper Triassic) in the hanging wall with folded limestones and marls (Corniola and Verde Ammonitco formations–Middle Jurassic) (Ghisetti, 1987; Pace et al., 2014; Leah et al., 2018; Lucca et al., 2019). The thrust fault core is affected by S-C foliations developed within the marly layers revealing the tectonic transport direction (NNE). Coordinates: 42.435051, 13.699116. **Michele Fondriest**

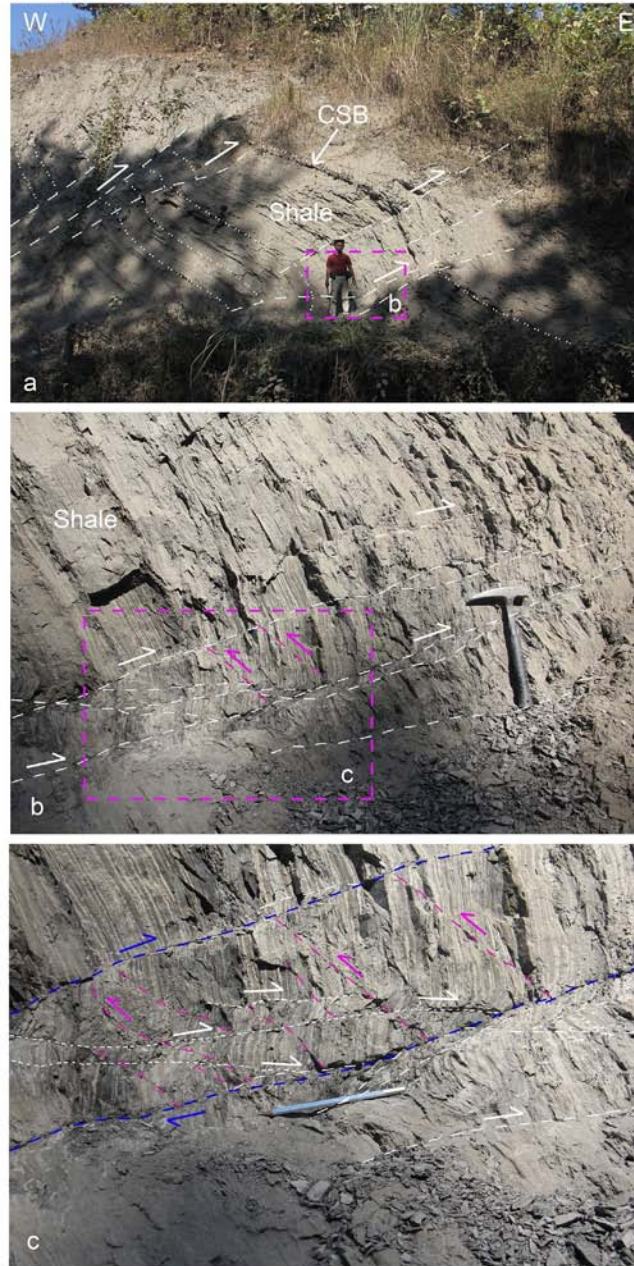


FIGURE 3.101 Thrust zone, Bandarban anticline, Bangladesh. Thrust zone developed in the Tertiary sedimentary rock of the Chittagong-Tripura Fold Belt (CTFB), Bangladesh (Hossain et al., 2019, 2020). Shear zone occurred in the Mid-Miocene to Late-Miocene Boka Bil Formation with small thrust component in the eastern flank of the Bandarban structure near the Bandarban Bus Stand area along the Bandarban-Chimbuk road cut section (latitude: 22.18763 degrees, longitude: 92.21560 degrees). The exposure shows several well-developed shears dipping opposite to that of the bedding (thinly bedded shale unit with calcareous sandstone band: Boka Bil Formation). Exposure trends E-W. Photographs faces N. Dm to cm-scale slip noted. Although the exposure is very close to the axial zone, shale bed dips steeply and variably, ranging from 50 to 69 degrees (at the lower part of the exposure). The east-verging shears sometimes show high-dips. The overall attitudes of the shear is ~ 245 degrees/35–40 degrees. (a) Shear bends with minor thrust component developed in the thinly bedded shale with calcareous sandstone band (Boka Bil Formation). More than two shears with dm to cm-scale slips show eastward verging (white half arrow). Along the shear plane, shale beds are highly compacted and are brittle-ductile deformed. Dash lines: shear planes; dotted lines: bedding planes. CSB, calcareous sandstone band. Rectangle marked the position of the latter figure. The author in the figure is 1.64 m long, as a marker. (b) Zooming of figure “a” demonstrates well-developed shear planes. Length of the hammer: 0.30 m. (c) Zooming of the figure “b” exhibits a well-developed shear zone (blue dash lines) with secondary shears: R and R’ (Katz et al., 2004), white and pink dash lines, respectively. Approximately E-W principal stress axis (σ_1) orientation inferred. Length of the pencil is 0.15 m. **Md. Sakawat Hossain**

References

- Adamoli, L., Bigozzi, A., Ciarapica, G., Cirilli, S., Passeri, L., Romano, A., Duranti, F., Venturi, F., 1990. Upper triassic bituminous facies and hettangian pelagic facies in the gran sasso range. *Bollettino della Societa Geologica Italiana* 109, 219–230.
- Agard, P., Yamato, P., Jolivet, L., Burov, E., 2009. Exhumation of oceanic blueschists and eclogites in subduction zones: timing and mechanisms. *Earth-Science Reviews* 92, 53–79.
- Alania, V., Chabukiani, A., Enukidze, O., Razmadze, A., Sosson, M., Tsereteli, N., Varazanashvili, O., 2017. Structural model of the eastern Achara-Trialeti fold and thrust belt using seismic reflection profiles. *Geophysical Research Abstracts* 19, EGU2017-5064.
- Alania, V., Beridze, M., Enukidze, O., Chagelishvili, R., Lebanidze, Z., Maqadze, D., Razmadze, A., Sadradze, N., Tevzadze, N., 2020. The geometry of the two orogens convergence and collision zones in Central Georgia: new data from seismic reflection profiles. In: Bonali, F.L., Pasquaré, M.F. (Eds.), *Building Knowledge for Geohazard Assessment and Management in the Caucasus and Other Orogenic Regions*. NATO Science for Peace and Security Series C: Environmental Security. Springer. https://doi.org/10.1007/978-94-024-2046-3_6.
- Anastasio, D.J., Teletzké, A.L., Kodama, K.P., Parés, J.M., Gunderson, K.L., 2020. Geologic evolution of the Peña flexure, Southwestern Pyrenees mountain front, Spain. *Journal of Structural Geology* 131, 103969.
- Andersen, T., Austrheim, H., 2006. Fossil earthquakes recorded by pseudotachylytes in mantle peridotite from the Alpine subduction complex of Corsica. *Earth and Planetary Science Letters* 242, 58–72.
- Andreani, M., Baronnet, A., Boullier, A.M., Gratier, J.P., 2004. A microstructural study of a “crack-seal” type serpentine vein using SEM and TEM techniques. *European Journal of Mineralogy* 16, 585–595.
- Angelier, J., 1984. Tectonic analyses of fault slip data sets. *Journal of Geophysical Research* 89, 5835–5848.
- Antonellini, M., Mollema, P., 2002. Cataclastic faults in the Loiano sandstones; Northern Apennines, Italy. *Bollettino Società Geologica Italiana* 121, 163–178.
- Austrheim, H., Andersen, T.B., 2004. Pseudotachylytes from Corsica: fossil earthquakes from a subduction complex. *Terra Nova* 16, 193–197.
- Aydin, A., 1978. Small faults formed as deformation bands in sandstone. *Pure and Applied Geophysics* 116, 913–930.
- Babar, M., Kaplay, R.D., Mukherjee, S., Kulkarni, P.S., 2017. Evidences of deformation of dykes from Central Deccan Volcanic Province, Aurangabad, Maharashtra, India. In: Mukherjee, S., Misra, A.A., Calvès, G., Nemčok, M. (Eds.), *Tectonics of the Deccan Large Igneous Province*. 445. Geological Society, London, pp. 337–353. Special Publications.
- Balsamo, F., Bezerra, F.H., Vieira, M., Storti, F., 2013. Structural control on the formation of iron oxide concretions and Liesegang bands in faulted, poorly lithified Cenozoic sandstones of the Paraíba basin, Brazil. *Geological Society of America Bulletin* 125, 913–931.
- Barchi, M.R., Lemmi, M., 1996. Geologia dell’area del M. Coscerno-M. di Civitella (Umbria sud-orientale). *Bollettino della Societa Geologica Italiana* 115, 601–624.
- Barker, S.L.L., Cox, S.F., Eggins, S.M., Gagan, M.K., 2006. Microchemical evidence for episodic growth of antitaxial veins during fracture-controlled fluid flow. *Earth and Planetary Science Letters* 250, 331–344.
- Berger, A., Herwegh, M., 2019. Cockade structures as a paleo-earthquake proxy in upper crustal hydrothermal systems. *Scientific Reports* 9, 1–9.
- Bezerra, F.H.R., Rossetti, D.F., Oliveira, R.G., Medeiros, W.E., Brito Neves, B.B., Balsamo, F., Nogueira, F.C., Dantas, E.L., Andrades Filho, C., Goes, A.M., 2014. Neotectonic reactivation of shear zones and implications for faulting style and geometry in the continental margin of NE Brazil. *Tectonophysics* 614, 78–90.
- Bose, N., Mukherjee, S., 2019a. Field documentation and genesis of the back-structures from the Garhwal Lesser Himalaya, Uttarakhand, India. In: Sharma, V.I.M., Kumar, S. (Eds.), *Crustal Architecture and Evolution of the Himalaya-Karakoram-Tibet Orogen*. vol. 481. Geological Society of London, pp. 111–125. Special Publications.
- Bose, N., Mukherjee, S., 2019b. Field documentation and genesis of back-structures in ductile and brittle regimes from the foreland part of a collisional orogen: examples from the Darjeeling–Sikkim Lesser Himalaya, India. *International Journal of Earth Sciences* 108, 1333–1350.
- Brozzetti, F., Boncio, P., Cirillo, D., Ferrarini, F., de Nardis, R., Testa, A., Liberi, F., Lavecchia, G., 2019. High-resolution field mapping and analysis of the August–October 2016 coseismic surface faulting (Central Italy earthquakes): slip distribution, parameterization, and comparison with global earthquakes. *Tectonics* 38, 417–439.
- Butler, R.W.H., 1989. The influence of pre-existing basin structure on thrust system evolution in the Western Alps. In: Cooper, M.A., Williams, G.D. (Eds.), *Inversion Tectonics*. vol. 44. Geological Society, London, pp. 105–122. Special Publications.
- Byrne, T., 1994. Sediment deformation, dewatering and diagenesis: illustrations from selected mélange zones. In: Maltman, A. (Ed.), *The Geological Deformation of Sediments* (Chapter 8). Chapman & Hall, pp. 239–260.
- Caine, J.S., Evans, J.P., Forster, C.B., 1996. Fault zone architecture and permeability structure. *Geology* 24, 1025–1028.
- Caine, J.S., Ridley, J., Wessel, Z.R., 2010. To reactivate or not to reactivate—nature and varied behavior of structural inheritance in the proterozoic basement of the eastern Colorado Mineral Belt over 1.7 billion years of earth history. In: Morgan, L.A., Quane, S.L. (Eds.), *Through the Generations: Geologic and Anthropogenic Field Excursions in the Rocky Mountains from Modern to Ancient*. Geological Society of America Field Guide. vol. 18, pp. 119–140.
- Calamita, F., Decandia, F.A., Deiana, G., Fiori, A.P., 1991. Deformation of S-C tectonites in the scaglia cinerea formation in the Spoleto area (South-East Umbria). *Bollettino della Societa Geologica Italiana* 110, 661–665.
- Calamita, F., Ben M’Barek, M., Di Vincenzo, M., Pelorosso, M., 2004. The Pliocene thrust system of the Gran Sasso salient (Central Apennines, Italy). In: Pasquare, G., Venturini, C. (Eds.), *Mapping Geology in Italy*. APAT, Servizio Geologico d’Italia, S.EL.CA, Firenze, pp. 227–234.
- Calamita, F., Satolli, S., Turtù, A., 2012. Analysis of thrust shear zones in curve-shaped belts: deformation mode and timing of the Olevano-Antronodoco-Sibillini thrust (Central/Northern Apennines of Italy). *Journal of Structural Geology* 44, 179–187.

- Calamita, F., Di Domenica, A., Pace, P., 2017. Macro- and meso-scale structural criteria for identifying pre-thrusting normal faults within foreland fold-and-thrust belts: insights from the Central-Northern Apennines (Italy). *Terra Nova* 30, 50–62.
- Cardello, G.L., Doglioni, C., 2014. From Mesozoic rifting to Apennines orogeny: the Gran Sasso range (Italy). *Gondwana Research* 27, 1307–1334.
- Casas, A.M., Pardo, G., 2004. Estructura pirenaica y evolución de las cuencas sedimentarias en la transversal Huesca-Oloron. In: Colombo, F., Liesa, C.L., Meléndez, G., Pocovi, A., Sancho, C., Soria, A.R. (Eds.), *Itinerarios geológicos por Aragón*. vol. 1. Geo Guías (Sociedad Geológica de España), pp. 63–96. ISBN: 84-930,160-2-0.
- Childs, C., Nicol, A., Walsh, J.J., Watterson, J., 1996. The growth of vertically segmented normal faults. *Journal of Structural Geology* 18, 1389–1397.
- Compagnoni, R., Groppo, C., 2006. Gli amianti in Val di Susa e le rocce che li contengono. *Rendiconti della Società Geologica Italiana* 3, 21–28.
- Cowan, H.A., 1991. The North Canterbury earthquake of September 1, 1888. *Journal of the Royal Society of New Zealand* 21, 13–24.
- Cox, S.F., Munroe, S.M., 2016. Breccia formation by particle fluidization in fault zones: implications for transitory, rupture-controlled fluid flow regimes in hydrothermal systems. *American Journal of Science* 316, 241–278.
- Dasgupta, S., Mukherjee, S., 2017. Brittle shear tectonics in a narrow continental rift: asymmetric non-volcanic Barmer basin (Rajasthan, India). *The Journal of Geology* 125, 561–591.
- Del Sole, L., Antonellini, M., 2019. Microstructural, petrophysical, and mechanical properties of compactive shear bands associated to calcite cement concretions in arkose sandstone. *Journal of Structural Geology* 126, 51–68. <https://doi.org/10.1016/j.jsg.2019.05.007>.
- Del Sole, L., Antonellini, M., Calafato, A., 2020a. Characterization of sub-seismic resolution structural diagenetic heterogeneities in porous sandstones: combining ground-penetrating radar profiles with geomechanical and petrophysical in situ measurements (Northern Apennines, Italy). *Marine and Petroleum Geology* 117, 104375.
- Del Sole, L., Antonellini, M., Soliva, R., Ballas, G., Balsamo, F., Viola, G., 2020b. Structural control on fluid flow and shallow diagenesis: insights from calcite cementation along deformation bands in porous sandstones. *Solid Earth*. <https://doi.org/10.5194/se-2020-81>.
- Deseta, N., Andersen, T.B., Ashwal, L., 2014. A weakening mechanism for intermediate-depth seismicity? Detailed petrographic and microtextural observations from blueschist facies pseudotachylytes, Cape Corse, Corsica. *Tectonophysics* 610, 138–149.
- Doblas, M., 1998. Slickenside kinematic indicators. *Tectonophysics* 295, 187–197.
- Dutta, D., Biswas, T., Mukherjee, S., 2019. Arc-parallel compression in the NW Himalaya: evidence from structural and palaeostress studies of brittle deformation from the clasts of the Upper Siwalik, Uttarakhand, India. *Journal of Earth System Science* 128, 125.
- El Ouardi, H., Karaoui, B., Mahmoudi, A., El Azmi, M., Zouhair, M., 2016. Microtectonic analysis of the copper-bearing deposits of Bouskour mining district at Saghro inlier (Anti-Atlas, Morocco). *Geo-Temas* 16, 113–116.
- El-Wahed, M.A.A., Kamha, S.Z., 2010. Pan-African dextral transpressive duplex and flower structure in the Central Eastern Desert of Egypt. *Gondwana Research* 18, 315–336.
- Federico, L., Crispini, L., Scambelluri, M., Capponi, G., 2007. Different PT paths recorded in a tectonic mélange (Voltri Massif, NW Italy): implications for the exhumation of HP rocks. *Geodinamica Acta* 20, 3–19.
- Fodor, L., Sztanó, O., Kövér, S., 2013. Pre-conference field trip: mesozoic deformation of the northern transdanubian range (Gerecse and Vértes Hills). *Acta Mineralogica-Petrographica. Field Guide Series* 31, 1–34.
- Fogarasi, A., 1995. Sedimentation on tectonically controlled submarine slopes of Cretaceous age, Gerecse Mts., Hungary—working hypothesis. *Általános Földtani Szemle* 27, 15–41.
- Fondriest, M., Smith, S.A.F., Di Toro, G., Zampieri, D., Mitterpergher, S., 2012. Fault zone structure and seismic slip localization in dolostones, an example from the Southern Alps. Italy. *Journal of Structural Geology* 45, 52–67.
- Frenzel, M., Woodcock, N.H., 2014. Cockade breccia: product of mineralisation along dilational faults. *Journal of Structural Geology* 68, 194–206.
- Ghisetti, F., 1987. Mechanisms of thrust faulting in the gran sasso chain, central apennines, Italy. *Journal of Structural Geology* 9, 955–967.
- Ghisetti, F., Vezzani, L., 1991. Thrust belt development in the central Apennines (Italy): northward polarity of thrusting and out-of-sequence deformations in the Gran Sasso Chain. *Tectonics* 10 (5), 904–919.
- Ghosh, S.K., 1993. *Structural Geology: Fundamentals and Modern Developments*. Pergamon Press, Oxford.
- Greiling, R.O., Garfunkel, Z., Zachrisson, E., 1998. The orogenic wedge in the central Scandinavian Caledonides: Scandian structural evolution and possible influence on the foreland basin. *GFF* 120, 181–190.
- Hancock, P.L., 1985. Brittle microtectonics: principles and practice. *Journal of Structural Geology* 7, 437–457.
- Hardy, S., Poblet, J., 1994. Geometric and numerical model of progressive limb rotation in detachment folds. *Geology* 22, 371–374.
- Hirth, G., Tullis, J., 1994. The brittle-plastic transition in experimentally deformed quartz aggregates. *Journal of Geophysical Research - Solid Earth* 99, 11,731–11,747.
- Hogan, P.J., Burbank, D.W., 1996. Evolution of the Jaca piggyback basin and emergence of the External Sierra, southern Pyrenees. In: Friend, P.F., Dabrio, C.J. (Eds.), *Tertiary Basins of Spain: the Stratigraphic Record of Crustal Kinematics*. vol. 6. Cambridge Univ. Press, pp. 153–160.
- Hoogerduijn Strating, E.H., Vissers, R.L.M., 1994. Structures in natural serpentinite gouges. *Journal of Structural Geology* 16, 1205–1215.
- Hossain, M.S., Khan, M.S.H., Chowdhury, K.R., Abdullah, R., 2019. Synthesis of the tectonic and structural elements of the Bengal Basin. In: Mukherjee, S. (Ed.), *Tectonics & Structural Geology: Indian Context*. Springer International Publishing AG, Cham. https://doi.org/10.1007/978-3-319-99341-6_6.
- Hossain, M.S., Khan, M.S.H., Abdullah, R., Chowdhury, K.R., 2020. Tectonic development of the Bengal Basin in relation to fold-thrust belt to the east and to the north. In: Biswal, T.K., Ray, S.K., Grasemann, B. (Eds.), *Structural Geometry of Mobile Belts of the Indian Subcontinent*. Springer Nature Switzerland AG, pp. 91–109. https://doi.org/10.1007/978-3-030-40593-9_4.
- Jaroszewski, W., 1984. *Fault and Fold Tectonics (Translated)*. J. Wiley & Sons. 565 p.
- Karanth, R.V., Gadhave, M.S., 2007. Structural intricacies: emergent thrusts and blind thrusts of central Kachchh, western India. *Current Science* 93, 1271–1280.
- Karkanis, P., 1995. The slip-fiber chrysotile asbestos deposit in the Zidani area, northern Greece. *Ore Geology Reviews* 10, 19–29.

- Katayama, I., Parkinson, C.D., Okamoto, K., Nakajima, Y., Maruyama, S., 2000. Supersiliciclinopyroxene and silica exsolution in UHPM eclogite and pelitic gneiss from the Kokchetav massif, Kazakhstan. *American Mineralogist* 85, 1368–1374.
- Katz, Y., Weinberger, R., Aydin, A., 2004. Geometry and kinematic evolution of Riedel shear structures, Capitol Reef National Park, Utah. *Journal of Structural Geology* 26, 491–501.
- Kodama, K.P., Anastasio, D.J., Newton, M.L., Pares, J.M., Hinnov, L.A., 2010. High-resolution rock magnetic cyclostratigraphy in an Eocene flysch, Spanish Pyrenees. *Geochemistry, Geophysics, Geosystems* 11, Q0AA07.
- Leah, H., Fondriest, M., Lucca, A., Storti, F., Balsamo, F., Di Toro, G., 2018. Coseismic extension recorded within the damage zone of the Vado di Ferruccio Thrust Fault, Central Apennines, Italy. *Journal of Structural Geology* 114, 121–138.
- Lucca, A., Storti, F., Balsamo, F., Clemenzi, L., Fondriest, M., Burgess, R., Di Toro, G., 2019. From submarine to subaerial out-of-sequence thrusting and gravity-driven extensional faulting: Gran Sasso Massif, Central Apennines, Italy. *Tectonics* 38, 4155–4184.
- Ludman, A., West Jr., D.P. (Eds.), 1999. The Norumbega Fault System of the Northern Appalachians. vol. 331. Geological Society of America Special Paper, p. 199.
- Martins-Ferreira, M.A.C., Chemale Jr., F., Dias, A.N.C., Campos, J.E.G., 2018a. Proterozoic intracontinental basin succession in the western margin of the São Francisco Craton: constraints from detrital zircon geochronology. *Journal of South American Earth Sciences* 81, 165–176.
- Martins-Ferreira, M.A.C., Campos, J.E.G., Von Huelsen, M.G., 2018b. Tectonic evolution of the Paranoá basin: new evidence from gravimetric and stratigraphic data. *Tectonophysics* 734, 44–58.
- Masoch, S., Fondriest, M., Preto, N., Secco, M., Di Toro, G., 2019. Seismic cycle recorded in cockade-bearing faults (Col de Teghime, Alpine Corsica). *Journal of Structural Geology* 129, 103889.
- Millán, H., 1996. Estructura y cinemática del frente de cabalgamiento surpirenaico en las Sierras Exteriores Aragonesas. Tesis Doctoral, Universidad de Zaragoza. 330 pp.
- Misra, A.A., Mukherjee, S., 2017. Dyke-brittle shear relationships in the Western Deccan Strike Slip Zone around Mumbai (Maharashtra, India). In: Mukherjee, S., Misra, A.A., Calvès, G., Nemčok, M. (Eds.), *Tectonics of the Deccan Large Igneous Province*. vol. 445. Geological Society, London, Special Publications, pp. 269–295.
- Misra, A.A., Bhattacharya, G., Mukherjee, S., Bose, N., 2014. Near N–S paleo extension in the western Deccan region in India: does it link strike-slip tectonics with India-Seychelles rifting? *International Journal of Earth Sciences* 103, 1645–1680.
- Misra, A.A., Sinha, N., Mukherjee, S., 2015. Repeat ridge jumps and microcontinent separation: insights from NE Arabian Sea. *Marine and Petroleum Geology* 59, 406–428.
- Mooney, W., Beroza, G., Kind, R., 2007. Fault zones from top to bottom. In: Handy, M.R., Hirth, G., Hovius, N. (Eds.), *Tectonic Faults—Agents of Change on a Dynamic Earth*. Dahlem Workshop Report. vol. 95. The MIT Press, Cambridge, MA, United States, pp. 2–46.
- Mukherjee, S., 2010a. Structures at meso- and micro-scales in the Sutlej section of the Higher Himalayan Shear Zone in Himalaya. *e-Terra* 7, 1–27.
- Mukherjee, S., 2010b. Microstructures of the Zaskar shear zone. *Earth Science India* 3, 9–27.
- Mukherjee, S., 2012a. Tectonic implications and morphology of trapezoidal mica grains from the Sutlej section of the Higher Himalayan Shear Zone, Indian Himalaya. *The Journal of Geology* 120, 575–590.
- Mukherjee, S., 2012b. A microduplex. *International Journal of Earth Sciences* 101, 503.
- Mukherjee, S., 2013a. *Deformation Microstructures in Rocks*. Springer.
- Mukherjee, S., 2013b. Higher Himalaya in the Bhagirathi section (NW Himalaya, India): its structures, backthrusts and extrusion mechanism by both channel flow and critical taper mechanism. *International Journal of Earth Sciences* 102, 1851–1870.
- Mukherjee, S., 2013c. Channel flow extrusion model to constrain dynamic viscosity and Prandtl number of Higher Himalayan Shear Zone. *International Journal of Earth Sciences* 102, 1811–1835.
- Mukherjee, S., 2014a. *Atlas of Shear Zone Structures in Meso-scale*. Springer.
- Mukherjee, S., 2014b. Review of flanking structures in meso- and micro-scales. *Geological Magazine* 151, 957–974.
- Mukherjee, S., 2015. A review on out-of-sequence deformation in the Himalaya. In: Mukherjee, S., Carosi, R., van der Beek, P., Mukherjee, B.K., Robinson, D. (Eds.), *Tectonics of the Himalaya*. vol. 412. Geological Society, London. Special Publication, pp. 67–109.
- Mukherjee, S., 2017. Airy's isostatic model: a proposal for a realistic case. *Arabian Journal of Geosciences* 10, 268.
- Mukherjee, S., 2019. Particle tracking in ideal faulted blocks using 3D co-ordinate geometry. *Marine and Petroleum Geology* 107, 508–514.
- Mukherjee, S., Agarwal, I., 2018. Shear heat model for gouge free dip-slip listric normal faults. *Marine and Petroleum Geology* 98, 397–400.
- Mukherjee, S., Chakraborty, M., 2020. 3D-slip analyses of listric faults with ideal geometries. *Marine and Petroleum Geology* 112, 104092.
- Mukherjee, S., Koyi, H.A., 2010a. Higher Himalayan Shear Zone, Sutlej section: structural geology and extrusion mechanism by combination of simple shear, pure shear and channel flow in shifting modes. *International Journal of Earth Sciences* 99, 1267–1303.
- Mukherjee, S., Koyi, H.A., 2010b. Higher Himalayan Shear Zone: Zaskar Indian Himalaya-Microstructural studies and extrusion mechanism by a combination of simple shear and channel flow. *International Journal of Earth Sciences* 99, 1267–1303.
- Mukherjee, S., Tayade, L., 2019. Kinematic analyses of brittle roto-translational planar and listric faults based on various rotational to translational velocities of the faulted blocks. *Marine and Petroleum Geology* 107, 326–333.
- Mukherjee, S., Bose, N., Ghosh, R., Dutta, D., Misra, A.A., Kumar, M., Dasgupta, S., Biswas, T., Joshi, A., Limaye, M., 2020. *Structural Geological Atlas*. Springer. ISBN: 978-981-13-9825-4.
- Navabpour, P., Angelier, J., Barrier, E., 2007. Cenozoic post-collisional brittle tectonic history and stress reorientation in the High Zagros Belt (Iran, Fars Province). *Tectonophysics* 432, 101–131.
- Novakova, L., 2010. Detailed brittle tectonic analysis of the limestones in the quarries near Vápenná village. *Acta Geodynamica et Geomaterialia* 7, 1–8.

- Novakova, L., 2014. Evolution of paleostress fields and brittle deformation in Hronov-Poříčí Fault Zone. Bohemian Massif. *Studia Geophysica et Geodaetica* 58, 269–288.
- Oliva-Urcia, B., Beamud, E., Garcés, M., Arenas, C., Soto, R., Pueyo, E.L., Pardo, G., 2016. New magnetostratigraphic dating of the Palaeogenesyntectonic sediments of the west-central Pyrenees: tectonostratigraphic implications. *Geological Society, London, Special Publications* 425, SP425–5.
- Oliva-Urcia, B., Beamud, E., Arenas, C., Pueyo, E.L., Garcés, M., Soto, R., Valero, L., Pérez-Rivarés, G., 2019. Dating the northern deposits of the Ebro foreland basin; implications for the kinematics of the SW Pyrenean front. *Tectonophysics* 765, 11–34.
- Pace, P., Calamita, F., 2015. Coalescence of fault-bend and fault-propagation folding in curved thrust systems: an insight from the Central Apennines, Italy. *Terra Nova* 27, 175–183.
- Pace, P., Di Domenica, A., Di Calamita, F., 2014. Summit low-angle faults in the Central Apennines of Italy: younger-on-older thrusts or rotated normal faults? Constraints for defining the tectonic style of thrust belts. *Tectonics* 33, 756–785.
- Pace, P., Pasqui, V., Tavarnelli, E., Calamita, F., 2017. Foreland-directed gravitational collapse along curved thrust fronts: insights from a minor thrust-related shear zone in the Umbria-Marche belt, central-northern Italy. *Geological Magazine* 154, 381–392.
- Passchier, C.W., Trouw, R.A.J., 2005. *Microtectonics*. Springer, Berlin. 371 pp.
- Pease, V., Argent, J., 1999. The northern Sacramento mountains, SW United States, Part I: structural profile through a crustal extensional detachment system. In: MacNiocaill, C., Ryan, P. (Eds.), *Continental Tectonics*. vol. 164. Geological Society of London Special Publication, pp. 179–198.
- Pease, V., Foster, D., Wooden, J., O’Sullivan, P., Argent, J., Fanning, C., 1999. The northern Sacramento mountains, SW United States, Part II: exhumation history and detachment faulting. In: MacNiocaill, C., Ryan, P. (Eds.), *Continental Tectonics*. vol. 164. Geological Society of London Special Publication, pp. 199–237.
- Petit, J.P., 1987. Criteria for the sense of movement on fault surfaces in brittle rocks. *Journal of Structural Geology* 9, 597–608.
- Placer, L., Vrabec, M., Celarc, B., 2010. The bases for understanding of the NW Dinarides and Istria Peninsula tectonics. *Geologija* 53, 55–86.
- Polino, R., Dal Piaz, G.V., Gosso, G., 1990. Tectonic erosion at the Adria margin and accretionary processes for the Cretaceous orogeny of the Alps. *Mémoires. Société Géologique France* 156, 345–367.
- Poljak, M., Živčić, M., Zupančič, P., 2000. The seismotectonic characteristics of Slovenia. *Pure and Applied Geophysics* 157, 37–55.
- Price, N.A., Johnson, S.E., Gerbi, C.C., West Jr., D.P., 2012. Identifying deformed pseudotachylite and its influence on the strength and evolution of a crustal shear zone at the base of the seismogenic zone. *Tectonophysics* 518–521, 63–83. <https://doi.org/10.1016/j.tecto.2011.11.011>.
- Pueyo, E.L., Millán, H., Pocovi, A., 2002. Rotation velocity of a thrust: a paleomagnetic study in the External Sierras (Southern Pyrenees). *Sedimentary Geology* 146, 191–208.
- Ramsay, J.G., Huber, R., 1983. The techniques of modern structural geology. In: *Strain Analysis*. vol. 1. Academic Press, New York, NY, p. 307.
- Rattenbury, M.S., Townsend, D.B., Johnston, M.R., 2006. *Geology of the Kaikoura Area*. Scale 1:250000. GNS Science, Lower Hutt, New Zealand.
- Ravna, E.J.K., Andersen, T.B., Jolivet, L., De Capitani, C., 2010. Cold subduction and the formation of lawsonite/eclogite—constraints from prograde evolution of eclogitized pillow lava from Corsica. *Journal of Metamorphic Geology* 28, 381–395.
- Reinoso, F., Díaz-Alvarado, J., Fernández, C., 2020. Structural characteristics of the “Puquios chaos” and its relationship with the Andean middle Cretaceous extensional tectonics at 27°S, northern Chile. *Journal of South American Earth Sciences* 98, 102454.
- Rodríguez-Pintó, A., Pueyo, E.L., Serra-Kiel, J., Samsó, J.M., Barnolas, A., Pocovi, A., 2012. Lutetian magnetostratigraphic calibration of larger foraminifera zonation (SBZ) in the Southern Pyrenees: the Isuela section. *Palaeogeography, Palaeoclimatology, Palaeoecology* 333, 107–120.
- Rothery, E., 1988. En-echelon vein array development in extension and shear. *Journal of Structural Geology* 10, 63–71.
- Rykkelid, E., Fossen, H., 2002. Layer rotation around vertical fault overlap zones: observations from seismic data, field examples, and physical experiments. *Marine and Petroleum Geology* 19, 181–192.
- Sasvári, Á., Csontos, L., Palotai, M., 2009. Structural geological observations in tölgyhát quarry (Gerecse mts., Hungary). *Földtani Közlöny* 139, 55–66.
- Shaikh, M., Maurya, D.M., Mukherjee, S., Vanik, N., Padmalal, A., Chamyal, L., 2020. Tectonic evolution of the intra-uplift Vigodi-Gugriana-Khirsara-Netra Fault System in the seismically active Kachchh Rift Basin, India: implications for the western continental margin of the Indian plate. *Journal of Structural Geology* 140, 104124.
- Shimamoto, T., Togo, T., 2012. Earthquakes in the lab. *Science* 338, 54–55.
- Sibson, R.H., 1975. Generation of pseudotachylite by ancient seismic faulting. *Geophysical Journal International* 43, 775–794.
- Sibson, R.H., Toy, V.G., 2006. The habit of fault-generated pseudotachylite: presence vs. absence of friction-melt. In: Abercrombie, R., McGarr, A., Di Toro, G., Kanamori, H. (Eds.), *Earthquakes: Radiated Energy and the Physics of Faulting*. Geophysical Monograph Series, vol. 170, pp. 153–166.
- Silva-Casal, R., Aurell, M., Payros, A., Pueyo, E.L., Serra-Kiel, J., 2019. Carbonate ramp drowning caused by flexural subsidence: the South Pyrenean middle Eocene foreland basin. *Sedimentary Geology* 393, 105538.
- Simpson, C., 1985. Deformation of granitic rocks across the brittle-ductile transition. *Journal of Structural Geology* 7, 503–511.
- Smyth, J.R., 1980. Cation vacancies and the crystal chemistry of breakdown reactions in kimberlitic omphacites. *American Mineralogist* 65, 1185–1191.
- Špaček, P., Sýkorová, Z., Pazdírková, J., Švancara, J., Havří, J., 2006. Present-day seismicity of the south-eastern Elbe Fault System (NE Bohemian Massif). *Studia Geophysica et Geodaetica* 50, 233–258.
- Spray, J., 1992. A physical basis for the frictional melting of some rock-forming minerals. *Tectonophysics* 204, 201–221.
- Srivastava, D.C., John, G., 1999. Deformation in the Himalayan Frontal Fault Zone: evidence from small-scale structures in Mohand-Khara area, NW Himalaya. In: Jain, A.K., Manickavasagam (Eds.), *Geodynamics of the NW Himalaya*. Gondwana Research Group Memoir, pp. 273–284.
- Suppe, J., Medwedeff, D.A., 1990. Geometry and kinematics of fault-propagation folding. *Eclogae Geologicae Helveticae* 83, 409–454.
- Swanson, M., 1992. Fault structure, wear mechanisms and rupture processes in pseudotachylite generation. *Tectonophysics* 204, 223–242.
- Tari, G., 1994. *Alpine Tectonics of the Pannonian Basin*. Ph.D. thesis, Rice University, Texas, USA. 501 p.

- Tavarnelli, E., 1994. Analisi geometrica e cinematica dei sovrascorrimenti compresi fra la valnerina e la conca di Rieti (Appennino Umbro-Marchigiano-Sabino). *Bollettino della società Geologica Italiana* 113, 249–259.
- Tavarnelli, E., 1999. Normal faults in thrust sheets: pre-orogenic extension, post-orogenic extension, or both? *Journal of Structural Geology* 21, 1011–1018.
- Teisseyre, H., 1959. Einige Bemerkungen über die Methodik der Mikrostrukturen in der tektonischen Forschung. *Freiberger Forsch.*, Hft. c.57.
- Tesi, T., Collettini, C., Viti, C., Barchi, M.R., 2013. Fault architecture and deformation mechanisms in exhumed analogues of seismogenic carbonate-bearing thrusts. *Journal of Structural Geology* 55, 1–15.
- Tjia, H.D., 1964. Slickensides and fault movements. *Geological Society of America Bulletin* 75, 683–686.
- Togo, T., Shimamoto, T., 2012. Energy partition for grain crushing in quartz gouge during subseismic to seismic fault motion: an experimental study. *Journal of Structural Geology* 38, 139–155.
- Törő, B., Pratt, B.R., Renaut, R.W., 2013. Paleoseismic Indicators in the Lacustrine Green River Formation (Eocene, USA)—Characteristics and Implications. vol. 45 *Geological Society of America Abstracts with Programs*, p. 357.
- Trouw, R.A.J., Passchier, C.W., Wiersma, D.J., 2010. *Atlas of Mylonites and Related Microstructures*. Springer.
- Tullis, T.E., Bürgmann, R., Cocco, M., Hirth, G., King, G.C.P., Oncken, O., Otsuki, K., Rice, J.R., Rubin, A., Segall, P., Shapiro, S.A., Wibberley, C.A.J., 2007. Group report: rheology of fault rocks and their surroundings. In: Handy, M.R., Hirth, G., Hovius, N. (Eds.), *Tectonic Faults—Agents of Change on a Dynamic Earth*. Dahlem Workshop Report. vol. 95. The MIT Press, Cambridge, MA, United States, pp. 183–204.
- Valenta, J., Gazdova, R., Kolinsky, P., 2011. Seismo-hydrological monitoring in the area of the Hronov-Porčí fault zone, northern Czech Republic, Central Europe. vol. 2011 *American Geophysical Union. Fall Meeting*, pp. S11B–S2211.
- Vanik, N., Shaikh, H., Mukherjee, S., Maurya, D.M., Chamyal, L.S., 2018. Post-Deccan trap stress reorientation under transpression: evidence from fault slip analyses from SW Saurashtra, western India. *Journal of Geodynamics* 121, 9–19.
- Vanossi, M., Cortesogno, L., Galbiati, B., Messiga, B., Piccardo, G., Vannucci, R., 1984. *Geologia delle Alpi Liguri: dati, problemi, ipotesi*. Memorie della Società Geologica Italiana 28, 5–75.
- Vignaroli, G., Rossetti, F., Rubatto, D., Theye, T., Lisker, F., Phillips, D., 2010. Pressure-Temperature-Deformation-time (P-T-d-t) exhumation history of the Voltri Massif HP-complex, Ligurian Alps, Italy. *Tectonics* 29, TC6009.
- Vignaroli, G., Rossetti, F., Belardi, G., Billi, A., 2011. Linking rock fabric to fibrous mineralization: a basic tool for the asbestos hazard. *Natural Hazards and Earth Science Systems* 11, 1267–1280.
- Woldřich, J.N., 1901. Earthquake in the north-eastern Bohemia on January 10, 1901 [in Czech]. *Transaction of the Academic Sciences of the Czech Republic, Series II* 10, 1–33.
- World Health Organization, 1986. *Asbestos and Other Natural Mineral Fibres*. Environmental Health Criteria, Geneva. No. 53.
- Yajoui, Z., 2019. *Ediacaran-Cambrian Evolution of the Northeastern Edge of Sagro Inlier (Eastern Anti-Atlas, Morocco): Insights From Physical Structural Analysis and Metallogenic Implication*. Moulay Ismail University. PhD thesis.
- Yao, L., Shimamoto, T., Ma, S., Han, R., Mizoguchi, K., 2013. Rapid postseismic strength recovery of Pingxi fault gouge from the Longmenshan fault system: experiments and implications for the mechanisms of high-velocity weakening of faults. *Journal of Geophysical Research* 118, 1–17.

Chapter 4

Boudins and mullions

Local brittle–ductile extension partially or completely separate clasts. These segmented clasts are called boudins. Asymmetric boudins can be used to decipher shear sense (Goscombe et al., 2004). See Abe et al. (2013) for fracture patterns in boudinage. Mullions are *linear fluted structures developed within a rock or at lithological interfaces* (Twiss and Moores, 2007). Depending on their geneses, Twiss and Moores (2007) classified them into three types: fold mullion, fault mullion, and irregular mullion. The viscosity contrast between the boudinaged/mullion material and the host rock is one of the controlling factors of their geometries (Sokoutis, 1990; Talbot, 1999; Schmalholz et al., 2008; Schmalholz and Maeder, 2012). Maeder et al. (2009) used the term “segment structure” to describe boudins and mullions together (Figures 4.1–4.31). Mukherjee (2014a,b) reviewed terms to describe boudins in the light of flanking structures. See Mukherjee et al. (2020) for shear fabrics from other terrains, and Mukherjee (2017) for symmetric structures in shear zones.

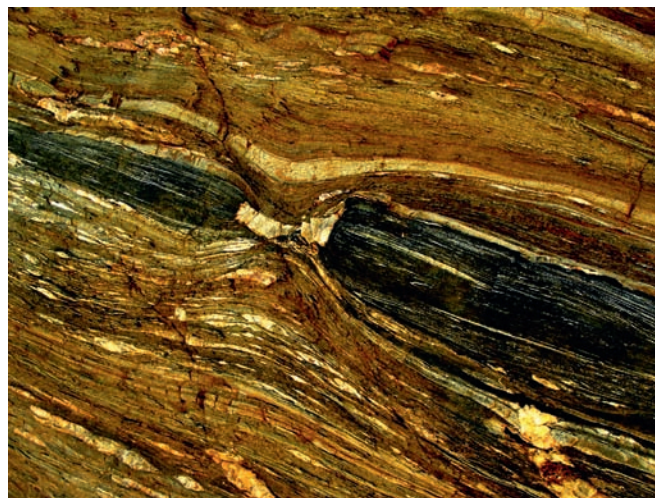


FIGURE 4.1 Photograph from the Gaub Canyon, Namibia, showing a boudinaged metabasalt layer enveloped by metaturbidites in the Southern Marginal Zone of the Damara Belt. The rocks deformed during the Neoproterozoic to Cambrian, Pan African assembly of Gondwana (e.g., Barnes and Sawyer, 1980), with peak metamorphic conditions in the amphibolite facies. The rock assemblage comprises metamorphosed basalt, sandstone, mudstone, and chert, which represent intercalated continental and oceanic materials that were likely deformed in an accretionary prism (Kukla and Stanistreet, 1991). The photo highlights the rheological contrasts that develop through the intercalation of lithologies of variable viscosity. In this case, the basaltic layer has fractured in the boudin neck, allowing the formation of a quartz vein, whereas metasediments are locally folded to fill the gap between the boudins of metabasalt. This provides an example of mixed brittle–viscous deformation at temperatures in excess of the brittle to viscous transition in quartzofeldspathic rocks, and a possible geological analogue to the mixture of transient creep and episodic brittle failure inferred to be responsible for deep tremor and slow slip in active subduction zones (Fagereng et al., 2014). Photo width: ~2 m. Ake Fagereng



FIGURE 4.2 Structure related to dyke, 2. Schistose quartz-andesite dike (black) in sharp contact with Umm-Maghra granodioritic gneiss (white) country rock. The dike was later faulted and segments underwent left-lateral rotation. Wadi Umm-Maghra NE Sinai, Egypt. Readers are encouraged to seek an alternate logical interpretation of the structural geology of the snap. **Yehuda Eyal**



FIGURE 4.3 Boudinaged quartz vein within metagreywacke. Kumbhalgarh Formation, ~85 km northwest of Udaipur, Rajasthan, India. **Swagato Dasgupta**

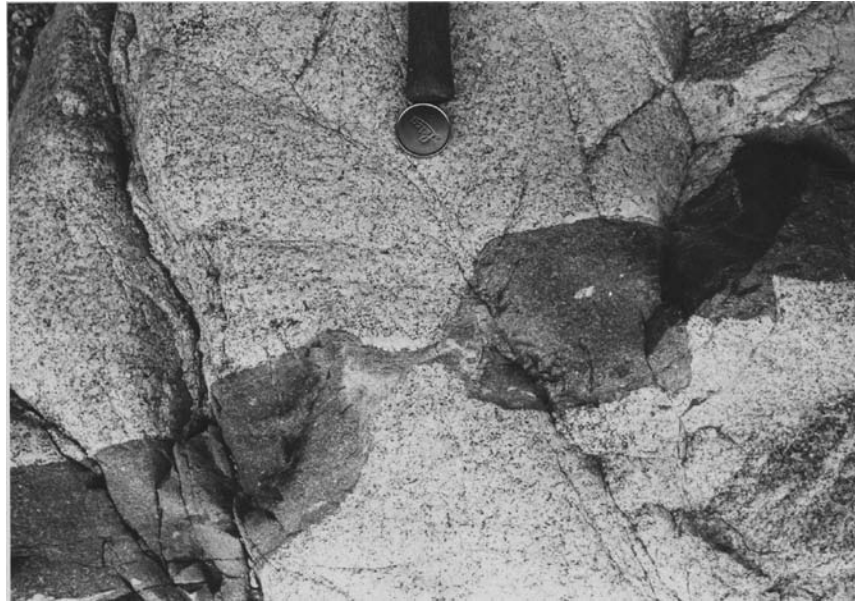


FIGURE 4.4 Boudin. Boudin in Schistose quartz-andesite dike. Intrusion of the andesitic dike occurred before final solidification of the granodiorite when it was still hot and ductile. Wadi Umm-Maghra NE Sinai, Egypt. See Eyal (1980) for detail. **Yehuda Eyal**



FIGURE 4.5 A set of composite boudins (Ghosh, 1993; Ghosh and Sengupta, 1999) with two orders of boudinage. The rock is a migmatite with interlayered amphibolites and quartzofeldspathic gneisses. The small boudins are nested within the larger boudins of the multilayered unit. A layer-normal compression stretched and boudinaged the more competent thinner layers of amphibolites in the central part. With continued deformation, the multilayer as a whole extended and successively boudinaged into composite boudins. Oppositely oriented bending folds near the separation zone of the larger boudins. Pen length: 15 cm. Chhotonagpur Gneissic Complex, Ratanpahar, Jasidih, Jharkhand, India. **Sudipta Sengupta and Sadhana M. Chatterjee**



FIGURE 4.6 Asymmetric Boudins. The shear band type asymmetric boudin in a ductile shear regime near the village Kapadkhan in the northern flank of the Almora klippe (Patel et al., 2015; Singh and Patel, 2017); this is a common shear sense indicator (Singh, 2014). GPS location is N 29° 39.93', E 79°42.49'. **Paramjeet Singh**

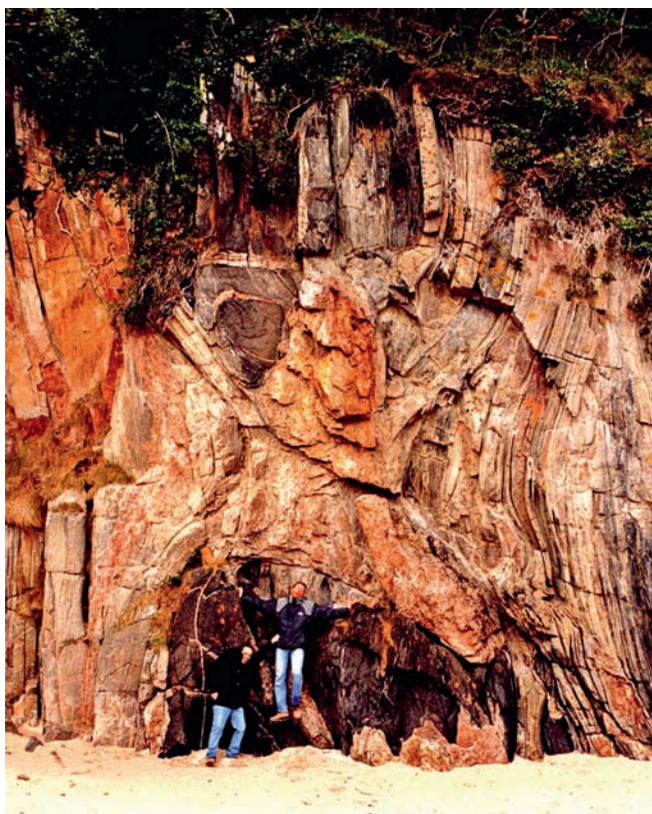


FIGURE 4.7 Boudinaged amphibolite layer within a migmatite gneiss sequence on the shoreline of northern Scotland, near Durness. The dilatation space is filled by two different rock types: the migmatite gneiss layers are symmetrically inflected toward the core. The granite melt from the surrounding migmatite is attracted by the boudin neck free space. **Guido Gosso**



FIGURE 4.8 Boudin, 1. Rock type: Quartzite and metagreywacke. Structure name: Boudin. Location: Tocantinzinho river bank in the Moquem Salient, Chapada dos Veadeiros Region, Northern Goiás State, Brazil. Facies: Lower to intermediate greenschist. Description: Boudinage in a context of (low?) competence contrast between a quartzite layer and an adjacent metagreywacke. The boudins are barrel-shaped with slightly concave extremities. The neck folds are gentle to open and quartz fills up the interboudin space. The brittle-ductile strain imprinted in these necked boudins can be seen in most of the Moquem Salient. **Marco Martins-Ferreira**



FIGURE 4.9 Boudin, 3. Rock type: Orthogneiss. Structure: Boudin. Location: São Luis dos Campos Belos, Arenópolis Magmatic Arc, Western Goiás State, Brazil. Facies: Intermediate amphibolites. Description: Orthogneissic banding with evidence of shearing and boudinage. Different types of boudins occur. At the middle-left of the photo, asymmetric shear boudins can be seen in a thin leucosome band and at the center and middle-right, foliation parallel domino boudins occur affecting a melanosome band. What other structures can you interpret from this image? **Marco Martins-Ferreira**



FIGURE 4.10 Boudin, 4. Rock type: Orthogneiss. Structure: Boudin. Location: São Luis dos Campos Belos, Arenópolis Magmatic Arc, Western Goiás State, Brazil. Facies: Intermediate to higher amphibolites. Description: Orthogneissic banding showing asymmetric shear band boudins. This picture is a zoom from the middle-left region of Figure 4.9. **Marco Martins-Ferreira**



FIGURE 4.11 Boudin, 5. Rock type: Orthogneiss. Structure: Boudin. Location: São Luis dos Campos Belos, Arenópolis Magmatic Arc, Western Goiás State, Brazil. Facies: Intermediate to higher amphibolites. Description: Melanocratic band showing evidence of right-lateral shearing forming gentle folds and boudinage. Boudins present straight extremities indicative of high competence contrast, possibly due to anatexis in the leucocratic bands. Pegmatite with feldspar crystals up to 1 cm occurs, filling the boudins' necks and neck folds range from gentle to tight. **Marco Martins-Ferreira**



FIGURE 4.12 Fold and boudin. Rock type: Orthogneiss. Structure: Fold and Boudin. Location: São Luis dos Campos Belos, Arenópolis Magmatic Arc, Western Goiás State, Brazil. Facies: Intermediate to higher amphibolites. Description: Folded and boudinaged bands of orthogneiss. Possible sheath folds can be seen in the central portion of the photo. **Marco Martins-Ferreira**



FIGURE 4.13 Boudin, 2. Rock type: Quartzite and metagreywacke. Structure: Boudin. Location: Tocantinzinho river bank in the Moquéim Salient, Chapada dos Veadeiros Region, Northern Goiás State, Brazil. Facies: Lower to intermediate greenschist. Description: Boudinage in a context of (low?) competence contrast between a quartzite layer and adjacent metagreywacke. Boudins are lenticular- or pillow-shaped and neck folds are gentle to open. **Marco Martins-Ferreira**



FIGURE 4.14 Pinch and swell structures ~3 ft long. The swells are subelliptical. Rock types: sandstone and mudstone. From the western side of the Rakhavdav complex, Udaipur district, Rajasthan, India. **Moloy Sarkar**

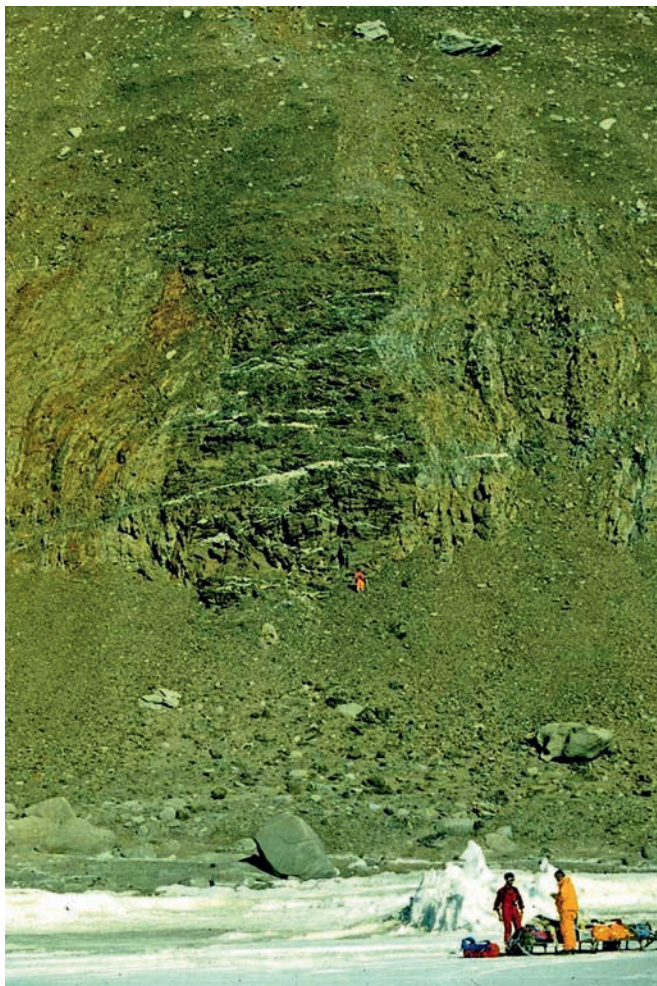


FIGURE 4.15 Pinch and swell structures in two metabasic dykes discordantly hosted by high-grade gneisses on the shoreline facing the Italian Antarctic base at Terra Nova Bay, Northern Victoria Land, Antarctica. Gentle ductile shortening of white veins transecting the thicker dyke neck zone indicates veining penecontemporaneous to pinching and synchronous brittle and ductile deformation in the dyke. A geologist in yellow pants stands for scale atop the scree. **Guido Gosso**

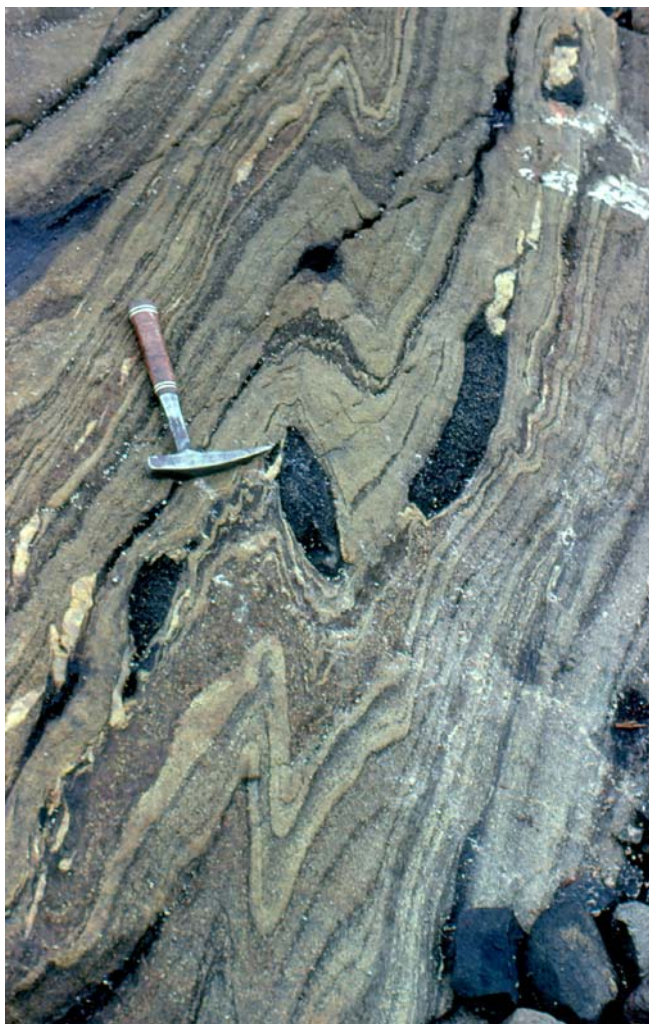


FIGURE 4.16 **Folded amphibolite boudins.** Folded amphibolite boudins and interlayered metaclastic rocks of the Old House Cove Group, Fleur de Lys Supergroup, at Southern Arm, White Bay, Newfoundland (Hibbard, 1988). The combination of extension (boudinaged amphibolite) and shortening (prominent fold) recorded here is likely the result of two distinct deformation phases rather than a single progressive, noncoaxial deformation. On the basis of regional observations, the layer-parallel main phase foliation and boudinage have been attributed to the Early Ordovician obduction of ophiolite over the Fleur de Lys rift-drift sequence (Hibbard, 1983, 1988); the late stage folding has been associated with the Silurian shortening of the terrane. **James Hibbard**

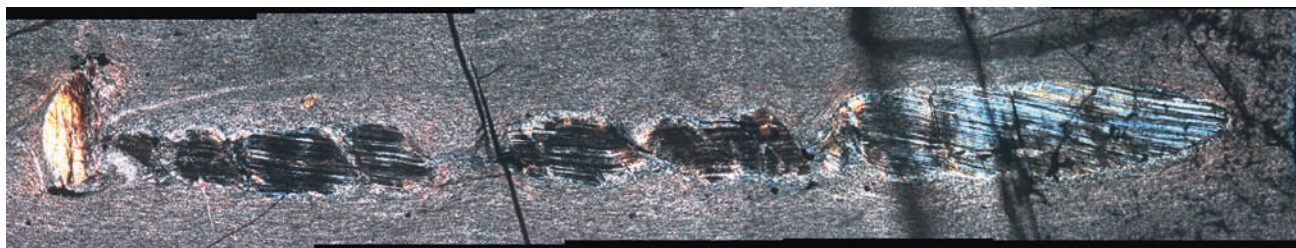


FIGURE 4.17 **Microboudinage structure in an ultramylonitized peridotite.** The boudinage occurred in a mantle orthopyroxene deformed on the [001](100) slip system (e.g., Christensen and Lundquist, 1982). The boudin fragments show patched undulose extinction and subgrains, and are mantled by fine recrystallized grains. Note that the boudin fragment, at left, is rotated 90 degrees with respect to the overall orientation of the clasts. This might make the flow heterogeneous at the edge of the clast. Top-to-left shear. Location: Archipelago of Saint Peter and Saint Paul (Brazil). Crossed polarized light. Width of the view: 7 mm. **Suellen Olívia Cândida Pinto, Leonardo Evangelista Lagoeiro, Luiz Sérgio Amarante Simões, and Paola Ferreira Barbosa**

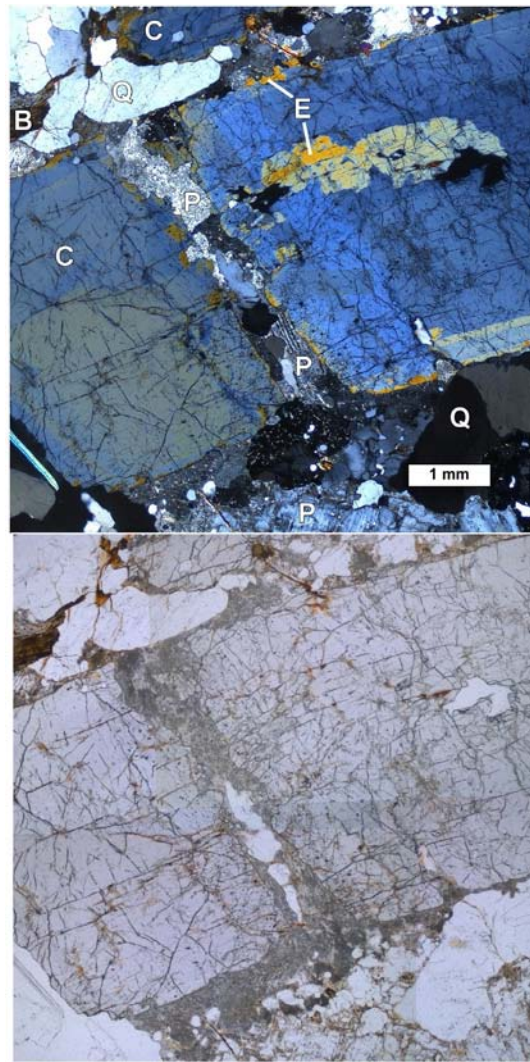


FIGURE 4.18 Bent and microboudinaged magmatic epidote in an epidote pegmatite. The Wenatchee Ridge Orthogneiss cuts the Late Cretaceous pluton (Washington). Among the least deformed are rare magmatic epidote (and clinozoisite) bearing muscovite \pm garnet tonalites. Remarkably, the magmatic epidote ranges up to ~ 10 cm in length. It commonly displays minor deformation in the form of kinks and microboudins, likely developed late as the magma was injected into the slightly younger tonalite pluton. Note the microboudin of the cm-scale clinozoisite crystal, with plagioclase (P) and quartz (Q) crystallized in the gap. Plagioclase is commonly slightly sausseritized, and more Fe-rich epidote (E, very late magmatic?) commonly rims the epidote (or clinozoisite) phenocrysts. Minor biotite (B) is present in a few pegmatites. The large epidote crystals commonly show slight folding, kinking, and deformation twinning. **Jerry F. Magloughlin**



FIGURE 4.19 Chocolate tablet boudins. Lameta Ghat, Jabalpur, Madhya Pradesh, India. **Sreejita Chatterjee**



FIGURE 4.20 A quartz vein boudinaged into nearly rectangular units. Jabalpur, Madhya Pradesh, India. Sreejita Chatterjee



FIGURE 4.21 Rectangular boudinaged quartz veins in calc-schist. A sense of slip of the boudinaged clast near the hammer is top-to-right. South Delhi Fold Belt. Taleti village, Ambaji, Gujarat, India. See [Mukherjee \(2010a,b, 2013a,b, 2014a,b\)](#) and [Mukherjee and Koyi \(2010a,b\)](#) for other boudin varieties from different shear zones. Narayan Bose and Soumyajit Mukherjee



FIGURE 4.22 Boudinaged quartz veins in calc-schist. One of the boudinaged quartz clasts near the center of the photograph is deformed internally and deviates significantly from a rectangular shape. South Delhi Fold Belt. Taleti village, Ambaji, Gujarat, India. **Narayan Bose and Soumyajit Mukherjee**



FIGURE 4.23 Pseudoboudins. A layer of pseudoboudins embedded in chlorite schist is folded asymmetrically due to shearing within the Singhbhum Shear Zone, Jharkhand, India. Pseudoboudins, occurring in a series of rounded pods or lenses, formed due to differential collapse and pinching of the silica-rich vein prior to their crystallization. The individual boudins, showing irregular “cauliflower” shapes, are not as elongated (aspect ratio > 1) as found in the extensional boudinaged structures. **Susanta Kumar Samanta and Dipak C. Pal**



FIGURE 4.24 Boudinaged and sheared vein. Boudinaged and sheared quartz vein within an amphibolites schist, near Kankavli, Maharashtra, India. Namrata Soreng



FIGURE 4.25 Asymmetric rotating domino boudins within low-grade metamorphic carbonate sequence. The domino boudins are made up of dolomite while the surrounding rock is calcite marble. At low-grade conditions, dolomite intercalations act as more competent layers. The calcite marble deforms crystal plastically forming foliated calcite mylonite. The intercalated dolomite layers remain nearly rigid and disrupt into rectangular boudins. The rectangular shape of the dolomite dominos indicates high viscosity contrast during deformation (Fossen, 2010). The domino boudins are asymmetric ones and parallel mylonitic foliation. The individual dominos are separated by small-scale shear zones that die out as soon as they leave the dolomite layer. Some dilatation occur across the interboudin surfaces. Significant rotation of the domino boudins is present, which kept the row of boudins aligned with the general foliation of the calcite mylonite. The stretch magnitude varies along the boudin layers, but usually remains low. Rarely, domino boudins separate completely. Asymmetric domino boudins indicate sinistral shear. Other shear criteria in the field confirmed this. However, asymmetric boudins can be problematic shear-sense indicators (Goscombe and Passchier, 2003), thus requiring additional studies. Triassic limestone and dolomite (Schefer et al., 2010). Photo width ~ 20 cm. Brzeće, Kopaonik Mts., SE Serbia. Coordinates: N43°18'44.05", E20°50'59.75". László Fodor



FIGURE 4.26 Mullions and vertical columns with their characteristic highly penetrative nature in Neoproterozoic quartzites exposed in the western border of the Kalahari Desert, southeast region of Angola, near the Vipongo area. The elongated columns forming the mullions are bound by planes of subvertical northeast-southwest cleavages probably associated with regional transposed folds. Their cylindrical geometry is associated with intense stretching of the rock parallel to the mullions by constriction. These structures in the Kalahari Desert call attention with their appearance of a stack of telegraph poles or even a cut forest with their shopped vertical tree trunks spread along the hill side. Strong brittle to brittle-ductile cleavages in quartzites developed by partitioned sinistral transpression. **Roberto Vizeu Lima Pinheiro**

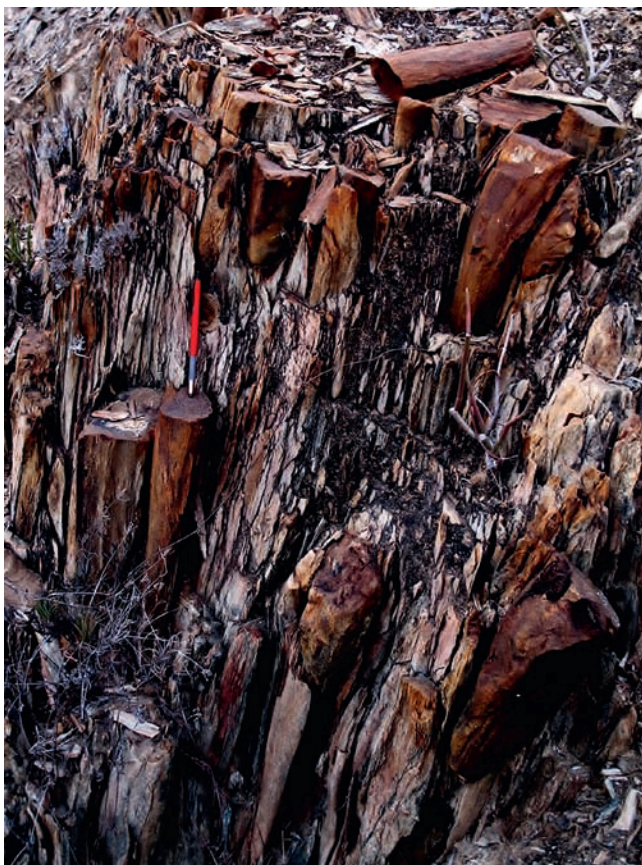


FIGURE 4.27 See the caption of Figure 4.26.



FIGURE 4.28 See the caption of Figure 4.26.



FIGURE 4.29 See the caption of Figure 4.26.



FIGURE 4.30 Mullions within the Precambrian orthoquartzite of the Aravalli Supergroup. Zawar mine area, Udaipur, Rajasthan, India.
Rohini Das



FIGURE 4.31 Gray conglomerate overlying the red mud horizon at Wine Strand, Ballyferriter, County Kerry, Ireland. A flame-type structure is present at the boundary between the units. Is it of primary sedimentary origin due to a density gradient? Or is it a mullion structure of tectonic origin? **Kieran F. Mulchrone and Patrick Meere**

References

- Abe, S., Ural, J., Kettermann, M., 2013. Fracture patterns in nonplane strain boudinage—insights from 3-D discrete element models. *Journal of Geophysical Research: Solid Earth* 118, 1304–1315.
- Barnes, S., Sawyer, E., 1980. An alternative model for the Damara mobile belt: Ocean crust subduction and continental convergence. *Precambrian Research* 13, 297–336.
- Christensen, N.I., Lundquist, S.M., 1982. Pyroxene orientation within the upper mantle. *The Geological Journal of America Bulletin* 93, 282.
- Eyal, Y., 1980. Synplutonic dikes in the Wadi Um-Mara Area, Sinai. *Tectonophysics* 67, 35–44.
- Fagereng, A., Hillary, G.W.B., Diener, J.F.A., 2014. Brittle-viscous deformation, slow slip, and tremor. *Geophysical Research Letters* 41, 4159–4167.
- Fossen, H., 2010. *Structural Geology*. Cambridge University Press, New York.
- Ghosh, S.K., 1993. *Structural Geology: Fundamentals and Modern Developments*. Pergamon Press, Oxford. 598 pp.
- Ghosh, S.K., Sengupta, S., 1999. Boudinage and composite boudinage in superposed deformation and migmatization. *Journal of Structural Geology* 21, 97–110.
- Goscombe, B.D., Passchier, C.W., 2003. Asymmetric boudins as shear sense indicators—an assessment from field data. *Journal of Structural Geology* 25, 575–589.
- Goscombe, B.D., Passchier, C.W., Hand, M., 2004. Boudinage classification, end member boudin types and modified boudin structures. *Journal of Structural Geology* 26, 739–763.
- Hibbard, J., 1983. *Geology of the Baie Verte Peninsula, Newfoundland*. Nfld. Dept. Mines & Energy Memoir 2. 279 p.
- Hibbard, J., 1988. Stratigraphy of the Fleur de Lys Belt, northwestern Newfoundland. In: Winchester, J. (Ed.), *Later Proterozoic Stratigraphy of the North Atlantic Lands*. Blackie and Son Ltd., Glasgow, pp. 200–211.
- Kukla, P.A., Stanistreet, I.G., 1991. Record of the Damaran Khomas Hochland accretionary prism in central Namibia: refutation of an “ensialic” origin of a Late Proterozoic orogenic belt. *Geology* 19, 473–476.
- Maeder, X., Passchier, C.W., Koehn, D., 2009. Modelling of segment structures: boudins, bone-boudins, mullions and related single- and multiphase deformation features. *Journal of Structural Geology* 31, 817–830.
- Mukherjee, S., 2010a. Microstructures of the Zaskar Shear Zone. *Earth Science India* 3, 9–27.
- Mukherjee, S., 2010b. Structures at meso- and micro-scales in the Sulej section of the Higher Himalayan Shear Zone in Himalaya. *e-Terra* 7, 1–27.
- Mukherjee, S., 2013a. *Deformation Microstructures in Rocks*. Springer.
- Mukherjee, S., 2013b. Higher Himalaya in the Bhagirathi section (NW Himalaya, India): its structures, backthrusts and extrusion mechanism by both channel flow and critical taper mechanism. *International Journal of Earth Sciences* 102, 1851–1870.
- Mukherjee, S., 2014a. Review of flanking structures in meso- and micro-scales. *Geological Magazine* 151, 957–974.
- Mukherjee, S., 2014b. *Atlas of Shear-zone Structures in Meso-scale*. Springer.
- Mukherjee, S., 2017. Review on symmetric structures in ductile shear zones. *International Journal of Earth Sciences* 106, 1453–1468.
- Mukherjee, S., Koyi, H.A., 2010a. Higher Himalayan Shear Zone, Zaskar Indian Himalaya-microstructural studies and extrusion mechanism by combination of simple shear and channel flow. *International Journal of Earth Sciences* 99, 1083–1110.
- Mukherjee, S., Koyi, H.A., 2010b. Higher Himalayan Shear Zone, Sulej section: structural geology and extrusion mechanism by combination of simple shear, pure shear and channel flow in shifting modes. *International Journal of Earth Sciences* 99, 1267–1303.

- Mukherjee, S., Bose, N., Ghosh, R., Dutta, D., Misra, A.A., Kumar, M., Dasgupta, S., Biswas, T., Joshi, A., Limaye, M., 2020. Structural Geological Atlas. Springer, ISBN: 978-981-13-9825-4.
- Patel, R.C., Singh, P., Lal, N., 2015. Thrusting and back-thrusting as post-emplacement kinematics of the Almora klippe: insights from Low-temperature thermochronology. *Tectonophysics* 653, 41–51.
- Schefer, S., Egli, D., Missoni, S., Bernoulli, D., Fügenschuh, B., Gawlick, H.-J., Jovanović, D., Krystyn, L., Lein, R., Schmid, S.M., Sudar, M., 2010. Triassic metasediments in the internal Dinarides (Kopaonik area, southern Serbia): stratigraphy, paleogeographic and tectonic significance. *Geologica Carpathica* 61, 89–109.
- Schmalholz, S.M., Maeder, X., 2012. Pinch-and-swell structure and shear zones in viscoplastic layers. *Journal of Structural Geology* 37, 75–88.
- Schmalholz, S.M., Schmid, D.W., Fletcher, R.C., 2008. Evolution of pinch-and-swell structures in a power-law layer. *Journal of Structural Geology* 30, 649–663.
- Singh, P., 2014. Exhumation History of Higher and Lesser Himalayan Crystallines in Kumaon-Garhwal region, NW-India: As Revealed by Fission Track Thermochronology (Unpublished Ph.D. thesis). Department of Geophysics. Kurukshetra University, Kurukshetra.
- Singh, P., Patel, R.C., 2017. Post-emplacement kinematics and exhumation history of the Almora klippe of the Kumaun-Garhwal Himalaya, NW India: revealed by fission track Thermochronology. *International Journal of Earth Sciences* 106 (6), 2189–2202.
- Sokoutis, D., 1990. Experimental mullions at single and double interfaces. *Journal of Structural Geology* 12, 365–373.
- Talbot, C.J., 1999. Can field data constrain rock viscosities? *Journal of Structural Geology* 21, 949–957.
- Twiss, R.J., Moores, E.M., 2007. Structural Geology, second ed. W. H. Freeman and Company, New York. 313 pp.

Chapter 5

Veins

Crosscutting veins found in almost all rock types are perhaps the easiest structures to pick up by novices. One can deduce stress directions by studying the attitude of veins (Fossen, 2016). Veins develop commonly orthogonal to the maximum instantaneous extension axis, and have been considered as a good shear sense indicator (Davis and Reynolds, 1996). Thus, careful study of vein systems (Figures 5.1–5.12) has proved fruitful in tectonic studies (Maeder et al., 2014). Passchier and Trouw (2005) described veins morphologically as fibrous and massive. These two types of veins can have either sharp or fuzzy margins. Leucosome veins cutting across alternate leucosome and melanosome layers are common in migmatites (Mukherjee, 2010, 2014). A recent review on veins of tectonic origin is available in Bons et al. (2012). See Mukherjee et al. (2020) for shear fabrics from other terrains.

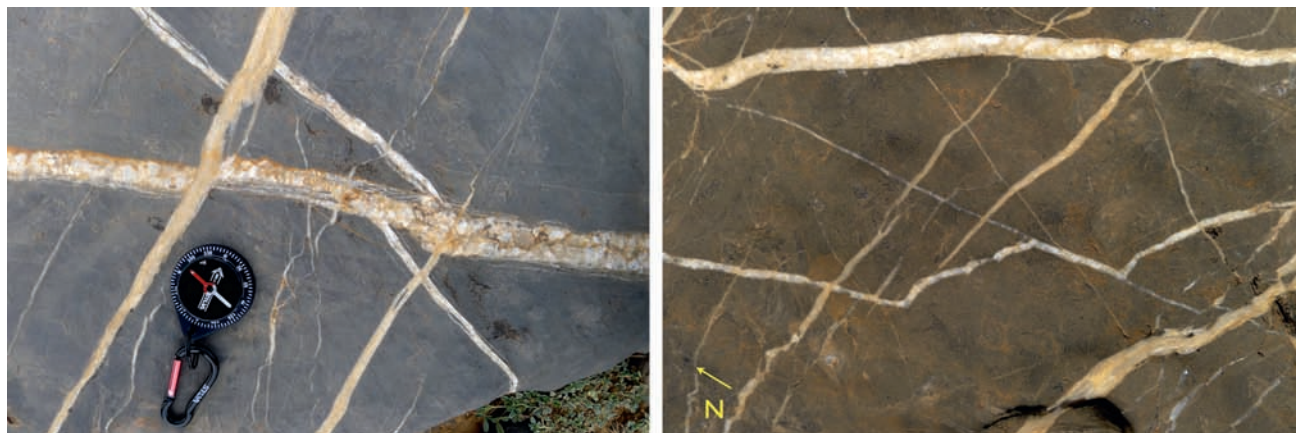


FIGURE 5.1 Vein interaction in a high-pressure cell in limestone. Veins are common in carbonates on the southern flank of the Jabal Akhdar Anticline in the Oman Mountains. The area exposes the autochthonous Hajar Supergroup, deposited in a predominantly passive margin environment and subject to a multi-phase deformation related to the convergence of the Arabian with the Eurasian plate when the Hawasina and the Semail Ophiolite nappes were emplaced onto the Arabian plate margin. This deformation resulted in several successive generations of calcite veins, stylolites, and calcite cemented faults formed in a changing stress regime in a near-lithostatic fluid pressure regime at several km depth at temperatures greater than 200°C. These are exposed in spectacular fashion and quality in a very large area, being perhaps the best exposed complex vein system on Earth. These two outcrop photos illustrate veins at a high angle to bedding in the Natih formation close to the contact with the overlying Muti formation. The first photo shows reasonably clear crosscutting relationships between three generations of veins at a high angle to bedding. The photo was taken looking down on the bedding surface. Veins of different generations have different morphologies, different amounts of solid inclusions, and different degrees of dissolution by later stylolites. We leave the reader to determine the relative sequence of the structures. The second picture shows an example of different vein generations, where overprinting relationships are not so clear. We interpret these patterns to be caused by the interaction of propagating fractures with preexisting veins, causing the fractures to reorient following mechanical heterogeneities. See Hilgers et al. (2006), Holland et al. (2009a,b), Holland and Urai (2010), and Virgo et al. (2013) for details. First picture: 23°14'48.23"N 57°9'15.67"E; the image width is about 30 cm. Second picture: 23°13'58.85"N 57°9'47.05"E; the image width is about 30 cm. **Janos L. Urai, Max Arndt, and Simon Virgo**



FIGURE 5.2 Veins related to dilatant faults are common in carbonates on the southern flank of the Jabal Akhdar Anticline in the Oman Mountains. The area exposes the autochthonous Hajar Supergroup, deposited in a predominantly passive margin environment and subject to a multiphase deformation related to the convergence of the Arabian with the Eurasian plate, when the Hawasina and the Semail Ophiolite nappes were emplaced onto the Arabian plate margin. This deformation resulted in several successive generations of calcite veins, stylolites, and calcite cemented faults formed in a changing stress regime in a near-lithostatic fluid pressure regime at several km depth at temperatures greater than 200°C. These are exposed in spectacular fashion and quality in a very large area, being perhaps the best exposed complex fault system on Earth. The pictures show profile views (looking along the bedding to the west) of an incipient normal fault in the damage zone of a larger fault that has an offset of several tens of m, with striations indicating normal, oblique slip, and strike slip motion. The location is in the Wadi Nakhr, the Grand Canyon of Oman. The fault in the outcrop clearly displaces an earlier set of bedding-parallel veins, and also a set of en-echelon veins that probably grew in the early stages of the deformation phase leading to the fault. The outcrop shows segmentation, drag of bedding, and a fault branch. On the right side of the picture is a weathered-out normal fault, defining a small graben structure. The location is the Fault Wadi Nakhr, 23°11'2.15"N 57°12'23.81"E; the width of the first picture is about 4 m. The second picture is a detail of the first one. For details, see [Holland et al. \(2009a,b\)](#). Janos L. Urai, Simon Virgo, and Max Arndt



FIGURE 5.3 Semiductile shear zone in limestone. Early Permian dark nodular limestones with intervening thin layers of shale were first affected by a late-diagenetic pressure solution along the bedding planes ([Novak, 2007](#)). A small-scale dextral shear zone offsets subvertical limestone beds for a few decimeters. Shearing was absorbed by the opening of the en-echelon extensional veins oblique to the shear zone along the principal shortening, and by a pressure solution perpendicular to the principal shortening direction. This is evidenced by markedly stylolitic solution planes, progressive thinning of beds toward the center of the shear zone, and the abrupt truncations of extensional veins along solution seams. This is a nice example of the semiductile deformation of carbonates under nonmetamorphic conditions, and presents a textbook example of the geometrical arrangement of minor structures in shear zones (cf. [Davis et al., 2012](#)). Rock type: thin-bedded nodular limestone with shale intercalations, Born Formation, early Permian. Field of view: ~1 m. Dovžan gorge, Karavanke mountains, Slovenia. Coordinates: 46°19'47" N, 14°19'47" E. Marko Vrabec



FIGURE 5.4 A quartz vein cut across gneissic foliations. Note that some of the quartzofeldspathic layers are connected with the vein. The gneissose foliation is warped, and we cannot confirm whether the foliation is curved due to any rotation of the vein. Higher Himalaya, Jhakri, Rampur district, Himachal Pradesh, India. Soumyajit Mukherjee

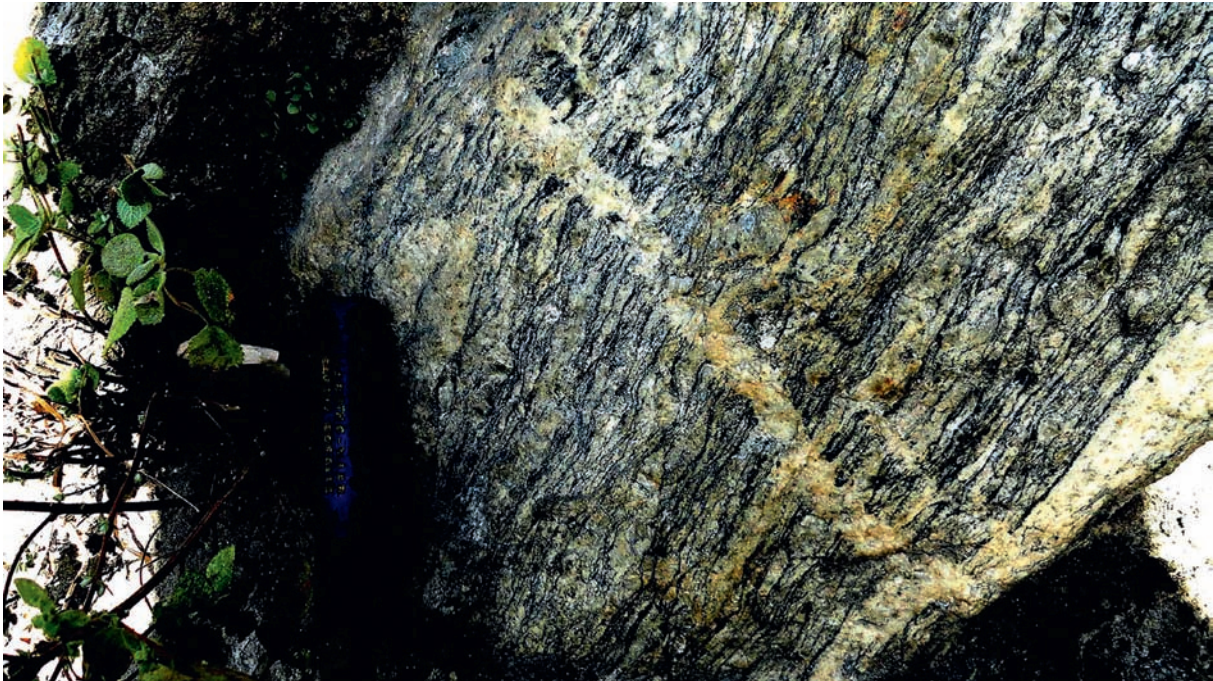


FIGURE 5.5 A quartz-rich vein in a mylonitized gneiss. The quartzofeldspathic foliation within the host rock is connected with the vein. Except for the bottom part of the vein, no clear-cut ductile shear sense can be deciphered from this exposure. Higher Himalaya, Jhakri, Rampur district, Himachal Pradesh, India. Soumyajit Mukherjee



FIGURE 5.6 The bottom part of Figure 5.5 is zoomed. Note a top-to-left (down) ductile shear sense deciphered near the bottom part of the sheared vein. Higher Himalaya, Jhakri, Rampur district, Himachal Pradesh, India. See [Mukherjee \(2007, 2010, 2013a,b\)](#) and [Mukherjee and Koyi \(2010\)](#) for regional geology. See [Mukherjee \(2014\)](#) for more such structures. Soumyajit Mukherjee



FIGURE 5.7 Drag fold. Different styles and intensities of drag noted across and along a quartz vein inside a gneiss ([Singh, 2014](#); [Singh et al., 2012](#); [Singh et al., 2020a,b](#)). Near the Gangotri area of the Vaikrita group of the Higher Himalayan Crystalline, the Garhwal region along the Bhagirathi River, India. Paramjeet Singh

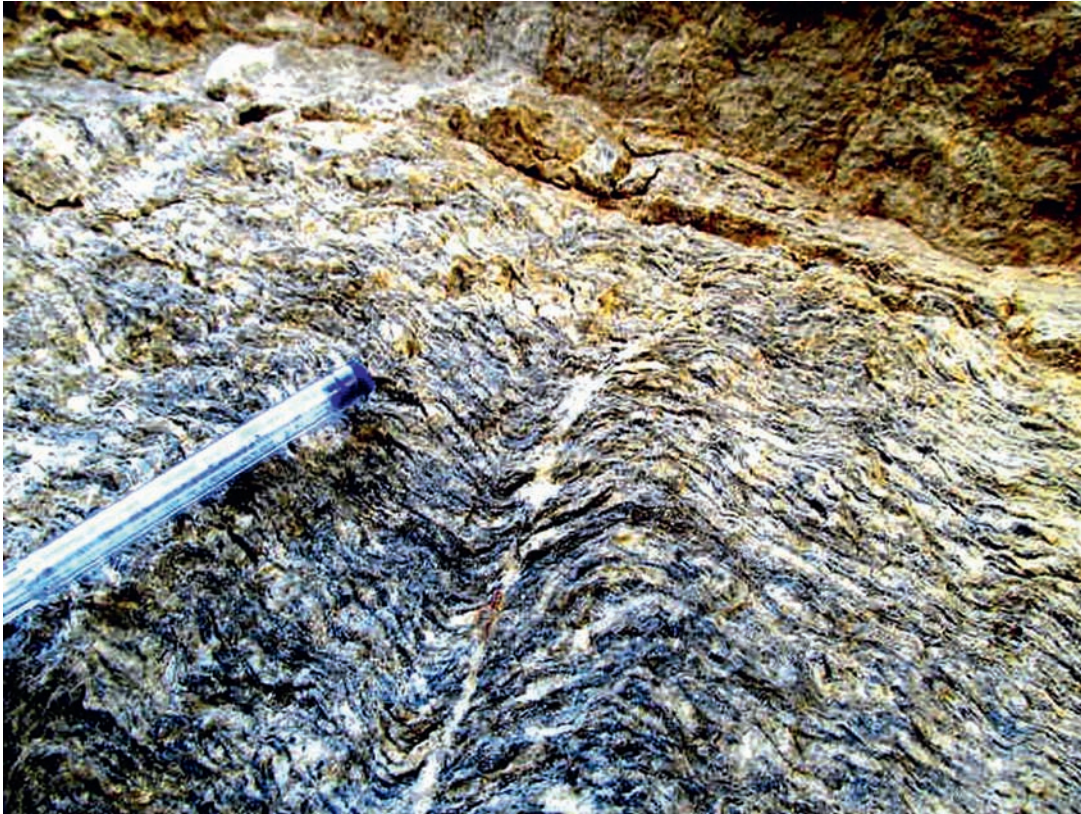


FIGURE 5.8 A thin-curved quartz vein within sheared gneiss, possibly top-to-right sheared. The foliation of the host rock is warped and does not show a clear-cut ductile shear sense. Higher Himalaya, Jhakri, Rampur district, Himachal Pradesh, India. Soumyajit Mukherjee



FIGURE 5.9 Quartz vein network defined mainly by two sets of veins. The set of veins dipping toward the left are usually thicker than that dipping toward the right. Chitradurga district, Karnataka, India. Aabha Singh

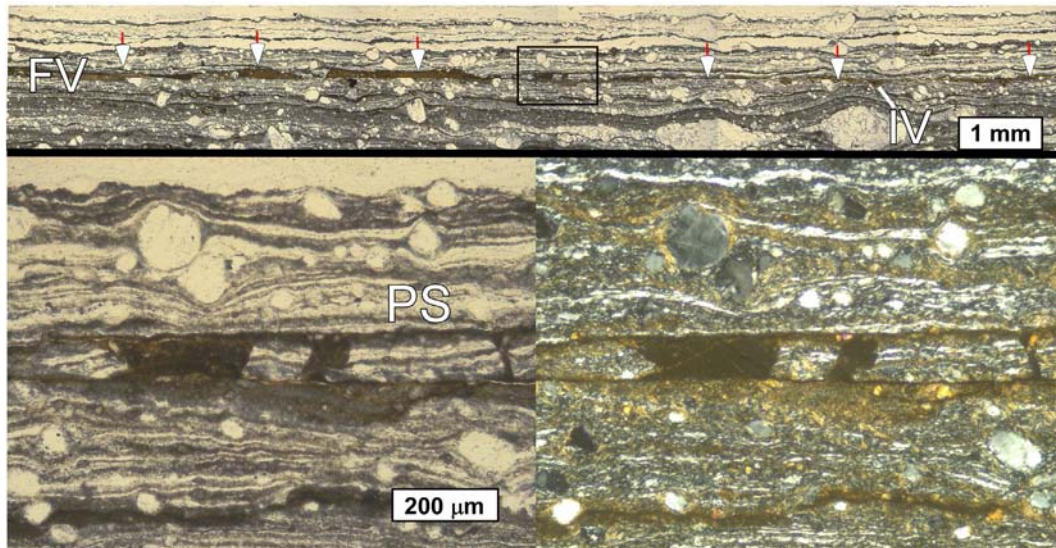


FIGURE 5.10 Microscale pseudotachylyte veins in mylonites. In the Wanapitei Fault east of Sudbury, Ontario, Canada, amphibolites are highly deformed into ultramylonites, displaying extreme grain-size reduction and porphyroclasts of hornblende and feldspar. The rock shows an extremely thin, almost cherty foliation, and in quartz-rich zones there is a strong crystallographic preferred orientation. A variety of brittle or semibrittle microstructures cut the ultramylonites, including exceptionally thin pseudotachylyte veins such as the one shown at the top (PPL photomicrograph). These veins are strongly concordant planar fault veins (FV, and white arrows) where the slip is localized along the mylonitic foliation. The veins commonly range from as little as 5 microns up to 100 microns thick. Despite their unusual thinness, they display several classic characteristics of mesoscopic pseudotachylyte veins: variations in clast abundance, paired shears (PS; PPL image at lower left), very small triangular injection veins (IV), flow banding parallel to the fault veins, and even concentric sheath-fold-like patterns. The lack of thicker pseudotachylyte veins suggests these are not the tips of larger faults, and thus they may represent brittle sliding within the cooling mylonites associated with micro- or nanoequakes. **Jerry F. Magloughlin**



FIGURE 5.11 Relay between two fractures. Relay between two fractures cemented by quartz affecting Ordovician phyllites. Playa de las Catedrales, Galicia, Spain (coordinates: 43°33'14.8"N, 7°09'31.6"W). **Irene Cantarero and Eloi Carola**



FIGURE 5.12 Fluid activity and dyke. The horizontal view is about 2.5 m. This is a demonstration of a very fluid behavior in aplitic (possibly anatectic) dikelets entraining angular, variably ductile blocks of dark dioritic rock. The complexities of interaction are indicated by the apparent “subduction” of the ductile aplite + diorite beneath a body of leucogranite, similar in composition to the aplite. A foliated quartz-diorite to tonalite block occurs along the left boundary of the most ductile region. Outcrop near Lovisa, Finland, on the Baltic coast. These rocks are a part of the Paleo Proterozoic Svecofinnian terrane, southern Finland. Granulite facies gneisses occur within a kilometer of this outcrop. **Jeff Greenberg**

References

- Bons, P.D., Elburg, M.A., Gomez-Rivas, E., 2012. A review of the formation of tectonic veins and their microstructures. *Journal of Structural Geology* 43, 33–62.
- Davis, G.H., Reynolds, S.J., 1996. *Structural Geology of Rocks and Regions*, second ed. John Wiley & Sons, Inc.
- Davis, G.H., Reynolds, S.J., Kluth, C.F., 2012. *Structural Geology of Rocks and Regions*, third ed. John Wiley & Sons. 839p.
- Fossen, H., 2016. *Structural Geology*, second ed. Cambridge University Press. ISBN: 9781107057647.
- Hilgers, C., Kirschner, D., Breton, J.-P., Urai, J.L., 2006. Fracture sealing and fluid overpressures in limestones of the Jabel Akhbar Dome, Oman Mountains. *Geofluids* 6, 168–184.
- Holland, M., Urai, J.L., 2010. Evolution of anastomosing crack–seal vein networks in limestones: insight from an exhumed high-pressure cell, Jabal Shams, Oman Mountains. *Journal of Structural Geology* 32, 1279–1290.
- Holland, M., Saxena, N., Urai, J.L., 2009a. Evolution of fractures in a highly dynamic thermal, hydraulic, and mechanical system—(ii) remote sensing fracture analysis, Jabal Shams, Oman Mountains. *GeoArabia* 14, 163–194.
- Holland, M., Urai, J.L., Muchez, P., Willemse, J.M., 2009b. Evolution of fractures in a highly dynamic thermal, hydraulic, and mechanical system; (I), Field observations in Mesozoic carbonates, Jabal Shams, Oman Mountains. *GeoArabia* 14, 57–110.
- Maeder, X., Passchier, C.W., Trouw, R.A.J., 2014. Complex vein systems as a data source in tectonics: An example from the UGAB valley, NW Namibia. *Journal of Structural Geology* 62, 125–140.
- Mukherjee, S., 2007. *Geodynamics, Deformation and Mathematical Analysis of Metamorphic Belts of the NW Himalaya*. Unpublished Ph.D. thesis, Indian Institute of Technology Roorkee, pp. 1–267.
- Mukherjee, S., 2010. Structures in meso- and micro-scales in the Sutlej section of the Higher Himalayan Shear Zone, Indian Himalaya. *e-Terra* 7, 1–27.
- Mukherjee, S., 2013a. Higher Himalaya in the Bhagirathi section (NW Himalaya, India): its structures, backthrusters and extrusion mechanism by both channel flow and critical taper mechanism. *International Journal of Earth Sciences* 102, 1851–1870.

- Mukherjee, S., 2013b. Channel flow extrusion model to constrain dynamic viscosity and Prandtl number of Higher Himalayan Shear Zone. *International Journal of Earth Sciences* 102, 1811–1835.
- Mukherjee, S., 2014. Atlas of Shear Zone Structures in Meso-scale. Springer.
- Mukherjee, S., Koyi, H.A., 2010. Higher Himalayan Shear Zone, Sutlej section: structural geology and extrusion mechanism by various combination of simple shear, pure shear and channel flow in shifting modes. *International Journal of Earth Sciences* 99, 1267–1303.
- Mukherjee, S., Bose, N., Ghosh, R., Dutta, D., Misra, A.A., Kumar, M., Dasgupta, S., Biswas, T., Joshi, A., Limaye, M., 2020. Structural Geological Atlas. Springer. ISBN: 978-981-13-9825-4.
- Novak, M., 2007. Depositional environment of upper carboniferous—lower permian beds in the Karavanke mountains (Southern Alps, Slovenia). *Geologija* 50, 247–268.
- Passchier, C.W., Trouw, R.A.J., 2005. Microtectonics, second ed. Springer.
- Singh, P., 2014. Exhumation history of the Higher and Lesser Himalayan crystallines in the Kumaon-Garhwal region, NW-India: As revealed from Fission Track Thermochronology. Unpublished Ph.D. thesis, Department of Geophysics, Kurukshetra University Kurukshetra.
- Singh, P., Patel, R.C., Lal, N., 2012. Plio-Pleistocene in-sequence thrust propagation along the Main Central Thrust zone (Kumaon-Garhwal Himalaya, India): New thermochronological data. *Tectonophysics*. <https://doi.org/10.1016/j.tecto.2012.08.015>.
- Singh, P., Singhal, S., Das, A.N., 2020a. U–Pb (zircon) geochronologic constraint on tectono-magmatic evolution of Chaurgranitoid complex (CGC) of Himachal Himalaya, NW India: implications for the Neoproterozoic magmatism related to Grenvillian orogeny and assembly of the Rodinia super-continent. *International Journal of Earth Sciences* 109, 373–390.
- Singh, P., Ao, A., Thakur, S.S., Rana, S., Sharma, R., Singh, A.K., Singhal, S., 2020b. Geology, Structural, Metamorphic and Mineralization studies along the Mandi-Kullu-Manali-Rohatang section of Himachal Pradesh, NW-India. (Accepted) Field excursion guide chapter in S. Mukherjee edited Field Extrusion guide book in Himalayan mountain ranges.
- Virgo, S., Abe, S., Urai, J.L., 2013. Extension fracture propagation in rocks with veins: insight into the crack-seal process using Discrete Element Method modeling. *Journal of Geophysical Research - Solid Earth* 118, 5236–5251.

Chapter 6

Various structures

This chapter presents various structures (Figures 6.1–6.83), some of which are not worked intensely by structural geologists. Grain boundary migration in rocks observed under optical microscope can constrain the temperature the rock underwent (Stipp et al., 2002). The stability of buildings and fracturing during earthquakes has been a research topic for geoscientists (Krishnan et al., 2006). Studies of faults and other structures have helped geoscientists with paleohydrology (Treiman, 2008). Figure 6.18 refers to strain rate, on which a recent paper from Bose and Mukherjee (2020) is available from a different terrain. Figures 6.82 and 6.83 are seismic image interpolation. Refer to Misra and Mukherjee (2018) for more such exercises.



FIGURE 6.1 Columnar joints, colonnade, and entablature. Thick solidifying lava flows develop contraction fractures that propagate from their cooling margins toward hotter interiors. These fractures, called columnar joints, divide a lava flow into columns, with polygonal (ideally hexagonal) shapes in plan. A subhorizontal basaltic lava flow of the Talisker Bay Group, Isle of Skye, Scotland, is shown in the figure. The lower part of the flow shows well-developed vertical columns, suggesting nearly horizontal isotherms (contours of constant temperature within the lava flow). Such a columnar tier is called a colonnade. The upper part of this flow shows a highly chaotic and distorted internal structure, as would develop during rainfall or stream flow supplying water into the cooling flow interior and disturbing isotherms. This tier is known as an entablature. The colonnade and the entablature, though with greatly different field appearances, are part of a single lava flow. Here, the combined thickness of both is 120 m. **Hetu Sheth**



FIGURE 6.2 Distinct colonnade and entablature tiers of a single basaltic lava flow from the Kizilcahamam volcanics near Ankara, Turkey. The flow dips toward the left. Individual lava flows can have multiple tiers of this kind, depending on the exact mode of emplacement and environmental conditions. **Hetu Sheth**



FIGURE 6.3 Dyke in meso-scale. Aplite dikes invade sheared albite granite across vertical joints, Marsa Alam area, Eastern Desert of Egypt. **Mohamed Th.S. Heikal**



FIGURE 6.4 Basaltic dikes. Basaltic dikes invade sheared albite granite across vertical joints, Marsa Alam area, Eastern Desert of Egypt. **Mohamed Th.S. Heikal**



FIGURE 6.5 Curved columnar joints (entablature) in Bagaces Formation ignimbrites, Guanacaste province, Costa Rica. The columns are curved and have six parallel sides (hexagonal) with heights between 1 and 5 m, and widths between 15 and 20 cm. The columns are 45 m high. See [Denyer and Alvarado \(2007\)](#) for detail. 10°39'25.52,244"N, 85°37'59.70,504"W. **Guido Sibaja Rodas**



FIGURE 6.6 Columnar joints. Columnar joints observed within Cambrian trachytic laccolith, in the area of Ouanguigui, Ougnat inlier, eastern Anti-Atlas, Morocco. **Zakarya Yajoui**



FIGURE 6.7 Southwestward panoramic view of the geothermal travertine area of Bridgeport, California. Photographed from the crest of the Hot Tub Ridge, which is an active and prominent fissure-ridge travertine deposit (Latitude N38°14'45", Longitude W119°12'18"; [Chesterman and Kleinhampl, 1991](#)). The Hot Tub Ridge is 84 m long, 7 m wide, and 4 m high ([De Filippis and Billi, 2012](#)). The Long Ridge (a 360 m long fissure ridge) and the Sierra Nevada mountains are also visible in the photograph. Fissure-ridge travertines are elongated mound-shaped deposits of travertine developed along open fissures, usually in active geothermal-tectonic areas. The ridges can be straight, slightly curved, or bifurcated in plan view, and are usually characterized by an axial extensional fissure extending along the crest of the ridge. The fissure ridge in the photograph is unique for its singular tripartition of the fissure at the ridge tip. In active fissure ridges, carbonate-rich hot waters that ascend along the axial fissure cause carbonate precipitation both within the fissure-ridge and over the ridge flanks, thus generating banded and bedded travertine deposits, respectively ([Hancock et al., 1999](#)). Most fissure ridges are located on the hanging wall of normal faults. The influence of active tectonics on the growth of fissure-ridge travertines may be moderate to important. The physicochemical attributes of fluids as well as their abundance (pore pressure) and climate oscillations (dry vs. wet periods) also play important roles in the fissure-ridge nucleation and growth ([Chesterman and Kleinhampl, 1991](#); [Hancock et al., 1999](#); [De Filippis and Billi, 2012](#)). **Luigi De Filippis and Andrea Billi**



FIGURE 6.8 Southeastward panoramic view of the Kamara active fissure ridge, in the Denizli extensional basin, southwest Turkey (Latitude N38°03'24", Longitude E28°58'16"; [De Filippis et al., 2012, 2013](#)). An open axial fissure is well exposed along the ridge crest and is partly filled by banded travertine dated through U–Th methods (1.7 ± 0.1 and 2.5 ± 0.1 ka; [De Filippis et al., 2012](#)). The ridge crest is also characterized by a system of en-echelon open subvertical fractures with an average strike of \sim N 120 degrees. The fracture aperture varies between approximately a few millimeters and a maximum of c. 20 cm, and it is usually larger in the central section of the fissure ridge than near its lateral closures. This fissure ridge is 63 m long, 15 m wide, and 6 m high. Dimensions of known fissure ridges on Earth vary (e.g., [Brogi and Capezzuoli, 2009](#)) up to a maximum of \sim 2 km long, 400 m wide, and 20 m high ([De Filippis et al., 2012](#)). Both flanks of the Kamara fissure ridge consist of bedded travertines dipping away from the axial fissure. This fissure ridge is singular for the presence of a fossil waterfall along the northeast flank and for the marked transverse asymmetry of the ridge. **Luigi De Filippis and Andrea Billi**

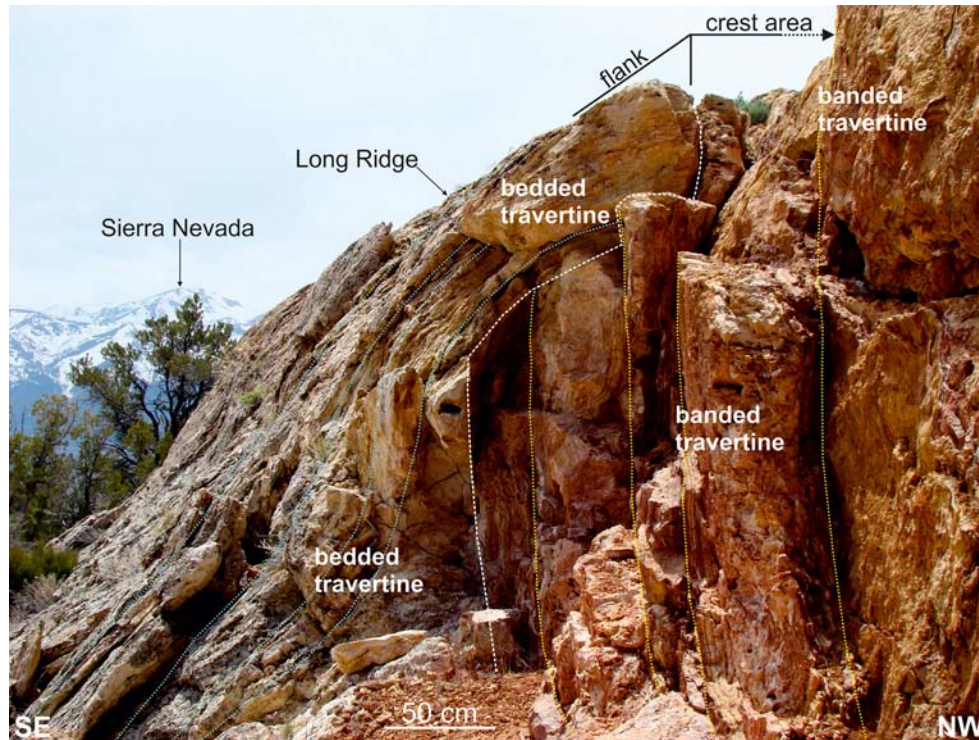


FIGURE 6.9 This photograph shows an exposure across the southeast flank of the Long Ridge (Latitude N38°14'43", Longitude W119°12'19"), which is a fissure ridge located in the geothermal area of Bridgeport (California). A subvertical banded travertine (dotted yellow lines) intruded within the axial sector of the fissure ridge, whose flanks are mostly formed by steep travertine beds (dotted turquoise lines). The bedded travertine is a porous and stratified flowstone deposit forming the bulk (flanks) of fissure ridges. The banded travertine, in contrast, is a nonporous, sparitic travertine filling the interior of fissure ridges with steep-to-vertical thick veins in the axial region and sill-like structures along the bedded travertine. The subvertical banded travertine usually cuts across the preexisting bedded travertine, which, in turn, may upward suture the banded travertine, thus providing evidence for the alternate growth of banded and bedded travertines. The ridge is unique because it exposes the reciprocal crosscutting and suturing relationships between banded and bedded travertines. From a paleoclimatic point of view, the bedded travertine growth is presumably connected with high stands of the water table during warm-humid periods (Faccenna et al., 2008), whereas the banded travertine growth is probably driven by coseismic exsolution events during low stands of the water table in cold-dry conditions (Uysal et al., 2009). Fissure ridges can thus provide unique information on the relationship between paleoclimate, groundwater systems, and tectonics (Faccenna et al., 2008; Uysal et al., 2009; Crossey and Karlstrom, 2012). Luigi De Filippis and Andrea Billi

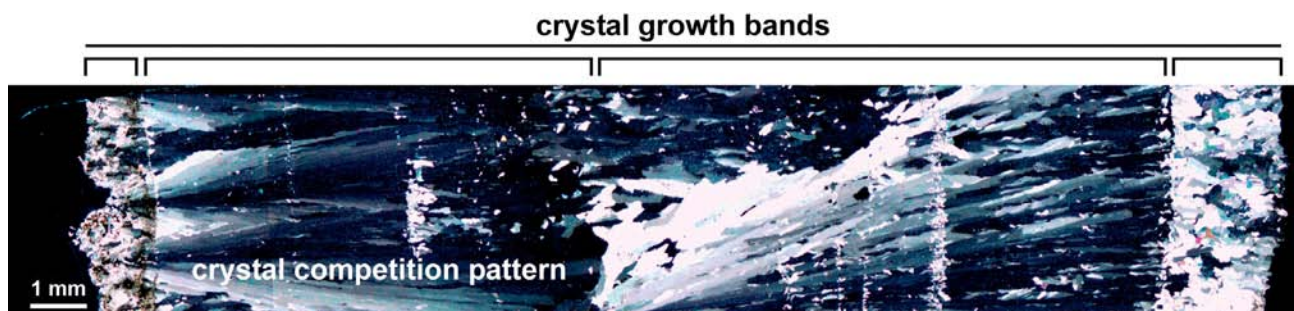


FIGURE 6.10 Microscopic view of a vein of banded travertine across the Akköy fissure-ridge (Denizli basin, Turkey, Latitude N 37°56'56", Longitude E 29°05'28"). The main features are a series of long fibrous calcite (and subordinate aragonite) crystals with a typical competition pattern (feather-like structures). Multiple succeeding bands of crystals attest to the multiphase growth history of the veins (Uysal et al., 2007; Van Noten et al., 2013). The crystals are usually perpendicular to the vein walls and their growth typically occurred toward the center of the vein (symmetric syntaxial growth) or from one wall toward the other wall (asymmetric syntaxial growth), as also confirmed by radiometric dating (Uysal et al., 2007). The force of crystallization along the veins can induce the uplift of the rock above the veins, in the case of sill-like veins (Gratier et al., 2012), and the transverse opening of fissure ridges, in the case of subvertical veins developed along the axial region of the ridges. Luigi De Filippis and Andrea Billi

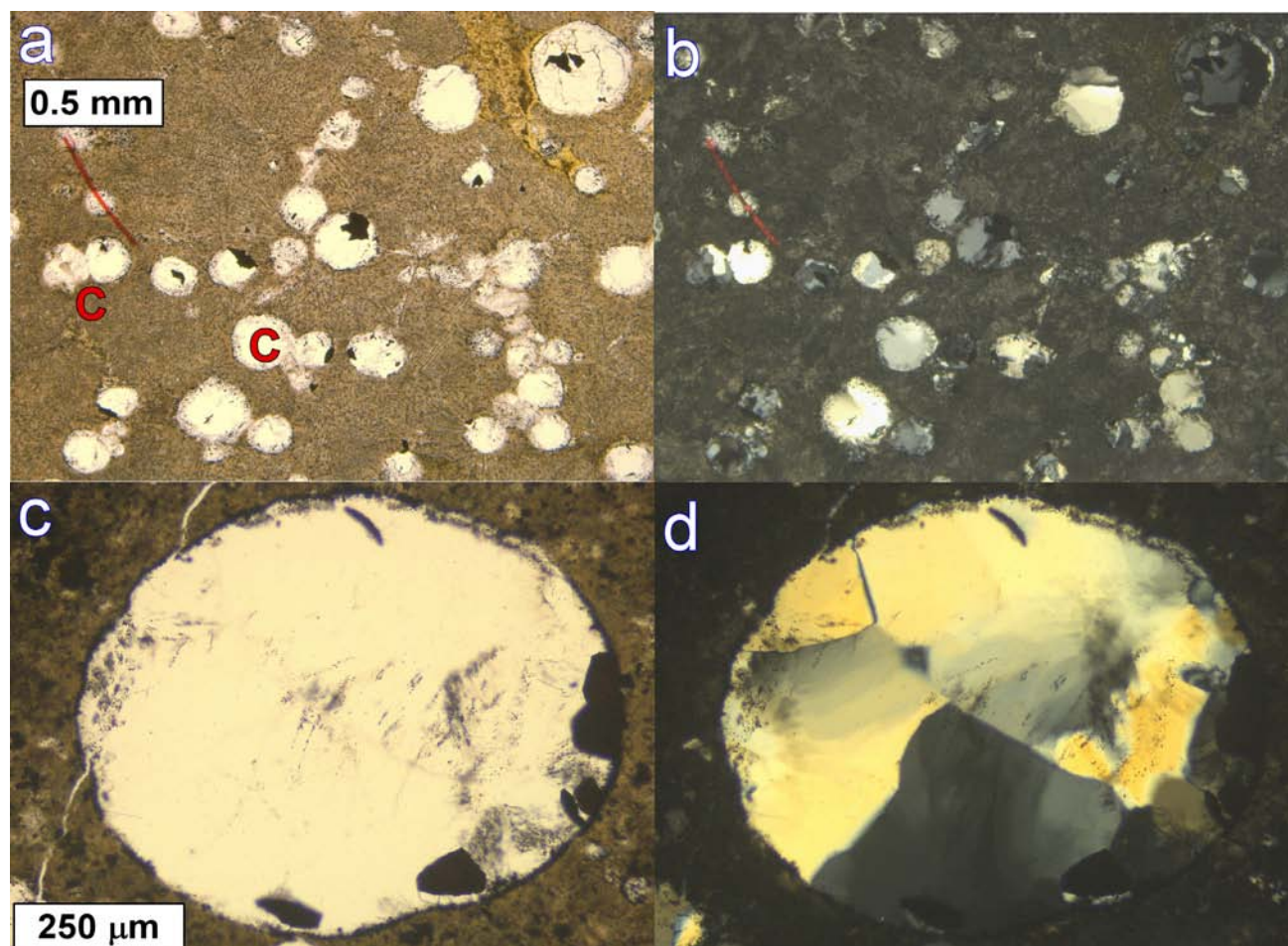


FIGURE 6.11 Abundant quartz amygdules in a pseudotachylyte vein. Pseudotachylyte is common in a variety of lithologies in the Nason Terrane of the Wenatchee Block of the North Cascade Mountains of Washington, United States. Most commonly, it cuts amphibolite facies pelitic to semipelitic schist, forming veins ranging from sub-mm up to at least 15 cm in thickness. Roughly 10% of specimens contain amygdules, bubble collapse structures, or, very rarely, vesicles. Shown here (a: PPL, b: XPL) are images from one specimen containing unusually abundant quartz amygdules. Nearly all the light-colored patches are quartz amygdules, several of which also contain opaque (hematite?) inside the amygdules. The amygdules commonly have a lining of titanite, which creates the “dusty” rims on many. Bubbles in the pseudotachylyte melt in places that underwent coalescence. The groundmass is highly dendritic, visible as faint lines. Shown in c (PPL) and d (XPL) is a large amygdule with numerous micron-scale opaque grains within the feather-textured polycrystalline quartz. The titanite-rich lining of the amygdule wall is visible; rarely, capillary apatite crystals extend into the amygdules. The curved opaque patch at the top may be a piece of the amygdule wall that became detached. The thin vein at the far left is an adularia vein; these are not uncommon cutting pseudotachylyte veins and related cataclasite zones. **Jerry F. Magloughlin**

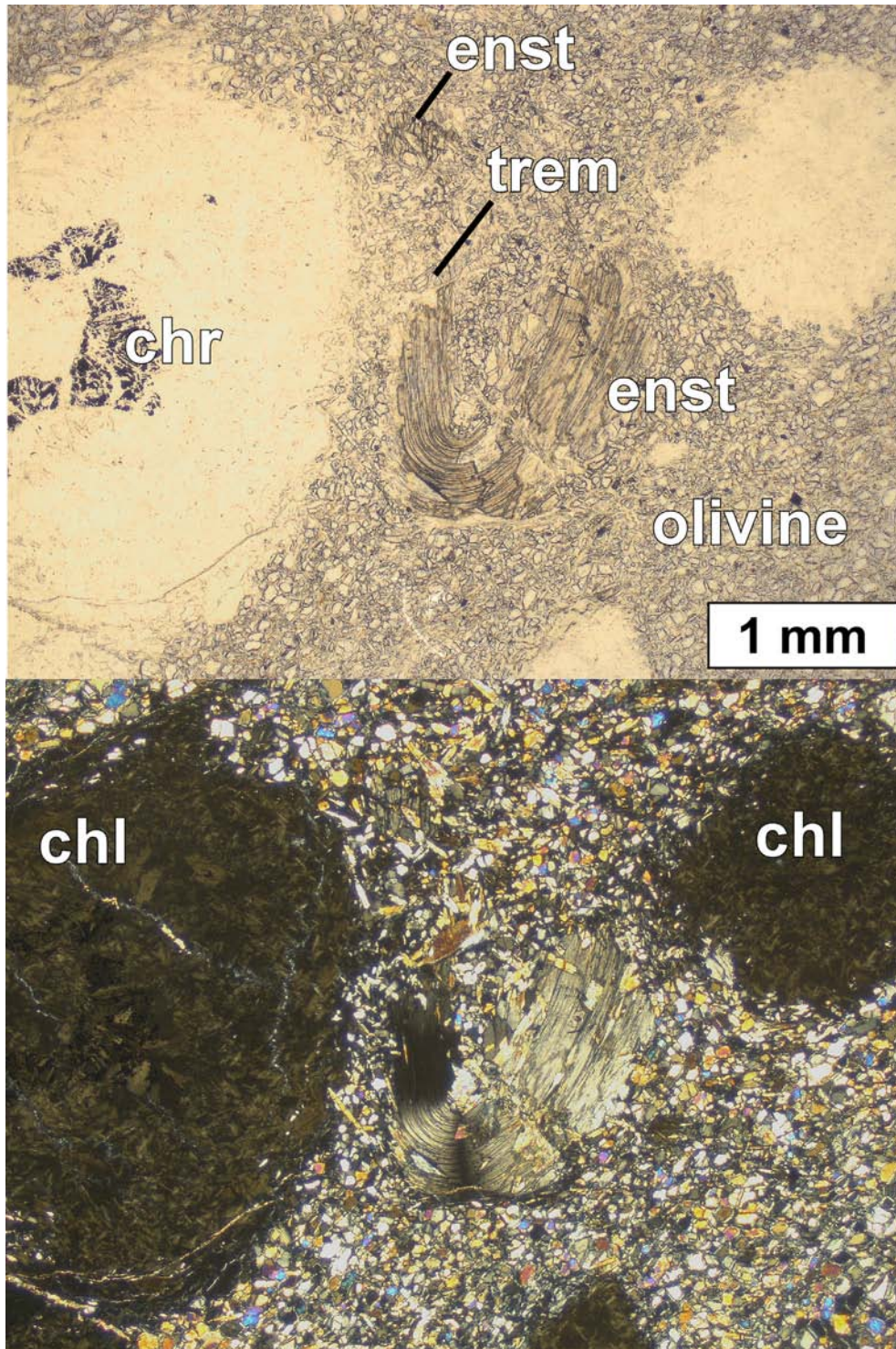


FIGURE 6.12 Plastic strain and folded enstatite in a chlorite harzburgite. PPL (top), XPL (bottom). Ultramafic bodies ranging from dm-scale to several hundred meters across occur mostly in the Wenatchee Ridge Orthogneiss pluton in the Nason Terrane of the North Cascade Mountains, Washington. Many are serpentinite, but harzburgite is also common. Rarely, cm-scale chlorite patches (chl) presumed to be retrogressed garnet occur, and these are commonly cut by thin calcite microveins (cmv). These chlorite pseudomorphs are commonly highly flattened into oblate spheroids, parallel to a strong foliation. Some contain irregular or spiral-shaped patterns of $\sim 1\text{--}50\ \mu\text{m}$ chromite grains (chr). The groundmass is fine-grained recrystallized olivine; enstatite is commonly altered or partly altered to talc. Minor tremolite (trem) is also present in this specimen, and is common in many of the other bodies. In one of the ultramafic bodies, flattening of chlorite pseudomorphs and foliation are not evident, and enstatite (enst) remains largely unaltered but displays strong and unusual evidence of deformation, showing bent, kinked, and even isoclinally folded crystals (folded into a “u” at the center of the images). Such grains may have been caught between garnet crystals prior to alteration of the garnet to chlorite. Note that the enstatite is smoothly folded as apparent by the extinction pattern in the XPL image at the bottom. **Jerry Magloughlin**



FIGURE 6.13 Extensional fractures with oriented calcite infill adjacent to the fault core in limestone. Alpine foreland basin, Clumanc, France. Amy Ellis



FIGURE 6.14 Fold-and-thrust system. Photo taken inside the Ordesa and Monte Perdido National Park (Spanish Pyrenees) to the North, in Llanos de Salarons. View of the Pico Blanco (2919 m). 30 T 740,355.09E 4,728,955.97N. Paleocene and Eocene limestones (Salarons and Gallinera Formations) in gray (Ternet et al., 2008). Four sheets of the Monte Perdido fold-and-thrust system consisting of anticlines associated with south-verging thrusts. Mechanically weak layers inside the Upper Cretaceous rocks act as detachment levels for these thrusts (Séguret, 1972). The absence in this sector of the Southern Pyrenees of the Upper Triassic Keuper shales, evaporites, and salts (i.e., the regional detachment level) could control the genesis and geometry of the Monte Perdido fold-and-thrust system (Muñoz et al., 2013). Ruth Soto



FIGURE 6.15 Fracture planes in sandstones. Photo taken inside the Ordesa and Monte Perdido National Park (Spanish Pyrenees), in Carriata. 30°T 740703.38E 4,727,360.52N. Campanian–Maastrichtian sandstones (Marboré Formation) (Ternet et al., 2008) showing spectacular vertical fracture planes oriented NNW-SSE and perpendicular to the horizontal bedding. In the Pyrenees, shortening was accommodated by the formation of basement and cover thrust systems, and also by the cleavage development of the Alpine age (Choukroune and Séguet, 1973). One of the effects of the Pyrenean compression is the formation of this kind of fracture that greatly influences the Ordesa and Monte Perdido National Park landscape, together with glacial and karst processes. Ruth Soto and Esther Izquierdo-Llavall



FIGURE 6.16 Thrust sheet stacking. Photo at Spanish French border to the south. View of the Ordesa and Monte Perdido National Park (Spanish Pyrenees), Monte Perdido peak (3355 m), Monte Perdido glacier, and Marboré lake. 31 T 257569.12E 4,731,539.75 N. Campanian–Maastrichtian sandstones (Marboré Formation) in brown-gray and Paleocene and Eocene limestones (Salarons and Gallinera Formations) in gray (Ternet et al., 2008). The Monte Perdido thrust sheet stacking at the northern end of the South Pyrenean fold-and-thrust belt consists of a beautiful and spectacular example of a thin-skinned fold-and-thrust system that forms the highest calcareous massif in Western Europe. It is located at the southern end of the Pyrenean Axial Zone and represents, due to its spectacular outcrops, a key area to understand the Pyrenean mountain building. With a WNW-ESE trend, it has 6 km of estimated southwards horizontal displacement affecting cover sediments (Séguret, 1972). **Ruth Soto**

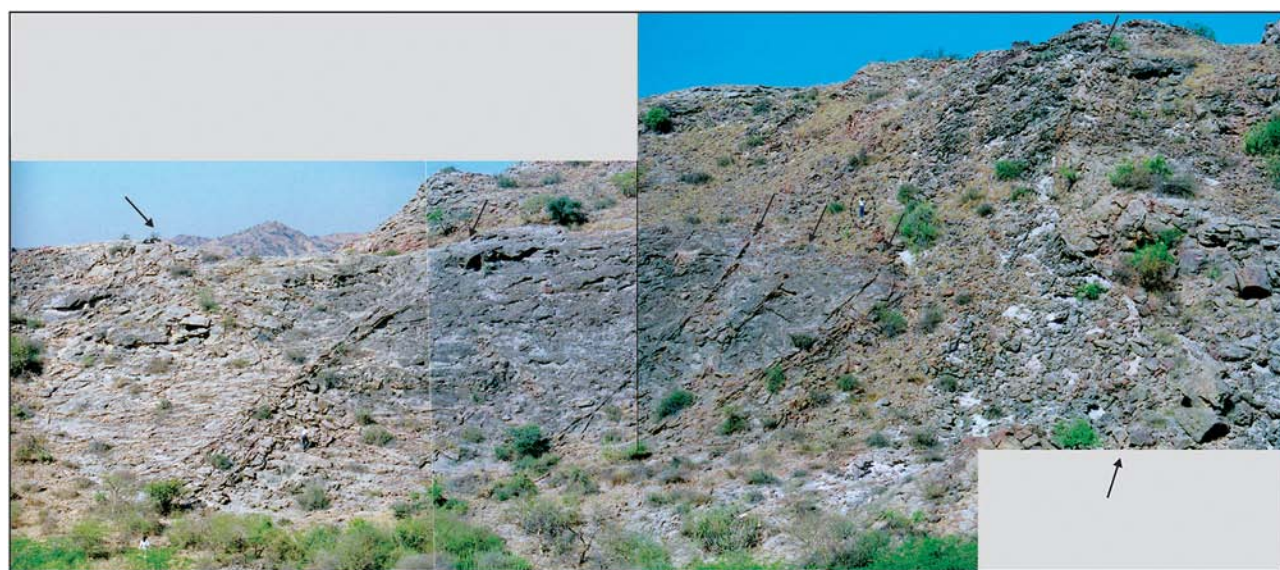


FIGURE 6.17 Shear-enhanced compaction bands. Bhuj Sandstone, Jawaharnagar, Kachchh, Gujarat, India. They formed at shallow burial conditions during the Kachchh basin compressional phase. These bands are seen on the backlimb zone of the ault-related fold, along E-W striking thrust faults. The compaction bands are displayed as thrust splays (arrow). One of the compaction bands on the extreme right side displays an “S” shaped feature. Scale person (circled) height: 165 cm. **George Mathew**



FIGURE 6.18 Photograph from the Matchless amphibolite, Kuiseb Canyon, Namibia, showing a lens (“phacoid”) of metabasalt enveloped by metapelite. The Matchless amphibolite is a hundreds of meters thick zone of predominantly mafic rocks, semicontinuous for hundreds of kilometers along the strike at a constant structural level within the Southern Zone of the Pan African Damara belt. The rocks experienced peak metamorphic conditions in the amphibolite facies, and were likely deformed and intercalated within an accretionary prism formed during the Neoproterozoic to Cambrian closure of the Khomas Sea (Kukla and Stanistreet, 1991). The continuity of the Matchless amphibolite has been difficult to explain, but it may be by subduction of a mid-ocean ridge where parts of the ridge were sliced off and accreted (Meneghini et al., 2014). Large metabasalt lenses, as in the photograph, have relatively high viscosity compared to surrounding metasediments. The scale of the phacoid in the photograph, and the existence of similar blocks of kilometers in the largest dimension, imply that where topographic highs subducted, accretionary prisms may contain relatively high strength lenses at kilometer-length scales. Cleavage wraps around these blocks, indicating ductile flow around phacoids, such that strain rate gradients between the matrix and phacoids may elevate stress at the phacoid boundary. This boundary therefore becomes a likely zone of frictional failure at appropriate pressure–temperature conditions. As a consequence, the length scale of phacoids, from m to several km, may control the length scales of brittle failure in mixed-lithology deforming zones (Fagereng, 2011). Ake Fagereng



FIGURE 6.19 Overprinting schistosity. Regional S1 schistosity overprinted by S2 and S3 expressed in the calcareous and pyrite-bearing sandstones of the Ayers Cliff Formation, southern Québec. S2 and S3 are identified by their intersection lineations L1–2 (upper right to lower left lines) and L1–3 (upper left to lower center lines) on the S1 plane. Reproduced from Perrot et al. (2018). Morgann G. Perrot



FIGURE 6.20 Schistosity and intersection lineation. Regional S1 schistosity (principal plane) on which is visible intersection lineations with the stratification, L0–1 highlighted by the horizontal undulations, and with the S2 schistosity, L1–2 expressed by the upper right to lower left lines overprinting the S1 principal plane. Impure, feldspar-rich sandstone of the Lac-Drolet member, southern Québec. Reproduced from Perrot et al. (2018). Morgann G. Perrot



FIGURE 6.21 Quartz clasts in schistose rock. A highly schistose rock with (elongated?) quartz clasts. Narwapahar, Jharkhand, India. Sanjukta De



FIGURE 6.22 The Sto. Domingo Anticline; the westernmost termination of the South Pyrenean sole thrust. Structural geologists used to simplify nature to understand processes. However, complex structures are common in fold-and-thrust belts: superposed, recumbent, plunging, conical folds, folded thrust, etc. This page is devoted to the San Marzal periclinal fold, a complex structure located in the External Sierras. The occurrence of Triassic evaporites acts as a regional detachment level and it is responsible for a thin-skin deformation style. In this picture, we can see a panoramic view of the Sto. Domingo anticline taken from the South (Puig Mone hill). The Internal Sierras (almost 3000 m in altitude) are seen on the back. The Jaca molassic (Campodarbe Fm) and turbiditic (Hecho group) basin are located between both ranges. The Santo Domingo anticline is the more prominent structure in the western termination of the External Sierras front (Nichols, 1987; Millán et al., 1995). The Sto. Domingo anticline is a large-scale detachment fold that, due to the increasing amount of tectonic shortening to the East, is transformed into a thrust that can be tracked 40 additional kilometers. It is a 20 km long fold (the westernmost 4 km are seen in this picture) striking WNW-NW and slightly oblique to the main Pyrenean trend. Apart from the western pericline termination, the rest of the structure seems to display a pseudohorizontal fold axis, although this may be partially conditioned by the outcropping conditions because most of the hinge is eroded. **Emilio L. Pueyo, Andrés Pocoví, Elisa M. Sánchez, and Belén Oliva-Urcia**

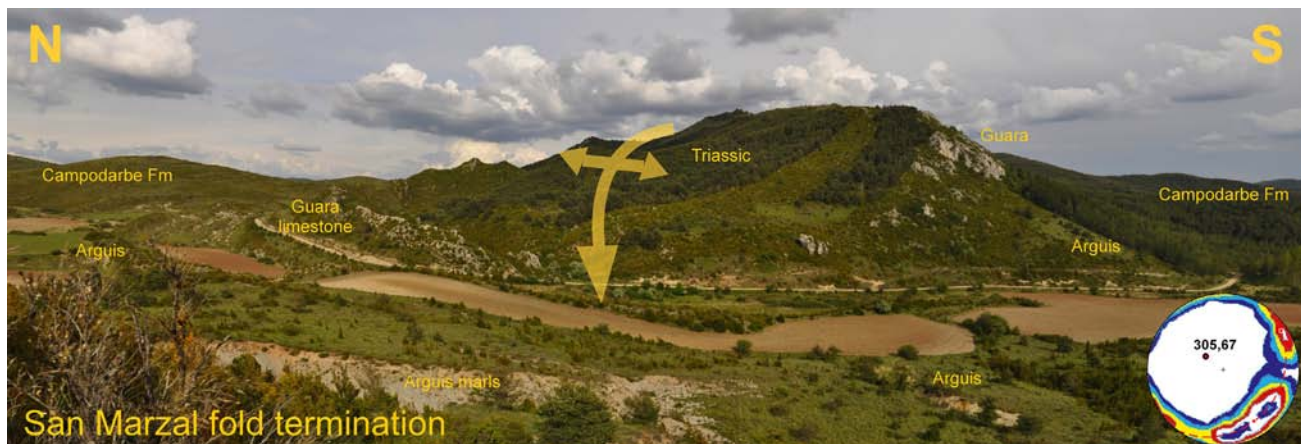


FIGURE 6.23 San Marzal pericline; the ending of the Southwestern Pyrenean sole thrust. In this picture, we observe the magnificent termination of the External Sierras thrust front: the Sto. Domingo anticline and its lateral termination, the San Marzal pericline. The Guara Eocene limestones define the fold termination in the landscape while the Arguis marls produce a depression. 4500 m of fluvial deposits (Campodarbe Fm) cover the anticline core. Although San Marzal might seem a regular fold-closure in the geologic map, another significant feature from this panoramic view is the noteworthy westward plunge of the fold termination; the fold axis is sinking beneath our position. Serial balanced cross-sections in the western part of the Sto. Domingo Anticline (Millán et al., 1995; Oliva-Urcia et al., 2012) characterize the wavelength (8–10 km) and amplitude (7 km) of the fold. The overall geometry may be fitted to a south verging cylindrical fold with pseudoparallel and near-vertical limbs. However, the fold axis undergoes dramatic changes in shortening along the strike that are responsible for significant clockwise rotations of the northern limb. In summary, this complex geometry seems to better fit to a conical fold with an elliptical cross-section describing parallel near-vertical limbs (Millán et al., 1995) caused by the lateral gradient of shortening (Pueyo et al., 2003) together with the lateral disappearance of the detachment level to the West. All these facts have produced a pinning effect and the superb conical geometry of the fold. **Emilio L. Pueyo, Andrés Pocoví, Elisa M. Sánchez, and Belén Oliva-Urcia**

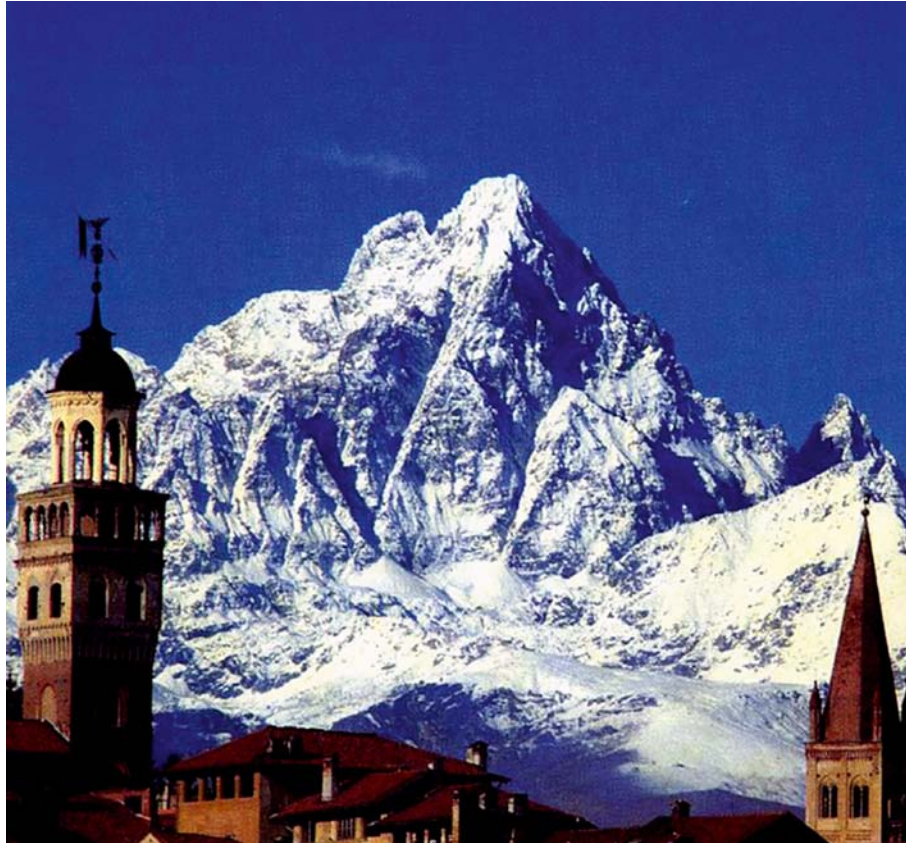


FIGURE 6.24 Active slope morphology operated by variably oriented fracture sets on the 1400-m high East wall of Monte Viso (3841 m). Early winter snow makes the structures shine more in a view from the town of Saluzzo (Western Alps of Southern Piedmont, Italy). Prominent debris cones at the base of the intersecting megafractures are being fed by rock falls and snow avalanches along ice-free couloirs; the intense deglaciation that affected this region in the last millennia is still rapidly degrading the in-rock permafrost relictual on most of the slopes at altitude > 3000 m. The front wall parallels N–S striking regional fractures and faults. **Guido Gosso**



FIGURE 6.25 Early lineations crossed by later crenulation lineations in Paleoproterozoic metasedimentary rock, lower unit of Lesser Himalayan Crystallines, Kameng valley, western Arunachal Himalaya. GPS location: N27°19'59.3"; E92°26'18.5" (Yin et al., 2010; Bikramaditya Singh and Gururajan, 2011). **Bikramaditya Singh**



FIGURE 6.26 Plumose structure or hackle plumes in quartzite at the contact between the Delhi Supergroup with the Mesoproterozoic basement gneisses, near Shrinagar ~15 km from Ajmer toward the northeast. Direction of divergence of the hackle lines connote the direction of propagation of the fractures. See [Hobbs et al. \(1976\)](#), [Twiss and Moores \(2007\)](#), and [Davis et al. \(2012\)](#) for details of these structures. **Eirin Kar**



FIGURE 6.27 A typical augen gneiss/granite mylonite at the Funatsu Shear Zone within the Hida Belt of southwest Japan (N36°20'3.5", E137°18'0"). Foliation made by elongated aggregates of fine-grained biotite and quartz ribbons is clear on the nearly horizontal surface. Pale pinkish grains: K-feldspar, white grains: plagioclase, black strings: biotite, gray lenticular parts: quartz. Scale: pencil 14 cm. The Funatsu Shear Zone is a late Triassic dextral ductile shear zone that developed in the SE margin of the Hida Belt, consisting mainly of augen gneiss (deformed Hida older granites). Hida older granites date ~250 Ma and mylonitization happened in the Late Triassic under upper greenschist to amphibolite facies ([Takahashi et al., 2010](#)). The Funatsu Shear Zone is regarded as the NE extension of the Cheongsan Shear Zone in the Korean Peninsula, which is regarded to be formed by collision between the north and the south China cratons ([Takahashi et al., 2010](#); [Ree et al., 2001](#)). Therefore, the Funatsu Shear Zone is important to study late Paleozoic to Mesozoic tectonics of East Asia. **Yutaka Takahashi**



FIGURE 6.28 Hydrothermal breccias. Hydrothermal breccia composed of angular clast from Ediacaran andesitic rock cemented by barite. This snap was taken within a fault structure in the Tassafte mining area, Saghro inlier eastern Anti-Atlas Morocco, where the ore bodies are hosted within Ediacaran volcanic rocks and Cambrian sedimentary succession (Yajoui, 2019). **Zakarya Yajoui**



FIGURE 6.29 Bedding–cleavage relation associated with regional folding. The relation is found in beds dipping toward the SE. The pen is parallel to the cleavage. Bedding dips more steeply than cleavage indicating that we are in the overturned limb of a larger-scale fold. See Till et al. (2008) and references therein for geology. Brooks Range, Alaska. N67°39.142', W152°17.179'. Hunt Fork Shale, Late Devonian (Dillon et al., 1986). **Victoria Pease**



FIGURE 6.30 Beautiful granodiorite mylonite in the coastal area of the Shirakami Mountains of north Japan ($N40^{\circ}27'47''$, $E139^{\circ}56'40''$). These mylonites originate from the Shirakami-dake Granites, which are the members of the Abukuma Granites. The K–Ar ages (biotite and hornblende) of the Shirakami-dake Granites are ~ 90 Ma (Fujimoto and Yamamoto, 2010). The mylonitization may have taken place ~ 90 Ma under upper greenschist to amphibolite facies condition. At this locality, granite mylonite is situated like a dyke in granodiorite mylonite, in which the foliations are parallel mutually. This occurrence indicates that the biotite granite had intruded into the hornblende-biotite granodiorite and these granite and granodiorite were mylonitized together (Takahashi, 2002). Scale bar: pencil 14 cm. “This mylonite zone in the Shirakami Mountains is a possible northern extension of the shear zone \sim Tanagura Tectonic Line, which is regarded as the NE extension of the Median Tectonic Line (Takahashi, 1999, 2002).” Therefore, granitic mylonites in the Shirakami Mountains are important to study the Mesozoic tectonics of the eastern margin of the Asian continent. **Yutaka Takahashi**



FIGURE 6.31 Biotite-rich granite with siltstone xenolith from the Tistung Formation. U–Pb dating of zircons from the granite yields a crystallization age at 480 ± 11 Ma (Gehrels et al., 2006). Location: Core of the Kathmandu klippe, Malekhu section, central Nepal Himalaya. **Subodha Khanal**

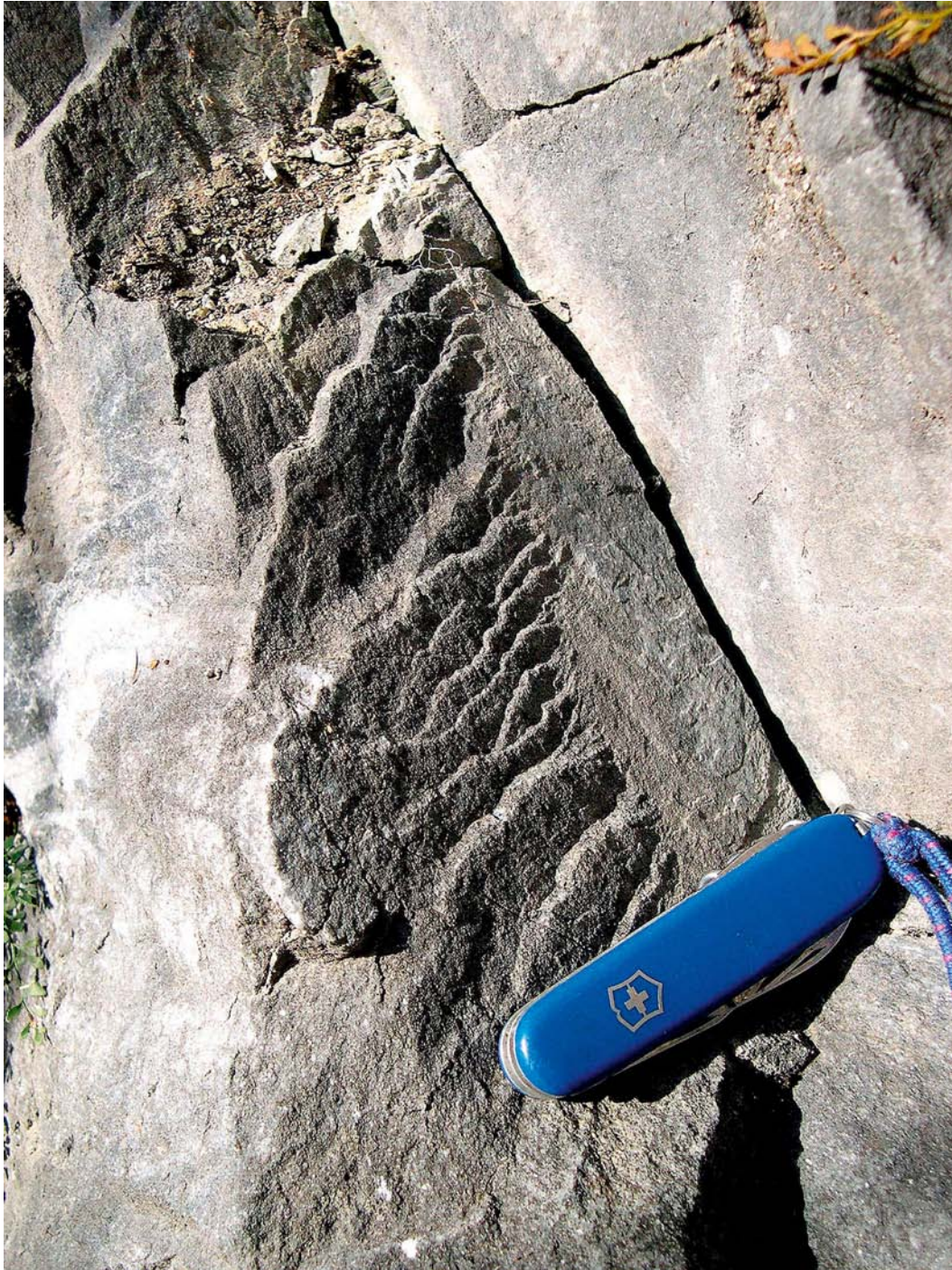


FIGURE 6.32 Tension fracture surface with fine plumose structure with concentric ribs perpendicular to the plume. The flaring fringe of hackles is at the edge of the joint surface. Each fringe consists of a series of alternating en-echelon cracks (also termed segments) and steps (also termed bridges) aligned along the parent joint (Frid et al., 2005). The fringe represents a direction of propagation of the fracture. This small exposure is located in a quarry near the village of Vapenna, Rychleby Mts, Czech Republic, Europe, Devonian crystalline limestones of Branna group (Novakova, 2008; Novakova et al., 2010). GPS coordinates: N50°16'35", E017°07'49". Lucie Novakova

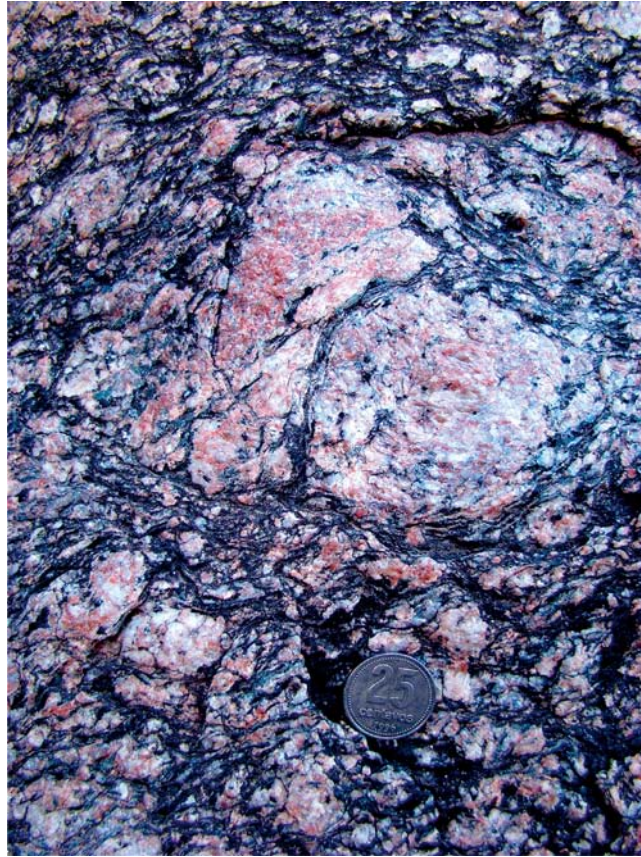


FIGURE 6.33 Rare structure named here “piggyback porphyroclasts” in granite mylonite to protomylonite. The structure shows two large porphyroclasts of K-feldspar occurring together in the central part of the photo and displaying strongly curved contacts due to crystal-plastic deformation. Notice the conjugate set of microfractures on the lower part of the contact zone inside the left porphyroclast. Subvertical curved contact between both porphyroclasts and linked conjugate microfractures suggest compression in the horizontal direction. Section oblique to the lineation and normal to the foliation. Width of view 206 mm. Location: Sierra de Velasco, La Rioja Province, NW Argentina. GPS point (WGS84): S 28°36'34.5"-W 67°10'41.1" Rock type: Mylonite to protomylonite. Formation name: Ortogneiss Antinaco (TIPA Shear Zone) Age (relative): Post-Lower Ordovician/Precarboniferous Facies/grade: medium grade. **Mariano A. Larrovere**



FIGURE 6.34 Mylonitized porphyritic granite. Mylonitization in porphyritic Sendra—Ambaji Granite (north of Hathidara village and Paniyari Talav), Banaskantha district, Northern Gujarat, India. The mylonitized porphyritic granite shows shear foliations. The general attitude of shear foliation is N50°E/60°SE. **Arindam Dutta, Shukla Dutta, and G.C Barik**



FIGURE 6.35 Spheroidally weathered Deccan basalt. Rounded fractures developed. From the hill near Ananta building, IIT Bombay campus, Mumbai, India. Souvik Sen and Soumyajit Mukherjee

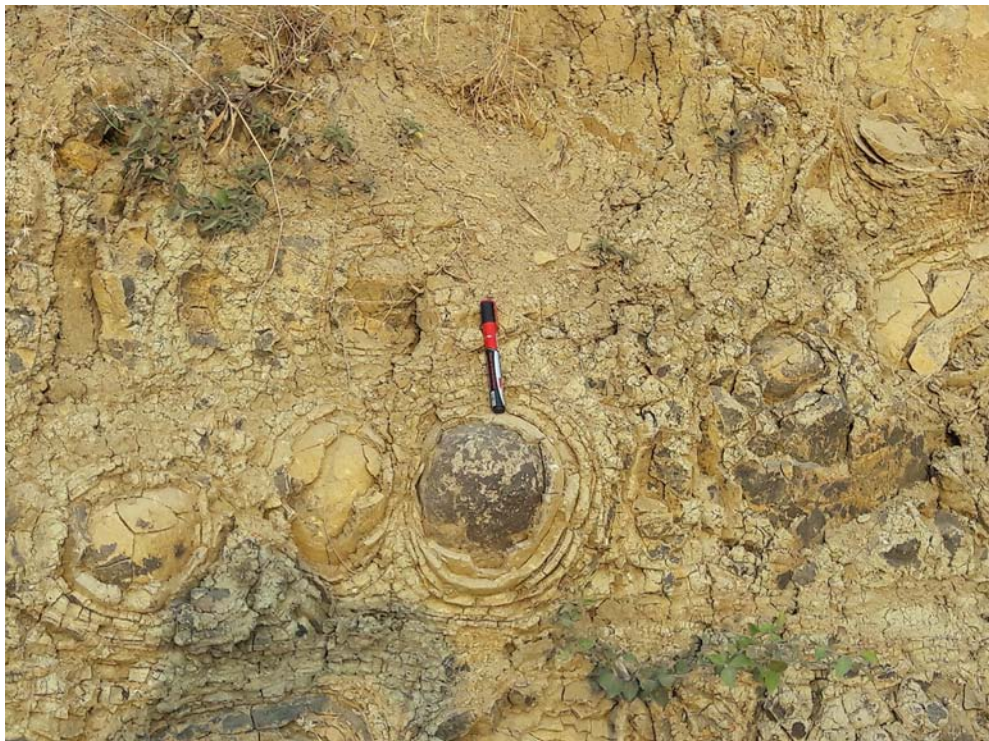


FIGURE 6.36 Spheroidal weathering, 1. Spheroidal weathering of basalt (Indore Formation) near Bhopal, India. Aasif Mohamad Lone



FIGURE 6.37 Spheroidal weathering, 2. Spheroidal weathering of basalt (Indore Formation) near Bhopal, India. This is a zoom of [Fig. 6.36](#).
Aasif Mohamad Lone



FIGURE 6.38 Spheroidal weathering, 3. Spheroidal weathering of basalt (Indore Formation) near Bhopal, India. Aasif Mohamad Lone



FIGURE 6.39 Three nonparallel fractures intersect to develop a triangular zone in the Deccan basalt, near Ananta building, IIT Bombay campus, Mumbai, India. Souvik Sen and Soumyajit Mukherjee



FIGURE 6.40 Remarkably rounded fracture plane, traced by placing pens, inside Deccan basalt. This curved fracture plane is not a product of spheroidal weathering. Near Ananta building, IIT Bombay campus, Mumbai, India. Souvik Sen and Soumyajit Mukherjee



FIGURE 6.41 Extension (tensile) joints in Archean granite gneisses near Perambalur, 50 km north of Tiruchirappalli, Tamil Nadu, India. Notice their abutting relations. Three sets of joints: an E–W trending numbered 1, N–S trending numbered 2, and an E–W trending numbered 3. The joint set 1 seems oldest and 3 the youngest. The extension direction is indicated perpendicular to the joint. Tensile joints decode extension directions. Pencil for scale, approximate length 10 cm. Location $11^{\circ}13'3.53''\text{N}$, $78^{\circ}45'40.84''\text{E}$. Achyuta Ayan Misra



FIGURE 6.42 Basalt porphyry from a dike within Dharwar rocks. Near Chakrapeta village, Kadapa district, Andhra Pradesh, India. Large phenocrysts of plagioclase feldspar are within a fine-grained matrix. The large phenocrysts in this photograph indicate two-stage cooling. Atanu Mukherjee



FIGURE 6.43 Axial planar cleavage in a small-scale fold. Penetrative axial planar cleavage approximately parallel to the pen. Well developed in smaller-scale folds that mimic the regional direction of thrusting. See [Till et al. \(2008\)](#) and references therein for regional geology. Brooks Range, Alaska. N67°33.673', W152°13.569', Hunt Fork shale, Late Devonian ([Dillon et al., 1986](#)). **Victoria Pease**



FIGURE 6.44 Bedding–cleavage relationship. Well-developed S-symmetry cleavage in mudstone layers interbedded with limestone (Jurassic). Esclagon, Pays Digno, France. Left side: north direction. **Amy Ellis**



FIGURE 6.45 Network of deformation bands. Network of well-developed deformation bands within the porous calcarenites of the Plio-Pleistocene Gravina Calcarenes Formation (Pace et al., 2018). The Gravina Calcarenes formation comprises lithoclastic-bioclastic calcirudites-calcarenes that onlap three isolated structural domains (Gargano, Murge, and Salento) of the Apulian foreland in southern Italy (Pomar and Tropeano, 2001; Festa et al., 2018). Deformation bands are strain localization tabular zones of mm to cm thick that accumulate low-displacement shear and/or volumetric deformation in porous rocks and sediments (Fossen et al., 2007). Deformation bands appear as light-colored, mm to cm thick structures forming protruding ridges in the pale cream bioclastic calcarenites. They are mostly compaction shear bands also associated with some pressure solution, oriented at high angles to bedding and widely distributed. Pure compaction bands also occur but are less diffuse. Compaction is evident as a reduction of pore space within the deformation band, relative to the porous host rock. Grain reorganization and pressure solution mainly accommodate strain localization. Location: Belvedere of the Matera town (40°39′50.96″N 16°36′57.84″E WGS84). Width of view ~2.1 m. **Paolo Pace and Raffaele Di Cuia**

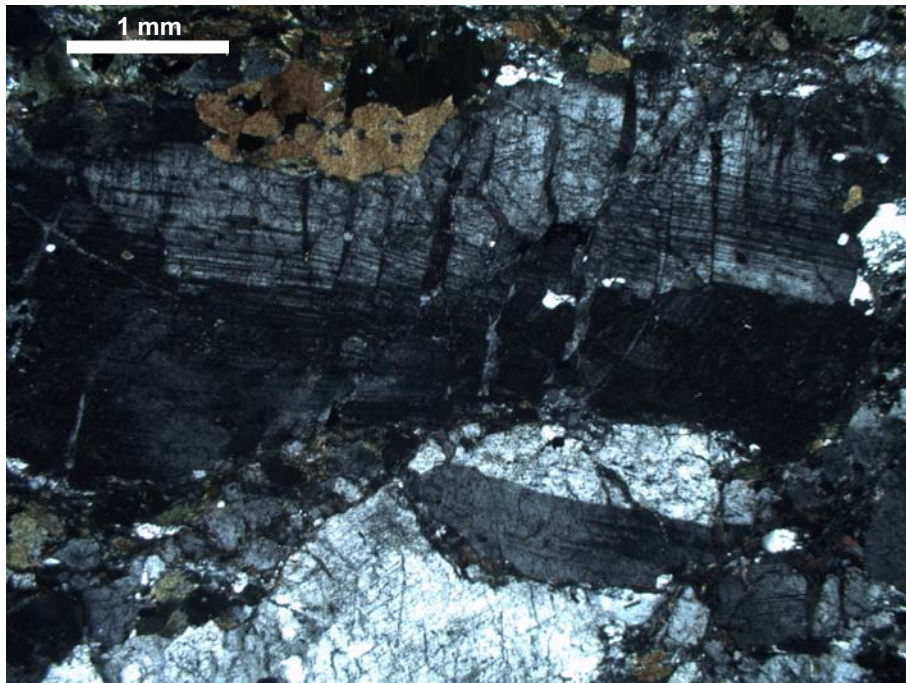


FIGURE 6.46 Recrystallization of plagioclase in granodiorite. Granodiorite of the Eagle Wash Intrusive Complex represents syntectonic Miocene (c. 19Ma) magmatism followed by rapid uplift and cooling during a period of detachment faulting (Pease and Argent, 1999; Pease et al., 1999). Note the low-temperature plasticity of the large plagioclase crystal in the central part of the image. Undulose extinction, deformation bands, and subgrain recrystallization along the deformation bands suggest >450°C temperature (Simpson, 1985; Brodie and Rutter, 1985). Sacramento Mountains, California, SW United States. Coordinates: N3853884, E710016. **Victoria Pease**



FIGURE 6.47 Ductile deformation of the Livada Detachment. Field view of mylonitic fabrics in the ductile Livada Detachment belonging to the North Cycladic Detachment System exposed in the Northern coast of Mykonos island (Metalleia, Greece). The photo shows intensely sheared granite with tight alternance of mm to cm thick whitish mylonitic and dark ultramylonitic layers. Mylonitic fabric is marked by an intensely sheared and elongated fine-grained quartz-feldspar-rich layer. The ultramylonitic fabric corresponds to thin dark layers with very few and very fine-grained porphyroclasts (white grains in dark layers). At the center of the photograph, a cm thick completely recrystallized ultramylonite layer with a characteristic glassy appearance. Width of view: ~ 30 cm. Coordinates: 37°28'21.63"N; 25°26'45.71"E. **Giovanni Musumeci, Raffaele Gazzola, and Chiara Frassi**

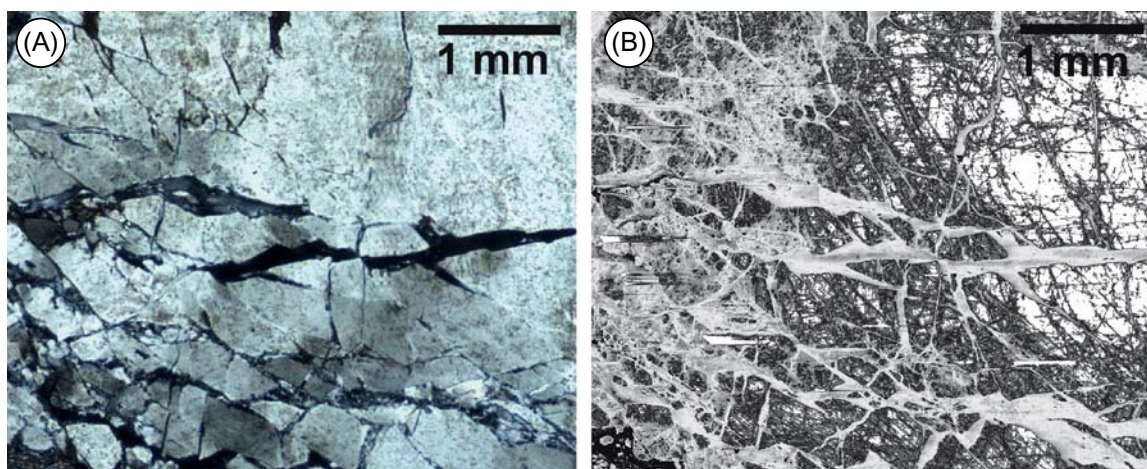


FIGURE 6.48 Microstructural evidence for repeated cycles of coseismic damage and viscous flow at the frictional to viscous transition in an ancient strike-slip fault. Large-displacement continental strike-slip faults are characterized by a core of ultrafine grained rocks surrounded by a “damage zone” of fractured rocks that can extend laterally outward for hundreds of meters. A notable characteristic of these faults is the extensive occurrences of so-called “pulverized” rocks that exhibit intragranular cracking and fragmentation down to the micron scale. A fundamental question is how deep these damage zones extend into the crust, and how do their physical characteristics change with depth (Mooney et al., 2007; Tullis et al., 2007)? The Paleozoic Norumbega Fault System in Maine, United States, is known to be one of the best ancient analogs for the San Andreas Fault currently exposed at Earth’s surface (Ludman and West Jr., 1999; Sibson and Toy, 2006). The Norumbega is exposed at a range of depths along its length, and in central Maine the mylonites along different fault strands preserve spectacular evidence for repeated coseismic brittle damage followed by viscous flow, representing the frictional to viscous transition. We conclude from our studies of these rocks that damage zones extend throughout the seismogenic zone, but are difficult to detect by geophysical or optical methods at depth owing to rapid microcrack healing and interseismic viscous flow. Some microstructural evidence is visible optically, but most of it can only be observed using cathodoluminescence (CL) and electron backscatter diffraction (EBSD) analysis. This figure pair from the Sandhill Corner shear zone (Price et al., 2012) illustrates the efficacy of CL imaging in extracting detailed microstructural history that is not visible optically. Optical (a) cross-polarized light and CL (b) images of a shattered plagioclase grain. Optically, the grain shows at least three generations of cross-cutting quartz-filled cracks and patchy extinction. The CL image reveals remarkable complexity not visible optically. The dark patches are extensive tensile microcrack networks in plagioclase. These are overprinted by a dense network of quartz-filled cracks, the finest of which are not visible optically. Plagioclase fragments are as fine as 1 μm . **Scott Johnson**

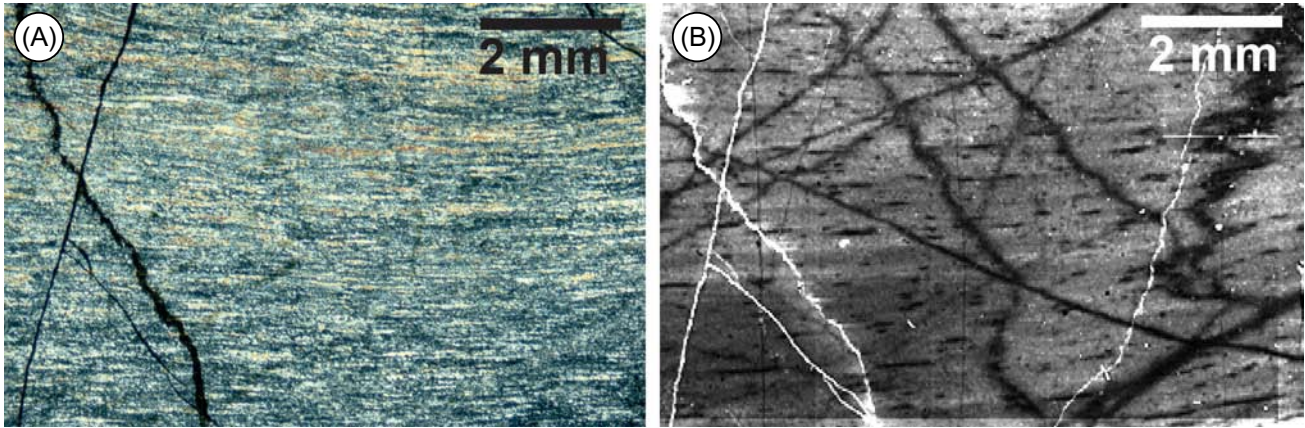


FIGURE 6.49 Optical (a) cross-polarized light and CL (b) images of a fine-grained (<40 μm) recrystallized quartz ribbon. Optically, the ribbon shows a typical recrystallized microstructure. The CL image shows a history of multiple overprinting fracture events preserved as dark bands in the quartz. Remarkably, the two earliest generations have been deformed and folded during viscous flow of the polycrystalline aggregate, suggesting at least three cycles of microcracking followed by viscous flow. All healed microcracks are lined with fluid inclusions. White lines in the CL image are open cracks, also visible optically. **Scott Johnson**



FIGURE 6.50 Intracrystalline deformation microstructures in vein quartz. Location: Fosset (Belgium), vein quartz in the Lower Devonian Anlier Formation of subgreenschist facies. Image width: 1 mm. Three sets of fine extinction bands in a single quartz crystal from an early orogenic quartz vein within quartzite deformed under subgreenschist conditions in the High-Ardenne slate belt (Belgium, France, Luxembourg, Germany), part of the Variscan orogenic belt. The optical axis is parallel to the thin section plane and is oriented top to bottom. The fine extinction bands orthogonal to the optical c-axis are broader (up to 10 μm) and more continuous than those inclined 40 degrees to the left (up to 5 μm) and 40 degrees to the right (up to 3 μm). C-axis misorientation between the fine extinction bands and the host crystal amounts to 5 degrees. Additionally, discontinuous fluid-inclusion trails run left to right through the image. Fine extinction bands in quartz have consistently been called “deformation lamellae” ([Christie et al., 1964](#)), for which tentatively a maximum of two sets of fine extinction bands in a single crystal has been postulated resulting from a tectonic deformation ([French and Koeberl, 2010](#); [Hamers and Drury, 2011](#)). In our tectonically deformed vein quartz, though, we identify multiple cases of quartz single crystals with three sets of fine extinction bands, as shown in this image. [Vernooij \(2005\)](#) also produced three sets of FEBs with a similar morphology as in this image, in a quartz single crystal deformed during a compression experiment. We believe two sets of fine extinction bands are more common than suggested in the literature. **Tine Derez and Manuel Sintubin**

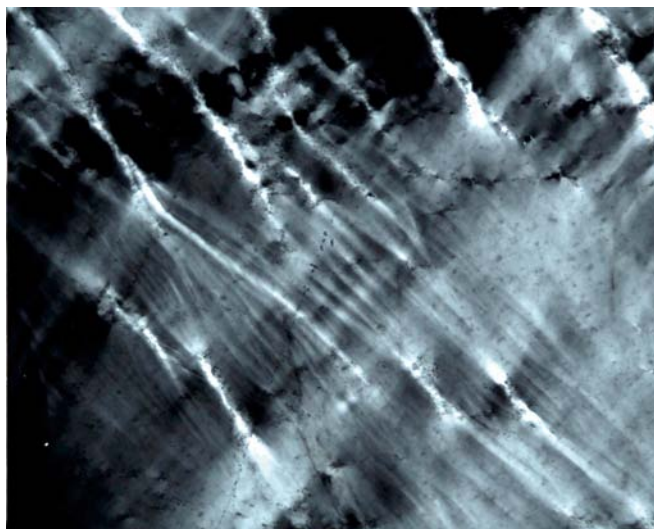


FIGURE 6.51 Intracrystalline deformation microstructures in vein quartz. Location: Herbeumont (Belgium), vein quartz from the Lower Devonian Anlier Formation of subgreenschist facies. Image width: 0.5 mm. Detail of a single quartz crystal in a late-orogenic quartz vein within metapelite deformed under subgreenschist conditions in the High-Ardenne slate belt (Belgium, France, Luxembourg, Germany), part of the Variscan orogenic belt. The optical axis is oriented top to bottom. The quartz single crystal contains three types of intracrystalline deformation microstructures. (1) Discontinuous localized extinction bands (LEBs) ($\sim 20\ \mu\text{m}$ wide, 50 degree dip to the right, contain a high amount of decrepitated fluid-inclusions, c-axis misorientation with the host crystal up to 20 degree) continue into diverging fine ($1\text{--}2\ \mu\text{m}$ wide) extinction bands. (2) Orthogonal to the LEBs, $\sim 50\ \mu\text{m}$ wide extinction bands (3) run diagonally from top right to bottom left. LEBs mostly occur in conjugate, orthogonally arranged sets. Conjugate LEBs are present outside the frame of this image. Mostly LEBs terminate at the crystal boundary, or proceed in a narrow tail geometry within a zone of undulatory extinction bordered by fluid inclusions. To our knowledge, LEBs have never been described to continue into diverging fine extinction bands before. Because these three deformation microstructures have been called a large variety of—often genetic—terms, we suggest using new descriptive terminologies: *fine extinction bands*, *localized extinction bands*, and *wide extinction bands*, as suggested by Derez et al. (2015). **Tine Derez and Manuel Sintubin**

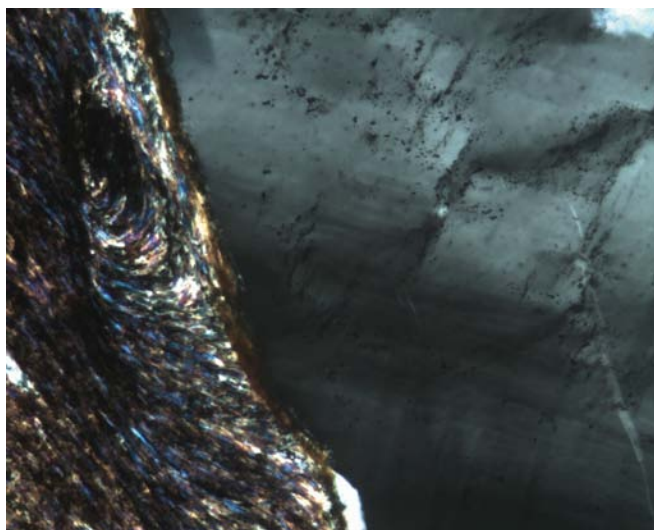


FIGURE 6.52 Intracrystalline deformation microstructures in vein quartz. Location: Bertrix (Belgium), vein quartz in the Lower Devonian Anlier Formation subgreenschist facies host rock. Image width: 0.5 mm. Detail of a quartz single crystal from a late-orogenic quartz vein from the High-Ardenne slate belt (Belgium, France, Luxembourg, and Germany), part of the Variscan orogenic belt, in contact with the slaty host rock. The quartz crystal, with the optical c-axis oriented approximately left to right, contains crosscutting fine extinction bands dipping 70 degrees to the left and 20 degrees to the right ($\sim 1\ \mu\text{m}$ in width). A conjugate set of localized extinction bands (LEBs) with square to rectangular $20\text{--}200\ \mu\text{m}$ wide subgrains, run top to bottom and top right to the center of the image. The rectangular subgrains are partly bound by en-echelon arranged fluid-inclusion planes dipping approximately 50 degrees to the left. From diverse genetic interpretations suggested for LEBs, our observations favor the fracturation-shear model of Van Daalen et al. (1999). The current genetic interpretations need refinement to explain the orientation of the fluid-inclusion planes, (1) dipping ~ 45 degrees with respect to the LEB orientation, (2) having the same orientation in both conjugate LEBs, and (3) being parallel to the maximum shortening direction as deduced by the method of Van Baelen (2010). Furthermore, the association between fine extinction bands and LEBs should be considered, as nearly all crystals containing LEBs consists of fine extinction bands (Derez et al., 2015). The visibility of the fine extinction bands depends on the section. **Tine Derez and Manuel Sintubin**

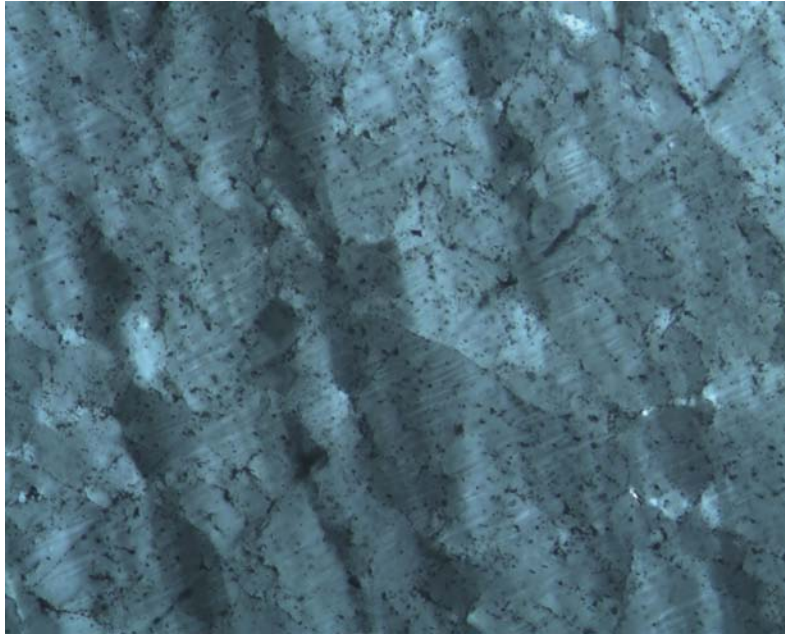


FIGURE 6.53 Intracrystalline deformation microstructures in vein quartz. Location: Bertrix (Belgium), vein quartz in Lower Devonian Anlier Formation subgreenschist facies host rock. Image width: 0.5 mm. Detail of a quartz single crystal from a synorogenic vein within quartzite deformed under subgreenschist conditions in the High-Ardenne slate belt (Belgium, France, Luxembourg, Germany), part of the Variscan orogenic belt. Fine extinction bands (1 μm wide) with misorientation up to 5 degrees and dipping ~ 15 degrees to the left are orthogonal to wide extinction bands that are $\sim 50 \mu\text{m}$ wide, and have a c-axis misorientation up to 20 degrees, and dip 70 degrees to the right. These parallel the optical axis. The wide extinction bands are partly bounded by fluid-inclusion planes perpendicular to their length, giving them a blocky character. Parallel to the wide extinction bands, localized extinction bands (LEBs) of rectangular subgrains, around $50 \mu\text{m}$ in width and a c-axis misorientation up to 60 degrees, can be observed, for example, in the upper left corner of the image. LEBs are very often observed to parallel wide extinction bands. In almost all crystals containing LEBs, fine extinction bands can almost always be observed, depending on the section. From this image, it can be difficult to distinguish wide extinction bands with a blocky character from LEBs. Furthermore, in the vein quartz of the High-Ardenne slate belt, adjoining wide extinction bands are observed to change into en-echelon LEBs. The same is also observed laterally along the wide extinction band orientation. Therefore, we believe LEBs exploit the orientation of previously formed wide extinction bands, as [Gay \(1974\)](#) suggested. **Tine Derez and Manuel Sintubin**

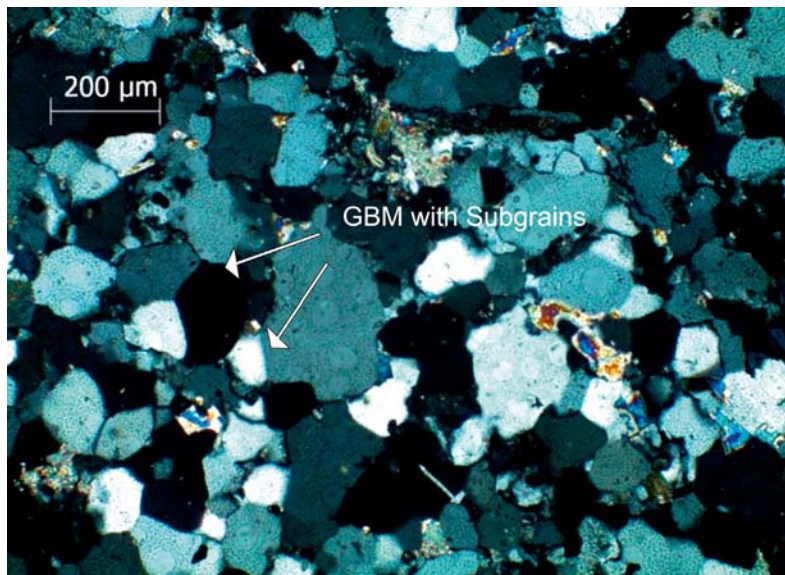


FIGURE 6.54 Quartzite shows “grain boundary migration” (GBM) during grain coarsening ([Barker, 1998](#)). This is a relatively high temperature phenomenon in which grain boundaries are so mobile that they sweep through the entire crystal to remove dislocations and produce subgrains. These grains are lobate and the grain size varies as it is collected away from the Godhra granite. These grains are strain-free and show straight extinction ([Passchier and Trouw, 2005](#)). Ankalwa ($23^{\circ}09'38.56''\text{N}$ – $73^{\circ}37'27.02''\text{E}$), Kadana Formation, Lunawada Group, Gujarat, India. See [Bose et al. \(2018\)](#) for the role of grain size in deformation. **Aditya Joshi, M.A.Limaye, and Bhushan S. Deota**

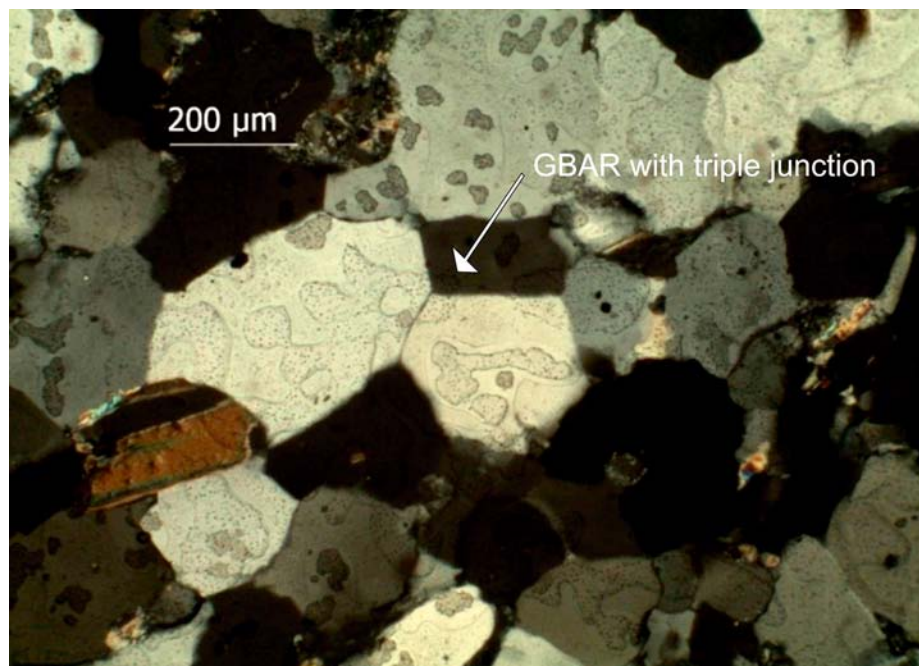


FIGURE 6.55 Grain boundary area reduction (GBAR) in quartzite. This is a high-temperature phenomenon where quartz grains grow by accommodating adjoining smaller grains, producing straight boundaries and triple junctions (Passchier and Trouw, 2005). Such recrystallization is found close to the Godhra Granite. GBAR occurs during deformation and their effect is more obvious and may become dominant after the deformation ceases (Bons and Urai, 1992). Chandsar (23°06'36.73"N-73°38'33.54"E), Kadana Formation, Lunawada Group, Gujarat, India. Aditya Joshi, M.A.Limaye, and Bhushan S. Deota

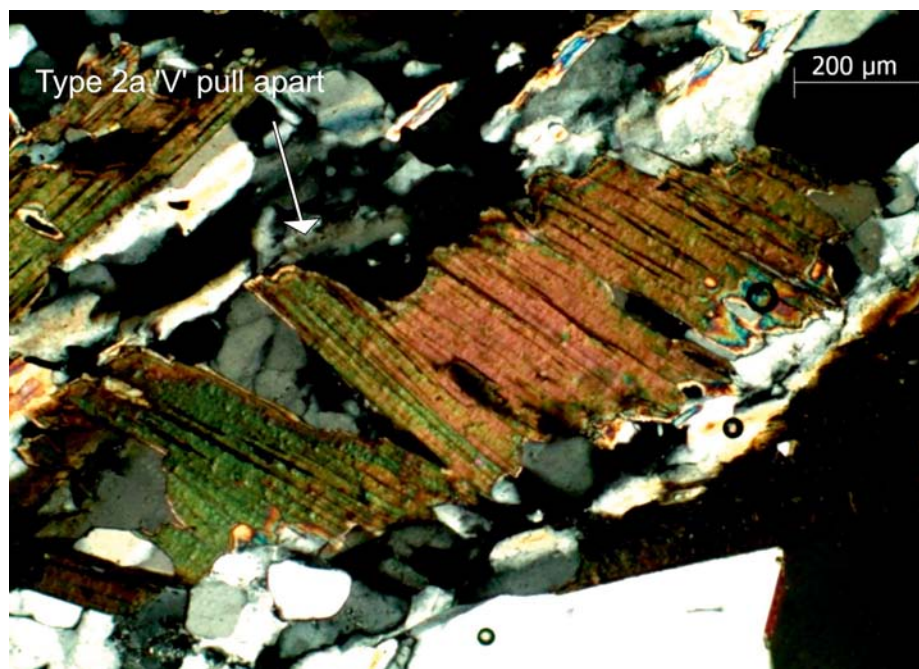


FIGURE 6.56 A "V" pull-apart microstructure of biotite in mylonite. Margins of the two fragments are nonparallel. Based on the sense of rotation, it is interpreted as a type 2a "V" pull apart (Samanta et al., 2001). Within the "V," coarse- and fine-grained quartz occurs. See Mukherjee (2010, 2013) for more examples of V pull aparts. Natyal (23°05'39.51"N-73°42'06.63"E), Kadana Formation, Lunawada Group, Gujarat, India. Aditya Joshi, M.A. Limaye, and Bhushan S. Deota

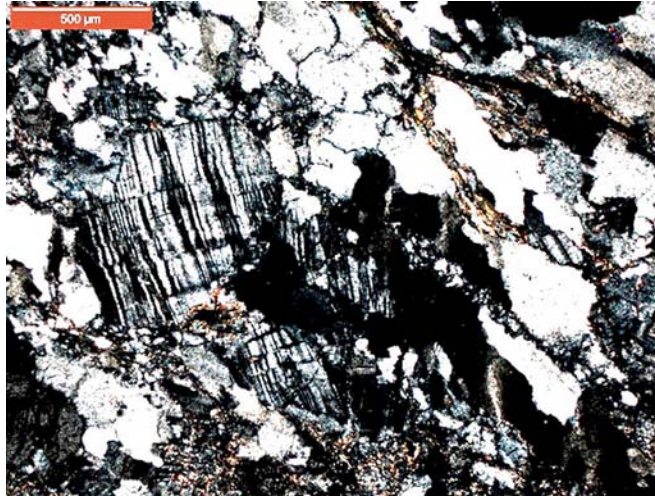


FIGURE 6.57 Microfaulted plagioclase grain found within brecciated granite, equivalent to Closepet Granite, from a brittle shear zone. The microfaulting is subperpendicular to the twin lamellae of the feldspar grain. The plagioclase grain in this rock is surrounded by more or less elongated and recrystallized quartz grains. The feldspar deforms plastically a little before it fractures (brittle deformation), whereas the quartz flows and recrystallizes in a ductile manner (Vernon, 2004; Passchier and Trouw, 2005). Crossed polars. Width of photomicrogram: 2 mm. Sample from Gogi Village along Gogi-Kurlagere fault, Bhima Basin, India. Atanu Mukherjee

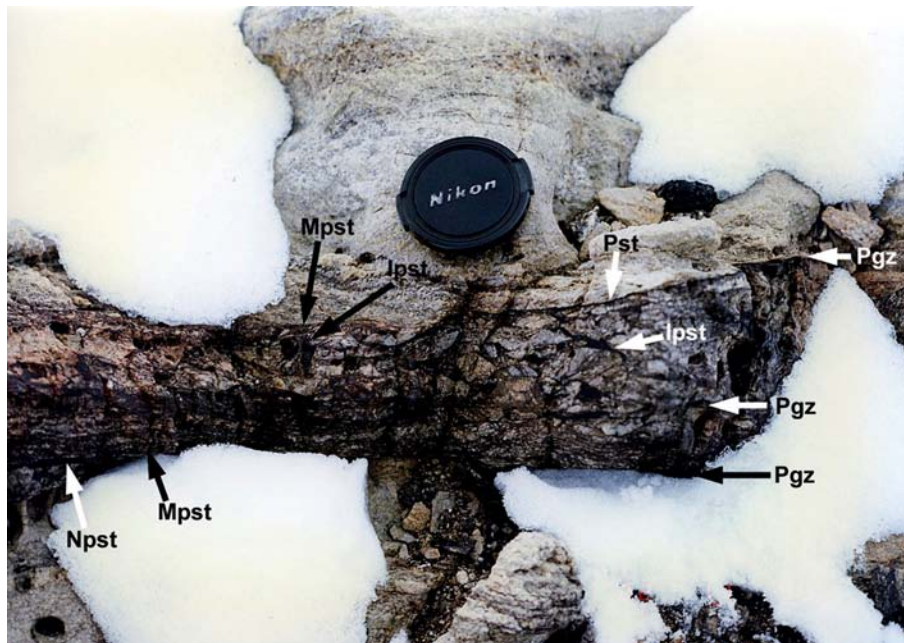


FIGURE 6.58 Fault veins and injection veins of dark-colored pseudotachylyte derived from frictional melting and seismic faulting under granulite-facies conditions. Three fault veins (Pst) of pseudotachylyte occur as pseudotachylyte-generating zones (Pgz) parallel to the foliation of the surrounding garnet-bearing quartzofeldspathic gneiss and two pyroxene-garnet mylonites. Injection veins (Ipst) are oblique to the foliation of the host rocks and bear microlites of vermicular garnet, pyroxene, and plagioclase. Many fault veins of pseudotachylyte mylonitized (Mpst) intensely. The mylonites derived from the fault veins comprise granulite-facies mineral assemblages, including fine-grained orthopyroxene, clinopyroxene, and garnet in their matrix. However, nonmylonitized pseudotachylytes (Npst) that were formed along the mylonitized fault veins often cut the mylonitic foliation. The new fault veins of pseudotachylytes also bear microlites of vermicular garnet, pyroxene, and plagioclase. These suggest that seismic faulting and mylonitization took place repeatedly under granulite-facies conditions. Mylonitization under granulite-facies conditions occurred during Proterozoic time (Owada et al., 2001) or before 2550 Ma (Crowe et al., 2002). Location: 67°07'01"S, 50°19'07"E, Tonagh Island, Napier Complex in East Antarctica. Tsuyoshi Toyoshima, Yasuhito Osanai, Masaaki Owada, Toshiaki Tsunogae, and Tomokazu Hokada

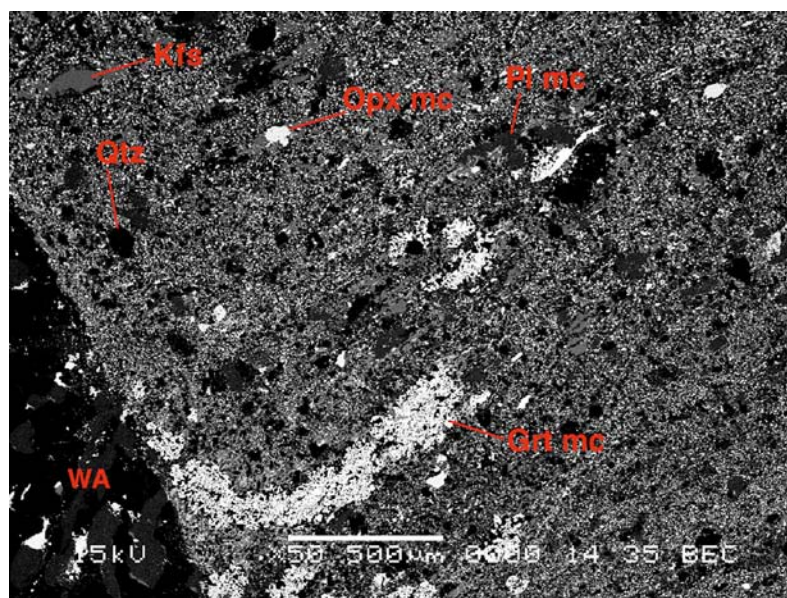


FIGURE 6.59 Backscattered electron image of a part of an injection vein of pseudotachylyte generated under granulite-facies conditions. The injection vein of pseudotachylyte bears microlites of vermicular garnet (Grt mc), orthopyroxene (Opx mc), and plagioclase (Pl mc) but was very weakly mylonitized. However, the fault veins of pseudotachylyte have been strongly mylonitized and changed to orthopyroxene-garnet mylonite under the granulite-facies conditions (Toyoshima et al., 1999). The granulite-facies mylonitization took place within ~2470–2550 Ma (Crowe et al., 2002) or during the Proterozoic time (Owada et al., 2001). Kfs: K-feldspar fragment, Qtz: quartz fragment, WA: host metamorphic rock. Location: 67°06'04"S, 50°15'35"E, Tonagh Island, Napier Complex in East Antarctica. Tsuyoshi Toyoshima, Yasuhito Osanai, Masaaki Owada, Toshiaki Tsunogae, and Tomokazu Hokada

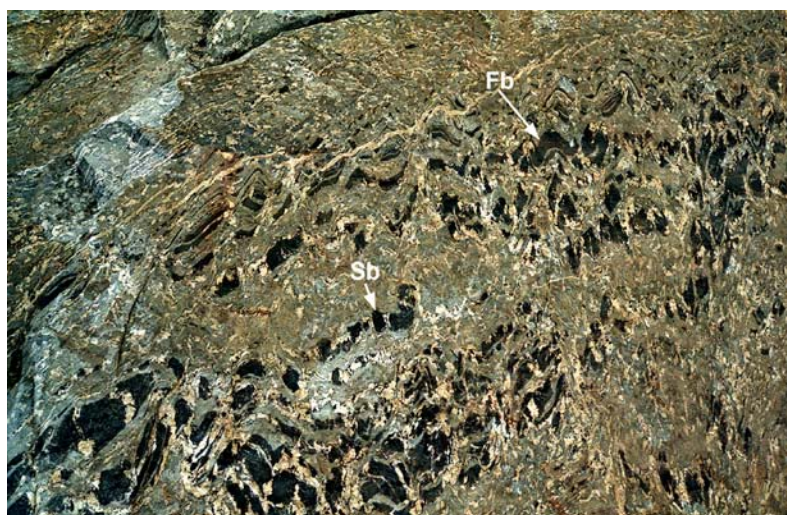


FIGURE 6.60 Amphibolite boudins folded and shortened by crustal shortening related to continental collision between East and West Gondwana. Folded (Fb) and shortened (Sb) boudins of dark-colored amphibolite layers in gray-colored biotite-hornblende gneiss matrix vary in length within 5–20 cm. The spaces (necks) between the boudins are filled with white quartzofeldspathic veins. The boudins are upright folded with wavelenghts up to ~30 cm. The vertical axial-plane foliations of the upright folds develop strongly on the right side of the photo. The boudins have originally pancake shapes with flattening parallel to compositional layering of the ambient gneiss, and resulted from the layer-normal shortening and thinning of crustal rocks between 640 and 600 Ma (Toyoshima et al., 1995). The folds are small-scale parasitic folds of a large-scale upright fold related to 600–560 Ma sinistral transpression and crustal shortening during the collision of parts of East and West Gondwana (Toyoshima et al., 2013). The folded and shortened boudins (Fb) suggest that the tectonic regime changed from layer-parallel extension to layer-parallel compression (Toyoshima et al., 2013). Osanai et al. (2013) presented SHRIMP U–PB ages for metamorphic rocks from the Sør Rondane Mountains, East Antarctica, and they recognized periods of ultrahigh-temperature metamorphism (remain metamorphic stage) within 750–700 Ma and granulite- to amphibolite-facies metamorphism during 640–600 Ma. Location: 72°09'40"S, 25°31'47"E, the southern part of Salen in the Sør Rondane Mountains, East Antarctica. Tsuyoshi Toyoshima, Masaaki Owada, and Kazuyuki Shiraishi



FIGURE 6.61 Eastern bank of Raman Nallah, Bandipora District of Jammu and Kashmir State (India), NW Himalaya. Interpret the structure. Any structures visible? Maqbool Yousuf



FIGURE 6.62 Mud cracks produced by desiccation in modern sediment are downward tapering, V-shaped fractures that display a crudely polygonal pattern in plan. Formed in siliciclastic sediments along with imprints of raindrops. At Jhamarkotra mine, Ajmer, Rajasthan, India. Moloy Sarkar



FIGURE 6.63 A structural geological exercise for students. Hand specimen, 12 cm in the longest dimension, from the Penokean (c. 1850 Ma) orogenic terrane of northeastern Wisconsin, United States. This is a lab exercise sample given to students in an undergraduate structural geology course. The objective is to derive a plausible history for the features displayed. The earliest material in evidence is a highly foliated granitic rock with indication of augen development and perhaps some shear sense. The foliated rock has apparently been intruded by a fine-grained mafic “dike” with a sharp boundary, or perhaps the basaltic rock is an enclave. Both foliated granitic rock and mafic material are cut by a fault without much apparent offset of the augen structure, to the right. On the right and bottom, granitic material that forms a somewhat diffuse mass transects the mafic rock and exhibits a crude foliation parallel to the foliation in the main granitic rock. If the mafic material is actually an enclave, the granitic material intruded before or during deformation. On the other hand, if this is a mafic dike intruding on the granitic rock, then perhaps it contributed to partial melting before the deformation. **Jeff Greenberg**

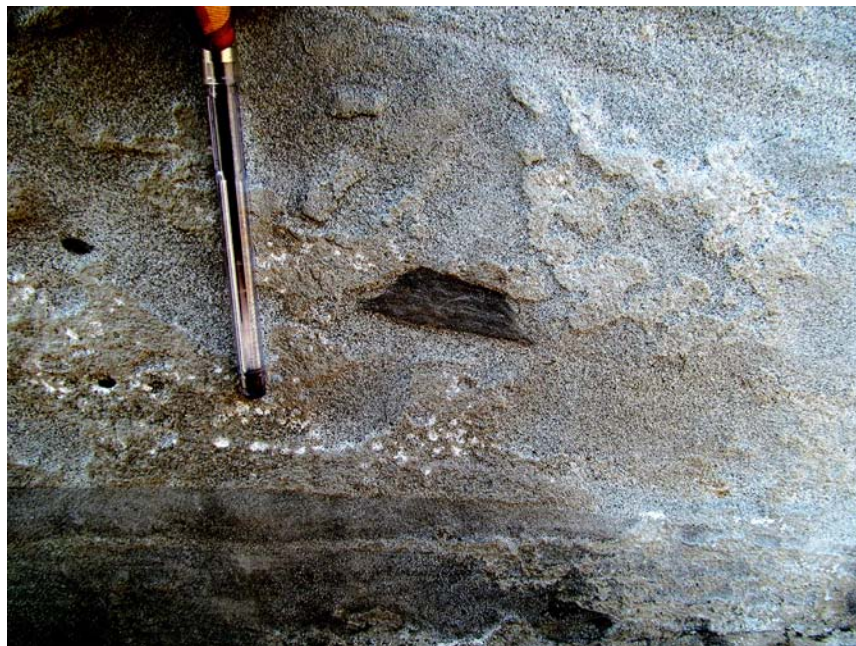


FIGURE 6.64 A very rare trapezoid-shaped mud inclusion within sandstone. Siwalik unit, near Mohand, Roorkee–Dehradun transect, Western Himalaya, Uttarakhand, India. [Mukherjee \(2012\)](#) recently reviewed trapezoid-shaped objects in geology (also see [Mukherjee, 2013, 2014](#)). **Rajkumar Ghosh**



FIGURE 6.65 Filled sand cracks in Paleoproterozoic Gulcheru Formation are related to microbial mat destruction features (78°32'E and 14°20' N), Madyalabodu area, Gulcheru Formation, Cudappah basin, Andhra Pradesh, India. A network of intersecting cracks with varied geometry from polygonal/spindle shapes in mud-free Gulcheru sandstones suggests the presence of a microbial mat contributed extra cohesion to the sand. They are formed on an exposed surface due to desiccation underwater in the presence of microbial communities. This filling of cracks from above by other sands brought in subsequently by aqueous currents (Bottjer and Hegadorn, 2007). **Sukanta Goswami**



FIGURE 6.66 This is a microbially induced sedimentary structure in Gulcheru Quartzite in SW margin of Cuddapah basin, 78°20'E and 14°18' N, Giddankipalle area, Gulcheru Formation, Andhra Pradesh, India. Within ripple troughs, complex crack patterns with sinuous forms occur. These are called Manchuriophycus/Rhysonetron (Eriksson et al., 2007). Shrinkage cracks within rippled sandstone confined to ripple troughs may form if microbial mats grew selectively, or attain a greater thickness in the ripple troughs where eroded cyanobacteria settle from currents under maximum and long-lasting water supply. **Sukanta Goswami**



FIGURE 6.67 Preservation of successive sets of ripples in sandy sediments with crests of each set being relatively sharp and unworked. Within the Gulcheru Quartzite, these successive ripple layers show switches in current directions. The absence of mud between successive rippled sandy beds is typical for palimpsest ripples. Nonamalgamation of two rippled sandstone beds can indicate the presence of biofilm or a mat providing organically mediated sand stabilization. The preservation of underlying ripples despite the deposition of an overlying sandy rippled bed connotes the presence of a microbial mat separating the two successive sand beds, protecting the earlier ripples from being reworked (Bottjer and Hegadorn, 2007). 78°30'E, 14°20'N, Madyalabodu area, Gulcheru Formation, Cudappah basin, Andhra Pradesh, India. **Sukanta Goswami**

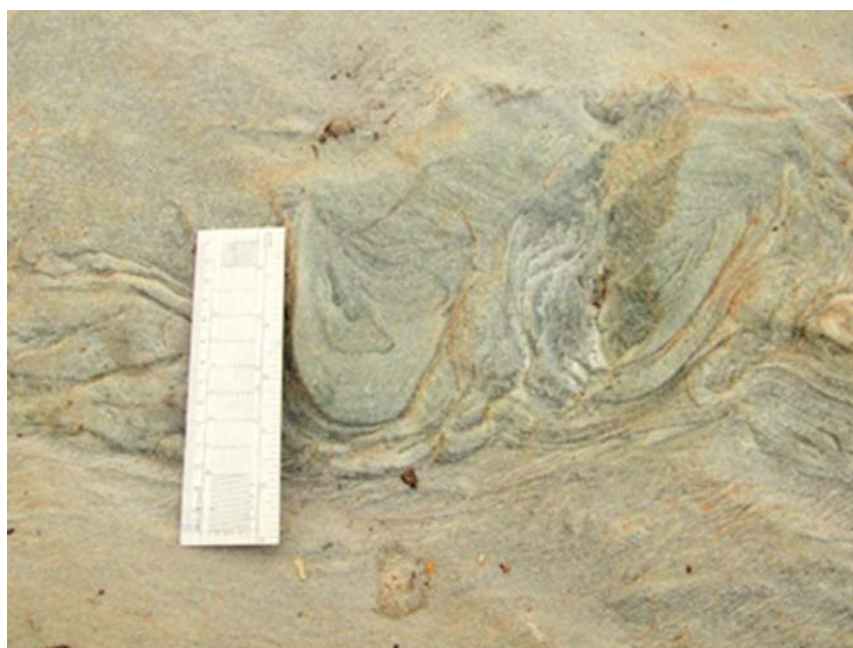


FIGURE 6.68 Convolute structure. Convolute structure in quartzite shows marked crumpling or complicated folding of laminations. According to Boggs Jr (2006), this structure can be produced due to liquefaction of sediments by processes such as differential overloading, earthquake shocks, and breaking waves. Ghatshila, Jharkhand, India. **Sanjukta De**



FIGURE 6.69 Ellipsoidal to bulbous chert nodules as structureless dense masses within carbonate rocks of Vempalle Formation, Motnupalapalle area, Cudappah basin, Andhra Pradesh, India. They range from a few centimeters up to 1 m. The occurrence of chert in Precambrian rocks indicates that they precipitated chemically from silica oversaturated water. Pore waters supersaturated with respect to silica and undersaturated with respect to calcium carbonate would favor the dissolution of calcium carbonate and the simultaneous precipitation of silica, especially with reduced pH (Knauth, 1979). Because alkaline marine surface waters are highly undersaturated with silica and nearly saturated with calcium carbonate, it is unlikely that chert nodules form from marine pore waters. Such conditions might occur under several sets of diagenesis involving meteoric pore waters enriched in silica from the dissolution of silicate minerals (Hefferan and O'Brien, 2010). Sukanta Goswami



FIGURE 6.70 Characteristics of sedimentary dikes in lacustrine organic rich and poor laminated lime mudstone deposits of the Eocene Green River Formation, Washakie Basin, Wyoming. Sedimentary dikes are up to 1.5 m long and several centimeters wide, filled with homogeneous lime mudstone or a mixture of fragmented material lacustrine sedimentary rocks and tuff material. In most cases, the infill is silicified, and in cases where a central conduit can be observed, filled with massive or laminated chert. If identifiable, the source of the cracks is a brecciated or massive silty lime mudstone layer, showing syneresis-like cracks. Often the dikes are represented by isolated blubs or horizontal sills in the laminated sediment, without a well-defined source interval. They show moderate sinuosity and branching. The dikes are more frequent and bigger in size at the base of a regional marker bed, and they can be traced for several tens of kilometers. Their morphological characteristics are similar to the ones found in several other stratigraphic levels below, which suggests a common origin. Similar structures have been previously described as “dewatering structures” (e.g., Tănăvsuu-Milkeviciene and Sarg, 2012) or sedimentary injection features (e.g., Hurst et al., 2011). Rhodes et al. (2007) interpreted these dikes as the result of desiccation. However the morphology and the infill of the cracks (with a central conduit) indicate dewatering, fluid migration, and sediment remobilization, which are related to tectonic activity at that time. Multiple filling indicates more than one fluidization event and remobilization of the sediments. Reproduced from Figure 22 of Törő et al. (2013). Balázs Törő, Brian R. Pratt, and Jennifer J. Scott



FIGURE 6.71 Broken bridge structure. A Mesozoic lamprophyre dyke displaying a minor broken bridge structure (e.g., Schofield et al., 2012) coincident with the axis of a minor fold in Ordovician sediments near Leading Ticks, Newfoundland, Canada. This coincidence is interpreted to be a demonstration of a preexisting structure influencing subsequent geological evolution (i.e., structural inheritance). This dyke forms a part of a radial suite surrounding a gabbroic body known as the Budgell Harbour Stock. The stock intruded during the rifting leading to the opening of the Atlantic Ocean (Peace et al., 2018a,b; Geng et al., 2019). **Alexander Peace**



FIGURE 6.72 Pyroclast deforming the previously deposited volcanoclastic succession. Notice the folding of the thin, hard, reddish horizon above the black layer around the metric-scale pyroclast. Also, observe the thickening of the black layer caused by the impact of the bomb (immediately to the left of the pyroclast). (Lens cap: 70 mm diameter). Cerro Gordo Volcano, Castilla La Mancha, Spain (coordinates: 38°50'01.8"N, 3°44'18.0"W). **Irene Cantarero and Eloi Carola**



FIGURE 6.73 Archaeoseismology. The instrumental record of seismic activity is less than 100 years old while the recurrence of major earthquakes is measured on a centennial to millennial scale. Archaeoseismology aims to extend this record throughout the period characterized by artificial structures. Ancient buildings bearing particular features of damage provide evidence for past earthquakes. These allow determining the parameters (date, intensity, epicenter, magnitude) of causative seismic events. Terms of structural geology are used in describing the damage produced by seismic loading. Examples of secondary, off-fault damages produced by seismic shaking are shown below on [Figures 6.70–6.75](#). V-shaped, extruded block bordered by conjugate faults. A wedge-shaped block of masonry, c. $7 \times 7 \text{ m}^2$, shifted toward the 240 degree azimuth by $\sim 20 \text{ cm}$ during the largest known earthquake in the Near East, in 1202 CE. Donjon of the Al-Marqab citadel, Syria, built by the Hospitaller knights in the late 12th century. Built of Roman concrete (rubble in lime), the external and internal walls are faced by dressed basalt blocks. Walls are up to 5 m thick and the diameter of the tower is 20 m. Between floors—where the extruded wedge is—the building is compact. Al-Marqab, south of Baniyas on the Mediterranean coast, Syria ($35^\circ 09' \text{N}$, $35^\circ 56' \text{E}$). See [Kázmér and Major \(2010\)](#) and [Kázmér \(2015\)](#) for detail. **Miklós Kázmér**



FIGURE 6.74 Distributed left-lateral strike-slip deformation in the Roman theater of Baelo Claudia, Gibraltar Straits, Spain ($36^\circ 05' \text{N}$, $5^\circ 46' \text{E}$). There are conspicuous displacements visible on the wall of the staircase and between the blocks forming the arch in the foreground. Displacement is larger upward (maximum 10 cm), indicating seismic shaking: the top part of the building oscillated with higher amplitude than the lower part, attached to the foundation. The town along the northern coast of the Gibraltar Straits flourished during the first to fourth century CE. After an earthquake of intensity IX–X MSK ~ 350 –395 CE, the city was abandoned. Active faults nearby and a landslide within the area of the Roman town contributed to the damage. Scale: stairs on the left are 20–25 cm high. Read [Silva et al. \(2005\)](#), [Kamh et al. \(2008\)](#), [Karakhanian et al. \(2008\)](#), and [Grützner et al. \(2012\)](#) for detail. **Miklós Kázmér**



FIGURE 6.75 Dropped keystones and adjacent blocks in the arches of the Colosseum, caused by earthquake shaking. The feature is a miniature analogue of rifting: extension produced open fissures, normal faulting, subsidence, and tilting of blocks. The Flavian amphitheater in Rome, Italy, world-wide known as Colosseum ($41^{\circ}53'N$, $12^{\circ}29'E$), was built between 70 and 76 CE. The external wall is composed of travertine blocks originally connected by iron pins and cramps embedded in lead, without mortar. Holes of uniform size between the blocks were made to steal the lead in times of scarce supply. Several earthquakes between 508 and 1703 CE affected Rome and the Colosseum. The heterogeneity of the soil beneath the foundations (lake sediments below the northern part as opposed to an abandoned bed of the river Tiberis below the southern part) yielded uneven vibration and settlement during earthquakes. This is why the southern perimeter wall of the Colosseum collapsed. The photo shows severely damaged arcades 23 and 24 between the collapsed and intact portions of the external wall on the eastern end of the amphitheater. These were closed by a brick wall during a restoration effort in 1805–1807, preserving the arches in their damaged form. Read [Korjenkov and Mazar \(2003\)](#), [Kamai and Hatzor \(2008\)](#), [Marco \(2008\)](#), and [Pau and Vestroni \(2008\)](#) for detail. Miklós Kázmér



FIGURE 6.76 Rotated blocks within the seawall of the crusader castle, Tartous, coastal Syria ($39^{\circ}53'N$, $35^{\circ}52'E$). The fortress, built in the 12th century, suffered the greatest damage probably during the 1202 CE earthquake. Blocks are c. 70 cm high. The counterclockwise rotation of four blocks together (left block toward the viewer) was caused by E-W strong seismic motion. There is a right-lateral strike-slip fault on the northern side of the leftmost blocks. The vertical component of the seismic waves rotated the blocks when the overburden was momentarily relieved, and seismic loading overcame friction. Read [Korjenkov and Mazar \(1999\)](#), [Meghraoui et al. \(2003\)](#), [Similox-Tohon et al. \(2006\)](#), and [Rodríguez-Pascua et al. \(2011\)](#) for detail. Miklós Kázmér

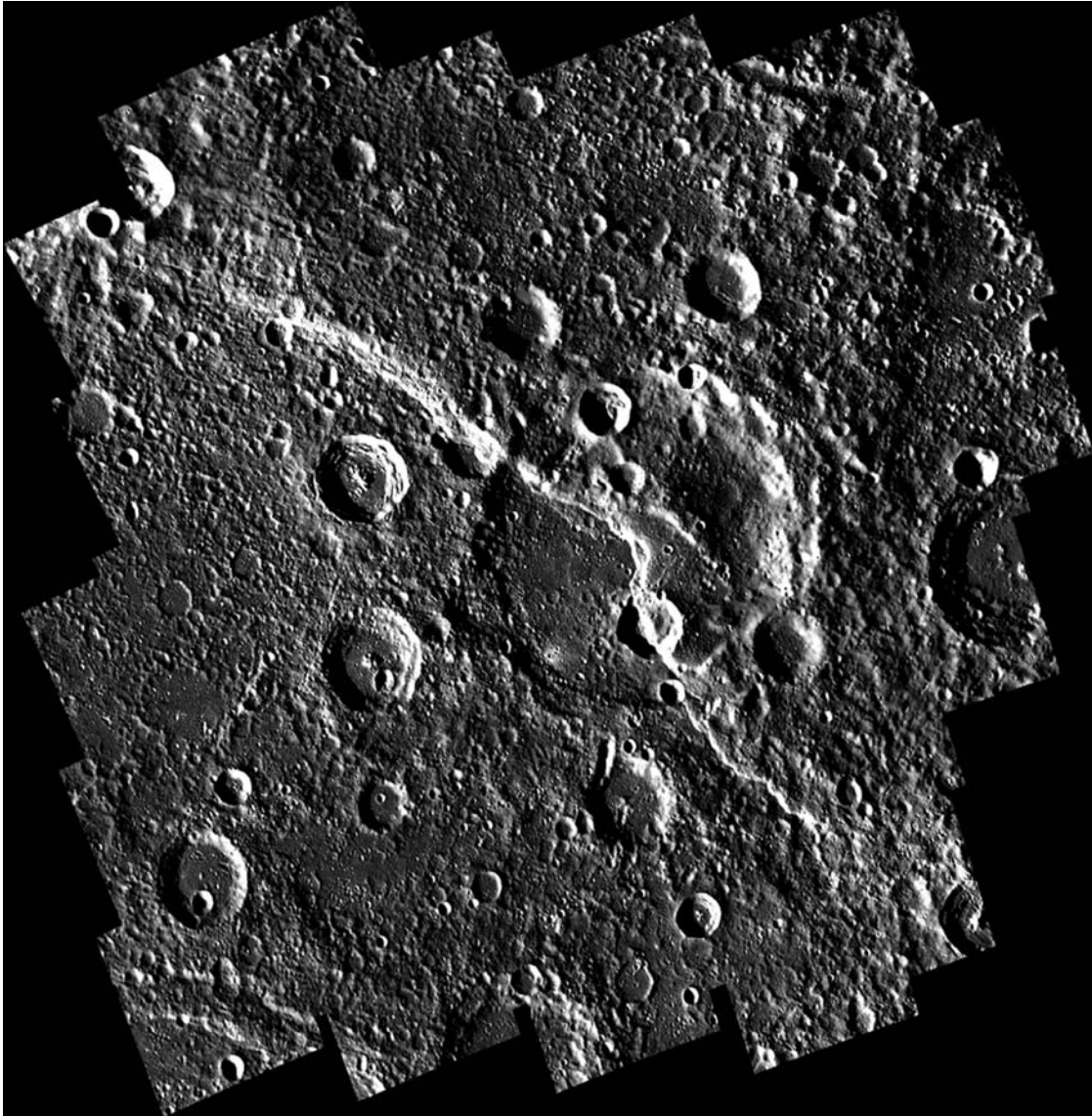


FIGURE 6.77 Carnegie Rupes is a >250 km long thrust fault-related landform on the innermost planet, Mercury. It crosscuts several large and small impact craters; the largest one, the Duccio crater near the center of the image, has a ~110 km diameter. As plate tectonics do not operate on Mercury, landforms such as the Carnegie Rupes form in response to global contraction caused by secular cooling of the planet's interior. More than 5000 such landforms have been identified on Mercury so far. The total shortening accommodated by these landforms corresponds to a decrease of Mercury's radius by as much as 7 km. This image is a mosaic of 48 individual photographs taken by the Mercury Dual Imaging System (MDIS) aboard the MErcury Surface, Space ENvironment, GEochemistry, and Ranging (MESSENGER) spacecraft. The image is shown in equirectangular projection centered at 58.31°N, 53.07°W. (Image credit: NASA/Johns Hopkins University Applied Physics Laboratory/Carnegie Institution of Washington). **Christian Klimczak and Paul K. Byrne**

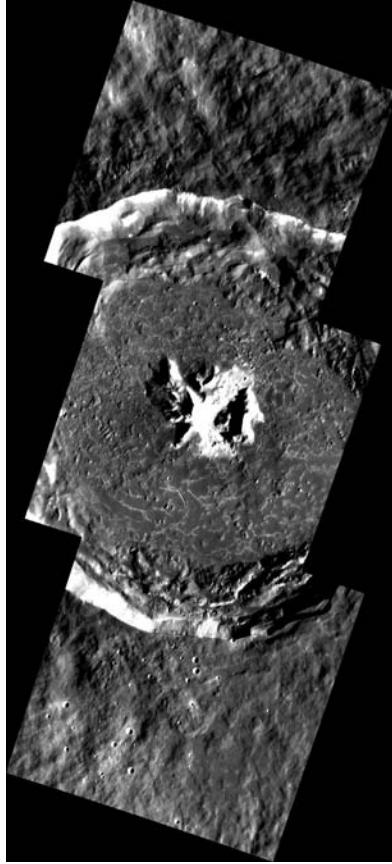


FIGURE 6.78 The floor of the Degas crater. The floor of the well-preserved, 50 km diameter Degas crater is covered with impact melt. As the impact melt sheet cooled, a generally hexagonal joint pattern developed. The central peak of Degas is made up of subsurface material uplifted by the impact. Over time, material from the tops of the central peaks has slid downslope. This exposed fresh material that appears bright in this image. The hummocky texture of the interior crater wall is due to landslides that developed after the crater formed. This mosaic, consisting of three Mercury Dual Imaging System (MDIS) photographs, is shown in equirectangular projection centered at 36.99°N, 127.24°W. (Image credit: NASA/Johns Hopkins University Applied Physics Laboratory/Carnegie Institution of Washington). **Christian Klimczak and Paul K. Byrne**

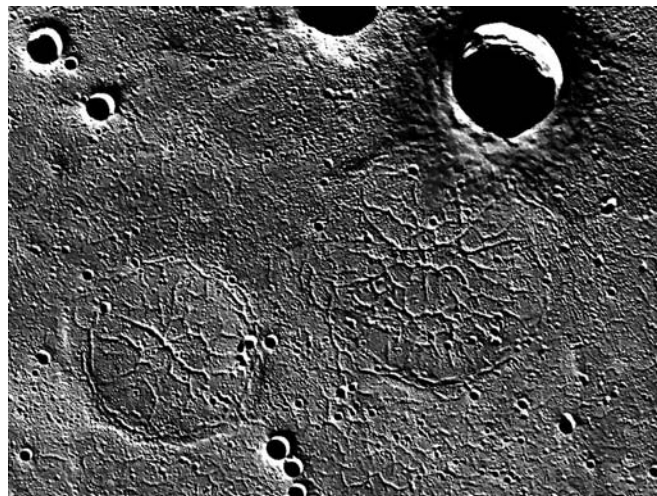


FIGURE 6.79 The interior of the volcanically buried Goethe impact basin. The Goethe impact basin is buried under a 1–2 km thick layer of lava. Two smaller craters near the basin center, 42 and 55 km in diameter, were also buried. The pooling and subsequent cooling of the thick lava sequence in these craters caused localized extension, and developed these large fractures. Circumferentially oriented fractures are superposed on rings of wrinkle ridges that likely demarcate the rims of the buried craters. Due to global contraction, Mercury is in a tectonic regime governed by large horizontal compressive stresses. Such a tectonic environment does not readily allow for extensional structures to form. Therefore, fractures such as those found in the volcanic units burying the Goethe basin can only form in areas that are protected from global contraction. This MDIS mosaic is shown in north polar stereographic projection; the center of the image is at 81.33°N and 52.32°W. (Image credit: NASA/Johns Hopkins University Applied Physics Laboratory/Carnegie Institution of Washington). **Christian Klimczak and Paul K. Byrne**

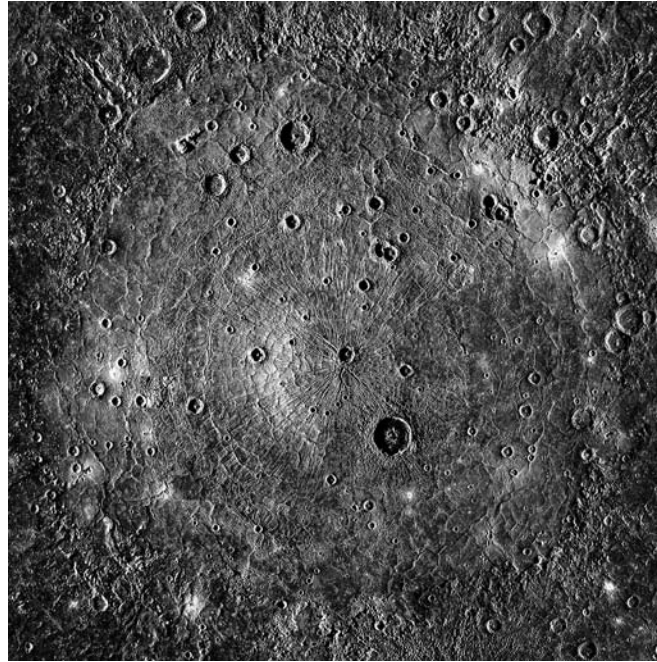


FIGURE 6.80 The Caloris basin is the largest preserved impact structure on Mercury. With an E-W diameter of 1640 km, the floor of the basin subtends ~ 40 degrees of the arc. The interior of the basin, which has been filled with voluminous low-viscosity lava, is replete with both contractional (wrinkle ridges) and extensional (graben) structures. The origin of these structures is not clear. The graben may have formed by thermal contraction of the interior lava, similar to what is observed within the Goethe basin, for example. Yet the pronounced radial orientations of the innermost graben are yet to be explained. The wrinkle ridges may be the result of the subsidence of the Caloris interior lava; however, in many places they remained active after the graben, and so could be due to the sustained global contraction of Mercury as its interior cooled. The image is in an orthographic projection centered at 31.5°N , 162.7°E . (Image credit: NASA/Johns Hopkins University Applied Physics Laboratory/Carnegie Institution of Washington). **Christian Klimczak and Paul K. Byrne**

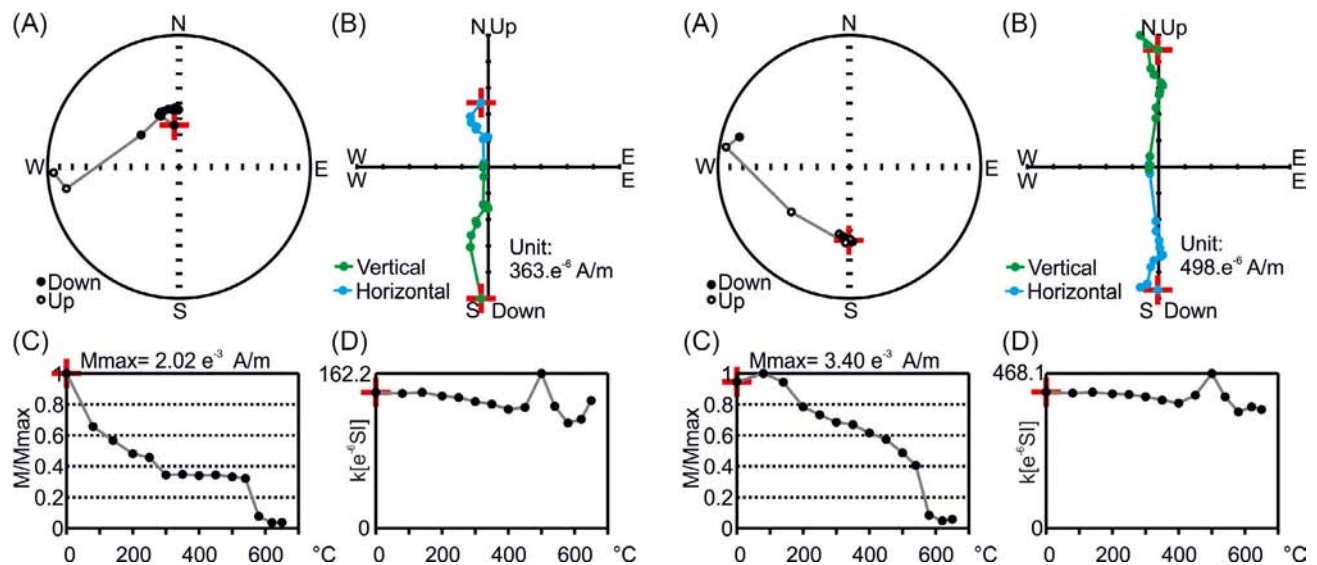


FIGURE 6.81 Paleomagnetic studies—thermal demagnetization. The tower karst in Guilin, Guangxi Zhuang Autonomous Region, is regarded as one of the most beautiful and spectacular landform assemblages in China as well as in the world (Tang and Day, 2000). This terrain is well known for its eye-catching limestone towers, which rise almost vertically from plains covered with rice paddies (Waltham, 2009). Bedrock exposures in Guilin are mainly of the upper Paleozoic, Mesozoic, and Cenozoic strata (Tang and Day, 2000). The upper Devonian rocks were studied for paleomagnetic research. The figures show thermal demagnetization of samples with normal polarity (A), and reverse polarity (B). The red cross represents the beginning of the demagnetization process: (a) Stereographic Lambert projection on the lower (solid circles) and upper hemisphere (open circles). (b) Zijdeveld (1967) plot projects the demagnetization vector on the horizontal plane (blue dots) and on the vertical plane (green dots). (c) Module plot presents magnetization during demagnetization, which is normalized by its maximum value. (d) Magnetic susceptibility plot proves the stability of the magnetic phases during the measurement heating. **Petr Schnabl and Lucie Novakova**

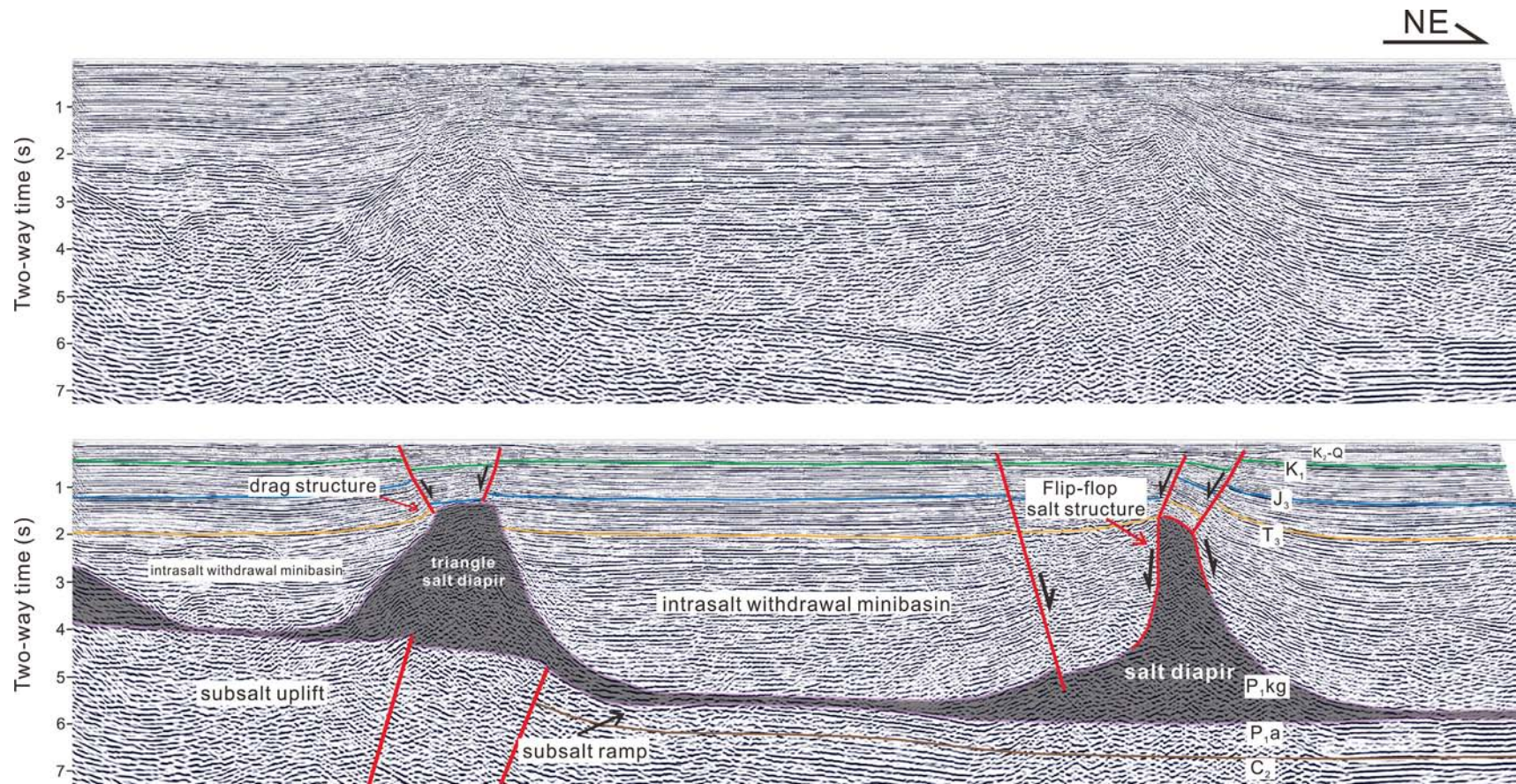


FIGURE 6.82 Structural geological interpretation from seismic image-1. (a) Uninterpreted and (b) interpreted seismic section showing salt structures in the Southern Precaspian Basin. Note that the asymmetric reflection geometry in the overburden on the salt diapir (right) could be characteristic of the “flip-flop” salt structure. It is a type of salt structure that bears similarity to reactive salt diapir, except that it is asymmetric and can itself drive normal faulting as it grows (Quirk and Pilcher, 2012). Wu et al. (2018) presented a few more seismic image interpretations for salt structures for the Precaspian Basin. Zhenyun Wu, Hongwei Yin, Hemin Koyi, and Xin Wang

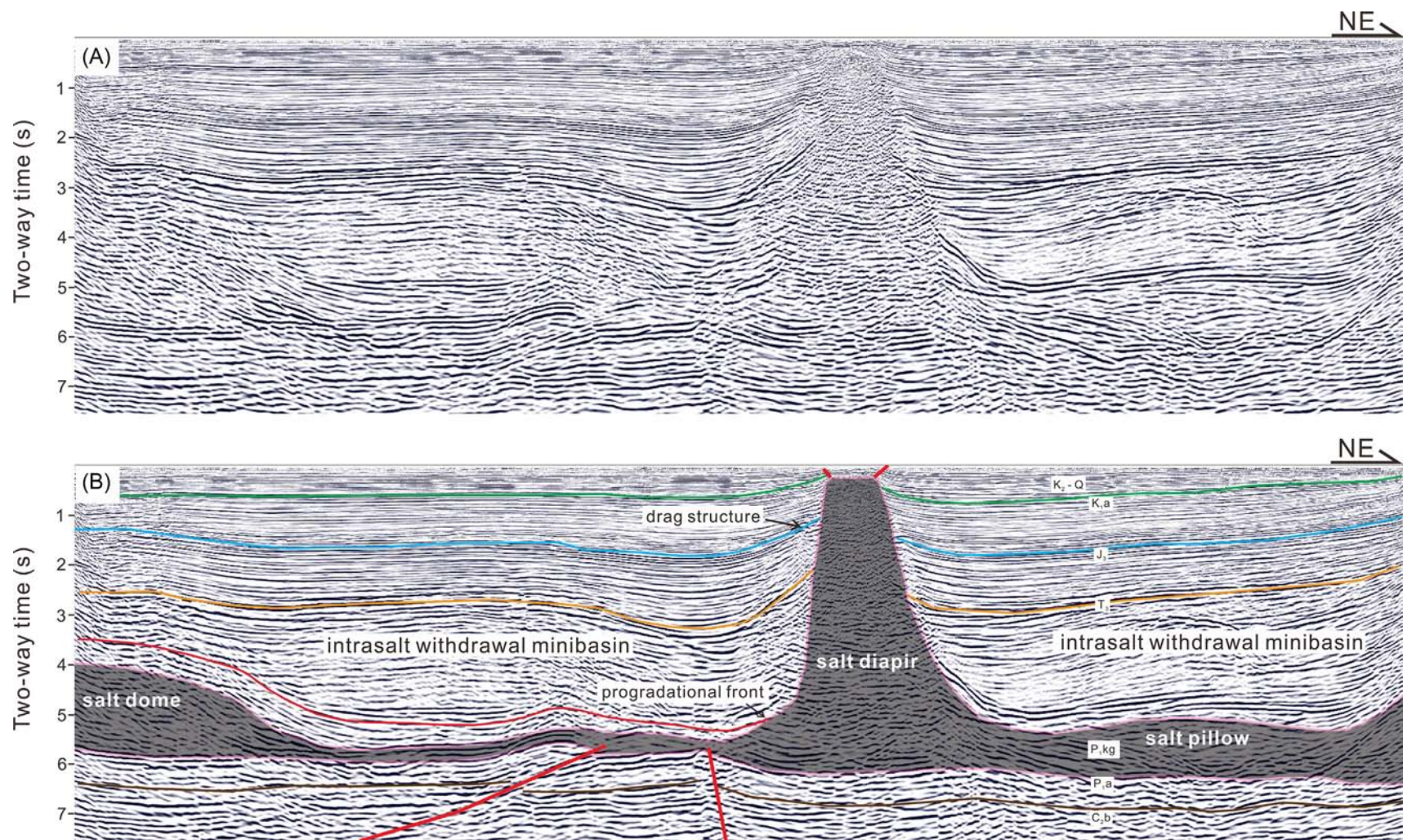


FIGURE 6.83 Structural geological interpretation from seismic image-2. (a) Uninterpreted and (b) interpreted seismic section showing salt structures in the Southern Precaspian Basin. A large salt diapir, accompanying many associated drag structures, occurs at the progradational front. A minor salt pillow (right) formed adjoining the salt diapir under the intrasalt withdrawal minibasin in this seismic section. Zhenyun Wu, Hongwei Yin, Hemin Koyi, and Xin Wang

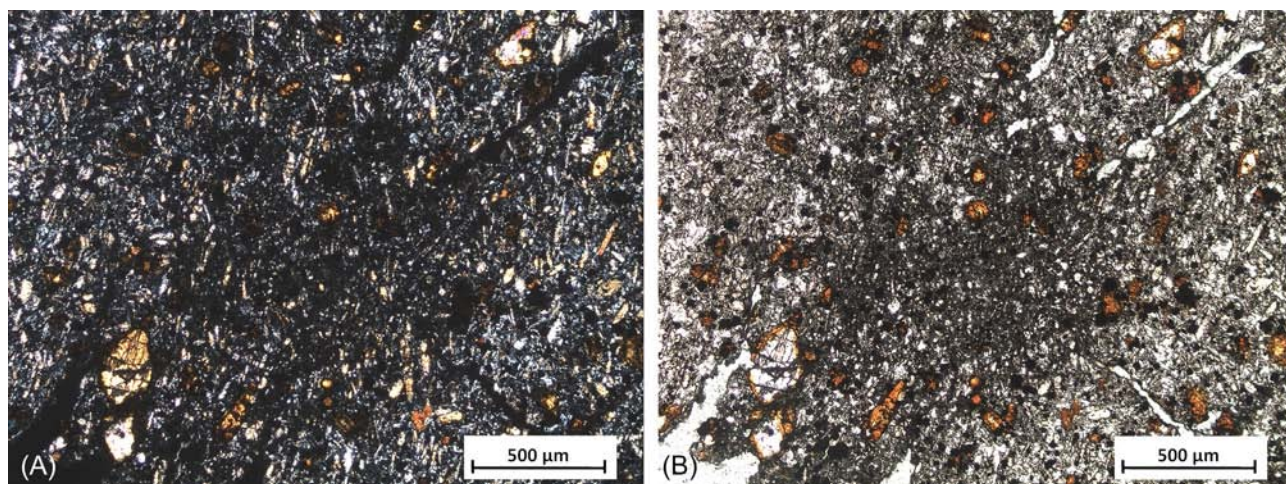


FIGURE 6.84 (A) Basalts in the active quarry north-east of the town of Sulikow in Poland contain olivine, plagioclase, pyroxene, and opaque magnetite (Kurdowski, 2014). Thin section image from a sunburn nephelinite out of a lava flow under plane polarized light. (B) Sample of Figure 6.84A under crossed nicols. See previous caption for detail. Note the analcite, which appears in dark clouds under plane polarized light (B). From such clusters of small analcite cracks developed into the rock itself. These cracks are filled with secondary minerals like zeolites or calcite. The unaffected rock is composed of olivine and clinopyroxene as phenocrysts and as microlites. Additional nepheline and opaque minerals form the microlites. The Landmark mountain of Görlitz town in Germany, known as the Landeskron, represents a volcano composed mainly of volcanic slag that formed 34 million years ago as a solidified lava lake (Meschede and Warr, 2019). Joerg Büchner, Lucie Novakova, and Petr Schnabl

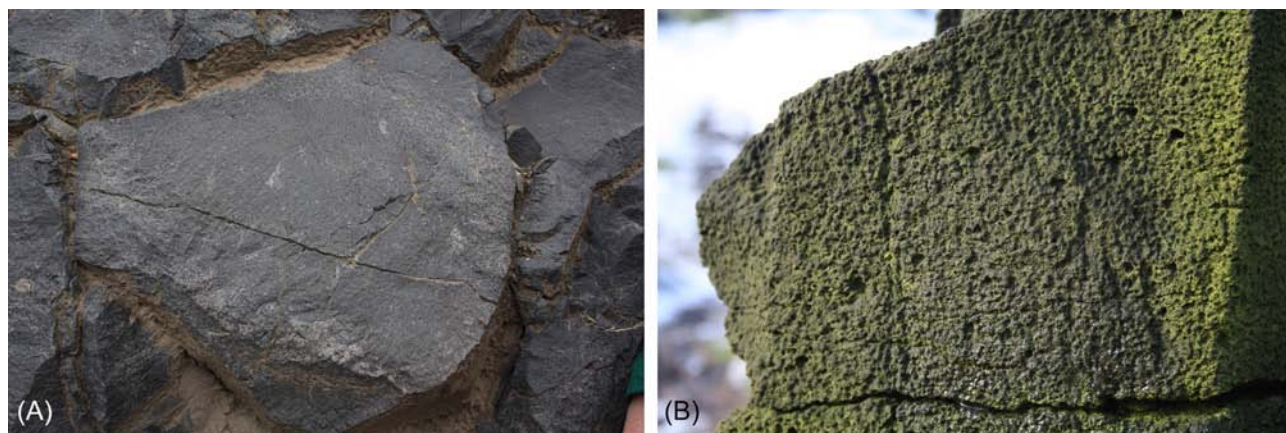


FIGURE 6.85 Cross-section of a nephelinitic column, partly affected by sunburn. Width of the image is c. 60 cm. (A) Cross-section view of columnar jointed nephelinite from a lava lake of the small scoria cone at Landeskron (Büchner and Tietz, 2012). Sunburn textures occur in lavas with a composition of olivine-bearing alkali basalt to basanite. The sunburn basalt is more fractured and less resistant than the fresh one, and so its identification is of interest in all types of basalts (Novakova et al., 2018). The cloudy distribution of sunburn affection is visible due to the whitish network like parts within the lava. (B) Increased affection of sunburn is evident by a surface-like pockmarked skin. Joerg Büchner, Lucie Novakova, and Petr Schnabl

References

- Barker, A.J., 1998. *Introduction to Metamorphic Textures and Microstructures*, second ed. Blackie, Glasgow, p. 264.
- Bikramaditya Singh, R.K., Gururajan, N.S., 2011. Microstructures in quartz and feldspars of the Bomdila gneiss from western Arunachal Himalaya, India: implications for geotectonic evolution of the Bomdila mylonitic zone. *Journal of Asian Earth Sciences* 42, 1163–1178.
- Boggs Jr., S., 2006. *Principles of Sedimentology and Stratigraphy*. Pearson Education.
- Bons, P.D., Urai, J.L., 1992. Syndeformational grain growth: microstructures kinetics. *Journal of Structural Geology* 14, 1101–1109.
- Bose, N., Mukherjee, S., 2020. Estimation of deformation temperatures, flow stresses and strain rates from an intra-continental shear zone: the Main Boundary Thrust, NW Himalaya (Uttarakhand, India). *Marine and Petroleum Geology* 112, 104094.
- Bose, N., Dutta, D., Mukherjee, S., 2018. Role of grain-size in phyllonitisation: insights from mineralogy, microstructures, strain analyses and numerical modeling. *Journal of Structural Geology* 112, 39–52.
- Bottjer, D., Hegadorn, J.W., 2007. In: Schieber, J., Bose, P.K., Eriksson, P.G., Banerjee, S., Sarkar, S., Altermann, W., Catuneau, O. (Eds.), *Atlas of Microbial Mat Features Preserved Within the Siliciclastic Rock Record*. Elsevier, pp. 53–71.
- Brodie, K.H., Rutter, E.H., 1985. On the relationship between deformation and metamorphism, with special reference to the behavior of basic rocks. In: Thompson, A., Ruby, D. (Eds.), *Metamorphic Reactions: Kinetics, Textures, and Deformation*. Springer, pp. 138–179.
- Broggi, A., Capezzuoli, E., 2009. Travertine deposition and faulting: the fault-related travertine fissure-ridge at Terme S. Giovanni, Rapolano Terme (Italy). *International Journal of Earth Sciences* 98, 931–947.
- Büchner, J., Tietz, O., 2012. Reconstruction of the Landeskrone scoria cone in the Lusatian Volcanic Field, Eastern Germany – long-term degradation of volcanic edifices and implications for landscape evolution. *Geomorphology* 151–152, 175–187.
- Chesterman, C.W., Kleinhampl, F.J., 1991. Travertine hot springs, Mono County, California. *California Geology* 44, 171–182.
- Choukroune, P., Séguret, M., 1973. Carte structurale des Pyrénées, 1/500.000. Université de Montpellier–ELF, Aquitaine.
- Christie, J.M., Griggs, D.T., Carter, B.J., 1964. Experimental evidence of basal slip in quartz. *Journal of Geology* 72, 734–756.
- Crossey, L.J., Karlstrom, K.E., 2012. Travertines and travertine springs in eastern grand canyon: what they tell us about groundwater, paleoclimate, and incision of grand canyon. *Geological Society of America Special Papers* 489, 131–143.
- Crowe, W.A., Osanai, Y., Toyoshima, T., Owada, M., Tsunogae, T., Hokada, T., 2002. SHRIMP geochronology of a mylonite zone on Tonagh Island: characterization of the last high-grade tectonothermal event in the Napier complex, East Antarctica. *Polar Geoscience* 15, 17–36.
- Davis, G.H., Reynolds, S.J., Kluth, C.F., 2012. *Structural Geology of Rocks and Regions*, third ed. Wiley, New York.
- De Filippis, L., Billi, A., 2012. Morphotectonics of fissure ridge travertines from geothermal areas of mammoth Hot Springs (Wyoming) and Bridgeport (California). *Tectonophysics* 548–549, 34–48.
- De Filippis, L., Faccenna, C., Billi, A., Anzalone, E., Brilli, M., Özkul, M., Soligo, M., Tuccimei, P., Villa, I., 2012. Growth of fissure ridge travertines from geothermal springs of Denizli basin, western Turkey. *Geological Society of America Bulletin* 124, 1629–1645.
- De Filippis, L., Faccenna, C., Billi, A., Anzalone, E., Brilli, M., Soligo, M., Tuccimei, P., 2013. Plateau versus fissure ridge travertines from quaternary geothermal springs of Italy and Turkey: interactions and feedbacks between fluid discharge, paleoclimate, and tectonics. *Earth-Science Reviews* 123, 35–52.
- Denyer, P., Alvarado, G.E., 2007. Mapa geológico de Costa Rica. Escala 1: 400.000. Librería Francesa, San José, Costa Rica.
- Derez, T., Pennock, G., Drury, M., Sintubin, M., 2015. Low-temperature intracrystalline deformation microstructures in quartz. *Journal of Structural Geology* 71, 3–23.
- Dillon, J.T., Brosge, W.P., Dutro, J.T., 1986. Generalized Geologic Map of the Wiseman Quadrangle. US Geological Survey Open-File Report 86-219, Alaska.
- Eriksson, P.G., Porada, H., Banerjee, S., Bouougri, E., Sarkar, S., Bumby, A.J., 2007. In: Schieber, J., Bose, P.K., Eriksson, P.G., Banerjee, S., Sarkar, S., Altermann, W., Catuneau, O. (Eds.), *Atlas of Microbial Mat Features Preserved Within the Siliciclastic Rock Record*. Elsevier, pp. 76–105.
- Faccenna, C., Soligo, M., Billi, A., De Filippis, L., Funicello, R., Rossetti, C., Tuccimei, P., 2008. Late Pleistocene depositional cycles of the Lapis Tiburtinus travertine (Tivoli, Central Italy): possible influence of climate and fault activity. *Global and Planetary Change* 63, 299–308.
- Fagereng, A., 2011. Frequency-size distribution of competent lenses in a block-in-matrix melange: imposed length scales of brittle deformation? *Journal of Geophysical Research* 116, B05302.
- Festa, V., Sabato, L., Tropeano, M., 2018. 1:5,000 geological map of the upper Cretaceous intraplateau-basin succession in the “Gravina di Matera” canyon (Apulia Carbonate Platform, Basilicata, southern Italy). *Italian Journal of Geosciences* 137, 3–15.
- Fossen, H., Schultz, R.A., Shipton, Z.K., Mair, K., 2007. Deformation bands in sandstone: a review. *Journal of the Geological Society, London* 164, 755–769.
- French, B.M., Koeberl, C., 2010. The convincing identification of terrestrial meteorite impact structures: what works, what doesn’t, and why. *Earth-Science Reviews* 98, 123–170.
- Frid, V., Bahat, D., Rabinovich, A., 2005. Analysis of en echelon/hackle fringes and longitudinal splits in twist failed glass samples by means of fractography and electromagnetic radiation. *Journal of Structural Geology* 27, 145–159.
- Fujimoto, Y., Yamamoto, M., 2010. On the granitoids in the Shirakami mountains and correlation to the Cretaceous to Paleogene granitoids distributed in the Northeast Japan. *Earth Science* 64, 127–144. In Japanese with English abstract.
- Gay, N.C., 1974. Modification of deformation lamellae during brittle-ductile deformation of quartzite. *Geological Society of America Bulletin* 85, 1237–1242.
- Gehrels, G.E., DeCelles, P.G., Ojha, T.P., Upreti, B.N., 2006. Geologic and U-Th-Pb geochronologic evidence for early Paleozoic tectonism in the Kathmandu thrust sheet, Central Nepal Himalaya. *Geological Society of America Bulletin* 118, 185–198.

- Geng, M., Farquharson, C.G., Welford, J.K., Peace, A.L., 2019. 3-D inversion of airborne gravity gradiometry data for the Budgell Harbour Stock, Newfoundland: a case history using a probabilistic approach. *Geophysics* 84, 1–62.
- Gratier, J.-P., Frery, E., Deschamps, P., Røyne, A., Renard, F., Dysthe, D., Ellouz-Zimmerman, N., Hamelin, B., 2012. How travertine veins grow from top to bottom and lift the rocks above them: the effect of crystallization force. *Geology* 40, 1015–1018.
- Grützner, C., Reicherter, K., Hübscher, C., Silva, P.G., 2012. Active faulting and neotectonics in the Baelo Claudia area, campo de Gibraltar (southern Spain). *Tectonophysics* 554–557, 127–142.
- Hamers, M.F., Drury, M.R., 2011. Scanning electron microscope-cathodoluminescence (SEM-CL) imaging of planar deformation features and tectonic deformation lamellae in quartz. *Meteoritics and Planetary Science* 46, 1814–1831.
- Hancock, P.L., Chalmers, R.M.L., Altunel, E., Çakir, Z., 1999. Travertines: using travertine in active fault studies. *Journal of Structural Geology* 21, 903–916.
- Hefferan, K., O'Brien, J., 2010. *Earth Materials*. John Wiley & Sons Ltd, Wiley-Blackwell, UK.
- Hobbs, B.E., Means, W.D., Williams, P.F., 1976. *An Outline of Structural Geology*. John Wiley & Sons.
- Hurst, A., Scott, A., Vigorito, M., 2011. Physical characteristics of sand injectites. *Earth-Science Reviews* 106, 215–246.
- Kamai, R., Hatzor, Y.H., 2008. Numerical analysis of block stone displacements in ancient masonry structures: a new method to estimate historic ground motions. *International Journal for Numerical and Analytical Methods in Geomechanics* 32, 1321–1340.
- Kamh, G.M.E., Kallash, A., Azzam, R., 2008. Factors controlling building susceptibility to earthquakes: 14-year recordings of Islamic archaeological sites in old Cairo, Egypt: a case study. *Environmental Geology* 56, 269–279.
- Karakhanian, A.S., Trifonov, V.G., Ivanova, T.P., Avagyan, A., Rukieh, M., Minini, H., Dodonov, A.E., Bachmanov, D.M., 2008. Seismic deformation in the St. Simeon monasteries (Qal'at Sim'an), northwestern Syria. *Tectonophysics* 453, 122–147.
- Kázmér, M., 2015. Damages to ancient buildings from earthquakes. In: Beer, M., Kougioumtzoglou, I., Patelli, E., Au, I.S.-K. (Eds.), *Encyclopedia of Earthquake Engineering*. Springer, Berlin, ISBN: 978-3-642-35343-7, pp. 500–506.
- Kázmér, M., Major, B., 2010. Distinguishing damages of two earthquakes—archaeoseismology of a Crusader castle (Al-Marqab citadel, Syria). In: Sintubin, M., Stewart, I., Niemi, T., Altunel, E. (Eds.), *Ancient Earthquakes*. vol. 471. Geological Society of America Special Paper, pp. 186–199.
- Knauth, L.P., 1979. A model for the origin of chert in limestone. *Geology* 7, 274–277.
- Korjenkov, A.M., Mazor, E., 1999. Seismogenic origin of the ancient Avdat ruins, Negev desert. *Israel Natural Hazards* 18, 193–226.
- Korjenkov, A.M., Mazor, E., 2003. Archaeoseismology in Mamshit (Southern Israel): cracking a millennium-old code of earthquakes preserved in ancient ruins. *Archäologischer Anzeiger* 2003 (2), 51–82.
- Krishnan, S., Ji, C., Komatitsch, D., Tromp, J., 2006. Case studies of damage to tall steel moment-frame buildings in southern California during large San Andreas earthquakes. *Bulletin of the Seismological Society of America* 96, 1523–1537.
- Kukla, P.A., Stanistreet, I.G., 1991. Record of the Damaran Khomas Hochland accretionary prism in Central Namibia: refutation of an “Ensialic” origin of a late Proterozoic orogenic belt. *Geology* 19, 473–476.
- Kurdowski, W., 2014. *Cement and Concrete Chemistry*. Springer, ISBN: 978-94-007-7945-7. 699 pp.
- Ludman, A., West Jr., D.P., 1999. The Norumbega fault system of the northern Appalachians. *Geological Society of America Special Papers* 331, 199.
- Marco, S., 2008. Recognition of earthquake-related damage in archaeological sites: examples from the Dead Sea fault zone. *Tectonophysics* 453, 148–156.
- Meghraoui, M., Gomez, F., Sbeinati, R., Van der Woerd, J., Mouty, M., Darkal, A.N., Radwan, Y., Layyous, I., Al Najjar, H., Darawchah, R., Hijazi, F., Al-Ghazzi, R., Barazangi, M., 2003. Evidence for 830 years of seismic quiescence from paleoseismology, archaeoseismology and historical seismicity along the Dead Sea Fault in Syria. *Earth and Planetary Science Letters* 210, 35–52.
- Meneghini, F., Kisters, A., Buick, I., Fagereng, A., 2014. Fingerprints of late Neoproterozoic ridge subduction in the Pan-African. *Geology, Damara belt, Namibia*. *Geology* 42, 903–906.
- Meschede, M., Warr, L.N., 2019. *The Geology of Germany: A Process-Oriented Approach*. Springer, ISBN: 978-3-319-76102-2. 303 pp.
- Millán, H., Pocoví, A., Casas, A., 1995. El frente de cabalgamiento surpirenaico en el extremo occidental de las Sierras Exteriores: sistemas imbricados y pliegues de despegue. *Revista de la Sociedad Geológica de España* 8, 73–90.
- Misra, A.A., Mukherjee, S., 2018. *Atlas of Structural Geological Interpretation From Seismic Images*. Wiley Blackwell. ISBN: 978-1-119-15832-5.
- Mooney, W., Beroza, G., Kind, R., 2007. Fault zones from top to bottom. In: Handy, M.R., Hirth, G., Hovius, N. (Eds.), *Tectonic Faults—Agents of Change on a Dynamic Earth*. The MIT Press, Cambridge, Mass., USA, pp. 2–46. Dahlem Workshop Report 95.
- Mukherjee, S., 2010. V-pull apart structure in garnet in macro-scale. *Journal of Structural Geology* 32, 605.
- Mukherjee, S., 2012. Simple shear is not so simple! Kinematics and shear senses in Newtonian viscous simple shear zones. *Geological Magazine* 149, 819–826.
- Mukherjee, S., 2013. *Deformation Microstructures in Rocks*. Springer.
- Mukherjee, S., 2014. *Atlas of Shear Zone Structures in Meso-Scale*. Springer.
- Muñoz, J.A., Beamud, E., Fernández, O., Arbués, P., Dinarès-Turell, J., Poblet, J., 2013. The Ainsa fold and thrust oblique zone of the Central Pyrenees: kinematics of a curved contractional system from paleomagnetic and structural data. *Tectonics* 32, 1142–1175.
- Nichols, G.J., 1987. The structure and stratigraphy of the Western external sierras of the Pyrenees, Northern Spain. *Geological Journal* 22, 245–259.
- Novakova, L., 2008. Main directions of the fractures in the limestone and granite quarries along the Sudetic Marginal Fault near Vápenná village, NE Bohemian Massif, Czech Republic. *Acta Geodynamica et Geomaterialia* 5, 49–55.
- Novakova, L., Hájek, P., Šťastný, M., 2010. Determining the relative age of fault activity through analyses of gouge mineralogy and geochemistry: a case study from Vápenná (Rychlebské hory Mts.), Czech Republic. *International Journal of Geosciences* 1, 66–69.
- Novakova, L., Schnabl, P., Büchner, J., 2018. The characterisation of sunburn basalts and their magnetic and petrographic properties. *Journal of Geosciences* 63 (4), 333–344.

- Oliva-Urcia, B., Casas, A.M., Pueyo, E.L., Pocoví, A., 2012. Structural and paleomagnetic evidence for non-rotational kinematics in the western termination of the external sierras (southwestern central Pyrenees). *Geologica Acta* 10, 1–22.
- Osanai, Y., Nogi, Y., Baba, S., Nakano, N., Adachi, T., Hokada, T., Toyoshima, T., Owada, M., 2013. Geologic evolution of the Sør Rondane Mountains, East Antarctica: collision tectonics proposed based on metamorphic processes and magnetic anomalies. *Precambrian Research* 234, 8–29.
- Owada, M., Osanai, Y., Tsunogae, T., Hamamoto, T., Kagami, H., Toyoshima, T., Hokada, T., 2001. Sm-Nd garnet ages of retrograde garnet bearing granulites from Tonagh Island in the Napier Complex, East Antarctica: a preliminary study. *Polar Geoscience* 14, 75–87.
- Pace, P., Battara, E., Riva, A., Borello, S., Ferretto, P., Di Cuia, R., 2018. The Matera Carbonate Structural High: An Outcrop Analogue for Hydrocarbon Plays in the Mediterranean Region. EAGE Eastern Mediterranean Workshop, Malta.
- Passchier, C.W., Trouw, R.A.J., 2005. *Microtectonics*. Springer-Verlag, Berlin.
- Pau, A., Vestroni, F., 2008. Vibration analysis and dynamic characterization of the colosseum. *Structural Control and Health Monitoring* 15, 1105–1121.
- Peace, A.L., Welford, J.K., Geng, M., Sandeman, H., Gaetz, B.D., Ryan, S.S., 2018a. Rift-related magmatism on magma-poor margins: structural and potential-field analyses of the Mesozoic Notre Dame Bay intrusions, Newfoundland, Canada and their link to North Atlantic opening. *Tectonophysics* 745, 24–45.
- Peace, A.L., Welford, J.K., Geng, M., Sandeman, H., Gaetz, B.D., Ryan, S.S., 2018b. Structural Geology Data and 3-D Subsurface Models of the Budgell Harbour Stock and Associated Dykes. Data in Brief, Newfoundland, Canada, pp. 1–7.
- Pease, V., Argent, J., 1999. The northern Sacramento mountains, SW United States, Part I: structural profile through a crustal extensional detachment system. In: Mac Niocaill, C., Ryan, P. (Eds.), *Continental Tectonics*. vol. 164. Geological Society of London Special Publication, pp. 179–198.
- Pease, V., Foster, D., Wooden, J., O’Sullivan, P., Argent, J., Fanning, C., 1999. The northern Sacramento mountains, SW United States, Part II: exhumation history and detachment faulting. In: Mac Niocaill, C., Ryan, P. (Eds.), *Continental Tectonics*. vol. 164. Geological Society of London Special Publication, pp. 199–237.
- Perrot, M., Tremblay, A., Ruffet, G., David, J., 2018. Detrital U-Pb and $40\text{Ar}/39\text{Ar}$ geochronology of the Connecticut Valley-Gaspé trough, southern Quebec and northern Vermont—Transitional tectonism from Salinic to Acadian orogenic cycles. *Tectonophysics* 745, 430–452.
- Pomar, L., Tropeano, M., 2001. The Calcarenite di Gravina formation in Matera (Southern Italy): new insights for coarse-grained, large-scale, cross-bedded bodies encased in offshore deposits. *AAPG Bulletin* 85, 661–689.
- Price, N.A., Johnson, S.E., Gerbi, C.C., West Jr., D.P., 2012. Identifying deformed pseudotachylite and its influence on the strength and evolution of a crustal shear zone at the base of the seismogenic zone. *Tectonophysics* 518–521, 63–83.
- Pueyo, E.L., Parés, J.M., Millán, H., Pocoví, A., 2003. Conical folds and apparent rotations in paleomagnetism (a case study in the Pyrenees). *Tectonophysics* 362, 345–366.
- Quirk, D.G., Pilcher, R.S., 2012. Flip-flop salt tectonics. In: Alsop, G.I., Archer, S.G., Hartley, A.J., Grant, N.T., Hodgkinson, R. (Eds.), *Salt Tectonics, Sediments and Prospectivity*. Vol. 363. Geological Society, London, pp. 245–264. Special Publications.
- Ree, J.H., Kwon, S.H., Park, Y., 2001. Pre-tectonic and post-tectonic emplacements of the granitic rocks in the south central Okcheon belt, South Korea: implications for the timing of strike-slip shearing and thrusting. *Tectonics* 20, 850–867.
- Rhodes, M.K., Malone, D.H., Carroll, A.R., 2007. Sudden desiccation of Lake Gosiute at ~49 Ma: downstream record of Heart Mountain faulting? *Mountain Geologist* 44, 1–10.
- Rodríguez-Pascua, M.A., Pérez-López, R., Silva, P.G., Giner-Robles, J.L., Garduño-Monroy, V.H., Reicherter, K., 2011. A comprehensive classification of earthquake archaeological effects (EAE) for archaeoseismology. *Quaternary International* 242, 20–30.
- Samanta, S.K., Mandal, N., Chakraborty, C., 2001. Development of different types of pull-apart microstructures in mylonites: an experimental investigation. *Journal of Structural Geology* 24, 1345–1355.
- Schofield, N., Heaton, L., Holford, S.P., Archer, S.G., Jackson, C.A.L., Jolley, D.W., 2012. Seismic imaging of ‘broken bridges’: linking seismic to outcrop-scale investigations of intrusive magma lobes. *Journal of the Geological Society* 169 (4), 421–426.
- Séguret, M., 1972. Etude tectonique des nappes et séries décollées de la partie centrale du versant sud des Pyrénées. Caractère synsédimentaire, rôle de la compression et de la gravité. PhD. thesis, University of Montpellier.
- Sibson, R.H., Toy, V.G., 2006. The habit of fault-generated pseudotachylite: presence vs. absence of friction-melt. In: *Earthquakes: Radiated Energy and the Physics of Faulting Geophysical Monograph Series*. vol. 170. American Geophysical Union, pp. 153–166.
- Silva, P.G., Borja, F., Zazo, C., Groy, J.L., Bardají, T., De Luque, L., Lario, J., Dabrio, C.J., 2005. Archaeoseismic record at the ancient Roman city of Baelo Claudia (Cádiz, South Spain). *Tectonophysics* 408, 129–146.
- Similox-Tohon, D., Sintubin, M., Muchez, P., Verhaert, G., Vanneste, K., Fernandez, M., Vanduycke, S., Vanhaverbeke, H., Waelkens, M., 2006. The identification of an active fault by a multidisciplinary study at the archaeological site of Sagalassos (SW Turkey). *Tectonophysics* 420, 371–397. Erratum: 435, pp. 55–62.
- Simpson, C., 1985. Deformation of granitic rocks across the brittle-ductile transition. *Journal of Structural Geology* 7, 503–511.
- Stipp, M., Stunitz, H., Heilbronner, R., Schmid, S.M., 2002. The eastern Tonale fault zone: a ‘natural laboratory’ for crystal plastic deformation of quartz over a temperature range from 250 to 700 °C. *Journal of Structural Geology* 24, 1861–1884.
- Takahashi, Y., 1999. Reexamination on the northern extension of the Tanagura Tectonic Line, with special reference to the Nihonkoku-Miomote Mylonite Zone. *Structural Geology* 43, 69–78. In Japanese with English abstract.
- Takahashi, Y., 2002. Granitic mylonites situated around the Shirakami Mountains. Northeast Japan. *Earth Science* 56, 215–216. In Japanese.
- Takahashi, Y., Cho, D.L., Kee, W.S., 2010. Timing of mylonitization in the Funatsu shear zone within Hida Belt of Southwest Japan: implications for correlation with the shear zones around the Ogcheon Belt in the Korean Peninsula. *Gondwana Research* 17, 102–115.
- Tānavsuu-Milkeviciene, K., Sarg, F.J., 2012. Evolution of an organic-rich lake basin—stratigraphy, climate and tectonics: Piceance Creek basin, Eocene Green River formation. *Sedimentology* 59, 1735–1768.

- Tang, T., Day, M.J., 2000. Field survey and analysis of hillslopes on tower karst in Guilin, Southern China. *Earth Surface Processes and Landforms* 25, 1221–1235.
- Ternet, Y., Baudin, T., Laumonier, B., Barnolas, A., Gil-Peña, I., Martín-Alfageme, S., 2008. Mapa Geológico de los Pirineos a E. 1: 400.000. IGME–BRGM, Madrid-Orleans.
- Till, A.B., Dumoulin, J.A., Harris, A.G., Moore, T.E., Bleick, H.A., Siwiec, B.R., 2008. Bedrock Geologic Map of the Southern Brooks Range, Alaska, and Accompanying Conodont Data. US Geological Survey Open-File Report, pp. 2008–1149.54.
- Törő, B., Pratt, B.R., Renaut, R.W., 2013. Seismically induced soft-sediment deformation structures in the Eocene lacustrine Green River Formation (Wyoming, Utah, Colorado, USA)—a preliminary study. In: Poster Abstract, Calgary. GeoConvention 2013: Integration Calgary. Poster Abstract.
- Toyoshima, T., Owada, M., Shiraishi, K., 1995. Structural evolution of metamorphic and intrusive rocks from the central part of the Sør Rondane Mountains, East Antarctica. In: Proceedings of the NIPR Symposium on Antarctic Geosciences 8, pp. 75–97.
- Toyoshima, T., Osanai, Y., Owada, M., Tsunogae, T., Hokada, T., Crowe, W.A., 1999. Deformation of ultrahigh-temperature metamorphic rocks from Tonagh Island in the Napier Complex, East Antarctica. *Polar Geoscience* 12, 29–48.
- Toyoshima, T., Osanai, Y., Baba, S., Hokada, T., Nakano, N., Adachi, T., Otsubo, M., Ishikawa, M., Nogi, Y., 2013. Sinistral transpressional and extensional tectonics in Dronning Maud land, East Antarctica, including the Sør Rondane Mountains. *Precambrian Research* 234, 30–46.
- Treiman, A.H., 2008. Ancient groundwater flow in the Valles Marineris on Mars inferred from fault trace ridges. *Nature Geoscience* 1, 181–183.
- Tullis, T.E., Bürgmann, R., Cocco, M., Hirth, G., King, G.C.P., Oncken, O., Otsuki, K., Rice, J.R., Rubin, A., Segall, P., Shapiro, S.A., Wibberley, C.A.J., 2007. Group report: rheology of fault rocks and their surroundings. In: Handy, M.R., Hirth, G., Hovius, N. (Eds.), *Tectonic Faults—Agents of Change on a Dynamic Earth*. vol. 95. The MIT Press, Cambridge, MA, pp. 183–204. Dahlem Workshop Report.
- Twiss, R.J., Moores, E.M., 2007. *Structural Geology*. WH Freeman and Company, New York, pp. 43–45.
- Uysal, I.T., Feng, Y., Zhao, J.X., Altunel, E., Weatherley, D., Karabacak, V., Cengiz, O., Golding, S.D., Lawrence, M.G., Collerson, K.D., 2007. U-series dating and geochemical tracing of late quaternary travertine in co-seismic fissures. *Earth and Planetary Science Letters* 257, 450–462.
- Uysal, I.T., Feng, Y., Zhao, J.X., Isik, V., Nuriel, P., Golding, S.D., 2009. Hydrothermal CO₂ degassing in seismically active zones during the late quaternary. *Chemical Geology* 265, 442–454.
- Van Baelen, H., 2010. Dynamics of a Progressive Vein Development During the Late-Orogenic Mixed Brittle-Ductile Destabilisation of a Slate Belt. Examples of the High-Ardenne Slate Belt (Herbeumont, Belgium). *Aardkundige Mededelingen*, p. 221. 24.
- Van Daalen, M., Heilbronner, R., Kunze, K., 1999. Orientation analysis of localized shear deformation in quartz fibres at the brittle–ductile transition. *Tectonophysics* 303, 83–107.
- Van Noten, K., Claes, H., Soete, J., Foubert, A., Özkul, M., Swennen, R., 2013. Fracture networks and strike–slip deformation along reactivated normal faults in quaternary travertine deposits, Denizli Basin, western Turkey. *Tectonophysics* 588, 154–170.
- Vernon, R.H., 2004. *A Practical Guide to Rock Microstructure*. Cambridge University Press.
- Vernooij, M.G.C., 2005. Dynamic Recrystallisation and Microfabric Development in Single Crystals of Quartz during Experimental Deformation. Unpublished PhD. thesis, Eidgenössische Technische Hochschule, Zürich.
- Waltham, T., 2009. The Karstlands of Southern China. vol. 25 Blackwell Publishing Ltd, The Geologists' Association & The Geological Society of London, *Geology Today*, pp. 232–238.
- Wu, Z., Yin, H., Zheng, J., 2018. Reactive salt Diapir, southern Precaspian Basin, Middle Asia. In: Misra, A.A., Mukherjee, S. (Eds.), *Atlas of Structural Geological Interpretation From Seismic Images*. Wiley Blackwell, Oxford, ISBN: 9781119158325, pp. 167–170.
- Yajoui, Z., 2019. Ediacaran-Cambrian Evolution of the Northeastern Edge of Sagro Inlier (Eastern Anti-Atlas, Morocco): Insights From Physical Structural Analysis and Metallogenic Implication. Moulay Ismail University. PhD thesis.
- Yin, A., Dubey, C.S., Kelty, T.K., Webb, A.A.G., Harrison, T.M., Chou, C.Y., Celerier, J., 2010. Geologic correlation of the Himalayan orogeny and Indian craton: part 2: structural geology, geochronology, and tectonic evolution of the eastern Himalaya. *Geological Society of America Bulletin* 122, 360–395.
- Zijderveld, J.D.A., 1967. AC demagnetization of rocks: analysis of results. In: Runcorn, S.K., Creer, K.M., Collinson, D.W. (Eds.), *Methods in Palaeomagnetism*. Elsevier, Amsterdam, pp. 254–286.

Author Index

A

Abdullah, R., 167f
 Abe, S., 173, 191f
 Acharyya, S.K., 7f
 Adachi, T., 1f, 232f
 Adamoli, L., 18f, 165f
 Agard, P., 153f
 Agarwal, I., 135f
 Agnon, A., 27f
 Ahuja, H., 85f
 Al Najjar, H., 240f
 Alania, V., 4f, 122f, 124f
 Alberti, M., 43f
 Al-Ghazzi, R., 240f
 Alsop, G.I., 1
 Altunel, E., 203f, 205f
 Alvarado, G.E., 202f
 Amit, O., 57f
 Anastasio, D.J., 11f, 163f
 Andersen, T.B., 131f, 161–162f
 Anderson, J.R., 40f
 Andrades Filho, C., 114f
 Andreani, M., 154f
 Angelier, J., 147–148f
 Antonellini, M., 115–116f, 118f
 Anzalone, E., 204f
 Ao, A., 194f
 Arbués, P., 208f
 Arenas, C., 11f, 163f
 Argent, J., 146f, 225f
 Armitage, I.A., 58–59f
 Ashwal, L., 162f
 Aurell, M., 11f, 163f
 Austrheim, H., 131f, 161–162f
 Avagyan, A., 239f
 Avila, S.P., 58–59f
 Aydin, A., 115f, 167f
 Azzam, R., 239f

B

Baba, S., 1f, 232f
 Babar, M., 125f
 Bachmanov, D.M., 239f
 Bahat, D., 218f
 Ballas, G., 115f
 Balsamo, F., 18f, 114–115f, 165–166f
 Banerjee, M., 85f
 Banerjee, S., 13f, 235f
 Baptista, L., 58–59f
 Barazangi, M., 240f
 Barchi, M.R., 142f

Bardaji, T., 239f
 Barker, A.J., 229f
 Barker, S.L.L., 154f
 Barnes, S., 173f
 Barnolas, A., 9f, 163f, 208–210f
 Baronnet, A., 154f
 Barrier, E., 147–148f
 Barrier, P., 58f
 Baudin, T., 9f, 208–210f
 Beamud, E., 11f, 163f, 208f
 Belardi, G., 155f
 Bell, T.H., 1, 25f
 Ben M'Barek, M., 7f, 127f
 Berger, A., 164f
 Beridze, M., 124f
 Berning, B., 58–59f
 Bernoulli, D., 185f
 Beroza, G., 157f, 226f
 Bezerra, F.H.R., 114f
 Bhadra, S., 67, 85f
 Bhaskar Rao, Y.J., 42f, 55f
 Bhattacharya, G., 121f
 Bigozzi, A., 18f, 165f
 Bikramaditya Singh, R.K., 25f, 73f, 214f
 Billi, A., 155f, 203–205f
 Biswal, T.K., 85f
 Biswas, A., 60f
 Biswas, R., 67
 Biswas, T., 1, 19f, 29f, 67, 111, 134f, 173, 191
 Bleick, H.A., 216f, 224f
 Boggs, S., 236f
 Boncio, P., 128f
 Bons, P.D., 1, 191, 230f
 Borja, F., 239f
 Bornemann, O., 53f
 Bose, M.K., 40f
 Bose, N., 1, 13f, 19f, 29f, 67, 78f, 111, 121f, 163f, 173, 191, 199, 229f
 Bottjer, D., 235–236f
 Boullier, A.M., 154f
 Bouougri, E., 235f
 Breton, J.-P., 191f
 Brill, M., 204f
 Brito Neves, B.B., 114f
 Brodie, K.H., 225f
 Brodzikowski, K., 31f
 Brogi, A., 204f
 Brosge, W.P., 216f, 224f
 Brozzetti, F., 128f
 Buatois, L.A., 58–59f
 Büchner, J., 246f
 Buick, I., 211f

Bumby, A.J., 235f
 Burbank, D.W., 11f, 163f
 Burchardt, S., 78f
 Burgess, R., 18f, 165–166f
 Bürgmann, R., 157f, 226f
 Burov, E., 153f
 Butler, R.W.H., 115f
 Byrne, T., 111

C

Caine, J.S., 111f
 Çakir, Z., 203f
 Calafato, A., 115f
 Calamita, F., 7f, 27f, 115f, 127f, 142f, 159f
 Calvín, P., 11f
 Calvo, J.P., 27f
 Campos, J.E.G., 146f
 Capezzuoli, E., 204f
 Capponi, G., 154f
 Cardello, G.L., 127f
 Caroir, F., 8f, 22f
 Carreras, J., 1
 Carroll, A.R., 237f
 Carter, B.J., 227f
 Casas Sainz, A.M., 11f
 Casas, A.M., 11f, 163f, 213f
 Cawood, P., 86f
 Celarc, B., 162f
 Celerier, J., 214f
 Cengiz, O., 205f
 Chabukiani, A., 4f, 122f
 Chagelishvili, R., 4f, 124f
 Chakraborty, C., 230f
 Chakraborty, M., 135f
 Chalmers, R.M.L., 203f
 Chamyal, L.S., 111, 149–152f
 Chemale, F., 146f
 Chesterman, C.W., 203f
 Chetty, T.R.K., 17f, 40f, 42f, 55f
 Childs, C., 136f
 Cho, D.L., 87f, 215f
 Chou, C.Y., 214f
 Choudhuri, M., 2f
 Choukroune, P., 209f
 Chowdhury, K.R., 167f
 Christensen, N.I., 181f
 Christie, J.M., 227f
 Ciarapica, G., 18f, 165f
 Cirilli, S., 18f, 165f
 Cirillo, D., 128f
 Claes, H., 205f
 Clark, C., 42f, 67

Clemenzi, L., 18*f*, 165–166*f*
 Clifton, H.E., 58–59*f*
 Cocco, M., 157*f*, 226*f*
 Collerson, K.D., 205*f*
 Collins, A.S., 40*f*, 42*f*
 Compagnoni, R., 153*f*
 Compaired, F., 11*f*
 Cordeiro, R., 58–59*f*
 Cortesogno, L., 154*f*
 Cowan, H.A., 161*f*
 Cox, S.F., 154*f*, 164*f*
 Crispini, L., 154*f*
 Crossey, L.J., 205*f*
 Crowe, W.A., 41*f*, 85*f*, 231–232*f*
 Csontos, L., 136*f*

D

Dabrio, C.J., 239*f*
 Dabrowski, M., 67*f*
 Dal Piaz, G.V., 153*f*
 Dantas, E.L., 114*f*
 Darawcheh, R., 240*f*
 Darkal, A.N., 240*f*
 Das, A.N., 194*f*
 Das, R., 85*f*
 Dasgupta, S., 1, 19*f*, 29*f*, 58–59*f*, 67, 111, 125*f*, 173, 191
 Dasgupta, T., 1
 Datta, S., 85*f*
 Davis, G.H., 67, 191, 192*f*, 215*f*
 Day, M.J., 243*f*
 De Capitani, C., 131*f*, 162*f*
 De Filippis, L., 203–205*f*
 de Keijzher, M., 52*f*
 De Luque, L., 239*f*
 de Nardis, R., 128*f*
 De Vicente, G., 27*f*
 de Wit, M.J., 40*f*
 Deb, S.K., 52*f*
 Decandia, F.A., 43*f*, 159*f*
 DeCelles, P.G., 217*f*
 Deiana, G., 159*f*
 Del Sole, L., 115*f*, 118*f*
 Deng, H., 3*f*
 Denyer, P., 202*f*
 Derez, T., 228*f*
 Deschamps, P., 205*f*
 Deseta, N., 162*f*
 DeWaele, B., 85*f*
 Di Calamita, F., 166*f*
 Di Domenica, A., 115*f*, 166*f*
 Di Toro, G., 18*f*, 156*f*, 164–166*f*
 Di Vincenzo, M., 7*f*, 127*f*
 Dias, A.N.C., 146*f*
 Díaz-Alvarado, J., 137–139*f*
 Diener, J.F.A., 173*f*
 Dillon, J.T., 216*f*, 224*f*
 Dinarès-Turell, J., 208*f*
 Doblas, M., 111, 147*f*, 153*f*
 Dobmeier, C., 85*f*
 Dodonov, A.E., 239*f*
 Doglioni, C., 127*f*
 Dorner, D., 228*f*
 Druguet, E., 1
 Drüppel, K., 89*f*

Drury, M.R., 227–228*f*
 Drury, S.A., 17*f*
 Dubey, C.S., 214*f*
 Dumoulin, J.A., 216*f*, 224*f*
 Duranti, F., 18*f*, 165*f*
 Dutro, J.T., 216*f*, 224*f*
 Dutta, A., 85*f*
 Dutta, D., 1, 19*f*, 29*f*, 67, 78*f*, 111, 134*f*, 173, 191, 229*f*
 Dyni, J.R., 51*f*
 Dysthe, D., 205*f*

E

Eggins, S.M., 154*f*
 Egli, D., 185*f*
 El Azmi, M., 120*f*
 El Ouardi, H., 120*f*
 Elburg, M.A., 191
 Ellouz-Zimmerman, N., 205*f*
 El-Wahed, M.A.A., 125*f*
 Engelder, T., 87*f*
 Engelmann, R., 89*f*
 Enukidze, O., 4*f*, 122*f*, 124*f*
 Eriksson, P.G., 235*f*
 Esestime, P., 7*f*, 27*f*
 Evans, J.P., 111*f*
 Evans, L.A., 1
 Exner, U., 67
 Eyal, Y., 57*f*
 Ez, V., 1

F

Faccenna, C., 204–205*f*
 Fagereng, A., 20*f*, 86*f*, 173*f*, 211*f*
 Fanning, C., 146*f*, 225*f*
 Farquharson, C.G., 238*f*
 Federico, L., 154*f*
 Feng, Y., 205*f*
 Fernández, C., 79*f*, 92–93*f*, 137–139*f*
 Fernandez, M., 240*f*
 Fernández, O., 208*f*
 Ferrarini, F., 128*f*
 Fiori, A.P., 159*f*
 Fitzsimons, I.C.W., 67
 Fletcher, R.C., 173
 Fodor, L., 136*f*, 160*f*
 Fogarasi, A., 160*f*
 Fondriest, M., 18*f*, 156*f*, 164–166*f*
 Forster, C.B., 111*f*
 Fossen, H., 1, 136*f*, 185*f*, 191
 Foster, D., 146*f*, 225*f*
 Foubert, A., 205*f*
 Frehner, M., 67
 French, B.M., 227*f*
 Frenzel, M., 164*f*
 Frery, E., 205*f*
 Frid, V., 218*f*
 Fügenschuh, B., 185*f*
 Fujimoto, Y., 83*f*, 217*f*
 Funicello, R., 205*f*

G

Gadhavi, M.S., 141*f*
 Gaetz, B.D., 238*f*

Gagan, M.K., 154*f*
 Galbiati, B., 154*f*
 Garcés, M., 11*f*, 163*f*
 García-Lasanta, C., 11*f*
 García-Sansegundo, J., 11*f*
 Garduño-Monroy, V.H., 240*f*
 Garfunkel, Z., 159*f*
 Gawlick, H.-J., 185*f*
 Gay, N.C., 229*f*
 Gazdova, R., 160*f*
 Gehrels, G.E., 217*f*
 Geng, M., 238*f*
 Gerbi, C.C., 157*f*, 226*f*
 Gerdes, A., 90*f*
 Gervais, F., 8*f*, 22*f*
 Ghisetti, F., 18*f*, 127*f*, 165–166*f*
 Ghosh, J.G., 40*f*
 Ghosh, R., 1, 19*f*, 29*f*, 67, 111, 173, 191
 Ghosh, S.K., 38*f*, 48*f*, 52*f*, 84*f*, 117*f*, 175*f*
 Gil-Peña, I., 9*f*, 208–210*f*
 Giner-Robles, J.L., 240*f*
 Gingras, M.K., 58–59*f*
 Glodny, J., 89*f*
 Godin, L., 1, 2*f*
 Goes, A.M., 114*f*
 Gogoi, M.P., 1, 28*f*, 42*f*, 45*f*, 49*f*
 Gogrichiani, K., 4*f*
 Golding, S.D., 205*f*
 Gomez, F., 240*f*
 Gómez-Gras, D., 27*f*
 Gomez-Rivas, E., 1, 191
 Gopalakrishnan, K., 17*f*
 Goscombe, B.D., 173, 185*f*
 Gosso, G., 153*f*
 Goswami, T.K., 1, 28*f*, 42*f*, 45*f*, 49*f*
 Gotowala, R., 31*f*
 Graseman, B., 67*f*
 Grasemann, B., 2*f*
 Gratier, J.-P., 154*f*, 205*f*
 Greiling, R.O., 89–90*f*, 159*f*
 Grier, A., 1
 Griggs, D.T., 227*f*
 Grimmer, J.C., 89–90*f*
 Groppo, C., 153*f*
 Groy, J.L., 239*f*
 Grujic, D., 67
 Grützner, C., 239*f*
 Gueguen, E., 43*f*
 Gunderson, K.L., 11*f*, 163*f*
 Gupta, S., 67, 85*f*
 Gururajan, N.S., 25*f*, 214*f*

H

Hada, S., 86*f*
 Hájek, P., 218*f*
 Hamamoto, T., 231–232*f*
 Hamelin, B., 205*f*
 Hamers, M.F., 227*f*
 Han, R., 158*f*
 Hancock, P.L., 147–149*f*, 203*f*
 Hand, M., 40*f*, 173
 Harayama, S., 87*f*
 Hardy, S., 4*f*, 122*f*
 Harris, A.G., 216*f*, 224*f*
 Harris, L.B., 1, 2*f*, 41*f*, 85*f*

Harrison, T.M., 214f
Hatzor, Y.H., 240f
Havří, J., 160f
Hawkins, J.E., 51f
Hazra, S., 38f, 48f, 84f
Healy, D., 67
Hefferan, K., 237f
Hegadorn, J.W., 235–236f
Heilbronner, R., 199, 228f
Hemmann, M., 53f
Herwegh, M., 164f
Hibbard, J., 39f
Hibsch, C., 58f
Hijazi, F., 240f
Hilgers, C., 191f
Hillary, G.W.B., 173f
Hinnov, L.A., 163f
Hirt, A., 89f
Hirth, G., 146f, 157f, 226f
Hobbs, B.E., 24f, 215f
Hofmeister, A.M., 67
Hogan, P.J., 11f, 163f
Hokada, T., 1f, 231–232f
Holdsworth, R.E., 1
Holland, M., 191–192f
Holt, R.W., 17f
Hoogerduijn Strating, E.H., 154f
Horie, K., 40f
Hossain, M.S., 167f
Huang, H., 55f
Huber, M.I., 45f
Huber, R., 153f
Hübscher, C., 239f
Hudleston, P.J., 1
Hurst, A., 237f

I

Insley, M.W., 7f
Ishikawa, M., 1f, 232f
Isik, V., 205f
Ito, M., 86f
Ivanova, T.P., 239f

J

Jaroszewski, W., 141f
Jena, S.K., 85f
Jercinovic, M.J., 24f
Ji, C., 199
John, G., 133f
Johnson, M.E., 58–59f
Johnson, R.C., 51f
Johnson, S.E., 157f, 226f
Johnston, M.R., 161f
Jolivet, L., 131f, 153f, 162f
Joshi, A., 1, 19f, 29f, 67, 111, 173, 191
Jovanović, D., 185f

K

Kagami, H., 231–232f
Kallash, A., 239f
Kamai, R., 240f
Kamh, G.M.E., 239f
Kamha, S.Z., 125f
Kaplay, R.D., 125f

Karabacak, V., 205f
Karakhanian, A.S., 239f
Karanth, R.V., 141f
Karaoui, B., 2f, 120f
Karig, D., 39f
Kariya, Y., 87f
Karkanas, P., 154f
Karlstrom, K.E., 205f
Katayama, I., 162f
Katz, Y., 167f
Kázmér, M., 239f
Kee, W.S., 87f, 215f
Kelsey, D.E., 40f
Kelty, T.K., 214f
Kettermann, M., 173
Khan, D., 52f
Khan, K., 85f
Khan, M.S.H., 167f
Khanal, S., 32f
Kihm, N., 53f
Kind, R., 157f, 226f
King, G.C.P., 157f, 226f
Kirby, S.H., 31f
Kirschner, D., 191f
Kisters, A., 211f
Kleinhampl, F.J., 203f
Kluth, C.F., 67, 192f, 215f
Knauth, L.P., 237f
Kodama, K.P., 11f, 163f
Koeberl, C., 227f
Koehn, D., 173
Koiava, K., 4f
Kolinsky, P., 160f
Komatitsch, D., 199
Komazawa, M., 87f
Kontny, A., 89f
Korjenkov, A.M., 240f
Koshimoto, S., 55f
Kövé, S., 136f, 160f
Koyi, H.A., 1, 2–3f, 29f, 52f, 73f, 78–79f, 83f, 121f, 183f, 194f
Krishnan, S., 199
Kronenberg, A.K., 31f
Krystyn, L., 185f
Kukla, P.A., 52f, 173f, 211f
Kulkarni, P.S., 125f
Kumar, M., 1, 19f, 29f, 67, 111, 173, 191
Kumar, N., 1
Kunze, K., 228f
Kuster, M., 228f
Kurdowski, W., 246f
Kwon, S.H., 55f, 215f

L

Labrousse, L., 8f, 22f
Lal, N., 23f, 50f, 194f
Lan, L., 1, 94f
Landis, C.A., 86f
Lario, J., 239f
Laumonier, B., 9f, 208–210f
Lavecchia, G., 128f
Lawrence, M.G., 205f
Layyous, I., 240f
Leah, H., 18f, 165–166f
Lebanidze, Z., 124f

Leeming, P.M., 41f, 85f
Lein, R., 185f
Lemmi, M., 142f
Leonardo Evangelista Lagoeiro, 95f, 102f
Liberi, F., 128f
Limaye, M., 1, 19f, 29f, 67, 111, 173, 191
Lin, A., 31f
Lisker, F., 154f
Lister, G.S., 67
Llorens, M.-G., 1
Lucca, A., 18f, 165–166f
Ludman, A., 226f
Luiz Sérgio Amarante Simões, 95f, 102f
Lundquist, S.M., 181f
Luzón, A., 11f

M

Ma, S., 158f
Madeira, P., 58–59f
Maeder, X., 173, 191
Mahadani, T., 1, 11f, 73f
Mahmoudi, A., 120f
Major, B., 239f
Malone, D.H., 237f
Mancktelow, N.S., 67, 80f
Mandal, N., 52f, 230f
Mandal, S., 32f
Mángano, M.G., 58–59f
Maqadze, D., 124f
Marco, S., 27f, 240f
Marshak, S., 87f
Martel, S., 2f
Martín-Alfageme, S., 9f, 208–210f
Martínez Peña, M.B., 11f
Martins-Ferreira, M.A.C., 146f
Maruyama, S., 17f, 162f
Masoch, S., 164f
Maurya, D.M., 111, 149–152f
Mazor, E., 240f
McClay, K.R., 7f
Means, W.D., 24f, 215f
Medeiros, W.E., 114f
Medwedeff, D.A., 122f
Meghraoui, M., 240f
Melo, C.S., 58–59f
Meneghini, F., 211f
Meschede, M., 246f
Messiga, B., 154f
Miklavič, B., 70f
Millán Garrido, H., 11f
Millán, H., 11f, 163f, 213f
Minini, H., 239f
Misra, A.A., 1, 19f, 29f, 67, 111, 121f, 125f, 173, 191, 199
Missoni, S., 185f
Mitra, S., 3f
Mittempergher, S., 156f
Mizoguchi, K., 158f
Mo, Y., 12f
Moghadam, R.H., 228f
Mohanty, D.P., 55f
Mollema, P., 116f
Montenat, C., 58f
Mooney, W., 157f, 226f
Moore, T.E., 216f, 224f

Moore, E.M., 173, 215f
 Mortimer, N., 20f
 Mouty, M., 240f
 Muchez, P., 191–192f, 240f
 Mukherjee, R., 1, 11f, 73f
 Mukherjee, S., 1, 2f, 10–11f, 13f, 19f, 28–29f, 31–32f, 42f, 45f, 49f, 52f, 67, 73f, 78–79f, 83f, 90f, 96f, 111, 121f, 125f, 134–135f, 147f, 149–152f, 163f, 173, 183f, 191, 194f, 199, 229–230f, 234f
 Mukhopadhyay, B., 40f
 Mulchrone, K.F., 67
 Muñoz, J.A., 208f
 Munroe, S.M., 164f

N

Nabelek, P.I., 67
 Nagesh, P., 55f
 Nakajima, Y., 162f
 Nakano, N., 1f, 232f
 Nakano, S., 87f
 Nash, C.R., 41f, 85f
 Navabpour, P., 147–148f
 Nelson, K.D., 20f
 Newton, M.L., 163f
 Nichols, G.J., 11f, 213f
 Nicol, A., 136f
 Nogi, Y., 1f, 232f
 Nogueira, F.C., 114f
 Novak, M., 192f
 Novakova, L., 147f, 160f, 218f, 246f
 Nuriel, P., 205f

O

O'Brien, J., 237f
 O'Sullivan, P., 146f, 225f
 Ojha, T.P., 217f
 Okamoto, K., 162f
 Oliván, C., 11f
 Oliva-Urcia, B., 11f, 163f, 213f
 Oliveira, R.G., 114f
 Oncken, O., 157f, 226f
 Osanai, Y., 1f, 231–232f
 Otsubo, M., 1f, 232f
 Otsuki, K., 157f, 226f
 Ott d'Estevo, P., 58f
 Owada, M., 1f, 231–232f
 Özkul, M., 204–205f

P

Pace, P., 27f, 115f, 127f, 142f, 166f
 Padmalal, A., 111, 152f
 Palotai, M., 136f
 Paltrinieri, W., 7f
 Pamplona, J., 79f, 92–93f
 Panigrahi, M.K., 85f
 Paola Ferreira Barbosa, 95f, 102f
 Pardo, G., 11f, 163f
 Parés, J.M., 11f, 163f, 213f
 Park, C., 55f
 Park, Y., 215f
 Parkinson, C.D., 162f
 Pasqui, V., 142f
 Passchier, C.W., 2f, 25f, 31f, 67, 78f, 84f, 88f, 90f, 111, 117f, 155f, 173, 185f, 191, 229–231f

Passeri, L., 18f, 165f
 Patel, R.C., 23f, 50f, 194f
 Pau, A., 240f
 Paul, J., 53f
 Payne, J.L., 40f
 Payros, A., 163f
 Pazdírková, J., 160f
 Peace, A.L., 238f
 Pease, V., 146f, 225f
 Peinl, M., 53f
 Pelorosso, M., 7f, 127f
 Pemberton, S.G., 58–59f
 Pennacchioni, G., 80f
 Pennock, G., 228f
 Pérez-López, R., 240f
 Pérez-Rivarés, F.J., 11f
 Pérez-Rivarés, G., 163f
 Perrot, M., 8f, 22f
 Petit, J.P., 147–149f, 154f
 Phillips, D., 154f
 Phillips, R.J., 12f
 Piccardo, G., 154f
 Pilcher, R.S., 244f
 Pinkstone, J., 31f
 Pizzi, A., 27f
 Placer, L., 162f
 Platt, J.P., 91f
 Plavsa, D., 42f
 Poblet, J., 4f, 122f, 208f
 Pocoví Juan, A., 11f
 Pocoví, A., 11f, 163f, 213f
 Podladchikov, Y.Y., 52f
 Polino, R., 153f
 Poljak, M., 119f
 Porada, H., 235f
 Pratt, B.R., 51f, 130f, 237f
 Praveen, M.N., 55f
 Preto, N., 164f
 Price, N.A., 157f, 226f
 Pueyo, E.L., 11f, 163f, 213f
 Puneekar, J.N., 1, 11f, 73f

Q

Quirk, D.G., 244f

R

Rabinovich, A., 218f
 Radwan, Y., 240f
 Raith, M., 85f
 Ramalho, R.S., 58–59f
 Ramsay, J.G., 1, 45f, 67, 153f
 Rana, S., 194f
 Rankin, L.R., 41f, 85f
 Rattenbury, M.S., 161f
 Ravna, E.J.K., 131f, 162f
 Razmadze, A., 4f, 122f, 124f
 Rebelo, A.C., 58–59f
 Ree, J.H., 215f
 Regenauer-Lieb, K., 67
 Reicherter, K., 239–240f
 Reinoso, F., 137–139f
 Remitti, F., 86f
 Renard, F., 205f
 Renaut, R.W., 51f, 130f, 237f
 Renda, P., 43f

Reynolds, S.J., 67, 191, 192f, 215f
 Rhodes, M.K., 237f
 Rice, J.R., 157f, 226f
 Ridley, J., 111f
 Ridolfi, M., 27f
 Robinson, D.M., 32f
 Rodas, G.S., 202f
 Rodrigues, B.C., 79f, 92–93f
 Rodríguez-Pascua, M.A., 27f, 240f
 Rodríguez-Pintó, A., 163f
 Roller, K., 228f
 Romano, A., 18f, 165f
 Rossetti, C., 205f
 Rossetti, D.F., 114f
 Rossetti, F., 154–155f
 Rothery, E., 136f
 Roy, P., 60f
 Røyne, A., 205f
 Rožič, B., 70f
 Rubatto, D., 154f
 Rubin, A., 157f, 226f
 Rudenach, M.J., 25f
 Ruffet, G., 8f, 22f
 Rukieh, M., 239f
 Rusciadelli, G., 27f
 Rutter, E.H., 87f, 225f
 Ryan, S.S., 238f
 Rykkelid, E., 136f

S

Sadradze, N., 124f
 Saha, P., 7f
 Saito, Y., 40f
 Sajinkumar, K.S., 55f
 Samanta, S.K., 230f
 Samsó, J.M., 163f
 Sánchez-Moreno, E.M., 11f
 Sandeman, H., 238f
 Sanishvili, A., 4f
 Santolaria, P., 11f
 Santosh, M., 17f, 40f, 42f, 55f
 Sarg, F.J., 51f, 237f
 Sarkar, S., 235f
 Sasvári, Á., 136f
 Sato, K., 17f
 Satolli, S., 7f, 27f, 159f
 Sawyer, E., 173f
 Saxena, N., 191–192f
 Sbeinati, R., 240f
 Scambelluri, M., 154f
 Schefer, S., 185f
 Scheltema, K.E., 24f
 Schmalholz, S.M., 52f, 173
 Schmeling, H., 78f
 Schmid, D.W., 173
 Schmid, S.M., 185f, 199
 Schnabl, P., 246f
 Scisciani, V., 7f, 27f
 Scott, A., 237f
 Secco, M., 164f
 Segall, P., 157f, 226f
 Séguret, M., 9f, 208–210f
 Sengupta, S., 38f, 48f, 52f, 84f, 175f
 Serra-Kiel, J., 163f
 Shaikh, H., 111, 149–151f

Shaikh, M., 111, 152f
 Shapiro, S.A., 157f, 226f
 Sharma, R., 194f
 Sheth, H.C., 199–200f
 Shimamoto, T., 158f
 Shimizu, I., 100–101f
 Shiraishi, K., 1f, 232f
 Sibson, R.H., 20f, 86f, 157f, 161f
 Silva, P.G., 239–240f
 Silva-Casal, R., 11f, 163f
 Similox-Tohon, D., 240f
 Simkhada, P., 32f
 Simpson, C., 146f, 225f
 Singaneni, S., 55f
 Singh, A.K., 194f
 Singh, P., 23f, 50f, 194f
 Singhal, S., 194f
 Sinha, N., 111
 Sintubin, M., 228f, 240f
 Siwiec, B.R., 216f, 224f
 Sjöström, H., 78f
 Smith, S.A.F., 156f
 Smyth, J.R., 162f
 Snoke, A.W., 67
 Soete, J., 205f
 Sokoutis, D., 173
 Soligo, M., 204–205f
 Soliva, R., 115f
 Sosson, M., 122f
 Soto, R., 11f, 163f
 Špaček, P., 160f
 Speranza, F., 7f
 Spray, J., 161f
 Srivastava, D.C., 133f
 Stanistreet, I.G., 173f, 211f
 Šťastný, M., 218f
 Stipp, M., 199
 Stockhert, B., 228f
 Storti, F., 18f, 114f, 165–166f
 Strozyk, F., 52f
 Stunitz, H., 199
 Sudar, M., 185f
 Suellen Olivia Cândida Pinto, 95f, 102f
 Suppe, J., 122f
 Švancara, J., 160f
 Swanson, M., 161f
 Swennen, R., 205f
 Sýkorová, Z., 160f
 Sztanó, O., 136f, 160f

T

Taira, A., 39f
 Takahashi, Y., 83f, 87f, 215f, 217f
 Talbot, C.J., 52f, 78f, 173
 Tánavsuu-Milkeviciene, K., 51f, 237f
 Tang, T., 243f
 Tari, G., 160f
 Tarnelli, E., 7f, 27f, 43f, 142f, 159f
 Tayade, L., 135f
 Teisseyre, H., 141f
 Teixell, A., 11f
 Teletzke, A.L., 11f, 163f
 ten Grotenhuis, S.M., 67, 90f
 Ternet, Y., 9f, 208–210f
 Testa, A., 128f

Tevzadze, N., 124f
 Thakur, S.S., 194f
 Theye, T., 154f
 Tietz, O., 246f
 Till, A.B., 216f, 224f
 Tjia, H.D., 111
 Togo, T., 158f
 Törő, B., 51f, 58–59f, 130f, 237f
 Torres, P., 58–59f
 Townsend, D.B., 161f
 Toy, V.G., 157f
 Toyoshima, T., 1f, 231–232f
 Tramutoli, M., 43f
 Treagus, S.H., 1, 94f
 Treiman, A.H., 199
 Tremblay, A., 8f, 22f
 Trifonov, V.G., 239f
 Tromp, J., 199
 Trouw, R.A.J., 25f, 67, 84f, 88f, 90f, 111, 117f, 155f, 191, 229–231f
 Tsereteli, N., 4f, 122f
 Tsunogae, T., 40f, 42f, 55f, 231–232f
 Tuccimei, P., 204–205f
 Tullis, J., 146f
 Tullis, T.E., 157f, 226f
 Turtù, A., 159f
 Twiss, R.J., 173, 215f

U

Uchman, A., 58–59f
 Upreti, B.N., 217f
 Urai, J.L., 52f, 54f, 191–192f, 230f
 Ural, J., 173
 Uysal, I.T., 205f

V

Valenta, J., 160f
 Valero, L., 11f, 163f
 Van Baelen, H., 228f
 Van Daalen, M., 228f
 Van der Woerd, J., 240f
 Van Gent, H., 52f
 Van Loon, A.J., 31f, 58f
 Van Noten, K., 205f
 Vanduycke, S., 240f
 Vanhaverbeke, H., 240f
 Vanik, N., 111, 149–152f
 Vanneste, K., 240f
 Vannucci, R., 154f
 Vanossi, M., 154f
 Varazanashvili, O., 122f
 Venkatasivappa, V., 55f
 Venturi, F., 18f, 165f
 Verhaert, G., 240f
 Vernon, R.H., 73f, 231f
 Vernooij, M.G.C., 227f
 Vestroni, F., 240f
 Vezzani, L., 127f
 Vieira, M., 114f
 Vignaroli, G., 154–155f
 Vigorito, M., 237f
 Villa, I., 204f
 Viola, G., 115f
 Virgo, S., 191f
 Vissers, R.L.M., 91f, 154f

Von Huelsen, M.G., 146f
 Vrabec, M., 162f

W

Waelkens, M., 240f
 Walsh, J.J., 136f
 Waltham, T., 243f
 Wang, C., 12f
 Wang, S., 12f
 Warr, L.N., 246f
 Watterson, J., 136f
 Weatherley, D., 205f
 Webb, A.A.G., 214f
 Weinberger, R., 167f
 Welford, J.K., 238f
 Wendzel, J., 53f
 Wessel, Z.R., 111f
 West, Jr.D.P., 157f, 226f
 Whittington, A.G., 67
 Wibberley, C.A.J., 157f, 226f
 Wiersma, D.J., 84f, 117f
 Willemse, J.M., 191–192f
 Williams, M.L., 24f
 Williams, P.F., 24f, 215f
 Williams-Straud, S.C., 53f
 Woldrich, J.N., 160f
 Woodcock, N.H., 164f
 Wooden, J., 146f, 225f
 Wu, Z., 244f

X

Xiao, W.J., 42f

Y

Yajoui, Z., 142f, 216f
 Yakymchuk, C., 1, 2f
 Yamamoto, M., 83f, 217f
 Yamato, P., 153f
 Yang, Q.Y., 55f
 Yao, L., 158f
 Yellappa, T., 42f, 55f
 Yin, A., 7f, 214f
 Yin, H., 244f
 Yoshida, S., 100f
 Yuen, D.A., 67

Z

Zachrisson, E., 159f
 Zampieri, D., 156f
 Zanella, F., 53f
 Zartman, R.E., 40f
 Zavala, C., 58–59f
 Zazo, C., 239f
 Zeibig, S., 53f
 Zhang, C., 3f
 Zhang, Z.C., 55f
 Zhao, J.X., 205f
 Zheng, J., 244f
 Zijderfeld, J.D.A., 243f
 Živčić, M., 119f
 Zouhair, M., 120f
 Zulauf, G., 53f
 Zulauf, J., 53f
 Zupančič, P., 119f

Subject Index

Note: Page numbers followed by *f* indicate figures.

A

Abundant quartz amydules, pseudotachylyte vein, [206f](#)
 Alkali feldspar, [29f](#)
 Angular folds, tourmaline-bearing garnet-mica schist, [21f](#)
 Anhydrite diapir in rock salt, [53f](#)
 Antigorite mylonite and asymmetric sheared composite olivine-pyroxene clasts, [99f](#)
 Aplite dikes, [201f](#)
 Archaeoseismology, [239f](#)
 Archean gneiss fold, [61f](#)
 Asymmetric folds, [17f](#)
 Asymmetric isoclinal fold, [50f](#)
 Asymmetric quartz shadow, [73f](#)
 Augen gneiss/granite mylonite, Funatsu Shear Zone, [87f](#)
 Ayishan detachment, Karakoram fault, [12f](#)

B

Basaltic dikes, [202f](#)
 Bedding-cleavage relationship, [224f](#)
 Bent and microboudinaged magmatic epidote, [182f](#)
 Biotite fish, [90f](#)
 Biotite + kyanite-bearing micaschists, Num orthogneiss, [98f](#)
 Boudins/mullions
 asymmetric boudins, [176f](#)
 calc-schist
 boudinaged quartz veins in, [184f](#)
 rectangular boudinaged quartz veins in, [183f](#)
 chocolate tablet boudins, [182f](#)
 composite boudins, [175f](#)
 definition, [173](#)
 fracture planes, boudinaged quartz vein within metagreywacke, [174f](#)
 gray conglomerate overlying red mud horizon, Wine Strand, [189f](#)
 low-grade metamorphic carbonate sequence, domino boudins within, [185f](#)
 metaturbidites, boudinaged metabasalt layer enveloped by, [173f](#)
 migmatite gneiss sequence, boudinaged amphibolite layer, [176f](#)
 neoproterozoic quartzites, mullions and vertical columns, [186–188f](#)
 pinch and swell structures, [180f](#)
 precambrian orthoquartzite, Aravalli Supergroup, [188f](#)

quartz vein boudinaged, [183f](#)
 ultramylonitized peridotite, microboudinage structure in, [181f](#)
 Boudinaged and sheared vein, [185f](#)
 Boudinaged limestone block, [137f](#)
 Boudinaged mafic layer set in quartzofeldspathic paragneiss, [44f](#)
 Boudinaged sheath fold, [38f](#)
 Boudinaged, folded, and faulted limestones blocks, [137f](#)
 Breakthrough fault-propagation fold, [122f](#)
 Bridge structure, [238f](#)
 Brittle deformation, Mykonos Detachment, [129f](#)
 Brittle-ductile composite thrust shear zone, [142f](#)
 Brittle-ductile thrust shear zone, [159f](#)
 Brittle faults and lineations-1, [149f](#)
 Brittle fault zones
 accretionary wedge, [145f](#)
 active Hronov-Poříčí Fault Zone, main faults of, [160f](#)
 along-dip segmented normal fault and fault-related fold, [136f](#)
 amphibolite gneiss, fault plane, [152f](#)
 antiformal stack duplex, [128f](#)
 asbestos mineralization, structural control on, [154–155f](#)
 brittle tectonics, [147f](#)
 centimeter-scale top-to-NW brittle reverse fault, [133f](#)
 Coal Creek fault zone/Central Front Range, Colorado, [111f](#)
 coseismic damage and viscous flow, repeated cycles, [157f](#)
 Cretaceous Bhuj Formation, sand-shale sequence, [127f](#)
 Cretaceous clastics, synlithification faults in, [160f](#)
 curvilinear fault-bend folding, [125f](#)
 definition, [111](#)
 erosive tectonic tools, [149f](#)
 experimental fault gouge, overlapped slip-zone structures in, [158f](#)
 fault slickenside containing calcite slickenfibers, [147f](#)
 fold-and-thrust tectonic belt, [141f](#)
 gravitational effect, synsedimentary normal fault, [130f](#)
 high-al omphacite, [162f](#)
 Kaikoura, [161f](#)
 mesoscopic conjugate set, [120f](#)
 NNE-SSW-trending Olevano-Antrodoco-Sibillini oblique thrust ramp, [159f](#)

polished fault surface, [152f](#)
 quartzite pebble, N-dipping subvertical fault plane, [135f](#)
 quartzite pebble, subvertical fault plane cuts, [134f](#)
 Raša fault, fault zone of, [119f](#)
 SE-dipping subparallel curved fault planes, [135f](#)
 sinistral strike-slip faulted pebble, [134f](#)
 slickolites, [148f](#)
 small-scale faults, uniform set of, [130f](#)
 subvertical brittle shear Y-planes bound tangentially curved brittle P-planes, [121f](#)
 tectonic grooves, striae of, [148f](#)
 top-to-SW brittle sheared/reverse faulted sandstone, [141f](#)
 white/red gouge, [119f](#)
 Y- and P-brittle shear planes, fascinating development of, [133f](#)
 Brittle shear planes-1, [150f](#)
 Brittle shear planes-2, [150f](#)

C

Calc-silicate gneiss, fold, [42f](#)
 Caloris basin, [243f](#)
 Chaibasa Formation, [17f](#), [46f](#)
 Chert, folded layer, [37f](#)
 Chevron folds
 Paleogene sandstones and shales, [5f](#)
 with planar limbs and sharp/pointed hinge, [18f](#)
 Chlorite strain shadows, [74f](#)
 Chrystalls Beach Complex
 coastal Otago, New Zealand, [20f](#)
 dilatational jog, [86f](#)
 Cleavage refraction across heterolithic sandstone-shale, [87f](#)
 Coal Creek fault zone
 in central eastern Front Range, Colorado, [111f](#)
 fault core, [112f](#)
 red gouge, polarized light micrograph, [118f](#)
 white and red clay-rich gouge, plain light of, [119f](#)
 Coalescing thrust-related folds, [127f](#)
 Columnar joints, [203f](#)
 Compton Formation in southern Québec, [22f](#)
 Conjugate folds in Neoproterozoic marble, [49f](#)
 Continuous flattening of a folded package, [92f](#)
 Convolute structure in quartzite, [236f](#)
 Crenulation cleavage, [23–24f](#), [26f](#)

Crenulation schistosity, [22f](#)
 Crosscutting veins
 definition, [191](#)
 dilatant faults, [192f](#)
 gneissic foliations, quartz vein, [193f](#)
 limestone
 high-pressure cell in, [191f](#)
 semiductile shear zone in, [192f](#)
 mylonitized gneiss, quartz-rich vein, [193–194f](#)
 quartz vein network, [195f](#)
 thin-curved quartz vein, [195f](#)

D
 Deformation bands network, [225f](#)
 Deposited volcanoclastic succession, pyroclast deform, [238f](#)
 Detachment folds, [4f](#)
 Dharwar rocks, Basalt porphyry from, [223f](#)
 Disharmonic fold, [9f](#)
 Double wedge thrust, [123f](#)
 Doubly plunging fold
 the Late Paleocene to Eocene sandstone, [58f](#)
 with prominent axial depression, [46f](#)
 Drag fold, [10f](#), [132f](#), [194f](#)
 Ductile deformation, Livada Detachment, [71f](#), [92f](#), [226f](#)
 Ductile deformed lenticular feldspar porphyroclast, [101f](#)
 Ductile shear sense indicator, [88f](#)
 Ductile shear zones
 antigorite mylonite and asymmetric sheared composite olivine-pyroxene clasts, [99f](#)
 around m-scale delta-type asymmetric-feldspar clast, [78f](#)
 augen gneiss, post D₂, syn-D₄ ultramylonite shear zone in, [85f](#)
 boudinaged quartz veins, [83f](#)
 calc schist, type 1 flanking structure within, [78f](#)
 chloritoid, syntectonic microscopic porphyroblast of, [96f](#)
 classic shearband boudin, [79f](#)
 definition, [67](#)
 deformed amygdules, [100f](#)
 deformed radiolarian fossils, [101f](#)
 dilatational jog, [86f](#)
 domino style normal faults, [67f](#)
 ductile sheared quartz vein, [74f](#)
 extensional shear bands, [70f](#)
 feldspar σ -type porphyroclast, [75f](#)
 fine-grained recrystallized matrix, plagioclase feldspar porphyroclast in, [84f](#)
 fold-boudin, evolutive sequence, [93f](#)
 foliation parallel train of boudins, schistose quartzite, [75f](#)
 fractured garnet porphyroblast, [97f](#)
 Funatsu Shear Zone, augen gneiss/granite mylonite at, [87f](#), [215f](#)
 garnet bearing schist, sigmoidal quartz lens in, [76f](#)
 granite mylonite, polished slab of, [83f](#)
 heterolithic sandstone-shale, cleavage refraction across, [87f](#)

imbricate thrust structure in flysch, [162f](#)
 incipient localized dextral shear zones, [81f](#)
 initial fracture, typical paired shear zones to, [81f](#)
 K-feldspar delta- mantled porphyroclast, [78f](#)
 kyanite-garnet gneiss, [91f](#)
 localized heterogeneous shear zone, [80f](#)
 mylonitic garnet-micaschists, asymmetric sheared granite pebble, [90f](#)
 mylonitic micaschists, asymmetric quartz ribbon from, [99f](#)
 mylonitic peridotite cropping, [100f](#)
 mylonitic quartz-mica-feldspar-matrix, kinematically grown magnetite (mag) in, [89f](#)
 mylonitized micaschist, [90f](#)
 Num orthogneiss, biotite + kyanite-bearing micaschists from, [98f](#)
 olivine, microstructure of, [95f](#)
 paleoproterozoic S-type Lesser Himalayan Granitoids, plane polarized light, [73f](#)
 parallelogram/sigmoid mud unit, [94f](#)
 plane polarized light, syntectonic microscopic garnet under, [97f](#)
 post-D3 sigmoidal quartz vein in amphibolite, Bastar Craton, Sambalpur, [71f](#)
 precursor heterogeneities, heterogeneous ductile shear zones on, [80f](#)
 quartzite veinlet, [77f](#)
 sheared quartzofeldspathic gneiss, asymmetric quartz porphyroclasts in, [85f](#)
 shear fabrics display, [101f](#)
 sigmoid inclusion pattern, syntectonically grown garnet with, [100f](#)
 soft-sediment, sigma clasts/S-C structures in, [91f](#)
 spiral, early foliations, sheared microscopic garnet with, [96f](#)
 stacked-folds-boudins, [93f](#)
 strike slip fault system, duplex structure, [84f](#)
 top-to-SW sheared sigmoid quartz veins, [141f](#)
 trapezoidal boudinaged quartz vein, [234f](#)
 ultramylonitic peridotite, delta-like structure in, [95f](#)
 ultramylonitic shear zone, titanite porphyroclast in, [94f](#)
 winged δ -microstructure of olivine, [100f](#)
 Y-planes in mafic schist, sigmoid brittle P-planes bound by, [88f](#)
 Ductile to brittle deformation, [68f](#)
 Dyke, [82f](#)

E
 Eastern bank of Raman Nallah, [233f](#)
 En echelon veins, [136f](#), [146f](#)
 Eocene limestone-shale sequences, Siang fold-and-thrust belt, [7f](#)
 Erosive tectonic tools, [149f](#)
 Extensional fault affecting the Jurassic succession, [113f](#)
 Extensional fractures, [208f](#)

F
 Fault breccia, [129f](#)
 Fault core, Coal Creek fault zone, [112f](#)
 Faulted vein, [140f](#)
 Fault-propagation fold, [126f](#)
 Fault-propagation fold and growth strata, [122f](#)
 Fault slickenside
 of amphibolite gneiss, [152f](#)
 calcite slickenfibers, [147f](#)
 striae of erosive tectonic tools, [149f](#)
 striae of tectonic grooves, [148f](#)
 Fault zone/overlap zone in a sand-shale sequence, [127f](#)
 Flanking structure, calc schist, [78f](#)
 Flower structure in the Precambrian quartzites, [125f](#)
 Fluid activity and dyke, [197f](#)
 Fluid-flow and asbestos mineralization, structural control, [154f](#)
 Fluidization features, [156f](#)
 Fold and boudin, [179f](#)
 Folded amphibolite boudins, [181f](#)
 Folds
 alternate layers of ferruginous and quartzose materials, folded banded iron formation, [19f](#)
 banded gneiss, small-scale folds, [32f](#)
 Bastar Craton-Rengali Province boundary shear zone, rotation of F₂ fold hinges, [41f](#)
 boudinaged sheath fold, [38f](#)
 Bowmore crenulation cleavage, [24f](#)
 calcareous matrix, quartzofeldspathic layers interlayered, [48f](#)
 calc-silicate, doubly plunging round hinge isoclinal fold, [39f](#)
 calc-silicate gneiss, fold, [42f](#)
 chevron-like fold in amphibolite, dismantle block, [28f](#)
 continental collision, upright folds and folded boudins resulting from, [1f](#)
 curved axial plane, noncylindrical fold with, [47f](#)
 curved hinge line, plane noncylindrical fold with, [48f](#)
 Cuspate folds of quartz vein, Udaipur, Rajasthan, [15f](#)
 definition, [1](#)
 dolomitic host rock, tightly folded quartz vein in, [30f](#)
 dolomitic rock, folded quartz vein in, [43f](#)
 fault-bend-fold, [2f](#), [5f](#)
 folded anhydrite layers, [52f](#)
 folded layer of chert, [37f](#)
 folded migmatitic rock, [16f](#)
 folded quartz vein, Bhedaghat, Jabalpur, [15f](#)
 folded quartz vein within meta-greywacke, [49f](#)
 fractured anhydrite, red salt, [53f](#)
 garnetiferous banded gneiss, crenulation cleavage in, [33f](#)
 Gravifossum, [58–59f](#)
 Gulcheru Quartzite, [10f](#)

Higher Himalayan gneisses, [31f](#)
 hornblende gneiss, recumbent fold plunging toward E in, [34f](#)
 high-grade quartzite rock, type 3 interference pattern/hook-shaped pattern in, [57f](#)
 horizontal E-W fold plunges, complex folding with, [55f](#)
 interlayered sandstones and mudstones, [20f](#)
 intrafolial folds, [33f](#)
 isoclinally folded chert layers, [38f](#)
 Karakoram fault, Ayishan detachment, [12f](#)
 khaki green shale, Jitpur, [14f](#)
 kink folded intercalated layers of shales and limestones, [13f](#)
 lacustrine organic rich dolomitic lime mudstone/oil-shale deposits
 disharmonic folding in, [51f](#)
 disturbed layer in, [27f](#)
 large-scale folded banded magnetite quartzite and magnetite garnet biotite schist intercalation, [19f](#)
 Los Cabos Series quartzites, similar folds within, [26f](#)
 lower greenschist facies quartzite rock, two-generation folding, [56f](#)
 mafic mineral-rich gneiss, feldspathic layer, [59f](#)
 mesoproterozoic garnetiferous mica schist, cross-nichol of, [25f](#)
 mesoscale, recumbent fold in, [9f](#)
 mesoscopic disharmonic folding, [43f](#)
 metamorphosed granitic host rock fold, amphibole-rich layer in, [32f](#)
 metasedimentary rock, stretched quartz boudins in, [30f](#)
 meta-siltstone, disjunctive spaced cleavage in, [24f](#)
 mica gneiss, microfolded cordierite in, [22f](#)
 Middle Siwalik, micaceous dafla sandstone of, [31f](#)
 morphology and genesis of fold, [1](#)
 neoproterozoic marble, conjugate folds in, [49f](#)
 neutral folding, [41f](#)
 nonuniform geometry, ptigmatic folds of, [46f](#)
 originally rectangular intraformational mudstone rip-up clast set, [51f](#)
 out-of-syncline fold accommodation fault, [3f](#)
 overprinting crenulation cleavages, [25f](#)
 parasitic fold, [34f](#)
 planar limbs and sharp/pointed hinge, chevron fold with, [18f](#)
 potassium salt, structures of, [54f](#)
 prominent axial depression, doubly plunging fold with, [46f](#)
 quartz vein, fractured ptigmatic fold, [54f](#)
 rock salt, anhydrite diapir, [53f](#)
 sheath fold, [38f](#)
 Siang fold-and-thrust belt, eocene limestone shale sequences, [7f](#)
 subvertical (100/78S) ferruginous quartzite layer, elongated dome and basin structures on, [52f](#)

thrust fault and related footwall syncline, Mt Prena, [7f](#)
 Tibetan Himalaya, folded strata in, [8f](#)
 tight isoclinal folds
 intensely deformed lower limb of, [17f](#)
 limbs and hinge regions, [28f](#)
 tourmaline-bearing garnet-mica schist, angular folds in, [21f](#)
 tri-shear fault-propagation fold, [3f](#), [123f](#)
 type 3 fold interference, [47f](#)
 type 2 interference pattern, [56f](#)
 type 3 interference pattern of folds, [45f](#)
 undeformed massive sandstone turbidite beds, rhythmic occurrence of, [20f](#)
 Variscan basement, fold interference pattern, [45f](#)
 Folded strata in the Tibetan Himalaya, [8f](#)
 Fold interference, [40f](#), [57f](#)
 Fold-related deformed growth strata, [4f](#)
 Foliated high-grade quartzofeldspathic gneisses, fold, [40f](#)
 Fractures
 developing triangular zone, three nonparallel fractures intersect to, [222f](#)
 fine plumose structure, tension fracture surface, [218f](#)
 fractured anhydrite, red salt, [53f](#)
 fractured garnet porphyroblast, [97f](#)
 initial fracture, typical paired shear zones to, [81f](#)
 placing pens/inside Deccan basalt, rounded fracture plane, [222f](#)
 quartz vein, fractured ptigmatic fold, [54f](#)
 Fracture planes in sandstones, [209f](#)

G
 Garnet porphyroblast, fold, [23f](#)
 Gently inclined folded quartzite, [34f](#)
 Grain boundary area reduction (GBAR), [230f](#)
 Grain boundary migration (GBM), [199](#), [229f](#)
 Grain-size reduced scapolite, [29f](#)
 Granodiorite of the Eagle Wash Intrusive Complex, [146f](#)
 Gran Sasso thrust system, [7f](#)
 Granulite-to amphibolite-facies metamorphism, [1f](#)
 Gravifossus structure
 in heterolithic sediments of laminated siltstones and sandstones, [59f](#)
 in trough cross-stratified sandstone, [58f](#)

H
 Hanging-wall meso-scale buttressing, [115f](#)
 Heterogeneous ductile shear zone, [80f](#)
 Highly foliated garnetiferous gabbroic rocks, [17f](#)
 Hook-shaped folds, [1](#)
 Horst-graben structure, [138f](#)
 Hydrothermal breccias, [216f](#)

I
 Imbricate thrusts, accretionary wedge, [145f](#)
 Imbricate thrust structure in flysch, [162f](#)

Interlayered sandstones and mudstones, fold, [20f](#)
 Intracrystalline deformation microstructures, vein-quartz, [227–229f](#)
 Intrafolial folds, [33f](#)

J
 Jurassic accretionary complex, [101f](#)

K
 Kharshoti River, Tetuldhangra, Ghatsila, India, [14f](#)
 Kumbhalgarh Formation, [15f](#), [49f](#)

L
 Laminated lacustrine micrites, [130f](#)
 Large-scale folds, [2f](#)
 Light-colored biotite-hornblende gneiss, [1f](#)
 Lineation, [153f](#)
 Listric fault, [151f](#)
 Livada Detachment, [68f](#), [71f](#)

M
 Meso-scale fault, [132f](#)
 Meso-scale structures, [55f](#)
 Mesoscopic conjugate set, [120f](#)
 Micaceous Dafla sandstone of Middle Siwalik, [31f](#)
 Mica fish, biotite, [90f](#)
 Mineral fish, [90f](#)
 Minor folds, [6f](#)
 Mykonos Detachment, [105f](#)
 Mylonite, [76f](#)
 Mylonitism, pseudotachylyte veins, [196f](#)
 Mylonitic shear zone, [103f](#)
 Mylonitized porphyritic granite, [219f](#)

N
 Nonparallel faults, [121f](#)
 Nonperiodic fold, [35f](#)
 Normal fault, [124f](#), [127f](#)

O
 Omphacite, [162f](#)
 Overprinting schistosity, [211f](#)

P
 Plagioclase feldspar porphyroclast, [84f](#)
 Planar subvertical axial plane, [18f](#)
 Plastic strain and folded enstatite in a chlorite harzburgite, [207f](#)
 Plunging anticline, [12f](#)
 Plunging folds, [8f](#)
 Polyphase megascale deformation structures, [60f](#)
 Pseudoboudins, [184f](#)
 Pseudotachylyte, [161f](#)
 Ptigmatic folds, [42f](#), [46f](#), [50f](#)
 Puquios tectonic unit, [140f](#)

Q
 Quartz clasts in schistose rock, [212f](#)
 Quartzite-mica schist rock in Ghatsila, [13f](#)

R

Reactivated brittle fault, [151f](#)
 Recumbent chevron folds, [10f](#)
 Recumbent fold, [6f](#), [9f](#)
 Recumbent fold plunging, [34f](#)
 Red salt in fractured anhydrite, [53f](#)
 Relay between two fractures, [196f](#)
 Reverse fault, [145f](#)

S

San Marzal pericline, [213f](#)
 Santo Domingo anticline, [11f](#)
 Scapolite porphyroclast, fold, [29f](#)
 S-C fabric, [72f](#)
 Schistose quartz-andesite dike, boudin, [174–175f](#)
 Schistosity and intersection lineation, [212f](#)
 Serpentine slip fibers, [153f](#)
 Shear band, [70f](#)
 Sheared dyke, [131f](#)
 Sheared intercalations of quartzites and phyllites, [79f](#)
 Sheared quartz vein, [72f](#)
 Sheared sigmoid quartz veins, [86f](#)
 Shear-enhanced compaction bands, [210f](#)
 Shear structure, [89f](#)
 Shear zone and mineralization, [120f](#)
 Shear zones
 active slope morphology, 1400-m high East wall of Monte Viso, [214f](#)
 Akköy fissure-ridge, banded travertine across, [205f](#)
 amphibolite boudins folded and shortened by crustal shortening, [232f](#)
 ancient strike-slip fault, frictional to viscous transition in, [226f](#)
 augen gneiss, post D₂, syn-D₄ ultramylonite shear zone in, [85f](#)
 Bagaces Formation ignimbrites, curved columnar joints, [202f](#)
 Bastar Craton-Rengali Province boundary shear zone, rotation of F₂ fold hinges, [41f](#)
 bedding-cleavage relationship, [224f](#)
 biotite in mylonite, “V” pull-apart microstructure of, [230f](#)
 biotite rich granite with siltstone xenolith, Tistung Formation, [217f](#)
 bulbous chert nodules as structureless dense masses, carbonate rocks of Vempalle Formation, [237f](#)
 caloris basin, [243f](#)
 coastal area of the Shirakami Mountains, granodiorite mylonite in, [217f](#)
 columnar joints/colonnade and entablature, [199f](#)
 dark-colored pseudotachylyte, fault veins and injection veins of, [231f](#)
 Denizli extensional basin, Kamara active fissure-ridge in, [204f](#)

developing triangular zone, three nonparallel fractures intersect to, [222f](#)
 Dharwar rocks, Basalt porphyry from, [223f](#)
 dropped keystones and adjacent blocks, [240f](#)
 extension (tensile) joints in Archean granite gneisses, Perambalur, [223f](#)
 external Sierras Front, magnificent termination of, [163f](#)
 fine plumose structure, tension fracture surface, [218f](#)
 floor of Degas crater, [242f](#)
 fold-and-thrust system, [208f](#)
 Funatsu Shear Zone, augen gneiss/granite mylonite at, [87f](#), [215f](#)
 geothermal travertine area, Bridgeport, California, [203f](#)
 grain boundary area reduction (GBAR), [230f](#)
 grain coarsening, grain boundary migration (GBM) during, [199](#), [229f](#)
 Gulcheru Quartzite, Cuddapah basin, [10f](#), [235f](#)
 incipient localized dextral shear zones, [81f](#)
 initial fracture, typical paired shear zones to, [81f](#)
 injection vein, backscattered electron image of, [232f](#)
 localized heterogeneous shear zone, [80f](#)
 Long Ridge, southeast flank of, [205f](#)
 matchless amphibolite, Kuiseb Canyon, Namibia, [211f](#)
 microfaulted plagioclase grain, [231f](#)
 mud cracks produced by desiccation in modern sediment, [233f](#)
 paleoproterozoic Gulcheru Formation, filled sand cracks in, [235f](#)
 paleoproterozoic metasedimentary rock, crenulation lineations in, [214f](#)
 Palghat Cauvery shear zone, [42f](#)
 piggyback porphyroclasts, [219f](#)
 placing pens/inside Deccan basalt, rounded fracture plane, [222f](#)
 plagioclase in granodiorite, recrystallization of, [225f](#), [227f](#)
 precursor heterogeneities, heterogeneous ductile shear zones on, [80f](#)
 quartzite, plumose structure/hackle plumes in, [215f](#)
 regional folding, bedding-cleavage relation associated with, [216f](#)
 Roman theater, distributed left-lateral strike-slip deformation in, [239f](#)
 sandstones, cleavage planes in, [209f](#)
 sandy sediments, ripples in, [236f](#)
 seawall of crusader castle, Tartous, [240f](#)
 sedimentary dikes in lacustrine, [237f](#)
 semiductile shear zone in, [192f](#)
 shear zones in, [1](#)
 single basaltic lava flow, distinct colonnade and entablature tiers, [200f](#)
 small-scale fold, axial planar cleavage, [224f](#)
 spheroidally weathered Deccan basalt, [220f](#)

thrust fault related landform on innermost planet, Mercury, [241f](#)
 thrust sheet stacking, [210f](#)
 ultramylonitic shear zone, titanite porphyroclast in, [94f](#)
 vein-quartz, intracrystalline deformation microstructures in, [227–229f](#)
 volcanically buried Goethe impact basin, [242f](#)
 within sandstone, trapezoid-shaped mud inclusion, [234f](#)
 Sheath fold
 in Bormesorthogneiss in Maures-Tanneron Massif, [37f](#)
 in Chitradurga district, Karnataka, India, [36f](#)
 in Late Oligocene-Early Miocene sandstone and mudstone, [39f](#)
 Sigma-structure in ultracataclastic, [159f](#)
 Sigmoidal quartz lens, garnet bearing schist, [76f](#)
 Sigmoidal-shaped ductile sheared quartz vein, [77f](#)
 Slip events, Central Italy seismic sequence, [128f](#)
 Soft-sediment deformation, [105f](#)
 Spectacular dextral shear zone, [69f](#)
 Spheroidal weathering, [220–221f](#)
 Stacked thrust sheet, [113f](#), [126f](#)
 Sto. Domingo Anticline, [213f](#)
 Strike-slip faulting and iron oxide deposits, [114f](#)
 Strike-slip faults, [157f](#)
 Structural geological exercise, [234f](#)
 Structural geological interpretation from seismic image, [244–245f](#)
 Subvertical (100/78S) ferruginous quartzite layer, elongated dome and basin structures, [52f](#)
 Superposed tectonics, [143f](#)
 Symmetric phi-structure, [98f](#)
 Synsedimentary normal fault, gravitational effect, [130f](#)
 Synthetic and antithetic normal faults, [139f](#)
 Synthetic secondary shear plane, [83f](#)

T

Talchir Formation, [14f](#)
 Tension gashes, [142–143f](#)
 Thermal demagnetization, [243f](#)
 Thrust-sheet, normal fault, [124f](#)
 Thrust sheet stacking, [210f](#)
 Tight folding, [36f](#)
 Tightly folded quartz vein in dolomitic host rock, [30f](#)
 Tight recumbent kink folds, [18f](#)
 Tistung Formation, [217f](#)

U

Ultramylonitic zone, [104f](#)

V

Volcanically buried Goethe impact basin, [242f](#)